Exploring the γ-ray sky around the stellar cluster Westerlund 2 with the H.E.S.S. Experiment

DISSERTATION

zur Erlangung des akademischen Grades

doctor rerum naturalium

(Dr. rer. nat.)

im Fach Physik

Spezialisierung: Experimentalphysik

eingereicht an der
Mathematisch-Naturwissenschaftlichen Fakultät der
Humboldt-Universität zu Berlin

von

Tim Lukas Holch, M.Sc.

Präsidentin der Humboldt-Universität zu Berlin:
Prof. Dr.-Ing. Dr. Sabine Kunst

Dekan der Mathematisch-Naturwissenschaftlichen Fakultät:
Prof. Dr. Elmar Kulke

Gutachter/innen:	1. Prof. Dr. Thomas Lohse
	2. Prof. Dr. Petra H. Huentemeyer
	3. Prof. Dr. Marek Kowalski
Tag der mündlichen Prüfung:	25.11.2020

Selbstständigkeitserklärung

Ich erkläre, dass ich die Dissertation selbständig und nur unter Verwendung der von mir gemäß § 7 Abs. 3 der Promotionsordnung der Mathematisch-Naturwissenschaftlichen Fakultät, veröffentlicht im Amtlichen Mitteilungsblatt der Humboldt-Universität zu Berlin Nr. 42/2018 am 11.07.2018 angegebenen Hilfsmittel angefertigt habe.

Tim Lukas Holch

Berlin, 23.08.2020

Abstract

This work presents a study of the γ-ray emission in the GeV to TeV energy range detected in the region of the stellar cluster Westerlund 2, which is located in the Carina arm of the Milky Way. The high quality data analysed in this work was obtained with the imaging atmospheric Cherenkov telescopes of the High Energy Stereoscopic System (H.E.S.S.) from 2006 to 2015 and comprises a total of $\sim$ 80 h of observation time. This roughly doubles the size of the dataset compared to a previous publication by the H.E.S.S. collaboration on Westerlund 2 from 2011. From the calibrated telescope data, individual air shower events are reconstructed using a H.E.S.S. internal reconstruction algorithm based on Hillas parameters with a multivariate background suppression method. The high-level analysis of the dataset is performed using the open-source software `gammapy` and applies common methods and procedures from γ-ray astronomy to produce extensive spectral and spatial models for the observed emission. The selection of the most appropriate models is performed by applying the Akaike information criterion, a concept from information theory. The results of the analysis are further on combined with data and findings from other wavelengths to probe different emission scenarios for the detected γ-ray signals.

Besides hints of a diffuse emission and the detection of multiple hotspots, the main results of the presented studies are the significant detections of three extended γ-ray sources around Westerlund 2. In addition to the known sources HESS J1026–582 and HESS J1023–575, an elongated elliptical γ-ray source, referred to as "TeV *jet* cloud", is newly found to the south east of HESS J1023–575. The TeV *jet* cloud shows a striking spatial coincidence with an elongated cloud structure seen in CO and H I radio data, which may originate from the high energy jet of a mircroquasar or an anisotropic supernova explosion. Another intriguing spatial agreement is seen between HESS J1023–575 and a spherical shell of hydrogen gas of similar extension which may be the remains of a supernova remnant that has merged with the interstellar medium. HESS J1023–575 and the gas cloud structures symmetrically align along the major axis of the TeV *jet* cloud. This suggests a connection of the components in a hadronic emission scenario where cosmic rays interact with the gas clouds. Combining the masses of the clouds with the measured γ-ray flux yields a high cosmic ray enhancement factor, suggesting active particle acceleration. If a microquasar would be found around the best-fit position of HESS J1023–575, this could be the first detection of a galactic high energy jet at TeV energies with Cherenkov telescopes, similar to the recent detection of the jets of SS 433 at TeV energies with the HAWC experiment.

A connection of the detected γ-ray signals with the Westerlund 2 star cluster can not be ruled out on the basis of kinematic distance estimates from CO radio data. The morphology of the γ-ray emission over the whole region shows a strong energy dependency, which suggests an intricate source complex with multiple superimposed components. Overall, the densely populated region around Westerlund 2 provides various associations for the detected γ-ray emission including the stellar winds from the stars of Westerlund 2. A conclusive association can however only be made for HESS J1026–582, which is widely accepted as a pulsar wind nebula in connection with the pulsar PSR J1028–5819. HESS J1023–575 and the TeV *jet* cloud propose a hadronic emission scenario with the coinciding cloud structures. For each source individually, a number of objects can be considered as potential counterparts. In combination, a yet undetected microquasar would however explain the big picture. To draw further conclusions, more multi-wavelength data is nevertheless needed.

Kurzzusammenfassung

In dieser Arbeit wird eine Analyse der hochenergetischen γ-Strahlung in der Region um den galaktischen Sternhaufen Westerlund 2 präsentiert, der sich im Carina Arm der Milchstraße befindet. Der dazu analysierte Datensatz beruht auf Observationen von Westerlund 2 mit den Cherenkov Teleskopen des High Energy Stereoscopic System (H.E.S.S.) Experiments von 2006 bis 2015 und umfasst $\sim 80\,\mathrm{h}$ Beobachtungszeit. Im Vergleich zur letzten Publikation der H.E.S.S. Kollaboration zu Westerlund 2 aus dem Jahr 2011 verdoppelt sich somit die Größe des Datensatzes. Aus den kallibrierten Rohdaten werden einzelne Luftschauerereignisse mit einem H.E.S.S. internen Algorithmus rekonstruiert, der auf Hillas Parametern und einer multivariaten Untergrungunterdrückung basiert. Für die weitere Datenanalyse wird die open-source Software `gammapy` benutzt, wobei gängige Analysemethoden aus der γ-Astronomie zum Einsatz kommen, um morphologische und spektrale Modelle der γ-Emission zu erstellen. Zur Modellauswahl wird dabei das Akaike-Informationskriterium aus der Informationstheorie angewandt. Die Ergebisse der Datenanalyse und Modellierung werden außerdem mit Daten und Resultaten aus anderen Wellenlängenbereichen kombiniert, um Schlüsse auf den Ursprung der detektierten Signale zu ziehen.

Neben Hinweisen auf eine diffuse γ-Emission und mehrere Hotspots um Westerlund 2 ist die Detektion von drei ausgedehnten γ-Strahlungsquellen das Hauptergebnis der dargelegten Analysen. Zusätzlich zu den bekannten Quellen HESS J1023–575 und HESS J1026–582 wird hier die Detektion einer neuen, elliptischen Quelle süd-östlich von HESS J1023–575 präsentiert. Diese neue Quelle, als "TeV *jet* cloud" bezeichnet, zeigt eine auffallende räumliche Übereinstimmung mit länglichen Gaswolken, die in CO und H I Radio Daten gefunden wurden. Der Ursprung dieser Gaswolken könnte der Jet eines Mikroquasars oder einer anisotropischen Supernova Explosion sein. Eine weitere auffallende räumliche Übereinstimmung zeigt HESS J1023–575 mit einer sphärischen Gaswolke, die ihren Ursprung auch in einer Supernova haben könnte. HESS J1023–575 und die Gaswolken sind dabei symmetrisch zur Hauptachse der neuen elliptischen γ-Quelle ausgerichtet, was eine Verbindung der beiden Quellen in einem hadronischen Emissionszenario nahelegt. Aus den Wolkenmassen und der γ-Emission ergibt sich eine klare Verstärkung der kosmischen Strahlung in der Region um Westerlund 2, was auf aktive Teilchenbeschleunigung hindeutet. Sollte ein Mikroquasar nahe der Position von HESS J1023–575 gefunden werden, könnte dieses die erste Detektion eines galaktischen hochenergetischen Jets mit Cherenkov Teleskopen darstellen. Ein ähnliches Ergebnis war die Detektion der Jets von SS 433 bei TeV Energien 2018 mit dem HAWC Experiment.

Eine Verbindung der γ-Strahlunssignale mit dem Sternhaufen Westerlund 2 kann anhand von kinematischen Distanzabschätzungen mittels CO Radiodaten nicht ausgeschlossen werden. Die Morphologie der γ-Emission in der gesamten Region zeigt jedoch eine starke Energieabhängigkeit, was auf die Überlagerung verschiedener Quellen hindeutet. Im Allgemeinen ist die Himmelsregion um Westerlund 2 dicht mit stellaren Objekten besiedelt, die die detektierten γ-Signale potentiell erklären können, unter anderem auch die Sternwinde von Westerlund 2. Eine schlüssige Assoziation kann jedoch nur zwischen HESS J1026–582 und dem Pulsar PSR J1028–5819 gefunden werden. Für HESS J1023–575 und die TeV *jet* cloud können verschiedene Szenarien und Objekte die detektierte γ-Strahlung erklären. Ein noch nicht gefundener Mikroquasar würde jedoch zum derzeitigen Stand das Gesamtbild am besten wiedergeben. Um detailliertere Aussagen treffen zu können werden weitere Observationen der Westerlund 2 Region in verschiedenen Wellenlängenbereichen benötigt.

Acknowledgements

Many people were involved at various stages of realising this thesis and supported me during my time as a PhD student. I would specifically like to thank:

- Prof. Thomas Lohse for introducing me to the world of astroparticle physics and giving me the opportunity to write this thesis as a member of the H.E.S.S. collaboration, for supervising my work and for supporting my ideas and projects over the past years
- Dr. Ullrich Schwanke for all our discussions, constant input and thorough guidance
- Veronika Schneider and Yulia Jagodzinski for putting up with my bureaucracy
- Dr. Gerrit Spengler for many fruitful discussions on statistical analyses and the problem of model selection
- Dr. Emma de Oña Wilhelmi for all our discussions and input on Westerlund 2
- Prof. Petra H. Huentemeyer and Prof. Marek Kowalski for volunteering to review this thesis

I would also like to thank:

- All my coffee-drinking as well as non-coffee-drinking colleagues in the experimental particle physics group at Humboldt University for all the lunches and coffee breaks we had together
- The DAQ-team and all its past members for taking me in, showing me how to run a scientific data acquisition system and all the fun we had fixing and improving the DAQ
- The hessnn task group for all the exciting projects and good times we had
- The dustbase crew for our exciting research projects on the side
- Albert, Volker and Frikkie for the good times on site
- My friends Timothée, Philipp, Elias, Constantin, Gerrit, Torsten, Frank and Kalle for listening and supporting me

And of course I especially want to thank my parents, my brothers and Clara for bearing with me throughout this long but exciting journey.

This research has made use of the SIMBAD database, operated at CDS, Strasbourg, France (see also [1]).

This work also made use of image data from the second Digitized Sky Survey. The Digitized Sky Surveys were produced at the Space Telescope Science Institute under U.S. Government grant NAG W-2166. The images of these surveys are based on photographic

data obtained using the Oschin Schmidt Telescope on Palomar Mountain and the UK Schmidt Telescope. The plates were processed into the present compressed digital form with the permission of these institutions. The National Geographic Society - Palomar Observatory Sky Atlas (POSS-I) was made by the California Institute of Technology with grants from the National Geographic Society. The Second Palomar Observatory Sky Survey (POSS-II) was made by the California Institute of Technology with funds from the National Science Foundation, the National Geographic Society, the Sloan Foundation, the Samuel Oschin Foundation, and the Eastman Kodak Corporation. The Oschin Schmidt Telescope is operated by the California Institute of Technology and Palomar Observatory. The UK Schmidt Telescope was operated by the Royal Observatory Edinburgh, with funding from the UK Science and Engineering Research Council (later the UK Particle Physics and Astronomy Research Council), until 1988 June, and thereafter by the Anglo-Australian Observatory. The blue plates of the southern Sky Atlas and its Equatorial Extension (together known as the SERC-J), as well as the Equatorial Red (ER), and the Second Epoch [red] Survey (SES) were all taken with the UK Schmidt. Supplemental funding for sky-survey work at the ST ScI is provided by the European Southern Observatory.

Contents

Chapter 1

Introduction

Stellar clusters have been an intriguing potential source of cosmic γ-rays that emerged as possible association to observed γ-ray emission in the past decades. The cosmic ray acceleration and thus the production of γ-ray emission is thereby thought to be powered by the interaction and collision of stellar winds (i.e. material driven away from stars by radiative and/or thermal pressure) with their environment. Westerlund 2 is a young star cluster in the Carina arm of the Milky Way that hosts some of the most massive stars and binary systems known in our galaxy. γ-Ray emission has been detected in its vicinity since the 1980s and due to the initial lack of potential counterparts, the stellar winds of Westerlund 2 posed an interesting explanation for the observed γ-ray signal. Since then, the multiwavelength view of the Westerlund 2 region has changed dramatically, e.g. with a number of γ-ray pulsars and diffuse γ-ray and X-ray emission found in the region. The detection of coincident clouds of molecular and atomic hydrogen have brought a wider choice of hadronic emission scenarios into consideration. In a previous publication by the H.E.S.S. collaboration from 2011 [2], two individual γ-ray sources were reported, namely HESS J1023–575 which coincides with Westerlund 2 and HESS J1026–582 which is positioned $\sim 0.5^\circ$ east of HESS J1023–575 in galactic coordinates. While HESS J1026–582 was classified as pulsar wind nebula (PWN) associated with the pulsar PSR J1028–5819, the emission of HESS J1023–575 could not be conclusively associated. Besides a potential association with the pulsar PSR J1023–5746 as a PWN, stellar winds scenarios are still proposed as a viable alternative. In a later publication of results from CO observations conducted with the NANTEN2 and the MOPRA telescopes, Furukawa et al. discuss different possible emission scenarios for HESS J1023–575 including hadronic scenarios connected to coinciding cloud structures and introduce a potentially undetected microquasar as a CR source in the region [3]. The authors however end their discussion with the words "HESS J1023–575 remains as one of the most enigmatic TeV γ-ray sources" [3].

In this thesis at hand, the analysis of an extensive dataset from $\sim 80\,\mathrm{h}$ of observations with the telescopes of the H.E.S.S. experiment is presented to gain further insights into the physical processes acting in the Westerlund 2 region. Using the open-source software package `gammapy`, the morphology and spectral properties of γ-ray source components are determined. These results are then put into context with data and findings from other wavelengths to explore potential counterparts to the γ-ray signals and according emission scenarios.

Chapter 2 starts with a brief introduction to γ-ray astronomy with outlines of the underlying particle acceleration and γ-ray production mechanisms. In Chap. 3, the concepts of ground-based γ-astronomy with the H.E.S.S. experiment are presented. A focus is thereby put on an extensive fitting procedure for counting experiments to determine spectral and spatial models that describe the measured data. Additionally, the problem of model selection and the determination of a goodness of fit is outlined. This is followed by an introduction of the stellar cluster Westerlund 2 in Chap. 4, with a focus on detected γ-ray signals in the region. Details and results from the analysis of the regarded H.E.S.S. dataset are shown in Chap. 5, starting with an overall determination of significant emission and confirmation of previously published results before going into a detailed spectral and morphological analysis of individual source components. In addition to the analysis of H.E.S.S. data, the chapter also presents a high-level analysis of radio data from the NANTEN telescope and the Southern Galactic Plane Survey with additional comparisons to data in the MeV to GeV regime and a brief search for counterparts in the optical band. The results from these analyses are discussed in Chap. 6 in the context of different emission scenarios for the individual detected sources of γ-ray emission. A summary of the work and conclusions are finally presented in Chap. 7.

Chapter 2

γ-Ray Astronomy

In 1912, Viktor Hess published the detection of ionising radiation at high altitudes in the atmosphere, which he measured with electrometers during several balloon flights. This discovery is commonly considered as the birth of cosmic ray (CR) research which today has evolved to the wide field of astroparticle physics.[1] CRs thereby refer to protons, electrons and positrons (together often referred to as simply *electrons*) and heavier nuclei that have their origin outside the Earth's atmosphere. Besides these cosmic charged particles, also uncharged particles like cosmic photons and neutrinos have been detected on Earth. γ-Ray astronomy is a branch of astroparticle physics that studies such cosmic photons in the high energy (HE, $100\,\mathrm{MeV} \leq E \leq 100\,\mathrm{GeV}$), very high energy (VHE, $100\,\mathrm{GeV} \leq E \leq 100\,\mathrm{TeV}$) and recently also ultra high energy (UHE, $E > 100\,\mathrm{TeV}$, see [5]) regime. As photons are uncharged, they are not deflected by electric or magnetic fields along their path towards Earth, making it possible to trace them back to their origin. By now, a multitude of ground- and space-based detectors has been built to image the sky in γ-rays and explore the extreme environments producing such energetic photons. Today, after more than a century of astroparticle science, large amounts of data from different experiments are accessible. By combining the findings from γ-ray astronomy with data from other wavelengths, detailed models and theories can be developed for the observed emission across the electromagnetic spectrum, which can help to understand the underlying physical processes.

This chapter briefly introduces the processes that produce HE, VHE and UHE γ-rays and presents selected sources of galactic CRs that are subject to the discussions in following chapters. Extensive information and further details on astroparticle physics and γ-ray astronomy can be found in the literature as e.g. in the books by Gaisser, Engel and Resconi [6], by Longair [7] and by de Angelis & Pimenta [8]. Additional, several extensive reviews have been published in journals (see e.g. [9, 10, 11]).

[1] Viktor Hess was however not the first scientist to conduct such experiments. See [4] for a detailed historical review on the topic.

2.1 Cosmic particle accelerators

The sources of cosmic γ-rays are extreme environments in which charged particles can be accelerated up to energies exceeding $10^{20}\,\mathrm{eV}$ (see e.g. the so called *Oh-my-god particle* with an estimated energy of $> 300\,\mathrm{EeV}$ [12]). These charged particles can then interact with magnetic fields, photon fields or other particles to produce high energy γ photons by passing on parts of their initial energy via bremsstrahlung, scattering and secondary decay processes. In the following, basic mechanisms to accelerate CRs and different production channels for γ-rays are briefly outlined. A very extensive review on cosmic particle accelerators in general has been recently published by Hofmann & Hinton [9].

2.1.1 Cosmic ray acceleration

One acceleration mechanism that is thought to produce high energy CRs is the so called diffusive shock acceleration. The main concept was first formulated by Fermi in 1949 [13] and is thus often referred to as Fermi acceleration. The idea behind this mechanism is that charged particles are accelerated through collisionless interactions with moving plasma through the turbulent magnetic fields generated by the moving ions. Consider a cloud of plasma (or even partly ionised gas) moving with velocity u into a certain direction. A charged particle that enters the cloud will diffuse through it by elastic scattering on the turbulent magnetic fields inside the cloud until it exits the cloud again. Depending on the direction in which the particle enters and exits the cloud relative to its direction of movement, the particle can gain energy in a head-on encounter or loose energy in a tail-on encounter. On average, a particle will however gain energy as head-on collisions are more frequent. The average energy gain is thereby proportional to $(u/v)^2$ with v being the initial velocity of the charged particle, whereas $v \gg u$. This process is commonly referred to as second order Fermi acceleration.

The situation changes when the plasma moves with supersonic speed through an ambient medium. In this case, a so called shock develops which sweeps through its environment and compresses and heats the surrounding particles. The so called shock front is thereby the contact discontinuity between the compressed plasma and the unshocked medium. In the reference frame of the shock, the so called *upstream* region contains the unshocked particles of the ambient medium which move towards the shock front with velocity u_1. The shocked particles *downstream* of the shock front move in randomised directions, yielding a reduced bulk-velocity u_2 with which the plasma moves away from the shock front. A charged particle that emerges the shock front upstream with a velocity $v_0 \gg u_1$ can cross the shock front[2] and effectively experience a head-on collision with a plasma of velocity $u = |u_1 - u_2|$. Figure 2.1 shows a sketch of the charged particle approaching the shock

[2]The particle needs a certain energy to be able to cross the shock front, i.e. to be injected into the accelerator. For details on electron and ion injection in non-relativistic shocks, see e.g. [14, 15].

front with velocity v_0 as well as the upstream and downstream velocities of plasma in the reference frame of the shock front.

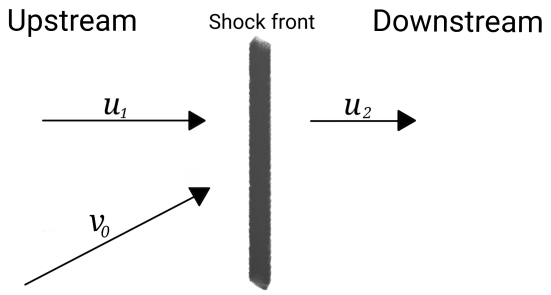

FIGURE 2.1: Schematic illustration of a shock in the shock front's reference frame. Upstream, plasma is approaching the shock front with velocity u_1. Downstream, plasma moves away from the shock front with velocity u_2. v_0 denotes the velocity of a charged particle approaching the shock front from upstream.

As in the case of a charged particle entering a cloud, the particle diffuses into the plasma. If it exits the plasma upstream, it gains energy and experiences another head-on collision with the approaching plasma. This way, charged particles can be temporarily trapped in shocks by repeatedly being reflected on the turbulent magnetic fields on either side of the shock front, gaining energy with every reflection. The energy gain per reflection is thereby proportional to u/v_0, therefore the name *first* order Fermi acceleration. As the probability for a charged particle to escape the shock after each reflection or "encounter" with the accelerator is finite, CRs with a power-law (PL) shaped energy distribution are produced (see e.g. [16]). This also holds for second order Fermi acceleration.

As the second order Fermi acceleration does not yield high enough acceleration to explain the observed CR spectrum regarding the velocities of cosmic gas clouds, the first order Fermi mechanism is the preferred explanation. Shocks in which charged particles can be accelerated via diffusive shock acceleration are thought to be produced by different kinds of phenomena that generate relativistic outflows such as pulsar wind nebulae (PWNe) and active galactic nuclei (AGNs). Other sites where diffusive shock acceleration is thought to take place are non-relativistic shocks as formed by supernova (SN) explosions and their associated remnants (SNRs). SNRs are thereby a prime candidate for the origin of CRs in our galaxy, as they can explain many characteristics that are observed in the spectrum of CRs [17].

More information on the physics of astrophysical shocks and the acceleration mechanisms like the complex interplay between magnetic fields that develop across shock fronts with charged particles travelling back and forth and their influence on the acceleration itself can be found in the literature. For further details and derivations of the second and first order Fermi acceleration, see e.g. chapter 12 in [6] or chapter 10 in [8]. An extensive review by Bell gives information and details on general CR acceleration [16], whereas

alternative acceleration mechanisms like unipolar conductors and magnetic reconnection are outlined in a review by Kotera & Olinta [18] and references therein.

2.1.2 γ-Ray production

High energy γ-rays can be produced by interaction processes of accelerated CRs in leptonic and hadronic processes as outlined in the following.

2.1.2.1 Leptonic scenario

In a leptonic scenario, a γ-ray is produced by an electron or a positron. The possible processes are thereby inverse Compton (IC) scattering and the production of bremsstrahlung or synchrotron radiation. Electrons and positrons can emit photons via bremsstrahlung or synchrotron processes when they are accelerated or decelerated in electric or magnetic fields.

A γ-ray produced by a high energy electron via bremsstrahlung can have up to 1/3 of the electron's initial energy [19]. The shape of the spectral distribution of the produced γ photons thereby follows the spectral distribution of the electrons. This is different for photons produced by synchrotron emission. For electrons with TeV energies, the energy E_{sync} of photons produced via synchrotron emission depends on the square of the initial energy of the individual electrons E_e and the strength of the magnetic field B the electrons move through and can be written as

$$E_{\mathrm{sync}} = 0.2 \frac{B}{10\,\mu\mathrm{G}} \left(\frac{E_e}{1\,\mathrm{TeV}} \right)^2 \mathrm{eV} \tag{2.1}$$

for an isotropic distribution of pitch angles[3] (the angle between the electron path and the magnetic field) as outlined in [21]. The energy spectrum of γ-rays that can be produced by synchrotron emission depends on the acceleration and the cooling times of the electrons and can result in spectra with complex patterns [11].

Synchrotron emission can however only produce VHE γ-rays under specific conditions as outlined in [22]. The main leptonic contribution to observed VHE γ-ray emission is thought to be produced via IC scattering. This process can produce γ-rays of up to $\mathcal{O}(100\,\mathrm{TeV})$ via the upscattering of low energy photons by relativistic electrons. A Feynman diagram of the process is shown in Fig. 2.2.

The photons can thereby originate from ambient photon fields such as the cosmic microwave background (CMB), optical photons from star light or photons from synchrotron

[3] This is commonly assumed but not necessarily the case as e.g. discussed in [20].

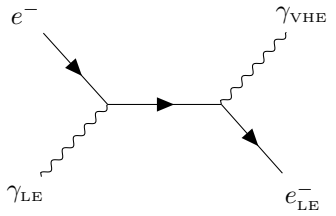

FIGURE 2.2: Feynman-diagram of inverse Compton scattering. A high energy electron upscatters a low energy photon to higher energies. The diagram is created with the Ti*k*Z-Feynman package [23].

emission. For sufficiently high radiation energy densities, populations of relativistic electrons can produce synchrotron photons that are then upscattered via IC scattering from electrons of the same population, a process also called synchrotron self-Compton emission [24]. The cross section for IC scattering is defined for two different energy regimes, called the Thomson regime for the low energies and the Klein-Nishina regime for the high energies. The Thomson regime holds, if the energy of the target photon in the electron's rest frame is much smaller than the electron's rest mass m_e, i.e. the non-relativictic case with $E_\gamma \ll m_e c^2$. In this case, the cross section is energy independent and can be described by the Thomson cross section

$$\sigma_{\mathrm{T}} = \frac{8\pi}{3} r_e^2 \tag{2.2}$$

with r_e being the classical electron radius $\frac{1}{4\pi\varepsilon_0}\frac{e^2}{m_e c^2}$. The Klein-Nishina regime holds when the target photon's energy in the electron's rest frame is much larger than the electron rest mass, i.e. the relativistic case with $E_\gamma \gg m_e c^2$. Here, the cross section is defined as

$$\sigma_{\mathrm{KN}} = \frac{3}{8}\sigma_{\mathrm{T}} \frac{m_e c^2}{E_\gamma} \left[\ln\left(\frac{2E_\gamma}{m_e c^2} \right) + \frac{1}{2} \right]. \tag{2.3}$$

It can be seen that σ_{KN} reduces towards higher energies, implying a steepening of the spectrum. The energy at which the Klein-Nishina regime begins depends on the energy of the target photons. For IC scattering on CMB photons the threshold is 300 TeV, on IR photons it is 10 TeV and on visible light it is 30 GeV [11]. A γ-ray spectrum of leptonic origin will thus show a spectral break at the energy of the transition between the Thomson and the Klein-Nishina regime. As for synchrotron emission, the cooling times of electrons define the shape of the resulting γ-ray spectrum. The cooling time, i.e. the time in which an electron will loose energy through IC scattering, is different for the Thomson and the Klein-Nishina regime in which cooling times are longer.

Overall, there are multiple factors that influence the spectral distribution of γ-rays of leptonic origin. In general, synchrotron and IC scattering produce two distinctive humps as seen in Fig. 2.3 for the example of the spectral energy distribution of the Crab Nebula measured by different γ-ray experiments. The inset shows the modelled synchrotron

and IC emission over the full electromagnetic spectrum. The transition between the γ emission from synchrotron and IC emission can clearly be seen at $\sim 5 \times 10^8$ eV in the blue datapoints.

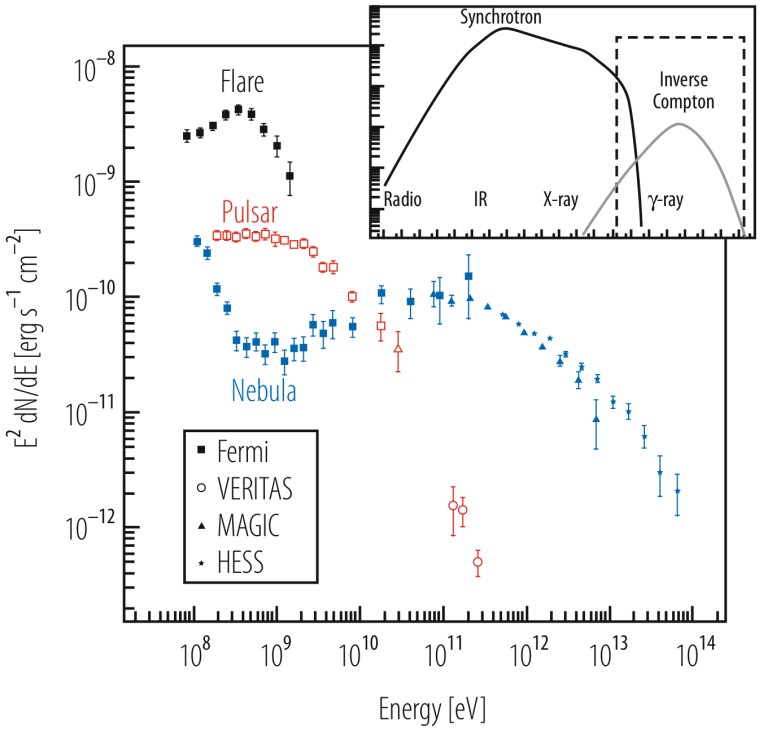

FIGURE 2.3: The plot shows the spectrum of the Crab Nebula measured by multiple γ-ray experiments with the inset illustrating the spectrum across the full electromagnetic spectrum. The figure is taken from reference [9], see Fig. 13.12 therein for further details.

As energetic CR electrons loose their energy through synchrotron emission on the timescales of $\mathcal{O}(10^5\,\mathrm{yr}/E_{\mathrm{TeV}})$ in our galaxy (with E_{TeV} being the electron energy in units of TeV), CR electrons with energies $> 1\,\mathrm{TeV}$ detected at Earth are assumed to be produced $< 2000\,\mathrm{pc}$ away [9]. γ-Ray emission of leptonic origin is thus thought to be confined to a closer region around an accelerator compared to CR hadrons.

2.1.2.2 Hadronic scenario

In addition to leptonic γ-ray production processes, γ-rays can also be produced in interactions of a primary hadronic CR with a proton, photon or heavy nucleus through the decay of secondary neutral pions (π^0). These are produced in a large fraction of hadronic interactions and decay into two photons with $> 99\%$ probability. In the inelastic scattering process of a primary hadronic particle, a number of secondary particles are produced proportional to the energy E_0 of the primary particle. The inelastic scattering of a CR proton p on a nucleus can be expressed as

$$\mathrm{p} + \mathrm{nucleus} \rightarrow \mathrm{p}' + \pi^{\pm} + \pi^0 + ... \quad \text{and} \quad \pi^0 \rightarrow 2\gamma; \quad \pi \rightarrow \mu\nu_\mu; \quad \mu \rightarrow e\nu_\mu\nu_e \tag{2.4}$$

where p′ is the scattered proton and $\pi^{\pm}$ are charged pions. Around half of the energy E_0 is thereby carried by the p′. The other half is transferred into secondary particles, with $\sim E_0/6$ in π^0s and thus in γ photons. The charged pions decay into a muon and a neutrino with muons eventually decaying into two neutrinos and an electron, making the detection of neutrinos from a γ-ray source a hint to a hadronic emission scenario.

The resulting γ-ray spectrum produced by a population of hadronic CRs of a power-law spectral distribution also follows a power-law shape at higher energies. Secondary electrons produced in the interaction can however produce a peak at lower energies via synchrotron emission.

2.1.2.3 Concluding remarks

The γ-ray spectrum of a source depends on a large variety of parameters regarding the initial acceleration processes of CRs and the properties of the local environment, which can all change on various timescales. Accelerated particles can interact with the ambient medium which in turn can influence the acceleration process. Furthermore, acceleration and cooling times of CRs also depend on the properties of their environment which can significantly influence the energy distribution of the produced γ-rays. Additionally, γ-rays propagating through the universe can scatter off photon fields which can change the spectrum observed at Earth. The challenge in γ-ray astronomy is thus to construct models that describe this interplay between different populations of interacting particles and environments and reproduce the properties of the observed γ-rays detected at Earth.

2.1.3 Selected sources of γ-ray emission

In the following, selected sources of galactic γ-rays are briefly introduced. These source types are further discussed in the context of the emission detect in the Westerlund 2 region below in Chap 6. For further general details regarding the γ-ray production and different source types see e.g. the reviews [9, 11] and references therein.

2.1.3.1 Supernova remnants

A supernova (SN) is the explosion of a star at the end of its life cycle. In general, the radiation pressure generated by the nuclear fusion processes inside the star can no longer compensate the star's own gravitational force causing the star to collapse. Stars of $\geq 8\,\mathrm{M}_{\odot}$ thereby create a so called core-collapse SN, where the infalling material gets reflected at the core and is ejected. For white dwarfs of $\sim 1.4\,\mathrm{M}_{\odot}$, the rising pressure in the collapsing star triggers the fusion of carbon which sets free enough energy to disrupt the star in a so called thermonuclear SN. In the explosions, material is ejected with velocities of several thousand km/s into the interstellar medium. The amount of kinetic energy

set free by highly massive stars can thereby exceed the order of 10^{51} erg. A shock wave travels outward from the explosion through the ambient medium which can be filled with matter ejected by the star in previous phases of its life. At the shock front, CRs can be accelerated via diffusive shock acceleration, resulting in the emission of photons across the electromagnetic spectrum. The resulting structures are referred to as a supernova remnants (SNRs) which expand over time until the pressure of the shock wave reduces to the pressure of the ambient medium. Depending on the mass of the star and the density of the ambient medium, this can take up to $\mathcal{O}(10^6\,\mathrm{yr})$. The spectrum of emission thereby changes over the different stages of the evolution of a SNR. Up to now, several SNR shells at different ages of their evolution have been observed in HE and VHE γ-rays. Prominent candidates are thereby RX J1713.7–3946 [25], HESS J1534–571 and HESS J1912+101 [26].

2.1.3.2 Pulsar wind nebulae

A pulsar is a rotating neutron star, which is the stellar remnant of a core-collapse SN. Pulsars can have strong magnetic fields which are twisted by their rotation and thereby power highly energetic outflows of magnetised plasma of electrons and positrons. These outflows, also called winds, have relativistic velocities and form a nebula over time which is referred to as a pulsar wind nebula (PWN). CRs can thereby be accelerated in the shock fronts of the pulsar winds colliding with the nebula. The rotational energy of the pulsar is thereby converted into accelerated particles. An important parameter of a pulsar is therefore its so called spin down power that drives the particle acceleration. For young PWNe, the pulsar winds can be confined inside the surrounding SNR shell. In the case of an asymmetric SN explosion, momentum can be transferred to the neutron star in a so called *kick*. The pulsar can thereby move away from its site of creation with a velocity of several 100 to $> 1000\,\mathrm{km/s}$. A pulsar can thus be located at a distance to its associated PWN. While PWNe are steadily bright in the HE and VHE regime, pulsed HE emission can often be detected directly from the pulsar. A large number of pulsars and PWNe have been detected up to now with the most prominent PWN being the Crab Nebula, which is commonly used as a standard candle in γ-ray astronomy.

2.1.3.3 Stellar clusters

Stellar clusters consist of a number of stars in close proximity to each other. They are often surrounded by dense clouds of gas from which the stars were initially formed. Massive stars are known to create so called stellar winds at different evolutionary phases of their lifecycle. These winds consist of ejected material from the outer layers of a star. In stellar clusters and especially in binary systems, the interaction of stellar winds are thought to produce shocks at which particles can be accelerated. By now, γ-ray emission has been detected in the regions of colliding wind binaries as well as stellar clusters such as

Westerlund 1 [27], the Cygnus cocoon [28] and recently from W 40 [29]. Westerlund 2 is another prominent star cluster from which γ-ray emission has been detected with several experiments as further outlined in Chap. 4.

2.1.3.4 Microquasars

Microquasars are smaller versions of quasars or active galactic nuclei on stellar scales. A microquasar is a binary system and consists of a rotating compact object such as a stellar mass black hole or a neuron star and a companion star from which the compact object is accreting matter. An accretion disk is formed around the compact object where the accreted material is heated and compressed, resulting in a so called corona of charged particles and photons. Furthemore, magnetic fields create relativistic jet outflows at the poles of the compact object which can extend up to several tens of parsecs into the interstellar medium (ISM). The interaction of magnetic fields, charged particles and photons from the jets, the accretion disk and the stellar winds of the companion star present complex sites where particles can be accelerated in leptonic and hadronic scenarios and photons up to VHE energies can be produced. Detailed discussions of γ-ray production mechanisms in microquasars can be found in the literature [30, 31]. The first detection of γ-rays from a microquasar was reported by the Fermi-LAT collaboration for Cygnus X-3 [32]. Since then, a number of microquasars have been detected in γ-rays, whereas the first detection of TeV γ-ray emission from microquasar jets has only recently been reported by the HAWC collaboration for the source SS 433 [33].

2.2 Modern γ-ray astronomy

Since the first experiments to study cosmic γ-rays in the 1960s, the field of γ-ray astronomy has greatly evolved. With numerous space- and ground-based detectors, a number of observatories today scan the γ-ray sky in different energy ranges. The most prominent space-based experiments are the Fermi Gamma-ray Space Telescope with its *Fermi Large Area Telescope* (Fermi-LAT) and the *Astro-Rivelatore Gamma a Immagini Leggero* (AGILE) satellite. Due to the limited size of these detectors, the accessible energy range is limited up to a few TeV as the traces of particles with higher energies can extend beyond the detector volume. For ground-based detectors, the energy threshold mainly depends on the photon collection area, whereas the detection of γ-rays towards lower energies becomes increasingly demanding. The main ground-based γ-ray observatories operating today are the *High Altitude Water Cherenkov Experiment* (HAWC), the *Major Atmospheric Gamma-ray Imaging Cherenkov telesopes* (MAGIC), the *Very Energetic Radiation Imaging Telescope Array System* (VERITAS) and the *High Energy Stereoscopic System* (H.E.S.S.). These ground-based experiments detect γ-rays in the energy range between a few tens of GeV up to $\mathcal{O}(100\,\mathrm{TeV})$. Together with space-based experiments,

the galactic and extragalactic γ-ray sky has been extensively monitored, which has lead to the detection of > 5000 individual γ-ray sources and large-scale diffuse emission regions. In the TeV regime, a total of ~ 200 sources has been detected. Even though many of the observed emission spectra and morphologies can be explained with theoretical models, the origin of the γ radiation for a large number of these sources is still uncertain. To get deeper insights, more data and detectors with better performance are needed. A new era of ground-based γ-ray astronomy is thus approaching with the construction of the *Cherenkov Telescope Array* (CTA) and the *Large High Altitude Air Shower Observatory* (LHAASO), which will significantly increase the sensitivity and resolution and extend the energy range of currently operating experiments. With the combination of γ-ray data with observations from other regimes of the electromagnetic spectrum as well as neutrino and gravitational wave data in so called multi-wavelength or multi-messenger analyses, astroparticle physics has become a valuable tool to test theoretical models and explore the most extreme phenomena in the universe.

Chapter 3

The H.E.S.S. Experiment and IACT data analysis

This chapter is devoted to the technical setup and main working principles of the H.E.S.S. experiment. The underlying physical concepts of ground-based γ-ray astronomy with imaging atmospheric Cherenkov telescopes (IACTs) as well as common analysis and reconstruction methods and calibration are briefly presented in the context of the H.E.S.S. experiment. Furthermore, tools and techniques used in the analyses presented in this work are outlined.

3.1 The H.E.S.S telescope array

The H.E.S.S. collaboration operates an array of IACTs in the Khomas Highland of Namibia at 1835 m above sea level, presenting optimal observation conditions for ground-based γ-ray astronomy. The array consists of five IACTs of two different sizes. Four telescopes (CT1–4) with a mirror area of $107\,\mathrm{m}^2$ (12 m dish diameter) are arranged in a square of 120 m side length with one larger telescope (CT5) with $614.5\,\mathrm{m}^2$ mirror area (28 m diameter) in the centre of the array. CT1–4 have a large FoV of 5° in diameter, making the telescopes optimal for studying VHE phenomena with energies from $\sim 30\,\mathrm{GeV}$ up $\sim 100\,\mathrm{TeV}$ in larger regions of the southern celestial sky including the galactic plane and its centre region. Figure 3.1 shows an image of the H.E.S.S. telescope array with the control room building in the foreground.

The first phase of H.E.S.S. (phase I) comprised CT1–4, which were built and commissioned from 2002 to 2004. In this setup, the telescope array operated until 2012. In 2012, CT5 was inaugurated and implemented into the existing array and its data acquisition, starting the second phase of the H.E.S.S. experiment (phase II) which made H.E.S.S. the first

FIGURE 3.1: The H.E.S.S. telescope array in the Khomas Highland of Namibia.

experiment to operate two different types of IACTs. Including CT5 significantly lowered the energy threshold of the system and improved the performance regarding the real-time reaction to transient phenomena with a new implementation of a fully automatic transients alert and real-time follow up system [34]. In 2015 and 2016, the cameras of CT1–4 were replaced [35]. The new camera electronics show significant performance improvements compared to the initial H.E.S.S. phase I cameras, allowing for a data taking rate increased by a factor of ~ 2.

3.2 Basic concepts of γ-ray astronomy with IACTs

This section briefly introduces the basic concepts of γ-ray astronomy using IACTs on the example of the H.E.S.S. experiment. For more detailed information, the reader is referred to the given references.

3.2.1 The Cherenkov effect

IACTs make use of the Cherenkov effect [36] to detect γ photons that enter the Earth's atmosphere. The Cherenkov effect comes into play when a charged particle moves through a dielectric medium with a velocity that is greater than the speed of light in that medium, in other words, if the so called Cherenkov condition

$$\frac{vn}{c} \geq 1 \tag{3.1}$$

is fulfilled, with v being the velocity of the charged particle, n as the refractive index of the dielectric medium and c being the vacuum speed of light. The Cherenkov effect can thus be seen as the electromagnetic pendant of a supersonic boom. The charged particle induces electromagnetic dipoles in the surrounding medium as it passes through. These dipoles swing back to an equilibrium in an asymmetric manner, causing the emission of so called Cherenkov photons. The angle θ at which Cherenkov photons are emitted along the path of the charged particle depends on the refractive index n and the ratio between the vacuum speed of light c and the velocity v and is given by

$$\theta = \arccos\left(\frac{c}{nv}\right). \tag{3.2}$$

The energy E emitted in Cherenkov photons per angular frequency interval $d\omega$ and travelled distance dx is given by the Frank-Tamm formula:

$$\frac{d^2E}{dxd\omega} = \frac{q^2}{4\pi}\mu(\omega)\omega\left(1 - \frac{c^2}{v^2n^2(\omega)}\right) \tag{3.3}$$

with q being the charge of the particle and μ the permeability of the dielectric medium (for a detailed derivation see e.g. [37, 7]).

For air, $\mu(\omega)$ can be assumed to be μ_0, the vacuum permittivity. To calculate the number N of Cherenkov photons that are emitted in a certain wavelength interval $d\lambda$ while neglecting the frequency dependency of n, the Frank-Tamm formula can be rewritten by using $d\omega = 2\pi d\nu$, $dE = Nhd\nu$ and $d\nu = -\frac{c}{\lambda^2}d\lambda$, resulting in

$$\frac{d^2N}{dxd\lambda} = \frac{2\pi\alpha Z^2}{\lambda^2}\left(1 - \frac{1}{\beta^2n^2}\right) \tag{3.4}$$

with the fine structure constant $\alpha = \frac{e^2}{4\pi\epsilon_0\hbar c} \approx \frac{1}{137}$ (e being the charge of an electron, the electric constant $\epsilon_0 = \frac{1}{\mu_0 c^2}$ and the reduced Planck constant $\hbar = \frac{h}{2\pi}$), $\beta = \frac{v}{c}$ and $q = Ze$ with Z being the charge number of the particle.

For a charged particle that moves through the atmosphere of the Earth, it is important to note that the refractive index changes with the density of air. Therefore, the number and emission angle of emitted Cherenkov photons also change with the atmosphere's density. With a generally increasing density towards the ground, it can be seen in Eq. 3.2 and Eq. 3.4 that the emission angle and number of emitted photons increases towards the ground. The height in the atmosphere where the Cherenkov condition given in Eq. 3.1 is fulfilled and thus the emission of Cherenkov photons starts depends on the air density as well as the rest mass m and initial energy E_0 of the charged particle entering the atmosphere, as seen in the equation of relativistic energy

$$E_0 = \frac{mc^2}{\sqrt{1-\beta^2}} \ . \tag{3.5}$$

By solving this equation for a given m and E_0 for β, the height in the atmosphere as of which a certain particle starts to emit Cherenkov photons can be determined with a given atmospheric model via Eq. 3.1. For charged high-energy particles, Cherenkov light emission typically starts at a height of several tens of kilometres. The emitted Cherenkov radiation of charged particles in the atmosphere is in the optical blue to UV range of the electromagnetic spectrum and peaks around 300 to 350 nm at the ground level due to absorption in the atmosphere.

3.2.2 Air showers

High energy cosmic γ-rays as well as leptons, protons and heavy nuclei that enter the Earth's atmosphere initiate so called air showers by decaying and producing cascades of secondary shower particles. γ-Rays undergo pair production and decay into e^+e^- pairs after they have travelled the mean distance of 1 radiation length through the atmosphere. From there on, the charged particles emit bremsstrahlung photons, which themselves undergo pair production as they travel through the atmosphere. A simple shower model for such electromagnetic (EM) cascades was first proposed by Heitler in 1936 [38], which is commonly used to approximately describe EM air showers. As the lateral spread of an EM air shower depends on the Coulomb scattering of the shower particles, the emission angles of the bremsstrahlung process as well as the opening angle of the pair production, an EM air shower has a rather well-defined shape that can be described by an ellipse. Protons and heavy nuclei interact with the atmosphere and decay in hadronic processes, initiating showers with hadronic, EM and muonic components. Due to the large number of possible decay and interaction processes in a hadronic shower, its propagation and shape can strongly vary. Compared to an EM air shower, a hadronic air shower penetrates deeper into the atmosphere and has a wider lateral spread with multiple sub-showers. For EM as well as hadronic air showers, secondary shower particles stop to decay further as their energy drops below a certain threshold as of which ionisation losses start to dominate. As this does not happen abruptly for all secondary shower particles at the same time, the shower cascade is said to fade as of a certain height in the atmosphere. For very energetic primary particles, the shower cascades can however penetrate down through the atmosphere with secondary shower particles reaching the ground level. Examples of an EM and a hadronic air shower are shown in Fig. 3.2.

Details about hadronic and electromagnetic air showers can be found in [6], with extensive derivations and outlines of detection techniques in Chap. 5, 15 and 16 of [6].

3.2.3 Detecting air showers with IACTs

As outlined above, cosmic high energy particles can initiate cascades of charged and uncharged particles in the atmosphere, producing extensive air showers. Depending on the energies of the charged particles in these showers, Cherenkov light is emitted which propagates down to the surface of the Earth where the light signal can be detected. An IACT facilitates a large spherical or parabolic mirror dish to capture this Cherenkov light of extensive air showers and project it into a highly sensitive camera which is positioned in the focal plane of the telescope[1]. An IACT thus records the intensity profile of air showers. The camera is therefore equipped with high performance photomultipliers (PMTs) that generate a voltage relative to the number of photons that hit a PMT. This voltage is read out via an analog to digital converter (ADC). A raw camera image consists of the individual ADC counts per pixel integrated over a few nanoseconds (16 ns for the H.E.S.S. telescopes in so called *charge mode*). This fixed readout window can however truncate the shower images of showers with energies > 1 TeV due to a dispersion of the arrival times of Cherenkov photons in the camera which can be larger than 16 ns. With the recently upgraded cameras on CT1–4, it is also possible to record the full waveforms of air showers (so called *sample mode*) [35].

The ADC counts of each individual PMT have to be converted to photoelectron (PE) counts for further analyses of the image data recorded by the telescopes. As the response of individual PMTs and the connected electronics can vary over time, frequent calibration of the camera is essential to correctly convert ADC counts to PE counts. Different calibration parameters have to be determined for each pixel:

- The noise level or *electronic pedestal*, which is determined by measuring the ADC counts with no light hitting the PMT.
- The response to a known light intensity (ideally single PEs) to determine a conversion coefficient to calculate PEs from ADC counts.
- The response for a uniformly illuminated camera also called *flatfielding*, to account for inhomogeneities in pixel responses (quantum and light collection efficiencies) over the camera.

Additionally, the reflectivity of an IACT's mirror dish has to be monitored, which can be done by analysing the rings of Cherenkov light produced by muons (see [40] for a very detailed study on IACT calibration using muon rings). A detailed description of the full calibration procedure of the initial H.E.S.S. cameras can be found in [41] with the calibration procedure of the upgraded cameras in [35].

[1] See [39] and [35] for details on the design of the small H.E.S.S. telescope structure and the recently upgraded cameras.

The imaging air Cherenkov technique uses the Earth's atmosphere as a calorimeter, which has the advantage that it can yield very large effective detection areas of $\mathcal{O}(10^5)\,\mathrm{m}^2$ and above. A disadvantage however is that atmospheric conditions can be highly variable and thus difficult to describe accurately. This sets a limit on the achievable accuracy of the measurements with an IACT and introduces systematic uncertainties (see also Sec. 3.5), especially when data taken under different conditions is combined. Due to the short duration of a few nanoseconds and the high frequency of air shower signals falling into the large detection area of an IACT, high performance electronics and trigger algorithms are essential to capture images of individual air shower events[2]. To increase the overall performance, current IACT based experiments make use of arrays of multiple telescopes to perform stereoscopic observations of air showers. This increases the sensitivity of a system and significantly improves the direction and energy reconstruction of primary shower particles.

Figure 3.2 shows a schematic illustration of how IACTs detect a cosmic high energy γ-ray (*left* panel) and proton (*right* panel). The primary particles initiate air showers that produce a distinctive distribution or pool of Cherenkov photons at the ground level. An IACT that is located within this pool of Cherenkov light can capture a fraction of the photons to record an image of the air shower. Due to the different decay processes in EM and hadronic air showers, the resulting air shower images have characteristic shapes which can be used to separate EM from hadronic shower events in the data analysis. Furthermore, the fraction of initial energy that ends up in Cherenkov photons in a hadronic air shower is around 1/3 compared to an EM air shower.

3.2.4 Monte Carlo simulations

In an IACT data analysis, Monte Carlo (MC) simulations set the basis for a chain of multiple analysis steps that are necessary to reconstruct a primary shower particle's properties. In general, a model has to be built that predicts the detectors' response to defined shower events that are observed under defined observation conditions. Recorded shower images can then be compared to this model to determine the properties of primary shower particles. The full simulation of a single shower event comprises multiple steps which make MC simulations computationally very demanding:

1. Simulate the air shower cascade initiated by the primary particle of defined properties (e.g. particle type, initial energy, altitude and azimuth of the origin, incident angle, atmospheric conditions).

2. Simulate the according propagation of emitted Cherenkov photons through the atmosphere.

[2]The trigger system of the initial H.E.S.S. telescope system is outlined in detail in [42].

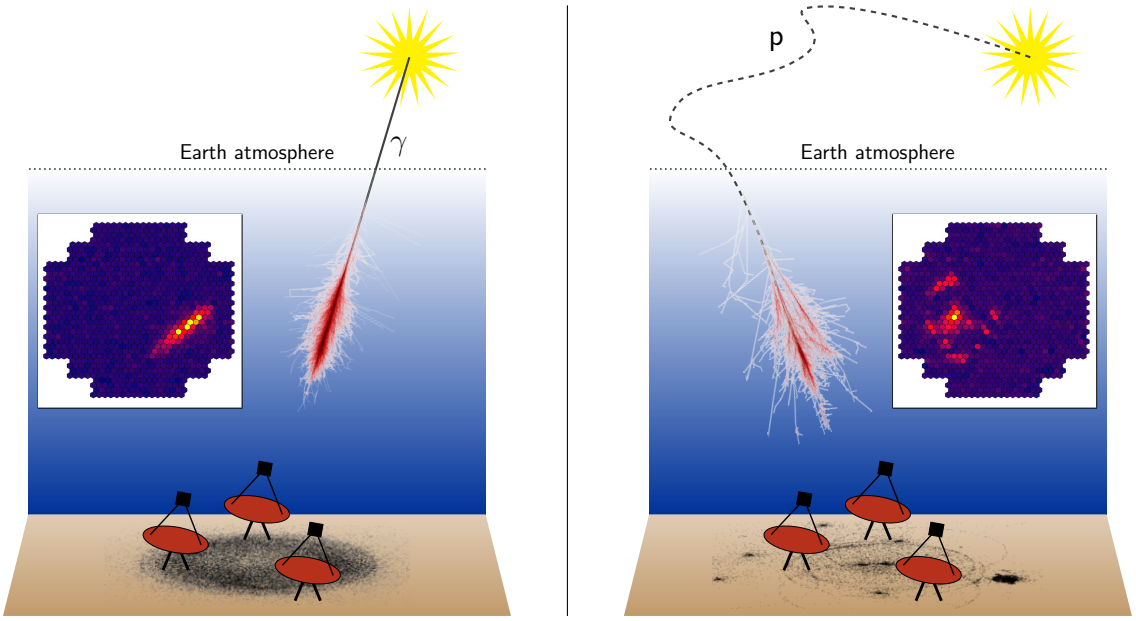

FIGURE 3.2: Schematic illustration of IACTs detecting extensive air showers initiated by a high energy γ-ray (*left*) and a high energy hadron (*right*). The CR source is illustrated by the yellow star. The red tracks depict the paths of secondary shower particles as determined in MC simulations (initial energy of 100 GeV each, see [43]). On the ground, the distributions of Cherenkov photons are shown in black (300 GeV γ-ray and 1 TeV hadron, see [44]). The insets exemplary show calibrated images of the respective shower types recorded with an IACT.

3. Simulate the detector's response to this Cherenkov light signal for a defined state of the system (e.g. camera configuration and electronic signal processing, telescope pointing position, mirror dish reflectivity).

As the detector's state can change over time due to hardware degradation and/or changing configurations, it is necessary to frequently monitor the system state and adapt the simulation parameters accordingly. As MC simulations are computationally very expensive, the state of a telescope array is usually determined for given time intervals also called *phases*. For the data taken in a certain phase, a matching set of simulations is then generated. To reduce systematic uncertainties and increase the reconstruction accuracy, the time intervals for which simulations are generated can be reduced. This has led to the development of so called *run wise* simulations [45]. In this scheme, simulations are generated for individual observation units also called *runs* for time intervals < 30 min. With this approach, detailed changes of the detector such as temporary hardware failures (e.g. broken pixels) and observation specific conditions (e.g. the specific night sky background) can be taken into account.

For the simulation of air shower cascades and the according Cherenkov light distribution, the software package `CORSIKA` [46] is frequently used. To simulate the responses of IACTs to these air showers, `CORSIKA` can be combined with the software package `sim_telarray` [47]. This combination is also used for the dataset presented in this work.

3.3 IACT event reconstruction

The properties of primary shower particles are reconstructed from calibrated shower images, taking into account the conditions under which the observations were performed. The main properties of interest are thereby the particle type, the position on the sky from which the initial particle originated as well as its initial energy. In the following, the main ideas for the reconstruction of these parameters are briefly outlined.

3.3.1 Extracting the γ-ray signal

The data recorded by IACTs consist of images of hadronic and EM air showers. While hadronic showers are much more abundant, the EM air showers are of primary interest. To extract these EM shower events, the shower images can be parametrised to group the events in phase spaces where shower types can be well separated. As EM showers show a rather confined elliptical shape compared to the wider spread of hadronic showers, describing the shower images with ellipses is a common approach which was first proposed by Hillas [48]. The shower images are modelled with a 2-dimensional ellipse, resulting in a set of parameters that describe the spatial distribution of PE counts in the image. To reduce background noise and night sky background, image cleaning methods can be applied prior to the fitting process. Five parameters that describe the dimensions and orientation of an elliptical shower image are illustrated in Fig. 3.4. Additionally, the total amplitude or *size* of a shower image is used as a descriptive parameter.

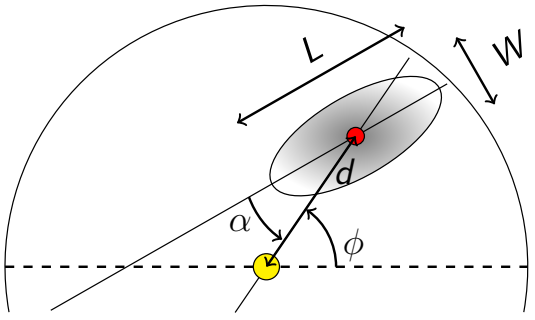

FIGURE 3.3: Parametrisation of an elliptical shower image. The red point denotes the centre of gravity of the image. The yellow point marks the centre of the camera plane. The dimensions and orientation of the so called shower ellipse are then defined by two angles and three distances.

To distinguish between EM (rather elliptical) and hadronic (in general rather non-elliptical) shower images, the ratio between parameters such as the width W and length L of a fitted ellipse can be used to define thresholds or so called *cuts* to decide if an event is accepted or rejected as γ-like signal. Introducing parameters determined from MC simulations, the parametrisation can be extended to also take into account statistical fluctuations. Furthermore, the shower images from stereoscopic observations can be combined to define scaled parameters that parametrise the whole air shower event instead of individual

camera images. This yields the Hillas based cut parameters *mean scaled width* and *mean scaled length* as e.g. applied in the H.E.S.S. event reconstruction as outlined in [49]. By introducing multivariate analysis techniques such as boosted decision trees, it has been possible to significantly improve the sensitivity of cut-based γ-hadron separation [50]. These boosted decision tree classifiers are also applied in the event reconstruction for the dataset analysed in this work.

3.3.2 Direction reconstruction

The direction from which the primary particle of an EM air shower originated can be well reconstructed from stereoscopic air shower observations by determining the intersection point of the major axes of the shower ellipses in the camera coordinate system[3] as illustrated in Fig. 3.4. The distance of this intersection point to the centre of the camera in the camera coordinate system is also called *offset*. Taking into account the telescopes' pointing position, the origin of a primary particle in celestial coordinates can then be determined via multiple coordinate transformation steps.

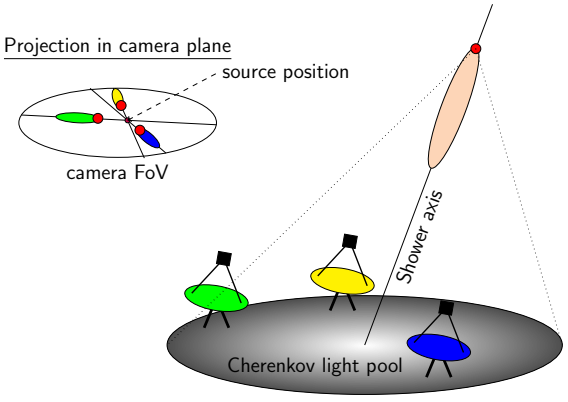

FIGURE 3.4: Illustration of a stereoscopic observation of a γ-induced air shower (light orange ellipse). The shower axis in the individual telescope images goes along the major axis of the projected ellipse. The interception point of the major axis of the projected shower ellipses in the camera coordinate system is the origin of the primary shower particle. See [51] for details on this approach.

The precision of this method depends on the accuracy with which the major axes of the shower ellipses can be determined. This in turn strongly depends on the extension and intensity of the shower ellipses in the camera images as well as the camera resolution. The shape and extension of a shower ellipse is strongly influenced by the so called impact parameter of the air shower. This parameter describes the distance between a telescope and the main shower axis and is thus defined for each observing telescope individually. Figure 3.5 shows a schematic illustration of a γ-ray induced air shower (not to scale) with simulated shower images seen by four telescopes. The according impact parameters projected onto the ground are marked by dashed lines.

[3] A detailed study on different direction reconstruction approaches and how to determine the interception point of the main shower ellipses' axes for stereoscopic IACT observations can be found in [51].

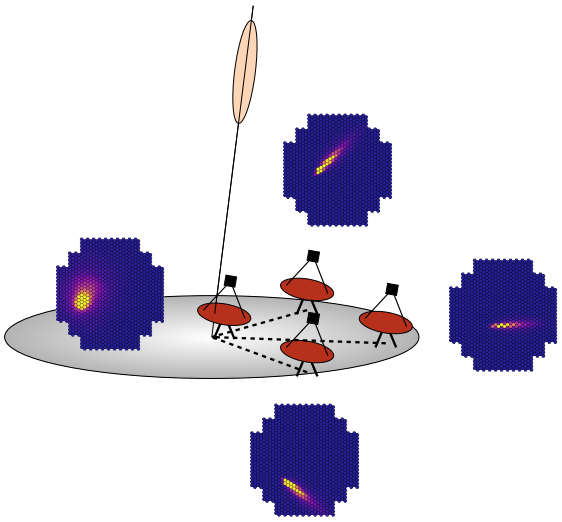

FIGURE 3.5: Schematic illustration of an array of four IACTs observing a γ-induced air shower. The shower ellipse is marked by the orange ellipse with the Cherenkov light pool marked by the grey shaded region. The distance between the main shower axis' interception point with the ground level and a telescope, the so called impact parameter, is marked by dashed lines. It can be seen how the impact parameter influences the projected shower image in the different telescopes' focal plane.

A precise direction reconstruction of γ-like air showers also requires an accurate pointing of the telescopes as well as an accurate alignment of the mirror facets on the telescope dishes. Additionally, varying deformations of the telescope structures at different pointing positions have to be taken into account. Apart from the pointing error itself (i.e. the deviation between the observed and expected position of a projected point-like light source in the focal plane), the so called point spread function (PSF) is an important parameter. It describes the width of a projected point-like light source in the focal plane of a telescope, which can strongly vary depending on the position of the light source in the telescope's field of view. Frequent pointing calibrations can be performed to model pointing errors and the PSF for the telescopes pointing to different positions in altitude and azimuth and light sources at different positions in the FoV. This is usually done by pointing the telescopes at bright stars and determining the position and spread of the projection on the closed lid of the telescope cameras. This way, a detailed model can be built to correct for pointing errors and PSF variations in the event reconstruction. A detailed outline of the mirror alignment procedure and PSF determination for the H.E.S.S. telescopes can be found in [52].

The precision with which the direction of an air shower can eventually be reconstructed depends on the accuracy of the optical setup of the telescopes (pointing error and PSF) as well as on the accuracy with which the major axes of the shower ellipses can be determined in the individual camera images. In combination, the accuracy with which the position of a γ-ray source can be determined with Cherenkov telescopes can be of the order of a few arcseconds [53], whereas the angular resolution strongly depends on the energy of the individual air shower and the pointing altitude of the telescopes. Often, a general angular

resolution of $\lesssim 0.1^\circ$ is stated for the resolution with which IACTs such as the H.E.S.S. telescope array can reconstruct the origin of individual air-showers.

3.3.3 Energy reconstruction

The energy of an air shower is proportional to the number of secondary particles and thus to the total number of produced Cherenkov photons. To estimate the total light content of an air shower it is however important to know the distance of a shower axis to the telescope to solve the ambiguity of a shower with lower energy located close to a telescope and a shower with higher energy that is located farther away. The total energy can thus be estimated by combining the total number of PEs measured in the camera with the impact parameter which can be reconstructed from the stereoscopic shower images. Using MC simulations for which the *true* shower energy is known and reconstructing the energy from the simulated shower images, energy migration matrices can be constructed to predict the bias and resolution of the energy reconstruction.

3.3.4 The lookup table approach

As outlined above, the intensity profile of an air shower as recorded by an IACT is strongly influenced by a large set of shower parameters and observation conditions such as telescope pointing, offset, initial energy and impact distance of the shower. To accurately reconstruct a primary shower particle's properties, the possible variations in shower images have to be taken into account. This can be done by generating large sets of MC simulations for γ-ray point sources of a given energy spectrum at different pointing altitudes and offsets with random impact distances. These events are then grouped by their parameters in tables to determine statistical properties and variations for different bins of the phase space. After reconstructing a shower's direction and impact parameter, lookup tables can be used to determine further shower parameters like the mean scaled width and length used to extract γ-like shower events. Depending on the simulated parameter ranges, bin sizes have to be chosen appropriately to allow for sufficient statistics in each bin. In the final event reconstruction, the bin wise properties can then be interpolated between neighbouring bins.

3.3.5 Advanced reconstruction algorithms

Besides the parameter based geometric reconstruction outlined above, advanced reconstruction algorithms have been developed within the H.E.S.S. collaboration as presented in the following.

3.3.5.1 Template and semi-analytic model fitting

Instead of parametrising the shower images, the image data can also be fitted directly to a model that predicts the shape of a shower image for given conditions and shower parameters. This can be done by using a semi-analytical shower model as done in the *Model* analysis developed for H.E.S.S. data analyses [54, 55]. Another approach is to generate shower image templates directly from MC simulations as done in the *ImPACT* shower reconstruction algorithm also used for H.E.S.S. data analyses [56].

3.3.5.2 Event reconstruction with convolutional neural networks

In recent years, machine learning techniques based on artificial neural networks have become a tool of choice when it comes to analysing large and complex data sets. With significant developments in parallel computing for tensor- or grid-like data using GPUs (graphics processing units), deep convolutional and recurrent neural networks have become very popular in the overall field of so called deep learning. In γ-ray astronomy, deep learning techniques pose an attractive solution to incorporate state-of-the-art machine learning techniques to refine or complement common event reconstruction algorithms. Within the H.E.S.S. collaboration, the author of this work has been participating in proof of concept studies to apply deep learning methods for particle identification as well as direction and energy reconstruction using convolutional neural networks [57, 58]. Furthermore, the author co-developed a software library to process hexagonally sampled data in the deep learning framework `pytorch` [59]. This software enables the direct processing of H.E.S.S. telescope image data with convolutional and recurrent neural networks, as the telescope images have hexagonal pixels.

In a recent study, deep learning based classifiers have been combined with existing advanced reconstruction algorithms in H.E.S.S. data analyses, showing a significantly improved performance [60].

3.4 High-level analysis, software and tools

This section presents the general concepts of high-level analyses of IACT data as employed in this work. The data thereby consist of the directional information (origin), the energy and the arrival time of signal-like shower events. In combination with the instrument response functions (IRFs) like energy dispersion, point spread function (PSF) and the exposure, analysis results like sky maps and energy spectra can be obtained. In the following, the main processes of creating sky maps, calculating detection significances, extracting spectral information and fitting the data to spatial and spectral models is outlined.

3.4.1 Data selection and reconstruction configurations

The first step in the analysis of H.E.S.S. data is to define criteria for data quality selection. The quality of a unit of H.E.S.S. data, a so called *run* (typically 28 min of observation), is assessed via multiple run parameters such as e.g.

- Stability of trigger rates to assess atmospheric conditions
- Run duration to avoid potential technical difficulties
- Telescope participation and number of active camera pixels to assess the quality of stereoscopic reconstruction
- Telescope pointing altitude and accuracy

Two levels of quality selection criteria are implemented in the H.E.S.S. event reconstruction scheme as applied in this work. The criteria are referred to as *detection* and *spectral* selection, where the *spectral* selection has the tightest set of criteria, thus rejecting more runs than the *detection* criteria to achieve highest data quality.

With a chosen set of quality selection cuts, the configuration for the event reconstruction has to be defined. This configuration defines cut parameters which are applied to individual air shower events within a run to define the parameter ranges for γ-like signal events. Cuts are e.g. defined for the minimum number of PE counts in a shower image and the Hillas parameters. For this, three main configurations are available in the applied H.E.S.S. event reconstruction scheme[4]

- *Standard cuts*: Optimised for strong γ-ray sources with power law spectrum with index of $2 \leq \Gamma < 3$; mainly used for spectral studies;
- *Hard cuts*: Higher energy threshold and angular resolution than standard cuts; optimised for faint sources with a power law spectrum with index of $2 \leq \Gamma < 3$; can be used for spectral an morphology studies;
- *Loose cuts*: Lower energy threshold and thus angular resolution compared to *standard* cuts; optimised for very bright γ-ray sources with a power law spectrum with index of $\Gamma > 3$;

Depending on the type of the analysed source, the instrument response functions (IRFs) can be optimised for point-like or for extended sources. These configurations can furthermore be combined with a choice of γ-hadron separation (cuts on Hillas parameters or boosted decision tree classifiers) and event reconstruction algorithms (Hillas parameter

[4]See also [61] for details on cut configurations.

based or advanced reconstruction). With the defined quality selection and reconstruction configuration, the final list of reconstructed γ-like events can be generated. This list includes the reconstructed properties of γ-like events that are regarded for the high-level data analysis.

3.4.2 Sky maps

A sky map is a 2-dimensional histogram that contains arbitrary properties of a region of the celestial sky, represented in spatial bins. In order to map a patch of the spherical sky onto a flat plane, a projection is needed. There are multiple projections with specific properties (e.g. conserving distances or areas) which are thus more or less suitable, depending on the conducted analysis. Also the position of the regarded sky region in the adopted coordinate system and the extension of the region have to be taken into account to make an appropriate choice. As the region analysed in this work is relatively small with around $5^\circ \times 5^\circ$ and positioned very close to the galactic plane, all sky maps presented in this work are generated in galactic coordinates with the plate carrée projection, which is an equidistant cylindrical projection. Positions are given in galactic longitude l and galactic latitude b.

From the dataset of γ-like events that pass the cut parameters of the reconstruction, so called count maps can be directly generated by spatially binning the distribution of air shower events. Depending on the total number of events and the bin size, the bins of a sky map may only be sparsely filled. To get a better visualisation, it is thus common to correlate the bins of a sky map with Gaussian or disk kernels of approximately the width of the uncertainty of the air shower direction reconstruction. As the acceptance for air showers and thus the exposure across the field of view of an IACT is not constant[5] and as a dataset can consist of multiple observation runs with different pointings, the raw count data has to be corrected for the inhomogeneous exposure in order to make the bin contents comparable across the map. Figure 3.6 shows a raw count map, a correlated count map and an exposure scaled count map of a simulated IACT observation. It can be seen in the sky maps that γ-like events are detected all over the sky map. This background is caused by cosmic ray-induced showers from hadrons, electrons or heavy nuclei that are misclassified as γ-like in the reconstruction. To extract the actual γ-ray signal, the background has to be modelled as outlined in the next section.

3.4.3 Background estimation

The raw counts in each bin or arbitrary region of a sky map are expected to be the sum of potential signal events and a number of background events. The background consists

[5] The acceptance also depends on the applied cut configurations in the reconstruction and the observation zenith angle.

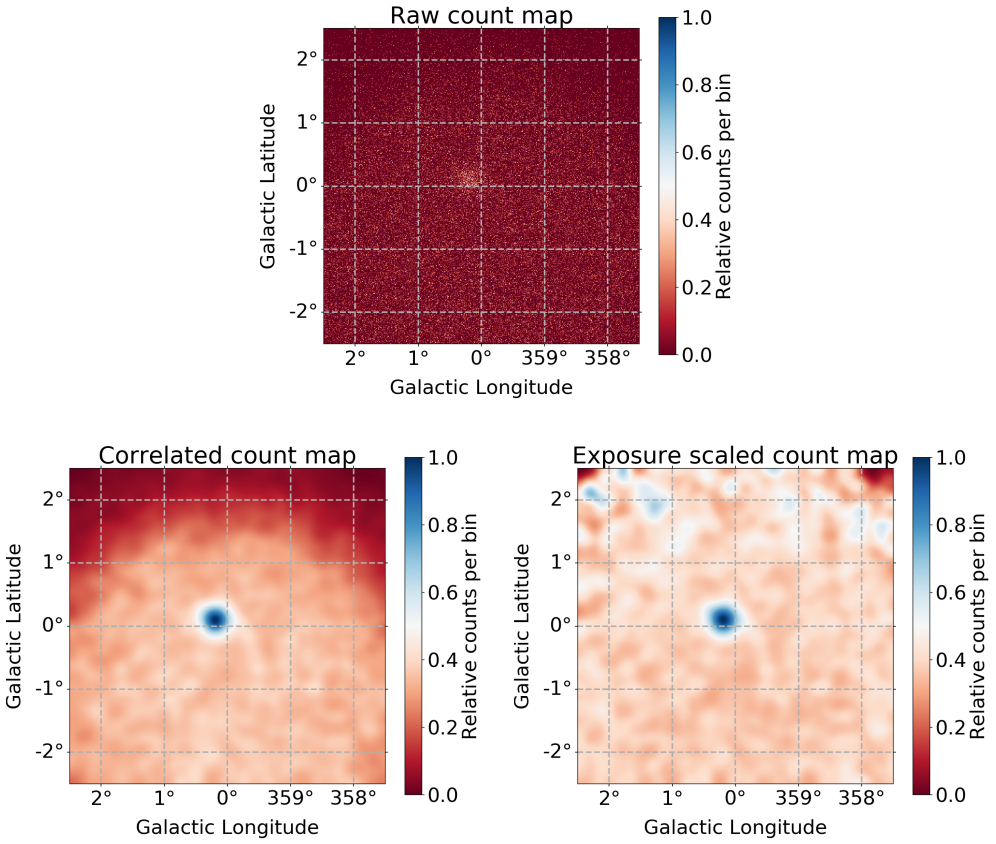

FIGURE 3.6: Raw count map (*top*), correlated count map (*bottom left*) and correlated and exposure corrected count map (*bottom right*) of a simulated γ-ray source. The Gaussian kernel applied to correlate the sky maps has a width of 0.1°.

of hadrons or electrons that are falsely classified as γ-like. In order to extract the actual signal on top of the background counts, also called excess, it is thus necessary to model the expected background contribution in each bin or region of a sky map and to subtract it from the total event count. This can be done by evaluating the counts in regions where no signal is expected, so called background or OFF regions. As pointed out before, the exposure of a dataset is in general not homogeneous over a sky map. Therefore, estimating the background from a region of different exposure, acceptance or size than the signal region will require a correction. This correction factor to compensate for these differences between ON and OFF regions is often denoted as α and is defined as

$$\alpha = \frac{\kappa_{\mathrm{ON}} \cdot t_{\mathrm{ON}} \cdot A_{\mathrm{ON}}}{\kappa_{\mathrm{OFF}} \cdot t_{\mathrm{OFF}} \cdot A_{\mathrm{OFF}}} \tag{3.6}$$

where κ is the acceptance, t the exposure time and A the size of the ON and OFF regions respectively. The number of excess counts in an ON region is then defined as

$$N_{\mathrm{excess}} = N_{\mathrm{ON}} - \alpha N_{\mathrm{OFF}} \tag{3.7}$$

with N_{ON} and N_{OFF} being the total counts in the ON and OFF regions respectively.

There are different approaches to background modelling for IACT data as outlined in detail in [62]. The two approaches applied in this work are the so called ring background method and the reflected regions method.

The reflected regions method assumes that the acceptance of an IACT camera is radially symmetric around the camera centre. An observed source is thereby not directly pointed at with the telescopes but at a certain offset (also called *wobble*) to allow for the determination of OFF regions with the same offset to the camera centre as the ON region. To not overestimate the background rate, the OFF regions should not include known sources of γ-ray emission, yielding the so called exclusion regions. By choosing more than one OFF region, the statistics for the background estimate can be increased, whereas the increased area of the OFF region has to be taken into account. Figure 3.7 shows an illustration of the method. When analysing IACT data with more than one pointing position, the OFF regions and according background counts have to be evaluated for every pointing of the telescopes separately. The reflected background method is usually not applied to generate background models for whole sky maps but rather to determine the signal and background rate of an individual ON region[6].

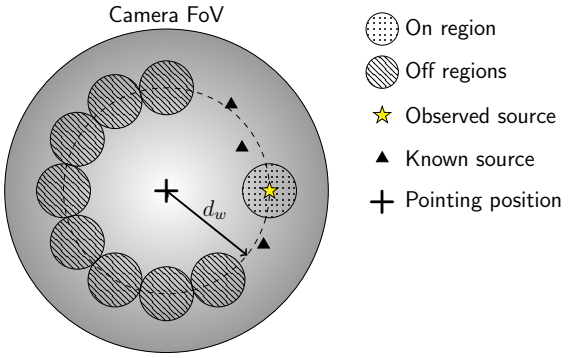

FIGURE 3.7: Illustration of the reflected background method.

The concepts of exclusion regions and exposure correction also apply to the ring background method. In this approach, the background is estimated from a ring-shaped OFF region around the ON region. An advantage of this approach is that it can be directly applied on count maps of a full dataset and does not have to be applied to each run of the dataset individually like the reflected regions method. To compensate for background estimation regions of inappropriate size caused by the position and size of exclusion regions, the so called *adaptive* ring background method can be applied. Here, the parameters of the ring from which the background is estimated is adjusted at every position of the sky map to ensure appropriate background estimation regions.

[6]The reflected regions method can however be applied multiple times with ON regions being equally distributed over the whole sky map even though this approach is rather computing intense as OFF regions have to be placed and evaluated for each run in the dataset and each pixel of the map (i.e. the ON region) separately.

3.4.4 Detection significance

An important parameter to calculate for an excess observed in an ON region (or a pixel of a sky map) is the significance of the detected signal. A very common approach to calculating this significance was introduced by Li and Ma. The proposed significance, commonly referred to as σ_{LiMa}, was published in 1983 [63] and is derived from a likelihood ratio test that probes the probability of measuring a signal in a certain region by chance on the basis of a separate background measurement. The significance is calculated from the counts in the signal region N_{ON} and in the background region N_{OFF} and the according α factor:

$$\sigma_{\mathrm{LiMa}} = \sqrt{2}\left(N_{\mathrm{ON}} \cdot \ln\left(\frac{(1+\alpha)N_{\mathrm{ON}}}{\alpha(N_{\mathrm{ON}}+N_{\mathrm{OFF}})}\right) + N_{\mathrm{OFF}} \cdot \ln\left(\frac{(1+\alpha)N_{\mathrm{OFF}}}{N_{\mathrm{ON}}+N_{\mathrm{OFF}}}\right)\right)^{1/2} . \quad (3.8)$$

The derivation can be found in the original publication [63].

3.4.5 3D fitting of IACT data & model selection

The so called 3D fit used in this thesis is an extensive fit procedure in which a spatial (2-dimensional) and spectral model (1-dimensional) is fitted simultaneously to binned air shower data. An advantage of combining spatial and spectral information in a fit is that complex morphologies with overlapping source components can be disentangled and described at appropriate spatial resolution. The 3D fit is thus a tool to fit models of arbitrary complexity to measured data, which therefore requires a way to eventually select a model that offers the most appropriate description of the measurements. The underlying theory to the whole procedure includes a wide range of topics from statistics and information theory like parameter estimation, hypothesis testing and model selection, which offers many different approaches to solve the initial problem of model fitting and selection. In the following, the individual steps of the approach that is applied in this work are outlined and motivated. The aim is thereby to go a bit further into detail than often done in the documentations of software frameworks or in publications that make use of this approach. As the applied 3D fit is a maximum likelihood method, an appropriate likelihood function has to be formulated and a goodness of fit test has to be determined. Furthermore a way has to be found to finally decide which of the tested models fits the observed data best.

3.4.5.1 The model definition

For a 3D fit, a data set D that holds the γ-ray event counts in spatial and spectral bins is needed. Furthermore, the fit has to be provided with the matching exposure and PSF

maps, the energy dispersion and a model that defines the expected background counts together with the spatial as well as spectral properties of the assumed source components. The counts predicted by model M in each of the spatial bins (j, k) as well as spectral bins l are given as

$$M(j,k,l) = B(j,k,l) + \mathrm{PSF}\left(E(j,k,l) \cdot \sum_m C_m^{spat}(j,k) \cdot C_m^{spec}(l)\right) \tag{3.9}$$

where B is the background model, E is the exposure map and C_m^{spat} and C_m^{spec} model the spatial and spectral contributions respectively for each of the m source components, which are folded with the energy dependent point spread function PSF, also taking into account the energy dispersion. The free model parameters $\theta_1 \ldots \theta_p$ which describe model M and which are optimised in the fit are thereby attributed to B and the spatial and spectral parts of C_m.

3.4.5.2 Finding an appropriate likelihood function

In a maximum likelihood fit procedure, the free model parameters are optimised to find the parameter configuration that maximises the probability that the observed counts D originate from the assumed model M. This is done by evaluating the discrepancy between predicted and measured counts by means of a statistic based on a likelihood function which should take into account the expected fluctuations of the underlying measurements. In such fitting procedures, χ^2-statistics like the Pearson's χ^2-statistic are commonly used. It is defined as

$$\chi^2 = \sum_i \frac{(D_i - M_i)^2}{M_i} \tag{3.10}$$

for the $i = j \cdot k \cdot l$ bins of data and model. The problem with this χ^2-statistic is that it assumes the difference between observed and expected counts to be Normal distributed, which is not appropriate for the case regarded in this work. As outlined in [64] and [65], the χ^2-statistic is not a good choice when modelling data from astrophysical as well as other counting experiments as the underlying statistical fluctuations in the data are of Poisson nature. Furthermore, the data may be sparsely sampled with very low bin counts which can affect the determined confidence intervals for model parameters and introduce a bias in the fit which can even exceed the statistical errors of the model parameters [66]. As an alternative, the so called *cash* statistic was suggested in 1979 by Webster Cash [64]. It is derived as two times the negative log-likelihood of the product of the bin-wise Poisson probabilities

$$P(D_i|M_i) = L(M_i|D_i) = \prod_i \frac{M_i^{D_i}}{D_i!} \exp(-M_i) \tag{3.11}$$

which can be written as

$$\tilde{C} = -2\ln(L) = -2\sum_i [D_i \ln M_i - M_i - \ln(D_i!)]. \tag{3.12}$$

Furthermore, Cash states the following in his paper [64]: Assume a model with a total of p parameters $\theta_1 \dots \theta_p$. These yield the minimum statistic value $(\tilde{C}_{min})_p$ when all p parameters are optimised. In the case that q of the p parameters are set to their *true* parameter values $\theta_1^T \dots \theta_q^T$ of the underlying generating distribution while the remaining $p-q$ parameters are optimised so that the statistic has reached a minimum $(\tilde{C}_{min})_{p-q}^T$, the difference between these two statistic values

$$\Delta\tilde{C} = (\tilde{C}_{min})_{p-q}^T - (\tilde{C}_{min})_p \tag{3.13}$$

is χ^2 distributed with q degrees of freedom according to Wilks' theorem. Thus, in the Poisson limit, it is possible to establish confidence intervals for a change in the model as shown in [67]. This provides a tool to determine confidence levels (CLs) for individual components within a model. This is done by calculating $\Delta\tilde{C}$ for the model with all parameters set to the best-fit values and a version of the best-fit model where the component for which a CL is to be determined is removed. The version of the model in which the component is removed is thereby assumed to have the set of *true* parameter values, thus yielding $(\tilde{C}_{min})_{p-q}^T$. In this test procedure, the null hypothesis that the regarded component is *not* there is therefore tested against the alternative hypothesis that the component has the parameters that were determined in the fit. As $\Delta\tilde{C}$ is χ^2 distributed with q degrees of freedom, a p-value and thus a significance can be calculated with which the null hypothesis can be rejected or failed to be rejected in favour of the alternative hypothesis. As a component is usually "switched on and off" by toggling the flux normalisation in the spectral part of the component between its best-fit value and 0, one might assume that $q = 1$ as only one parameter is changed. This is nevertheless not the case as the values of the remaining parameters of the component become irrelevant as the flux normalisation is set to 0 and can theoretically have arbitrary values. This means that q has to be the number of free fit parameters of the tested component.

This can be illustrated with an example: If $\tilde{C}$ of a model is reduced by 25 when adding a 2-dimensional Gaussian component (3 free parameters: galactic longitude, galactic latitude, containment radius) with a power law spectrum (two free parameters: flux normalisation and index), the p-value is determined for $\chi^2 = 25$ with 5 degrees of freedom, which yields a p-value of $\sim 1.39 \times 10^{-4}$, corresponding to a significance of $\sim 3.8\sigma$. In this case the

null hypothesis can be refuted with 3.8σ in favour of the alternative hypothesis. Often, this is translated to an expression like "the fitted Gaussian component has a significance of 3.8σ", which should not be confused with the LiMa significance of a signal region as introduced in Sec. 3.4.4.

Cash furthermore argues in [64] that as the term $\ln(D_i!)$ in Eq. 3.12 is only data dependent, it cancels when the change in the statistic between two models is calculated and can thus be dropped. This yields the practical version of the cash statistic

$$\tilde{C}^p = 2 \sum_i [M_i - D_i \ln M_i]. \tag{3.14}$$

This is the expression which is commonly referred to as *the cash statistic* in the literature. Also in software packages like `sherpa` and `gammapy`, this is the implemented version.

Even though Eq. 3.14 does not fully represent the original likelihood function from Eq. 3.12, it can still be used in a maximum likelihood fit as data-only dependent terms are constant and only shift the value of the likelihood but do not change the relative position of the maximum in the distribution when varying free model parameters. Using Eq. 3.14 or Eq. 3.12 in a maximum likelihood fit will therefore yield the same results.

It is not possible to determine a goodness of fit using the statistic $\tilde{C}^p$ as outlined in detail in App. A. To circumvent this issue, another alternative form of the cash statistic can be formulated, the so called C statistic:

$$C = 2 \sum_i [M_i - D_i + D_i(\ln D_i - \ln M_i)]. \tag{3.15}$$

This form of the cash statistic can be used for a maximum likelihood fit as well as for goodness of fit tests. It makes for a good test statistic as a reduced C statistic can be formulated analogous to a reduced χ^2 from which a goodness of fit can be approximated. Another approach is to determine the C statistic distribution of a best-fit model via parametric bootstrapping. This can be done by simulating so called *fake* data based on the best-fit model and performing the maximum likelihood fit on these simulated sets of measurements. The fake data is thereby generated by drawing samples of Poisson distributed counts from the best-fit model. The C statistic distribution of the best-fit model is then obtained from the set of final C statistic values from the fits of the model to the fake data. The goodness of fit can then be determined from the position of the C statistic value of the best-fit model and the observed data within the C statistic distribution from the simulations. More details on the C statistic, its derivation and methods to determine a goodness of fit can be found in App. A.

3.4.5.3 Model selection

A goodness of fit shows how good a model fits the observed data. The lower the C statistic value of a model, the smaller is the difference between the model's prediction and the observation. A possibly low C statistic is nevertheless not always favourable as the actual goal of the fitting procedure is to extract as much information as possible about the general *underlying distribution* that generated the observed data and not to reproduce the observation down to arbitrary detail. The true generating distribution is only known to nature and the experimenter can only try to extract the available information to make an approximation of it. Depending on the extent of the data (like size, resolution, exposure, temporal sampling etc.), only a limited amount of information about the generating distribution can be extracted. On top of this information, fluctuations are present in the data. The challenge is therefore to design and optimise a model that captures as much of the generating distribution as possible without characterising fluctuations as features. The more complex a model gets, the more information it can store. A model with arbitrarily many parameters will therefore be able to yield an arbitrarily low C statistic value (which is 0 if the model predicts the exact measured counts). Generally, it can be said that from a certain number of parameters on, the model will start to fit statistical fluctuations, a state called *overfitting*. Analogous is a model that *underfits*, meaning that the model has too few parameters to describe the general features of the generating distribution. In order to capture this turning point between under- and overfitting, a number of models should be tested. This selection of models is often referred to as the *candidate collection* which should include models over a certain range of complexity.

When a candidate collection is set up, the question is how to decide which model describes the generating distribution to an optimal extent given the available data. This can be done by evaluating the out-of-sample *predictive quality* or *predictive performance* of the models. The predictive quality describes how good a model describes or predicts future observations. The obvious way to assess this predictive quality is to test the model on independent observations that were not used for the model fit, a process called cross-validation. Data is nevertheless valuable, and often there is no adequate set of validation data available. This can be the case if all data is used for the model fit itself, or e.g. in the extreme case of a generating distribution that changes over time, conducting new observations may therefore not yield an appropriate set of validation data.

In such cases, so called information criteria can be applied, a concept from information theory. These information criteria use the predictive density of a model together with a bias correction or penalty term on the model's complexity to *approximate* the cross-validation performance. Many different information criteria have been developed in the past. A publication by Gelman et al. [68] gives a good overview of different information criteria and their motivation, and outlines the general concept of approximating the predictive performance of a model.

A very common information criterion is the Akaike information criterion (AIC) proposed by mathematician Hirotogu Akaike in 1973 [69]. The concept and derivation of the AIC is well explained in detail in [70]. In short, the AIC estimates the Kullback-Leibler divergence between a best-fit model and the underlying true distribution from which the observed data was generated. The Kullback-Leibler divergence is a concept from information theory and provides means to evaluate how different two distributions are from each other (see [71] for the original publication by Kullback and Leibler from 1951). Furthermore, it can be used as a measure of how much information is lost when a certain distribution is described with an approximation. In the given case, the best-fit model is the approximation that describes the generating distribution. A good approximation will thus yield a low Kullback-Leibler divergence, which is approximated by the AIC. The approximation with the lowest AIC score therefore describes the generating distribution best.

The AIC is defined as

$$\mathrm{AIC} = -2 \ln f(D|\hat{\theta}_p) + 2p \tag{3.16}$$

where $f(D|\hat{\theta}_p)$ is the likelihood of observing the data D assuming the best-fit model M with its parameters $\hat{\theta}_p$ and p is the number of free model parameters. In combination with the C statistic, the AIC score for a model is simply

$$\mathrm{AIC} = C + 2p. \tag{3.17}$$

As stated before, the model with the lowest AIC score $\mathrm{AIC}_{\mathrm{min}}$ should be preferred. To compare different models within the candidate collection in terms of their AIC scores, the difference between the preferred model and model m can be calculated as

$$\Delta\mathrm{AIC}_m = \mathrm{AIC}_m - \mathrm{AIC}_{\mathrm{min}}. \tag{3.18}$$

This difference is a value on the scale of information as outlined in [72] and provides means to rank the models in the candidate collection. The publication furthermore states that a model likelihood can be computed for each model in the collection as

$$L_m = \exp\left(-\frac{1}{2}\Delta\mathrm{AIC}_m\right) \tag{3.19}$$

that allows to deduce a *formal strength of evidence* for each model given the data. Taking the ratio of model likelihoods then allows to make statements about the empirical support of one model compared to another like "the evidence ratio between model A and model B is 42, the evidence for model A is thus 42 times stronger than for B". According to [73] and

[70], models that yield a ΔAIC up to 2 can be considered as having equal empirical support as the model with the lowest AIC score. It is however important to note that the AIC does not allow for a statistical interpretation of the difference between two or more models' AIC scores in the frequentist sense involving confidence levels or significances. The main difference as well as pros and cons between the here outlined information-theory based approach and common null-hypothesis significance testing (employing p-values) to model selection are discussed in a commentary by Mundry [74].

3.4.5.4 Concluding remarks

As the AIC score basically comes at no computation cost once the likelihood has been maximised, it makes more sense to first set up a collection of candidate models that are tested against each other via their AIC scores, and only perform the more computing intense goodness of fit evaluation via simulations for the sub-set of models that yield the lowest AIC scores.

Furthermore it can be noted that the AIC has gained in reputation when it comes to model selection problems in γ-ray astronomy and has recently come to use in a number of publications such as [75, 25, 76, 77, 78].

3.4.6 Extracting spectral information

Instead of performing a 3D fitting procedure, the spectral properties of a signal region can also be extracted using the reflected background method. This can be done by performing a maximum likelihood fit on the ON and OFF regions' count data using the so called W statistic or *wstat*. The difference to the C statistic is that here, the background is not modelled but directly related to the counts measured in the background region. The according likelihood function is derived from the product of the Poisson probabilities of observing N_{ON} counts in a signal region with an expected $M_{\mathrm{ON}} = M_{\mathrm{sig}} + M_{\mathrm{bg}}$ counts and N_{OFF} observed counts in an OFF region for an expected $M_{\mathrm{OFF}} = M_{\mathrm{bg}}/\alpha$. The data and model counts can then be binned in energy, resulting in the according likelihood

$$L = \prod_i \frac{(M_{i,\mathrm{sig}} + M_{i,\mathrm{bg}})^{N_{i,\mathrm{ON}}}}{N_{i,\mathrm{OFF}}!} \exp(-(M_{i,\mathrm{sig}} + M_{i,\mathrm{bg}})) \times \frac{(M_{i,\mathrm{bg}}/\alpha)^{N_{i,\mathrm{OFF}}}}{N_{i,\mathrm{OFF}}!} \exp(-M_{i,\mathrm{bg}}/\alpha). \tag{3.20}$$

Taking two times the negative logarithm of this likelihood yields the W statistic, which can then be written as

$$W = 2\sum_i \left[M_{i,\mathrm{sig}} + (1+\alpha^{-1})M_{i,\mathrm{bg}} - N_{i,\mathrm{ON}}\ln(M_{i,\mathrm{sig}} + M_{i,\mathrm{bg}}) - N_{i,\mathrm{OFF}}\ln(M_{i,\mathrm{bg}}/\alpha)\right] \tag{3.21}$$

whereas data-only dependent terms are neglected as they are constant in the optimisation process.

3.4.7 Employed software for reconstruction and analyses

The IACT data analyses presented in this thesis consist of multiple steps that make use of different software packages. The air-shower reconstruction from the raw H.E.S.S. data is done with the H.E.S.S. internal software `hap-18`, using a Hillas-parameter based reconstruction as outlined above. The applied γ-hadron separation is based on multivariate analysis methods as presented in [50]. The reconstructed air-shower properties are then exported to fits format[7] in order to perform the high-level data analysis with the open-source software `gammapy`[8] [79] in version 0.13. `gammapy` uses common `python` packages like e.g. `astropy` (specialised on general astronomical calculations with coordinates, units and transformations) with `iminuit` and `sherpa` (for model fitting) and provides specialised functionalities used for the analysis of general γ-ray data[9]. It thus provides the means to combine data from multiple experiments and perform joint analyses as e.g. presented in [80] for the example of a joint maximum likelihood fit on data from H.E.S.S., MAGIC, VERITAS, FACT and Fermi-LAT of the Crab nebula.

All analysis steps and results presented in this work are produced with the above software packages in the given versions if not stated otherwise.

3.5 Systematic uncertainties in IACT data analyses

An important aspect of an IACT data analysis are systematic uncertainties. These errors propagate through the analysis from the event reconstruction to the final physics results. The interplay of individual sources of systematic uncertainty (e.g. variable atmospheric conditions, temporary hardware failures, influence of chosen reconstruction parameters and cut configurations) throughout the different steps of an analysis is thereby not trivial. Final systematic errors can often only be roughly estimated, e.g. by performing reference observations of sources of more or less stable and known properties and monitoring the variation of the final results over time. Other approaches are to either simulate a γ-ray source with a given energy spectrum and determine the systematic errors from extensive

[7] See `https://fits.gsfc.nasa.gov/` for details.
[8] Github link: `https://github.com/gammapy/gammapy`
[9] See `https://gammapy.org/` for the official `gammapy` homepage for documentation and details on dependencies.

sets of varying MC simulations, to investigate the variation of the results when using independent analysis and reconstruction approaches or by varying analysis and reconstruction parameters.

The H.E.S.S. collaboration has published estimates of systematic uncertainties from observations of the Crab Nebula [61], a source that is considered a standard candle in γ-ray astronomy. In this publication, a final systematic uncertainty of flux measurements is given as 20% with a systematic error on the spectral slope of a power law fit of ± 0.1. In another study, the general precision of the energy scale and absolute flux level for ground-based γ-ray detectors is given as $10 - 15\%$ [81]. These values are commonly adopted in H.E.S.S. data analyses as systematic errors for power law spectra. For exponential cut-off power law spectra, an extensive estimation of the systematics was performed in a study on Vela Junior [82]. Here, a systematic error of 25% is given on the flux normalisation, ± 0.2 on the spectral index (for indices in the range from 1.5 to 2.2) and 20% on the cut-off energy.

For the following presented analyses of H.E.S.S. data, systematic errors are only explicitly stated for the spectra of individual γ-ray sources in the summary in Chap. 7. In order to assess the systematic uncertainties more thoroughly, especially systematic uncertainties on the determined source morphologies, further studies and cross-check analyses are needed. This would however go beyond the scope of this work and is thus suggested for future studies.

Chapter 4

The Westerlund 2 region

Westerlund 2 is a stellar cluster in the Carina arm of the Milky Way that was discovered by the Swedish astronomer Bengt Westerlund in 1961 [83]. Since then, the region around the star cluster has been monitored in multiple wavelengths from radio frequencies to VHE and has shown to be a complex environment that hosts a multitude of different objects and sources of emission from the whole electromagnetic spectrum. This chapter summarises information on the Westerlund 2 region gathered with different experiments and presents a number of important publications. In the first section, general facts about Westerlund 2 itself are presented. In the following sections, findings from selected publications on Westerlund 2 are outlined. A focus is thereby put on a chronological presentation of results from the HE and VHE regime to establish a context for the analyses and discussions presented in Chap. 5 and Chap. 6 of this work. Finally, the scope of this thesis is outlined.

4.1 The star cluster Westerlund 2

Westerlund 2 is a so called open and young massive star cluster (YMC) (see [84] for an extensive review on YMCs and [85] for a recent review on star clusters and their formation in general). It is considered one of the most massive star clusters in the Milky Way with a mass of $\sim 3.6 \times 10^4\, M_\odot$ [86] and is thus also considered to be one of the three currently known super star clusters in our galaxy [87]. Westerlund 2 is embedded in the stellar nursery and H II region[1] RCW 49, also referred to as NGC 3247 or GUM 29. The age of the star cluster is estimated to be $\leq 2\,\mathrm{Myr}$ whereas its distance to the Sun is poorly constrained with estimates ranging between ~ 2 and $\sim 8\,\mathrm{kpc}$ where even recent studies show large discrepancies. Table 4.1 shows selected distance and age estimates with corresponding references. A study published in 2018 by Drew et al. suggests a distance

[1] An H II region is a region of ionised atomic hydrogen. The ionisation is caused by UV radiation from hot stars in the environment. See [88] for details.

Year	Distance [kpc]	Age [Myr]	Ref.
2015	$6.0 \pm 0.4^{+1.2}_{-0.3}$	$\lesssim 1.5$	[94]
2013	2.85 ± 0.43	~ 2	[95]
2013	$4.16 \pm 0.07 \pm 0.26$	< 3	[96]
2011	6 to 9	n.a.	[97]

TABLE 4.1: Selected distance and age estimates for Westerlund 2. See also Tab. 3 in reference [98] for a more detailed collection of distance estimates.

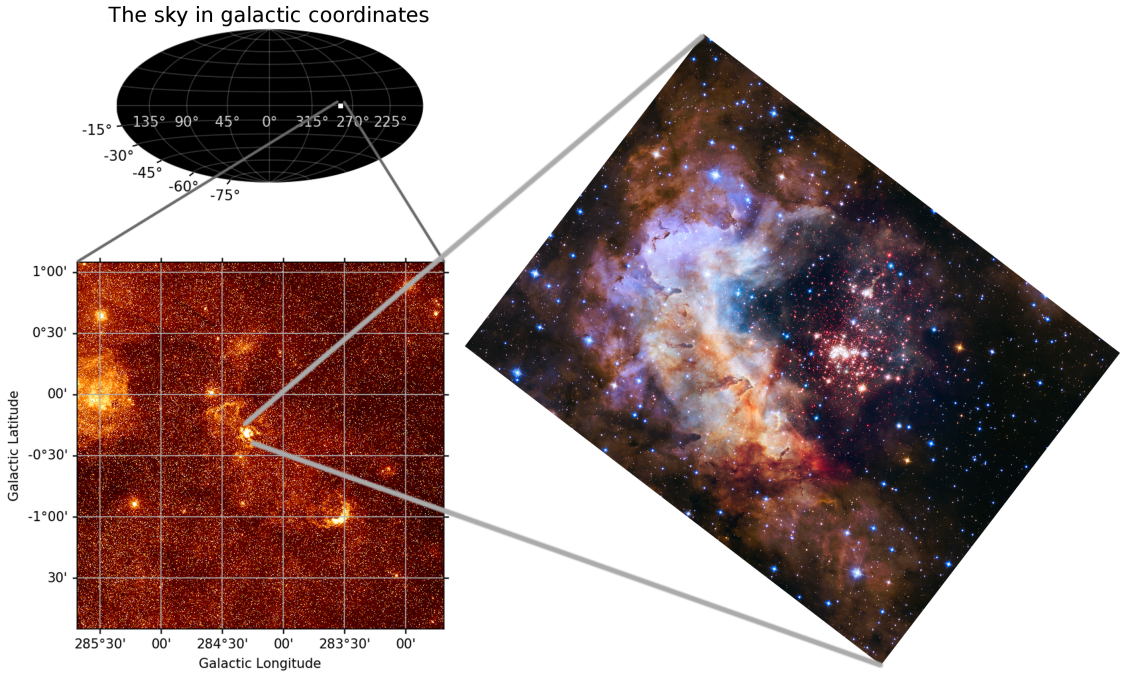

FIGURE 4.1: Locating Westerlund 2 on the galactic sky; The *lower left* sky map shows the Westerlund 2 region in the red optical band, revealing the stars and lobes of gas and dust in its environment. It is created from HiPS maps of the red channel data of the second Digitized Sky Survey (DSS2 red, see `http://alasky.u-strasbg.fr/DSS/DSS2Merged`). The *right* image is the official Hubble's 25^{th} anniversary image, composed from visible-light and near-infrared data (Credit: NASA, ESA, the Hubble Heritage Team (STScI/AURA), A. Nota (ESA/STScI), and the Westerlund 2 Science Team).

in the mid-range of recent estimates of (5 ± 1) kpc [89], which is also adopted in this work. The physical properties of the stellar content of Westerlund 2 was presented in great detail in a series of publications by Zeidler et al., who published a high-resolution multiband survey of Westerlund 2 with the Hubble Space Telescope [90, 91, 92, 93]. A further study based on Hubble Space Telescope data revealed that about 1/3 of the pre main sequence (PMS) stars in the Westerlund 2 star cluster are variable [86]. The centre of Westerlund 2 in galactic coordinates is given as $(l = 284.2669°, b = -0.3379°)$ as stated in the Simbad astronomical database[2]. Figure 4.1 illustrates the location of Westerlund 2 in galactic coordinates with the position estimates depicted in a face-on view of the Milky Way in Fig. 4.2.

[2] `http://simbad.u-strasbg.fr/simbad/`

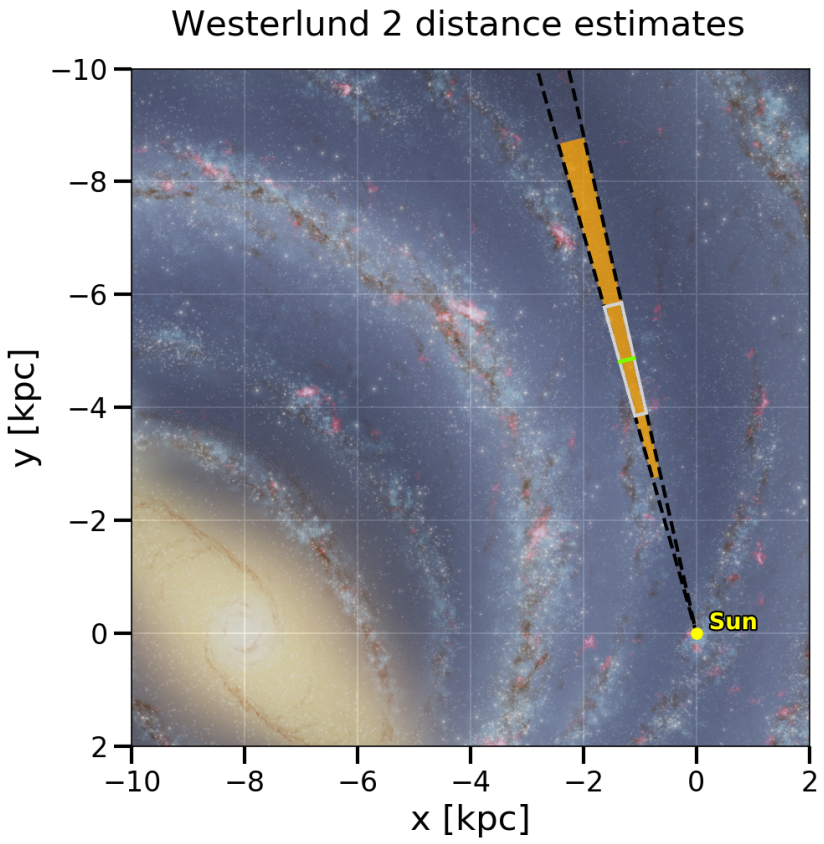

FIGURE 4.2: Distance estimates for Westerlund 2 in a face-on view of the Milky Way in Cartesian coordinates centred on the Sun. The black dashed lines mark the projection of a 1.5° radius view cone centred on Westerlund 2. The orange region marks the minimum to maximum distance estimates given in Tab. 4.1. The grey wedge with the green line denotes the (5 ± 1) kpc distance adopted in this work.
Background image credit: NASA/JPL-Caltech/R. Hurt (SSC/Caltech)

Due to its proximity to the tangent point of the Carina arm of the Milky Way, the region around Westerlund 2 is densely populated with clouds of molecular and atomic gas as well as stellar objects like pulsars and a multitude of stars of different types. Due to its young age, the cluster itself is expected to host very massive and hot stars. Among multiple detected O and B-type stars, it also hosts Wolf-Rayet (WR) type stars and binary systems such as the colliding wind binary (CWB) WR 20a with masses of $\sim 80\,M_\odot$, which are considered "two of the most massive stars with a direct mass determination known so far" [99]. In the vicinity of Westerlund 2, further massive stars and binaries have been found (e.g. WR 21a, WR 20aa and WR 20c) which may have been ejected from the cluster in the past [89].

Studies of radio data taken with the NANTEN2 telescope have suggested the formation of Westerlund 2 to be connected to the collision of two giant molecular clouds a few million years ago [100, 101].

4.2 Westerlund 2 in γ-rays

Space- and ground-based experiments have detected γ-ray emission from the region around Westerlund 2 since the early days of γ-ray astronomy, but due to the complex environment and comparably low resolution of the telescopes at that time, the nature and origin of the emission could not be pin-pointed. Even today, the origin of the γ-ray emission is still under debate with explanations ranging from PWNe over collective stellar winds to SNRs and microquasars. This section presents an overview of publications from the HE and VHE regime of the electromagnetic spectrum from the first detection of γ-ray emission from the Westerlund 2 region up to the population of currently known sources. Tables summarising the names and positions of γ-ray sources that were detected in the Westerlund 2 region over time can be found in App. B.

4.2.1 COS-B and EGRET

The first detection of γ-ray emission from the direction of Westerlund 2 is reported in the second COS-B catalogue from 1981 [102]. Two of the 25 sources with $E > 100\,\mathrm{MeV}$ listed in this catalogue, named 2CG 284–00 and 2CG2 88–00, are located in the Carina arm of the Milky Way. 2CG 284–00 coincides with Westerlund 2. The authors propose a possible connection between 2CG 284–00 and 2CG 288–00 as large extended features, but no clear statement about their origin is being made.

The next generation γ-ray telescope, the *Energetic Gamma Ray Experiment Telescope* (EGRET, measuring energies roughly from 30 MeV to 20 GeV) on board the Compton Gamma Ray Observatory satellite also detected emission from the region as reported in the first EGRET source catalogue in 1994 [103]. The source is listed as a high-confidence detection, named GRO J1021–58, and is associated with the previously detected source 2CG 284–00 (also labelled 2CG 284–01).

A source of γ-ray emission from the Carina region is also found in the second EGRET catalogue from 1995 [104]. There, the source around Westerlund 2 is called 2EG J1021–5835. Two other publications from 1997 based on the EGRET data also report significant emission above 1 GeV that is associated with the source 2EG J1021–5835 [105, 106].

A more detailed view is presented in the third EGRET (3EG) catalogue published in 1999. Instead of one source, it lists three significant sources that are associated with 2EG J1021–5835 [107]: 3EG J1013–5915, 3EG J1014–5705 and 3EG J1027–5817. The last source is marked as being inconsistent with a single point source, making it a candidate for either a possibly extended source or multiple unresolved sources.

With the publication of the 3EG catalogue and data from other wavelengths, enough information was available to search for possible counterparts of the unidentified γ-ray signals. Still in the year 1999, a first study was published that determines the significance

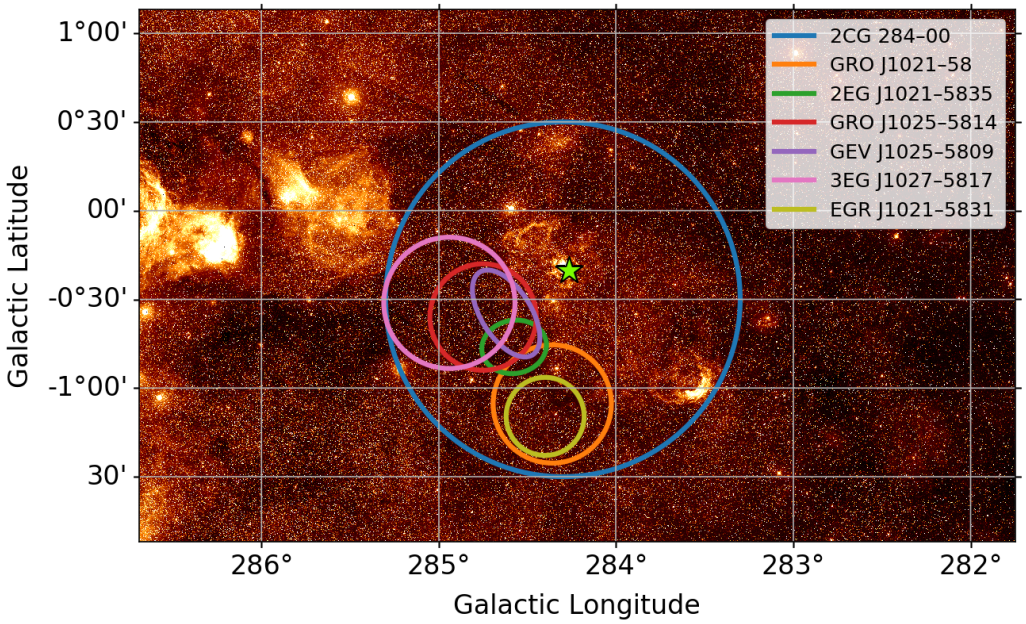

FIGURE 4.3: Saturated DSS2 red skymap of the Westerlund 2 region overlayed with 95% CL outlines of the sources listed in Tab. B.1. Only for 2CG 284–00, the 90% CL is shown instead. The position of Westerlund 2 is marked with a green star.

of the coincidences between γ-ray signals and other nearby objects like WR stars, OB stars or SNRs [108]. The study associates 3EG J1027–5817 with an OB star and lists it as a possible pulsar candidate but reports that an associated radio-pulsar is not found.

In a revised version of the 3EG catalogue from 2008 [109], the sources 3EG J1013–5915 and EG3 J1014–5705 are reported as *not* being detected, whereas the properties of the source 3EG J1027–5817 are updated under the name EGR J1021–5831.

Table B.1 lists the properties of above mentioned unidentified γ-ray sources found in COS-B and EGRET data. Figure 4.3 shows a saturated skymap of the Westerlund 2 region in the red optical band (DSS2 red, as shown in Fig. 4.1) overlayed with the 95% CL outlines of the source positions.

4.2.2 H.E.S.S., AGILE and Fermi-LAT

After the EGRET mission was terminated in the year 2000, the next γ-ray telescopes that observed the Westerlund 2 region were H.E.S.S. and a bit later the Fermi Large Area Telescope (Fermi-LAT) and the AGILE satellite. With increasing exposure of the experiments' data sets, the Westerlund 2 region could be resolved in more and more detail, leading to a multitude of source detections in the environment of the star cluster, of which some are listed in Tab. B.2. In the following, main publications presenting new insights to the γ-ray emission around Westerlund 2 are outlined in chronological order.

In 2007, the H.E.S.S. collaboration reported the detection of the extended VHE γ-ray source HESS J1023–575 [110] in 14 h of H.E.S.S. data. The paper discusses multiple emission scenarios connected to stellar winds in different settings without presenting a preferred emission scenario, stating that deeper observations are needed to draw further conclusions.

A study from 2008 on EGRET data associates the pulsar PSR J1028–5819 with 3EG J1027–5817 and suggests that it is *not* associated with HESS J1023–575 [111] due to the rather large angular displacement of the two sources of $\sim 1°$.

Shortly after the Fermi-LAT started to take science data in 2008, pulsed γ-ray emission was detected from the source PSR J1028–5819 and associated with 3EG J1027–5817 by the Fermi-LAT collaboration [112]. The first Fermi-LAT list of bright sources (0FGL, [113]) presents two sources around Westerlund 2 (see Tab. B.2). The source 0FGL J1024.0–5754 is thereby associated with HESS J1023–575 and thus with emission from the Westerlund 2 cluster. The source 0FGL J1028.6–5817 is stated to be associated with 3EG J1027–5817 and thus also with PSR J1028–5819.

In 2009 the first AGILE source catalogue was published [114]. The catalogue lists the source 1AGL J1022–5822 close to Westerlund 2 and states that the "source lies in the complex Carina region, and multiple source contributions are possible".

In the first source catalogue published by the Fermi-LAT collaboration (1FGL) in 2010, two sources close to Westerlund 2 are reported [115]. One source is LAT PSR 1FGL J1023.0–5746 which is coincident with HESS J1023–575. The other source is 1FGL J1028.4–5819, associated with PSR J1028–5819. Also in 2010, Saz Parkinson et al. published the discovery of another γ-ray pulsar in the region, PSR J1023–5746, also found in Fermi-LAT data [116]. The signal is coincident with HESS J1023–575. Furthermore, the X-ray source CXOU J102302.8–574606 detected with the Chandra X-Ray Observatory is presented as a counterpart. This proposes a PWN as possible emission scenario.

The H.E.S.S. Collaboration published an updated analysis of the Westerlund 2 data in 2011 [2]. In this paper, the VHE emission from the previously reported source HESS J1023–575 is resolved into two components, HESS J1023–575 and HESS J1026–582. The new component is associated with the pulsar PSR J1028–5819. Its spatial separation as well as the difference in spectral properties to HESS J1023–575 substantiate the hypothesis of two individual sources. The emission furthermore shows a clear energy dependent morphology. For HESS J1023–575, a PWN scenario in connection with PSR J1023–5746 as well as collective stellar winds from Westerlund 2 interacting with molecular clouds in the vicinity are discussed.

In 2012, the H.E.S.S. collaboration reported the detection of the γ-ray source HESS J1018–589 with two emission regions denoted A and B [117]. In 2015, pulsed emission was reported from HESS J1018–589 A [118]. The source lies 1.5° south of Westerlund 2 in galactic coordinates and is not further discussed in this work at hand.

Between 2012 and 2018, the Fermi-LAT collaboration published multiple source catalogues (see Tab. B.2) with increasing numbers of point-like and extended sources around Westerlund 2. The search for extended sources in Fermi-LAT data published in 2017 revealed two large-scale sources in the Westerlund 2 region: FGES J1023.3–5747 and FGES J1036.3–5834 [119]. FGES J1023.3–5747 coincides with HESS J1023–575 and is best described by a disk with a radius of 0.28° and thus perfectly agrees with the extension reported in the H.E.S.S. publication from 2011 [2]. The source FGES J1036.3–5834 is best described by a disk with a radius of $\sim 2.5°$, thus covering a region of the size equal to the FoV of the H.E.S.S. telescopes, making it very challenging to detect this emission with the H.E.S.S. telescopes. This large scale diffuse emission is further studied in [120], where an association to ambient gas and stellar winds from Westerlund 2 is being made. HESS J1023–575 is thereby associated with the pulsar PSR J1023–5746, suggesting a PWN scenario.

The H.E.S.S. Galactic Plane Survey from 2018 [121] also covers the Westerlund 2 region. No differences to previously published results are stated. HESS J1023–575 is thereby associated with multiple sources from Fermi-LAT catalogues and with Westerlund 2, whereas HESS J1026–582 is associated with G285.1–0.5 (PWN) and the pulsar PSR J1028–5819.

The second AGILE source catalogue was published in 2019 [122]. The catalogue lists multiple point-like and extended sources in the Carina region. In particular the two point-like sources 2AGL J1020–5752 and 2AGL J1029–5834 as well as extended sources for Westerlund 2 and HESS J1026–582 (see Tab. 3 in [122]) are in proximity to the stellar cluster.

In 2020 the Fermi-LAT collaboration published its fourth catalogue of sources (4FGL) comprising 8 years of data [123], with another updated list from 10 years of Fermi-LAT data (called "data release 2", 4FGL-DR2[3], initial release 22.05.2020) a few months later. In this catalogue, a total of 12 sources are presented within a 2.5° radius around Westerlund 2 in the energy range from 50 MeV to 1 TeV. Two of these sources are extended, best described by 2-dimensional disks. A DSS2 red skymap of the Westerlund 2 region is shown in Fig. 4.4 with a zoomed inset on Westerlund 2. The positions of the 4FGL-DR2 sources in the region are marked with yellow triangles. Furthermore, the positions and Gaussian extensions of HESS J1023–575 and HESS J1026–582 from the 2011 H.E.S.S. publication [2] are shown in light blue.

4.3 Selected findings complementing the γ-ray data

As the region around Westerlund 2 is densely populated with clouds of gas and multiple stellar objects, a multitude of publications covering this region of the galactic sky can be

[3]Taken from `https://fermi.gsfc.nasa.gov/ssc/data/access/lat/10yr_catalog/`; accessed 02.07.2020

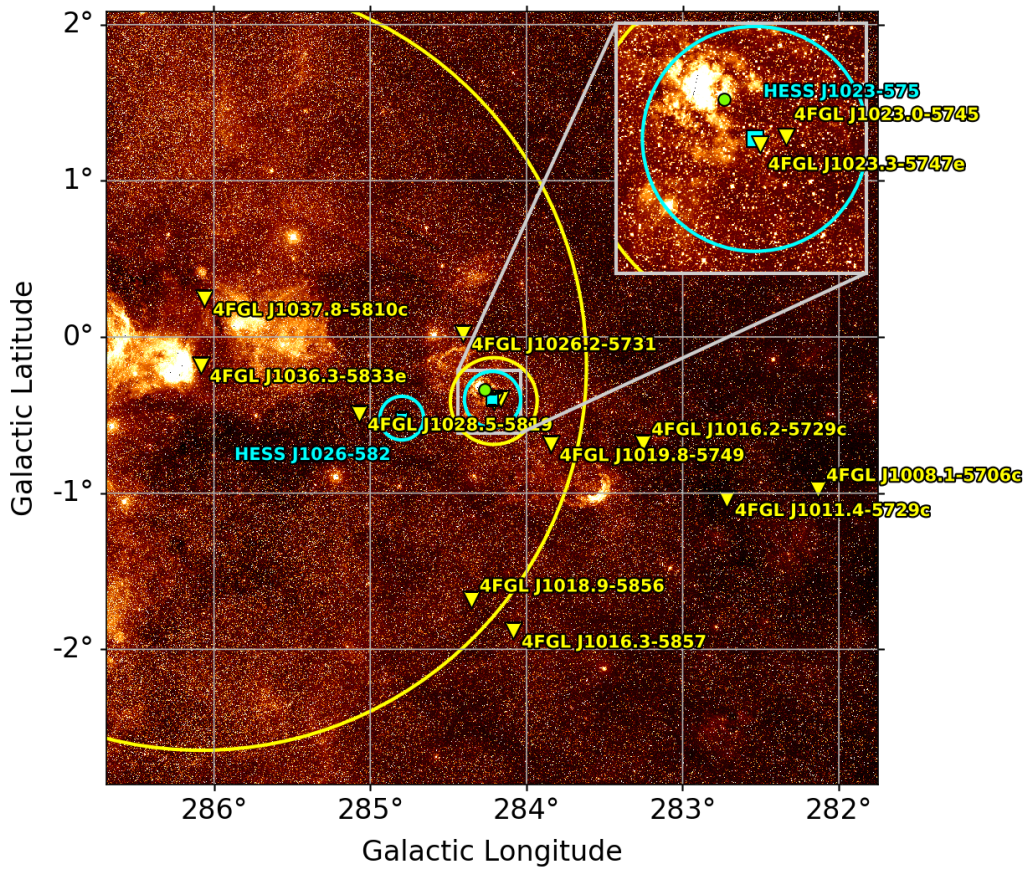

FIGURE 4.4: Saturated DSS2 red skymap of the Westerlund 2 region overlayed with source positions from the 4FGL-DR2 catalogue shown in yellow. The yellow rings mark the two extended sources in the region. The best-fit positions and extensions of the best-fit Gaussians from the 2011 H.E.S.S. paper on Westerlund 2 are shown in light blue. The position of Westerlund 2 is marked with a green dot.

found. In the pursuit of finding the origins of the detected HE and VHE γ-ray emission, X-ray and radio data play a vital role. In the following, a selection of recent publications based on X-ray, radio and neutrino data is presented that complement the findings from the HE and VHE regime and propose potential emission scenarios as further discussed in Chap. 6.

4.3.1 Radio data

Two clouds of molecular gas with a "peculiar *arc* and *jet*" shape that show a striking spatial coincidence with the γ-ray signal of HESS J1023–575 were discovered by analysing CO transition lines in NANTEN data published in 2009 [124]. The authors additionally found a shell-like cloud of atomic hydrogen coincident with HESS J1023–575. These results were further refined in 2014 with a study on data from the NANTEN2 and MOPRA

radio telescopes [3, 125]. This coincidence of γ-ray emission with gas clouds supports the hypothesis of a hadronic emission scenario in which accelerated particles interact with ambient atomic or molecular gas.

High-resolution radio continuum observations of RCW 49 revealed "hints of nonthermal components" [98]. Additionally, the publication reports bow-shocks, bubbles and jet-like structures in the RCW 49 region.

4.3.2 X-ray data

An extensive imaging study of the RCW 49 region was conducted with the Chandra X-ray Observatory and published in 2007, reporting 468 X-ray sources around and within Westerlund 2 [126]. The study further deduces spectral properties of WR and O-type stars in the region. Another Chandra study from 2008 by Nazé et al. reports soft and diffuse X-ray emission in the region of Westerlund 2 and outlines possible connections to HESS J1023–575 [127]. The authors refer to a study by Bednarek [128] which suggests a hybrid model for the emission from Westerlund 2 in which the X-ray and GeV emission is caused by synchrotron and inverse Compton radiation whereas the TeV emission is attributed to accelerated hadrons that interact with ambient gas. Leptons and hadrons are thereby accelerated by stellar winds originating from the star cluster. This model predicts a more extended TeV signal compared to the X-ray and GeV emission. Alternatively, Nazé et al. refer to a study by Anchordoqui et al. which proposes "photo-de-excitation of PeV cosmic ray nuclei after their parents have undergone photo-disintegration in an environment of ultraviolet photons" as potential origin of the TeV emission of HESS J1023–575 [129].

In 2009, a study on data taken with the Suzaku satellite revealed diffuse X-ray emission around the centre of Westerlund 2 with signs of a non-thermal component [130]. The authors note a high ratio between γ-ray and X-ray flux and suggest a hadronic emission scenario in connection with a super- or hypernova. This scenario is supported by the high abundance of α-elements in the region.

A recent extensive study by Townsley et al. from 2019 on star forming regions at keV energies presents a large mosaic of archival X-ray data of RCW 49 and Westerlund 2 [131]. The authors report > 3000 X-ray point sources as well as "spatially and spectrally complex diffuse X-ray emission" within the whole mosaic. Apart from a PWN connected to the pulsar PSR J1023–5746, traces of SN activity are reported.

4.3.3 Neutrinos

In an analysis of joint data sets from the ANTARES and IceCube experiments published in 2020, HESS J1023–575 is stated as "the most significant source candidate" from a list of 57 astrophysical objects for which neutrino flux upper limits are presented [132].

HESS J1023–575 is thereby given as source candidate with a post-trial significance of 42% with flux upper limits of $1.1 \times 10^{-8} (2.5 \times 10^{-6})\,\mathrm{GeV}^{-1}\mathrm{cm}^{-2}\mathrm{s}^{-1}$ for an assumed power law spectrum of index 2.0(2.5). A detection of neutrinos from HESS J1023–575 would support the hypothesis of a hadronic emission scenario.

4.4 The aim of this work

This thesis presents an analysis of the currently available set of high quality data gathered with the H.E.S.S. telescopes observing the Westerlund 2 region. A previous publication by the H.E.S.S. collaboration on Westerlund 2 was published in 2011 and presented data taken until June 2009. Since then, new observations of the Westerlund 2 region have been conducted, significantly extending the size of the available dataset. The aim of this work is to verify the previously published results from 2011 [2] and probe the new data set for further insights regarding the morphological and spectral properties of the VHE γ-ray signals in the Westerlund 2 region. Furthermore, selected emission scenarios suggested in a multiwavelength context are probed and discussed.

Chapter 5

Exploring the Westerlund 2 region with H.E.S.S. data

This chapter presents results of the analyses performed for this thesis which are based on data that the H.E.S.S. telescopes have taken observing the Westerlund 2 region. The following sections describe the dataset as well as the relevant steps and results of the conducted analyses. The results are further discussed and put into context in the following Chap. 6 with findings from other publications as summarised in the previous Chap. 4.

5.1 The dataset

H.E.S.S. has taken a total of $\sim 224\,\mathrm{h}$ of data observing the Westerlund 2 region in the time from March 2006 to June 2015. From the full dataset, $\sim 80.4\,\mathrm{h}$ (182 runs) pass the quality selection criteria for *detection* and $\sim 72.8\,\mathrm{h}$ (163 runs) for *spectral* analysis, with no CT5 data being available. All four H.E.S.S. phase I telescopes participated in the full list of runs regarded in this work. A full list of run numbers is given in App. C. In the H.E.S.S. publication from 2011 [2], $45.9\,\mathrm{h}$ of data are used in the analysis. Since then the quality selection criteria have been revised, resulting in only $39.3\,\mathrm{h}$ of the 2011 dataset to pass the current selection criteria. The size of the high quality dataset has therefore roughly doubled in size since the last H.E.S.S. publication on Westerlund 2. The data was taken with pointing zenith angles between $\sim 33°$ and $\sim 55°$ with a mean of $\sim 40°$. The distribution of pointing zenith angles is shown in the left panel of Fig. 5.1. Furthermore, the data is taken in wobble mode, mainly targeted to observe HESS J1023–575 and HESS J1018–589. The pointing positions in galactic coordinates are shown in the right panel of Fig. 5.1.

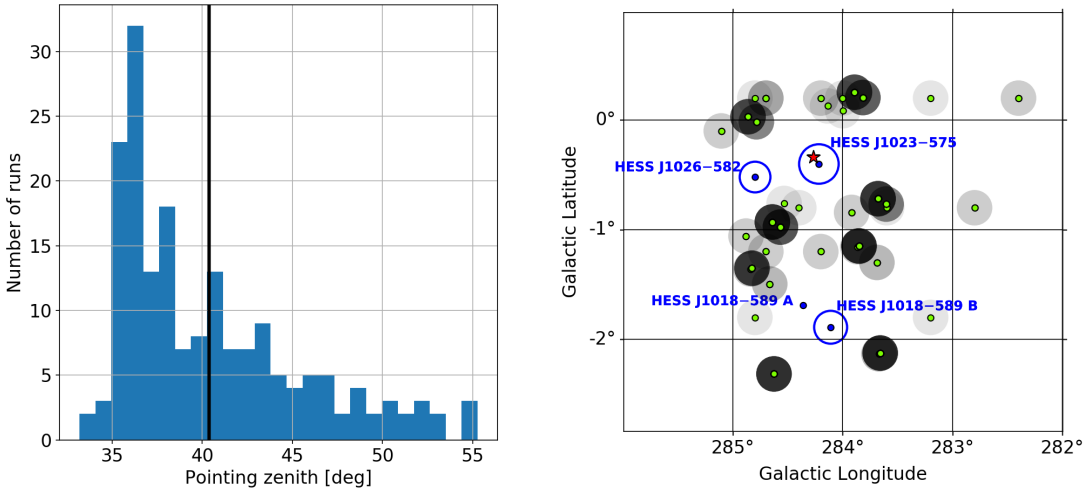

FIGURE 5.1: *Left*: Distribution of pointing zenith angles for the regarded 182 runs of data on Westerlund 2. *Right*: Pointing positions of the 182 runs in Galactic coordinates (green points). The γ-ray sources detected with H.E.S.S. are marked in blue. The grey to black shaded circles denote the increasing number of runs that were taken centred on a position. It can be seen that the dataset consists of mainly observations targeted at HESS J1023–575 and HESS J1018–589.

For the event reconstruction, a configuration is chosen that is optimised for extended and complex morphologies. This configuration is called *full enclosure*, meaning that no directional cut is applied to simulated shower events before lookup tables are generated for the analysis. Furthermore, the so called *hard* cut configuration is used in combination with a TMVA-based background suppression method (see Sec. 3.4.1 for details). This results in an energy threshold of $\sim 400\,\mathrm{GeV}$.

In combination, the dataset of the 182 selected runs has an exposure peaking $\sim 0.5°$ south of HESS J1023–575 with $\sim 2.5 \times 10^{10}\,\mathrm{m^2 s}$ as shown in Fig. 5.2. This detection-level dataset is used for all studies presented in the following to maximise the statistics for the morphological and spectral analyses.

5.2 Determining exclusion regions

Before starting an extensive analysis of the morphology and spectral properties of the Westerlund 2 region, it is important to determine proper exclusion regions to avoid contamination of the background estimate by potentially undetected γ-ray excess. Especially the diffuse γ-ray emission discovered in Fermi-LAT data [120] demands a careful definition of exclusion regions in order to properly characterise a potential diffuse excess at TeV energies.

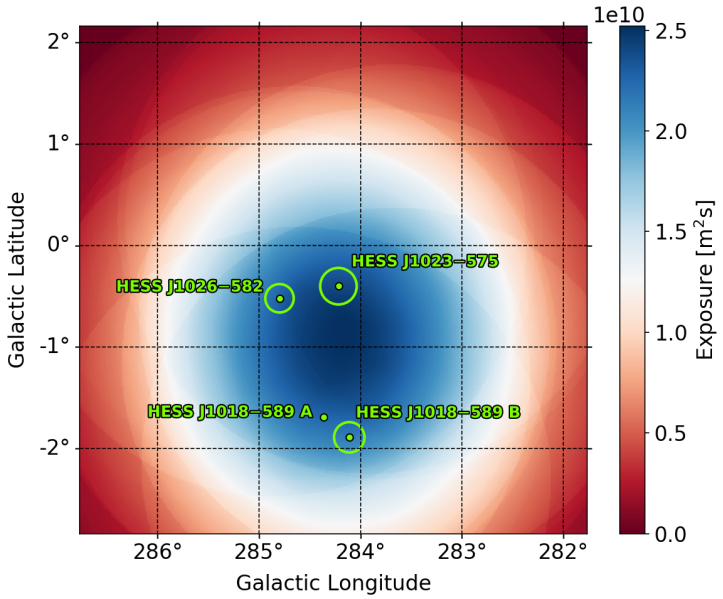

FIGURE 5.2: Exposure map of the combined 182 runs of H.E.S.S. data analysed in this thesis. The map has a pixel size of $0.01° \times 0.01°$.

Exclusion regions can be defined iteratively to optimise the area of the excluded regions to cover sufficient emission and still allow for a stable background estimate. This was for example done for the H.E.S.S. galactic plane survey [121], where 5σ contours in significance maps where extended iteratively by 0.3° to define the exclusion regions. This is not possible for this study, as it does not leave sufficient area for stable background estimates. Therefore, a different approach is taken as outlined in the following.

To construct exclusion regions, the detection level dataset using the hard cut configuration as outlined in Sec. 5.1 is used. The air-shower data is binned spatially in galactic coordinates into square bins with a side length of 0.01° while no binning in energy is applied. This setup provides adequate resolution with sufficient statistics per bin to determine morphological traits and define proper exclusion regions. The excess counts are calculated by generating a background model with the adaptive ring background method and subtracting the background counts per bin from the binned event counts. Figure 5.3 (*left*) shows the resulting excess map, correlated with a disk kernel of 0.09° radius (which is roughly the H.E.S.S. PSF). The sky map shows how the ring background method overestimates the background around the large extended source HESS J1023–575 in the centre of the sky map, resulting in an excess deficit in its vicinity. To shield signal regions from contaminating the background estimate, exclusion regions have to be introduced. A simple approach is to shield the known source regions in the FoV. To start, 0.15° or more are added to the extensions of known sources to form circular exclusion regions of at least 0.3° radius around each source. Regenerating the excess map with these *simple* exclusion regions results in the excess map shown in Fig. 5.3 (*right*), where it can be seen how the

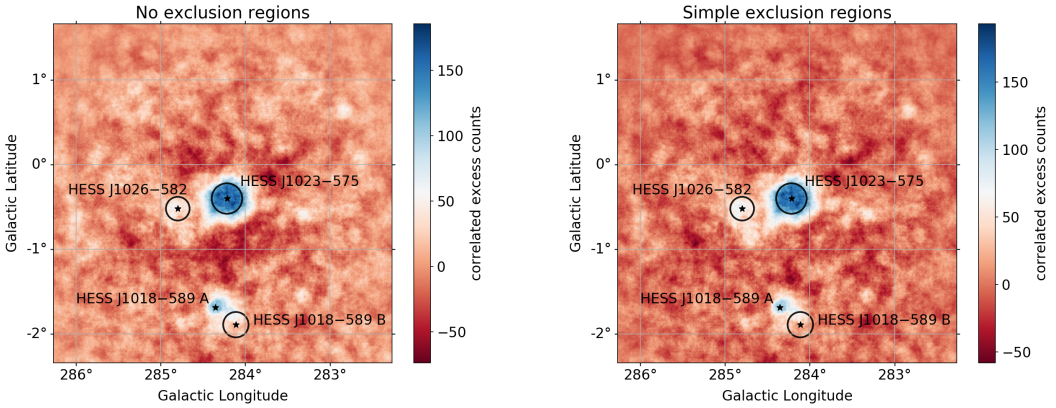

FIGURE 5.3: Excess maps created with no exclusion regions (*left)* and simple exclusion regions (*right)*. The background is estimated with the adaptive ring background method. The bins are correlated with a disk kernel of 0.09° radius. It can clearly be seen how the background in the centre is overestimated by not setting exclusion regions, which results regions of negative excess. The black stars show the positions of published H.E.S.S. sources in the FoV with the circles showing the 1σ containment for extensions.

emission around the centre source does no longer show the strong deficit as in the *left* map.

To further investigate if the exclusion regions are sufficiently shielding γ-ray emission, the residual distribution of a correlated significance map can be used. The LiMa significance (as introduced in Sec. 3.4.4) is thereby calculated from the correlated event and background counts for each bin of the sky map and the results are binned in a histogram. Figure 5.4 (*left*) shows this according distribution for the complete map and for the residual map of the background region, which is shown in Fig. 5.4 (*right*). The black areas depict the excluded regions. Adequate exclusion regions yield a background distribution following a Gaussian around 0 with a width of 1. Fitting a Gaussian to the background distribution shows that the exclusion regions already satisfy this criteria rather well with deviations only in the second decimal point (see the legend in Fig. 5.4 (*left*)). Nevertheless, regions of leaking excess emission and hotspots can still be seen around HESS J1023–575, especially to its west and south-east. Also the significance distribution in the background region shows an overabundance towards higher values, suggesting that apparent γ-ray emission is not sufficiently excluded.

To also prevent this emission from contributing to the background estimate, the exclusion regions are improved by adding regions to the west and south-east of HESS J1023–575. These regions are chosen in a way to allow for sufficiently large background regions for a proper background modelling, i.e. if the exclusion regions are set too large, no background regions can be defined for certain areas, resulting in an erratic background estimate. Figure 5.5 shows the significance distribution generated with the improved exclusion regions. By comparing Fig. 5.4 and Fig. 5.5, one can see how the fit of the background improves

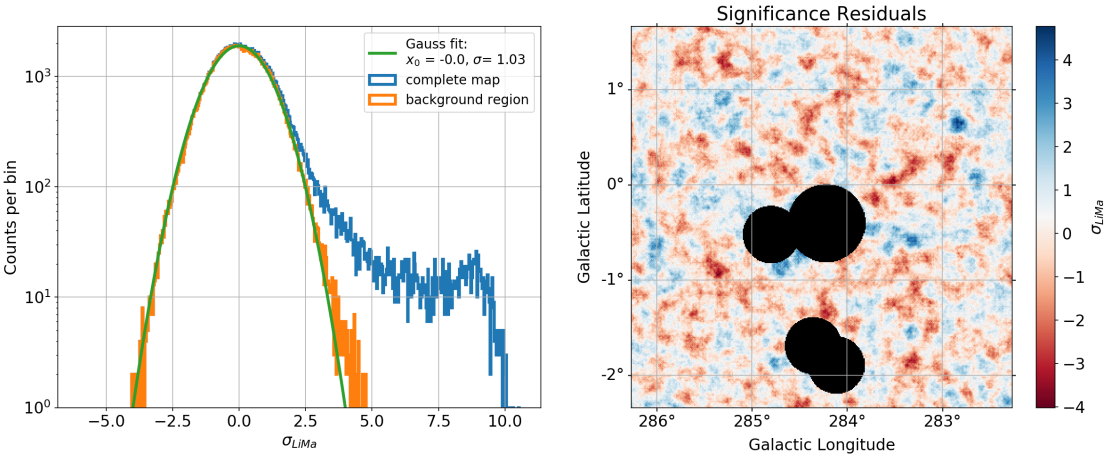

FIGURE 5.4: Significance distribution (*left*) of the correlated significance map shown (*right*). The black areas depict the exclusion regions. The background distribution is fitted with a Gaussian for which the fit parameters are shown in the legend. Leaking emission can still be seen around the central exclusion regions as well as hotspots to the west and south-east of the centre.

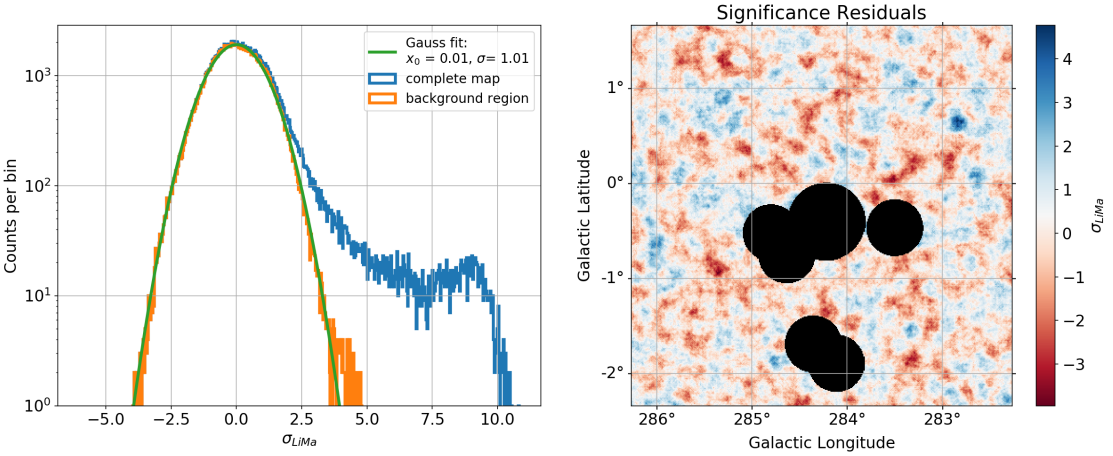

FIGURE 5.5: Significance distribution as shown in Fig. 5.4 but with improved exclusion regions. The hotspot and the leaking emission are excluded, resulting in an improved fit to the background distribution and overall higher significances in the signal regions.

and how the significances in the excluded regions increase. Figure 5.6 shows the according significance map of the Westerlund 2 region, saturated to the 5σ level.

As an additional test to probe if the exclusion regions are sufficient, the reflected background method can be used to search for emission which is not significantly detected using the ring background method. The reflected background method is more stable compared to the ring background method as it does not rely on a calculated exposure map. The individual background regions are defined per run around each telescope pointing position, directly resulting in regions of equal exposure. For the following study, this method is applied with circular signal regions of 0.05° radius on a grid with 0.05° spacing. This means

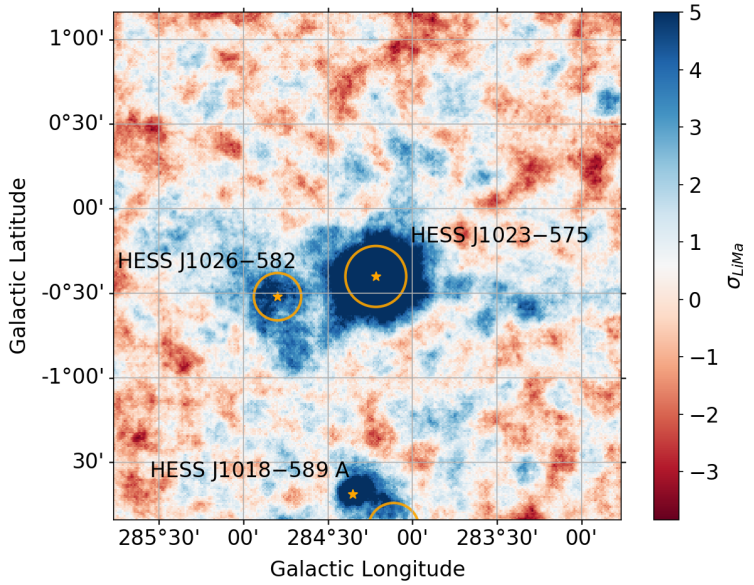

FIGURE 5.6: Saturated significance map generated with the improved exclusion regions. The orange stars and circles mark the locations and extensions of the known γ-ray sources in the FoV reported by H.E.S.S..

that neighbouring bins in the resulting map are correlated but that every air-shower event is included in at least one signal region. The resulting sky map shows the LiMa significance for a signal region centred on every bin. The map is shown in Fig. 5.7, overlayed with the 2, 4 and 6σ significance contours of the significance map shown in Fig. 5.6. It can be seen that excess emission is significantly detected over the whole sky map, even in regions that are not covered by the improved exclusion regions. To avoid a potential contamination of the background estimate with this emission, the exclusion regions are further adapted to also shield circular regions of 0.1° radius around every bin that shows a significance $> 4.5\sigma$ in Fig. 5.7.

Using these *final* exclusion regions in combination with the ring background method results in a further improvement of the background estimate with higher significances in the signal regions. Figure 5.8 shows the corresponding significance distribution. Here, it can be seen that the significance distribution of the background (orange histogram) follows a Gaussian without a peak towards higher significances as e.g. seen in Fig. 5.5. However, the overall background distribution shows a slight offset to the distribution of the complete map (blue histogram) in the range between ~ 0 and $\sim 2.5\sigma$. This means that a fraction of bins showing up-fluctuations of excess may be excluded from the background estimate, confirming that all potential excess is successfully shielded from the background regions.

The full significance map of the Westerlund 2 region generated with the final exclusion regions is shown in Fig. 5.9, saturated to the 5σ detection threshold to better visualise areas of significant γ-ray excess. The map reveals multiple lobes and hotspots of emission

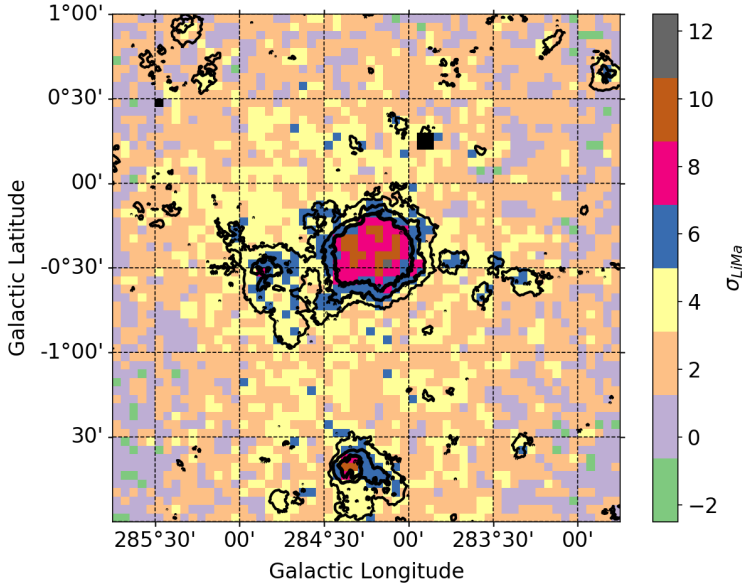

FIGURE 5.7: Significance map generated with the reflected background method for circular signal regions of 0.05° radius centred on each bin. The black lines show the 2, 4 and 6σ significance contours of the sky map shown in Fig. 5.6. It can be seen how γ-emission is significantly detected within the 2σ contours with the reflected background method. Bins coloured in black do not yield a valid significance value due to the interplay between size and position of signal regions, telescope pointing positions and exclusion regions.

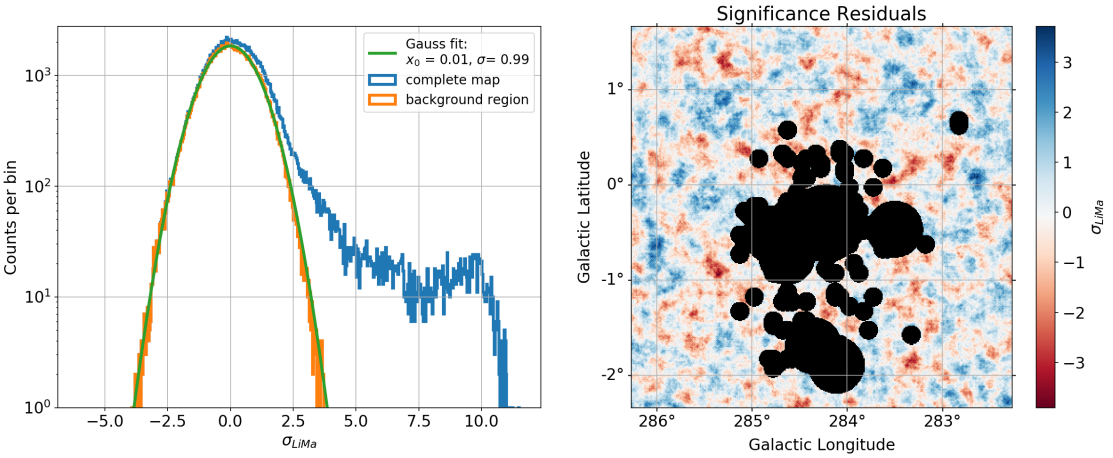

FIGURE 5.8: Significance distribution generated with the final exclusion regions.

around the known sources HESS J1023–575 and HESS J1026-582. The morphology of the emission is further analysed in Sec. 5.4.

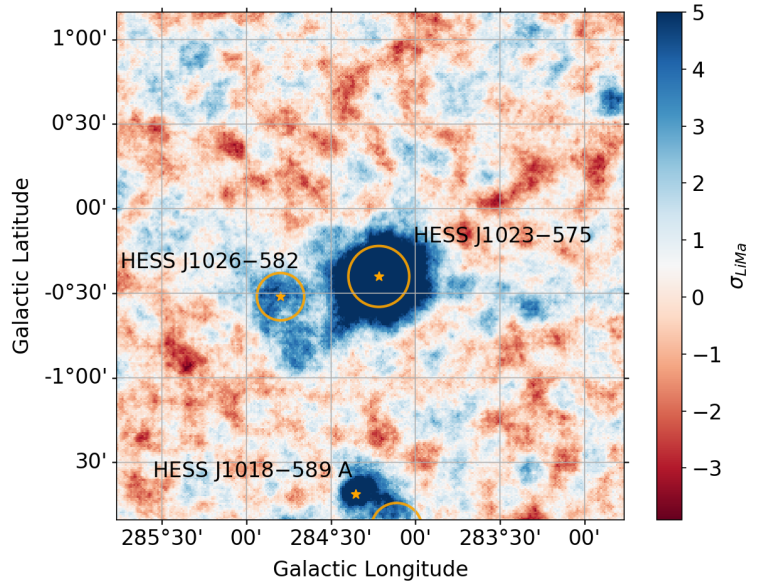

FIGURE 5.9: Saturated significance map generated with the final exclusion regions. The orange stars and circles mark the locations and extensions of the known γ-ray sources in the FoV reported by H.E.S.S..

5.3 Comparison to previously published results

With the exclusion regions being set, the detection significances and spectral properties of the known sources HESS J1023–575 and HESS J1026–582 can be determined and compared to the results from the previous H.E.S.S. publication on Westerlund 2 from 2011 [2]. Therefor the detection-level dataset generated with hard cuts is used as presented in Sec. 5.1. Furthermore, circular signal regions are chosen as in the 2011 paper with 0.22° (0.33°) radius around the source positions for detection (spectral) properties reported in the publication. To get a direct comparison, the flux is fitted with a power law of the form $\phi(E) = \phi_0 \cdot \left(\frac{E}{E_0}\right)^{-\Gamma}$ with the spectral index Γ, the flux normalisation ϕ_0 and the reference energy $E_0 = 1\,\text{TeV}$. Alternative spectral models for updated signal regions are discussed in detail in Sec. 5.5.

5.3.1 HESS J1023–575

Table 5.1 shows the detection significance and spectral properties of HESS J1023–575 from [2] (referred to as *HESS 2011*) and for the analysis of the here regarded dataset (referred to as *this work*). It can be seen that the number of excess counts is increased by a factor of ~ 3, which is explained by the larger dataset and the improved γ-hadron separation of the reconstruction algorithm. The spectral properties agree within the statistical error margins. A plot of the corresponding flux points and model fit is shown in Fig. 5.10 in the upper panel with corresponding residuals (the difference between flux points and model

divided by the model) in the panel below. The plot also shows the published best fit model with the according flux points[1] from the previous paper. A point to note is the significantly increased energy range of the fit to the new dataset, with the last significant flux point at around 80 TeV. Furthermore, a deviation of the flux points to the power law model can be seen with a slight curvature up to ~ 10 TeV and a more linear behaviour at higher energies. This might point to multiple sources being included in the large signal region, which is further investigated in Sec. 5.5.

HESS J1023–575	σ_{LiMa}	**Excess**	**Index** Γ	**Flux norm.** ϕ_0 **[1/(cm^2 s TeV)]**
HESS 2011	16	545	$2.58 \pm 0.19_{\text{stat}}$	$(3.25 \pm 0.50_{\text{stat}}) \times 10^{-12}$
This work	48	1613	$2.40 \pm 0.06_{\text{stat}}$	$(3.03 \pm 0.24_{\text{stat}}) \times 10^{-12}$

TABLE 5.1: Comparison of the detection significance and spectral properties from the 2011 H.E.S.S. paper on Westerlund 2 and this work using the same signal regions and spectral power law model.

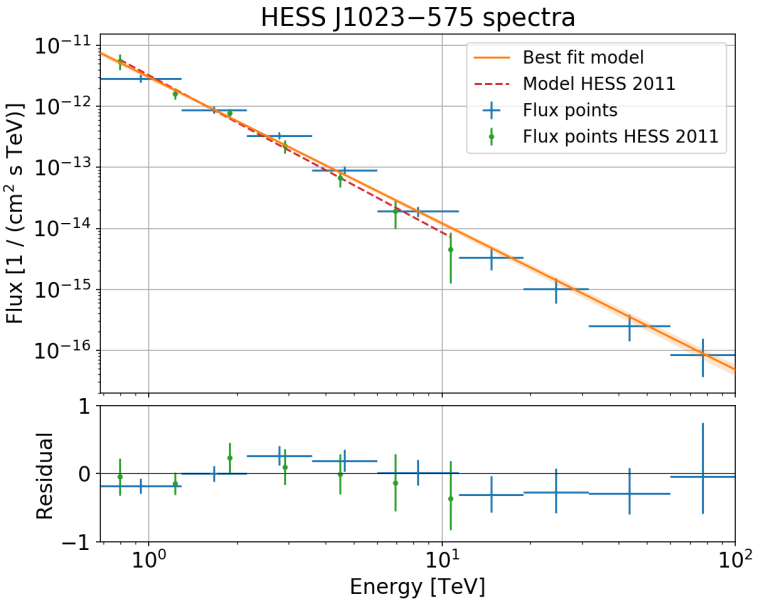

FIGURE 5.10: The upper panel shows the flux points and a fit to a power law spectrum for the HESS J1023–575 signal region as defined in [2]. The published best-fit model from the 2011 publication with the corresponding flux points is shown as well. The residuals (i.e. difference between flux points and model divided by model) of flux points to the according best fit model are shown in the lower panel.

5.3.2 HESS J1026–582

The result of a spectral fit to the signal region around HESS J1026–582 in this work confirms the previously published result. As seen in Tab. 5.2, the best fit model from

[1]Flux points taken from `https://www.mpi-hd.mpg.de/hfm/HESS/pages/publications/auxiliary/AA525_A46.html`

the here regarded dataset agrees with the model from the 2011 publication within statistical errors. The two models with according flux points and residuals are shown in Fig. 5.11. The residuals of the flux points to the best fit model show a deviation, suggesting that a power law may not be an appropriate model. Further studies on the spectral properties of HESS J1026–582 and alternative spectral models are presented in Sec. 5.5. As for HESS J1023–575, the number of excess events in the HESS J1026–582 signal region increased, yielding a significance higher by a factor of ~ 3 compared to the 2011 publication.

HESS J1026–582	σ_{LiMa}	**Excess**	**Index** Γ	**Flux norm.** ϕ_0 **[1/(cm^2 s TeV)]**
HESS 2011	7	169	$1.94 \pm 0.20_{\mathrm{stat}}$	$(0.99 \pm 0.34_{\mathrm{stat}}) \times 10^{-12}$
This work	24	748	$2.06 \pm 0.08_{\mathrm{stat}}$	$(0.97 \pm 0.17_{\mathrm{stat}}) \times 10^{-12}$

TABLE 5.2: Comparison of the detection significance and spectral properties from the 2011 H.E.S.S. paper on Westerlund 2 and this work using the same signal regions.

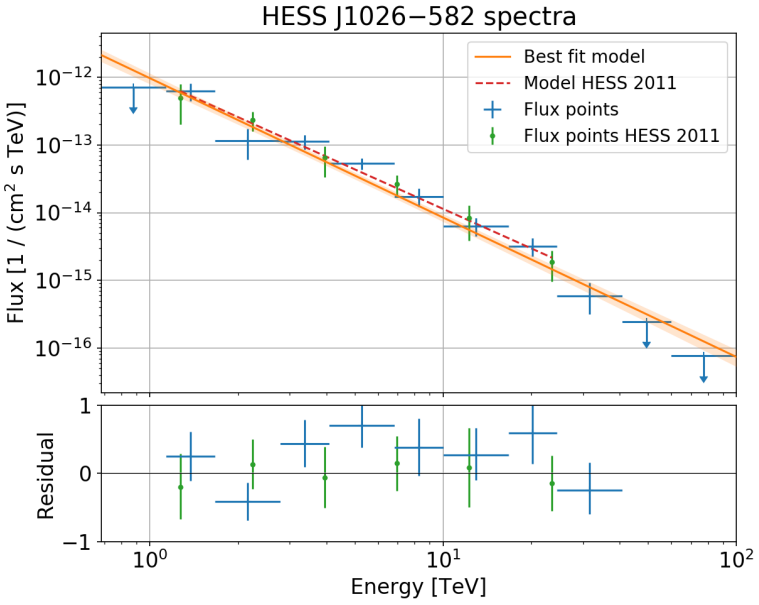

FIGURE 5.11: Flux points and the best fit to a power law spectrum for the HESS J1026–582 signal region as defined in [2] are shown in the upper panel. Flux points with a test statistic value < 4 are shown as upper limit. The published best-fit model from HESS 2011 with the corresponding flux points is shown as well. The residuals of flux points to the according best fit model are shown in the lower panel.

5.3.3 Probing energy dependent morphology

To investigate the morphology of HESS J1023–575 and HESS J1026–582 in more detail, the authors of HESS 2011 binned the data set into the two energy ranges from 0.7 TeV to 2.5 TeV and $>$ 2.5 TeV [2]. Doing the same for the dataset regarded in this work results in the significance maps shown in Fig. 5.12. As in HESS 2011, the morphology

of the emission is clearly energy dependent. Towards higher energies, the shape of the emission regions around HESS J1023–575 appears to change, whereas emission around HESS J1026–582 gets much brighter at higher energies, confirming the findings from the 2011 publication.

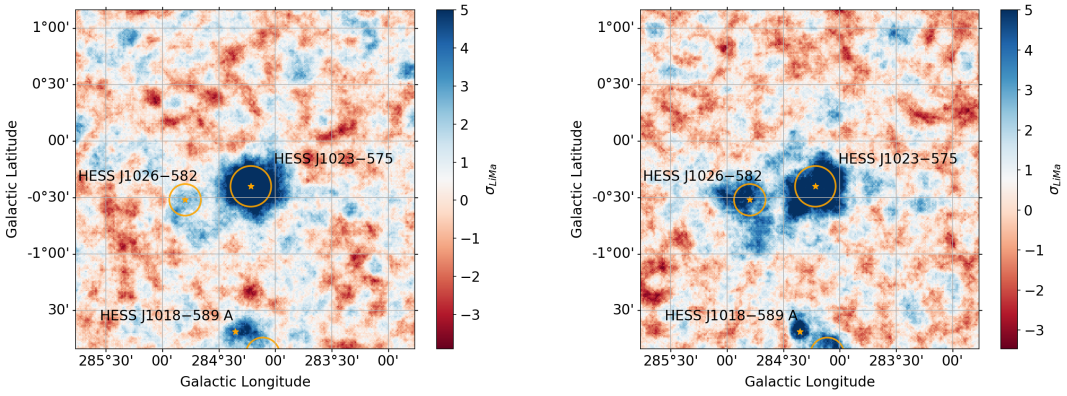

FIGURE 5.12: Saturated significance maps for the energy ranges from 0.7 TeV to 2.5 TeV (*left*) and > 2.5 TeV (*right*). An energy dependent change of morphology can clearly be seen.

Furthermore, a so called *slice* is used to explore the energy dependent morphology. A slice is created by defining a rectangular region or *box* in the reference frame of a sky map and creating a histogram of the uncorrelated excess counts within the box along one axis. For the following, the box is aligned along a line going through the best fit positions of HESS J1023–575 and HESS J1026–582 and is centred between the two sources. The resulting slice plot is shown in Fig. 5.13 (*left*), where the excess is shown per arcmin^2 inside the box along the long axis and fitted with two Gaussians for each energy bin as in Fig. 3 of the 2011 publication [2]. In contrast to the slice plot from [2], both signal regions now show a clear peak for HESS J1023–575 to the right and HESS J1026–582 to the left from the slice centre in both energy bins.

5.3.4 Concluding the comparison

In summary, the analysis of the updated dataset confirms the results published in [2]. The spectra of the two source regions HESS J1023–575 and HESS J1026–582 match the 2011 publication when fitted with a power law spectrum, with HESS J1023–575 showing a softer index than HESS J1026–582. Also the energy dependent morphology shows similar traits in the sky maps as also in the slice analysis. The increased statistics and better sensitivity of the new analysis however provide a basis for more elaborate morphology and spectral studies, which are presented in the following Sec. 5.4 and Sec. 5.5.

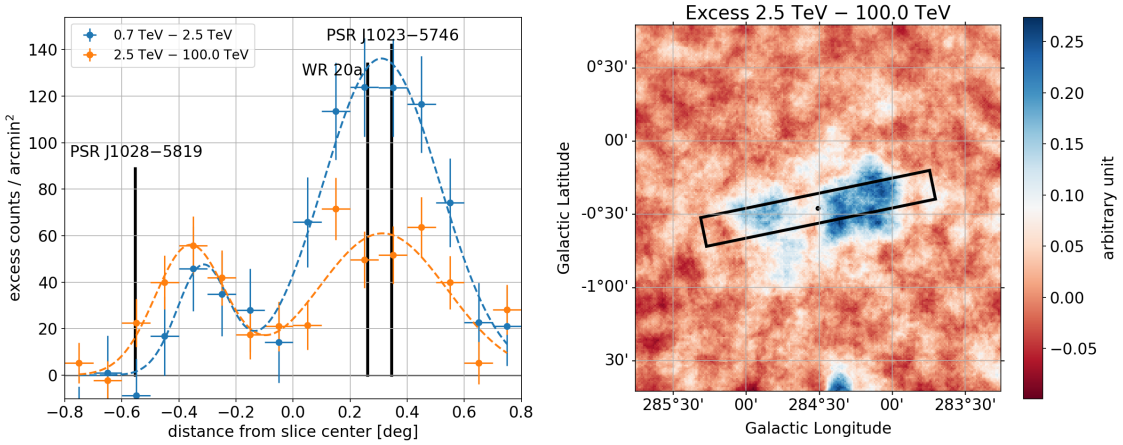

FIGURE 5.13: *Left*: Histogram of uncorrelated excess events along the horizontal axis of the box region shown in the sky map on the *right*. The positions of the massive Wolf-Rayet binary WR 20a as well as of two prominent γ-ray pulsars are also shown to get a direct comparison to the plot shown in Fig. 3 of HESS 2011 [2].

5.4 Morphology in the full energy range

The sky maps shown in the previous sections 5.2 and 5.3 exhibit emission with a complex and energy dependent morphology around Westerlund 2. The scope of this section is to inspect the significance of observed emission and determine individual components or regions showing significant excess. A special focus is put on the search for a large-scale or diffuse emission in the region as found in Fermi-LAT data [120].

All sky maps shown in this section are created with the ring background method, use a 0.01° binning and are correlated with a disk kernel of 0.09° radius, if not stated otherwise. Furthermore, the final exclusion regions as determined in Sec. 5.2 are used for all following studies. As for the studies presented above, the detection-level dataset with hard cuts and the full enclosure configuration is used.

5.4.1 Determining significant emission with the reflected regions method

The significance map in Fig. 5.9 shows many lobes and hotspots of emission in the vicinity of the known sources in the Westerlund 2 region, depicting significances around the detection threshold up to 5σ. Nevertheless, this does not mean that the emission is caused by real γ-ray sources. Single pixels or hotspots with higher significances are not a rarity in such sky maps, as statistical fluctuations in the data are expected to produce such artefacts. Especially in correlated sky maps, fluctuations or systematic effects such as erratic event reconstruction can be augmented, creating spatial features of higher significances. On the other hand, a clustering of weakly significant emission can be a hint towards a diffuse or large scale γ-ray signal being present. The difficulty is thus to elaborate if a

weak excess in a sky map is caused by mere statistics, a bias in the analysis, an unaccurate modelling of the background or if it could actually originate from one or multiple weak sources of γ-ray emission.

To verify the morphology seen in the Westerlund 2 sky maps, the reflected regions method can be used. It is applied as in Sec. 5.2, using the final exclusion regions and circular signal regions with 0.05° radius on a 0.05° spaced grid. The resulting map is shown in Fig. 5.14, overlayed with the $2, 4$ and 6σ contours of the respective significance map from Fig. 5.9. The sky map reveals emission at $> 5\sigma$ level from the reflected background method within the 2σ contours of the significance map generated with the ring background method. Furthermore, the overall significance distribution of the map peaks at a rather high $\sim 3.1\sigma$, hinting at a potential large-scale diffuse emission in the region.

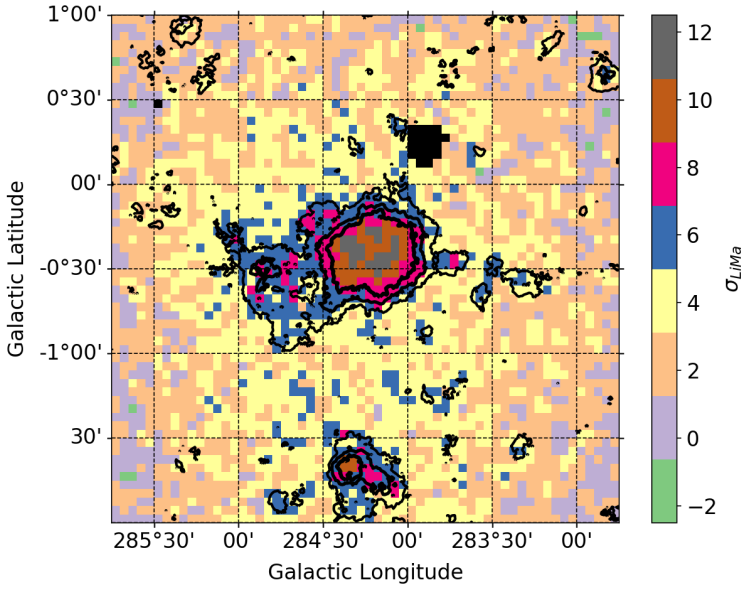

FIGURE 5.14: Significance map generated with the reflected background method for circular signal regions of 0.05° radius centred on each bin, using the final exclusion regions. The black lines show the $2, 4$ and 6σ significance contours of the sky map shown in Fig. 5.9. The bins coloured in black do not yield a valid result from the reflected regions method.

This suggests that the 2σ contours can be interpreted as outlines of significant emission on top of a diffuse signal as the one detected by Fermi-LAT. Nevertheless, before interpreting this apparent emission at the detection threshold as γ-ray signal, it is advisable to first get a better idea about what kind and at what scales artificial signal can be created in a sky map. This can be done by taking a closer look at the respective sky maps of a source where the shape and surroundings are well known. A good candidate is the well-studied AGN PKS 2155–304. As an extragalactic source, it appears as point-like and does not have any known γ-ray sources in its proximity of $\sim 2.5°$ radius, which makes it perfect to investigate the formation of artificial features. For this study, a detection level dataset with hard cuts and full enclosure configuration, comprising 755 runs with more than 360 h of observation

time with the four H.E.S.S. phase I telescopes is used. The runs were taken at a mean pointing altitude of $\sim 68.5°$ with different wobble offsets in RA and Dec from the source position, whereas $\sim 60\%$ of the runs are targeted $\pm 0.5°$ offset from PKS 2155–304 in RA (left and right in the shown sky maps). The reflected regions method is applied to this dataset with the same binning and settings as for the Westerlund 2 region. Furthermore, a circular exclusion region is defined at the position of PKS 2155–304 with a radius of 0.3°. The resulting significance map is shown in Fig. 5.15. It is saturated to the same scale as the map in Fig. 5.14 for comparability and also shows the $2, 4$ and 6σ contours from the respective ring background analysis of the region. Against expectations, the map shows highly significant emission with hotspots up to $> 9\sigma$, that appear to be clustering to the west, east and south of PKS 2155–304, following the telescope pointing positions (shown as white markers with blue crosses).

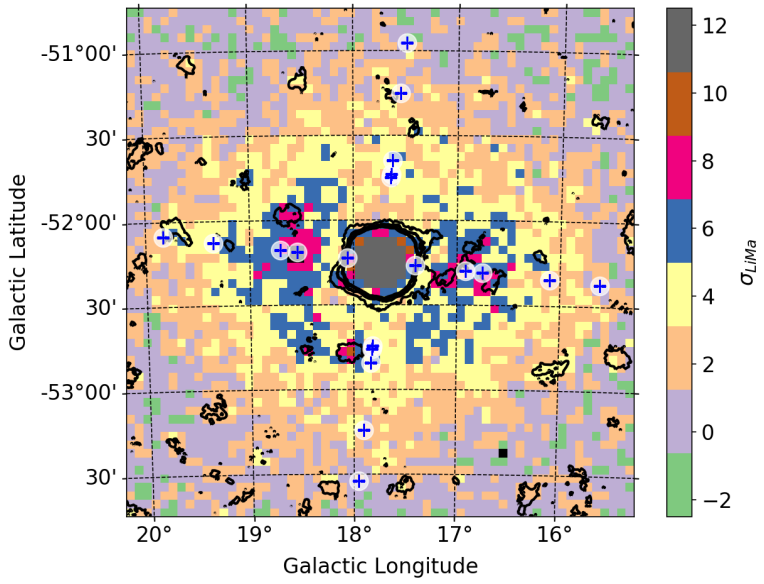

FIGURE 5.15: Significance map from 360 h of observation time on PKS 2155–304 generated with the reflected regions method for circular signal regions of 0.05° radius centred on each bin. The black lines show the 2, 4 and 6σ significance contours of the corresponding significance map generated with the ring background method. The white dots with the blue crosses mark the telescope pointing positions. The map is saturated to the same scale as the map in Fig. 5.14 for comparability.

There are different possible explanations for the apparent signal around PKS 2155–304. One possibility would be an incorrect background estimate. This could e.g. originate from incorrect exposure modelling or an inhomogeneous level of night sky background (NSB) across the map. This can however be ruled out in this case as the reflected regions method intrinsically models the exposure correctly. Furthermore, NSB effects would not create artefacts that are correlated with the pointing positions. Assuming radially homogeneous exposure and even NSB, the background model should thus only be affected by statistical fluctuations in the data. One problem with the reflected regions method is that the

number of OFF-regions and therefore the statistics for a background estimate depends on the size of the ON-region and its distance to the pointing positions as well as on the size and positions of the exclusion regions. For a dataset with strongly clustered pointing positions, as in this case, further systematics can be introduced. This is suggested by the strong correlation between pointing positions and hotspots seen in Fig. 5.15. Also the 2σ contours of the ring background method appear to correlate with the hotspots in the reflected regions map, suggesting that systematics within the reflected regions method can not be the only cause for the apparent signal.

In general, there are two possible explanations for the significant hotspots around PKS 2155–304:

1. There is γ-ray emission around PKS 2155–304 which has not been detected so far.
2. The emission is of artificial nature and is created by systematic effects that become visible due to the high and clustered exposure of the dataset. The hotspots and lobes of emission could for example consist of γ-ray events from PKS 2155–304 for which the direction is not reconstructed correctly (e.g. a systematic bias in the direction reconstruction for shower events of certain properties).

Option 1 is rather unlikely and would not help to assess the influence of systematic effects in the case of Westerlund 2. Therefore, the emission around PKS 2155–304 will be assumed to be caused by systematic effects. A detailed investigation of these features would go beyond the scope of this work and will thus not be discussed further. Assuming this emission to be caused by systematics is a conservative approach as the PKS 2155–304 dataset comprises ~ 4.5 times more observation time with much more clustered pointing positions compared to the Westerlund 2 dataset. Systematic effects should therefore be much more significant in the PKS 2155–304 dataset. Even if the emission is caused by real γ-ray sources, assuming it to be artefacts from the analysis can only overestimate the level of systematics to be compared to the features seen in the Westerlund 2 dataset.

As the PKS 2155–304 and the Westerlund 2 datasets have very different exposures, it is important to scale the two significance maps accordingly in order to make them comparable. This can be done by dividing each bin of the significance map by its respective exposure, thus creating maps that show the rate of detection significance in σ_{LiMa} per $\sqrt{\mathrm{m}^2 h}$. The scaled maps are shown in Fig. 5.16, saturated to show the same colour scale. It can be seen that the overall level of significance per exposure in the Westerlund 2 region (peaking at $\sim 1.8 \times 10^{-4} \sigma_{LiMa}/\sqrt{\mathrm{m}^2\mathrm{h}}$) is higher than for the PKS 2155–304 region (peaking at $\sim 0.5 \times 10^{-4} \sigma_{LiMa}/\sqrt{\mathrm{m}^2\mathrm{h}}$). This can be interpreted as a hint of diffuse emission around Westerlund 2.

As a final test, the energy flux of the potential artefacts can be used to decide if the features seen in the Westerlund 2 region can be regarded as γ-ray emission. This is done by stacking the observation runs and applying the reflected regions method to extract the

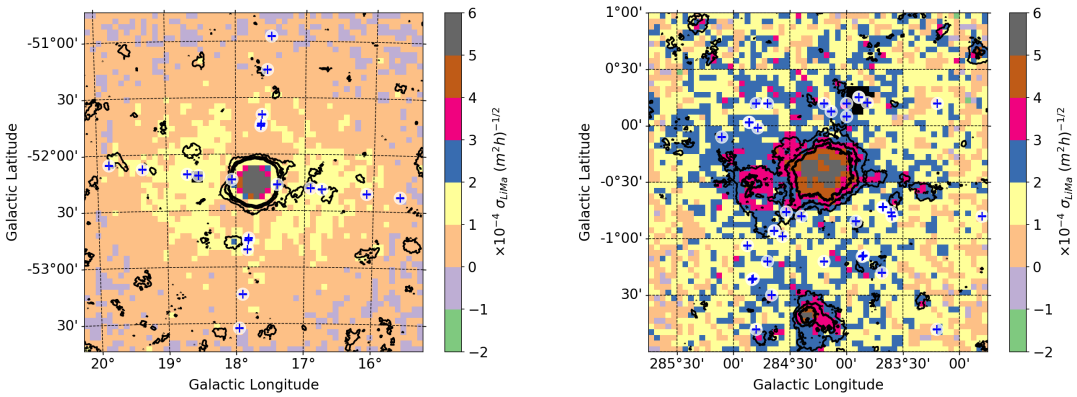

FIGURE 5.16: Exposure-scaled significance maps for the PKS 2155–304 (*left*) and the Westerlund 2 dataset (*right*). The white markers with blue crosses depict the different telescope pointing positions. It can clearly be seen that the Westerlund 2 region shows a higher level of significance per exposure compared to the region around PKS 2155–304. The sky maps are saturated to show the same colour scale.

energy spectrum per bin by fitting a power law spectrum. As the previously used binning of $0.05° \times 0.05°$ yields very low statistics per bin, the grid is increased to $0.1° \times 0.1°$ bins and the integration radius for each ON region is increased to 0.2°. Additionally, the *improved* exclusion regions are used in order to allow for better statistics for the background estimation. The amplitude of the resulting fit per bin gives the reference flux at 1 TeV. The resulting flux maps are shown in Fig. 5.17, where grey bins depict regions where the fit does not converge and results in unrealistic parameter values. Comparing the two maps shows that also here, the flux is higher in the Westerlund 2 region.

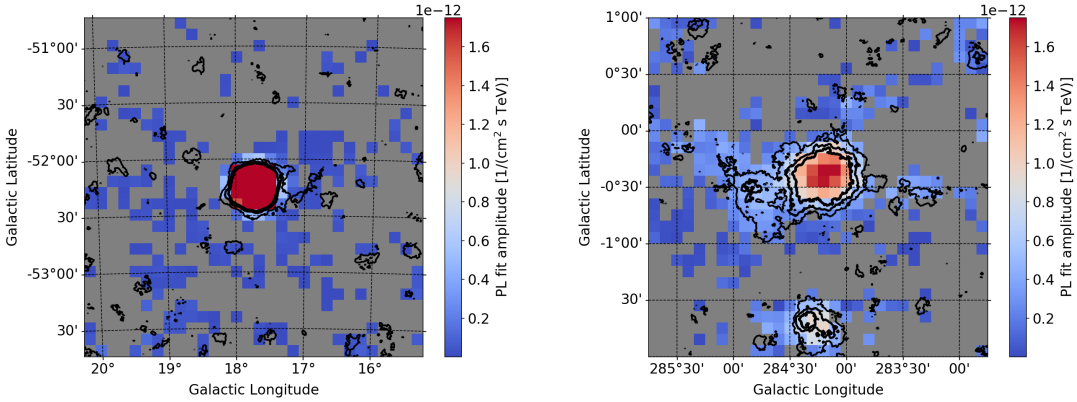

FIGURE 5.17: Flux maps of the regions around PKS 2155–304 (*left*) and Westerlund 2 (*right*). The bins show the amplitude of a fitted power-law spectrum, saturated to show the same scale. Grey bins depict regions where the fit does not converge and provides unrealistic parameter values. The black contours depict the $2, 4$ and 6σ contours from the respective significance maps.

In combination, these findings suggest that the emission around Westerlund 2, especially within the 2σ contours, is of physical origin and not caused by systematic effects. The 2σ contours seen in Fig. 5.14 around Westerlund 2 can therefore be interpreted as outlines

of emission from γ-ray sources. Furthermore, a hint of a diffuse emission as reported in Fermi-LAT data is seen with the reflected regions method. Further discussions are presented in Sec. 6.2. To get deeper insights and quantify this potentially diffuse emission, a dataset with higher exposure and especially covering a larger field of view is needed.

5.4.2 Slice analysis

To further probe the morphology of the emission in the Westerlund 2 region, a slice analysis as used in Sec. 5.3 is applied. A slice analysis makes use of the ring background method, but it does not correlate the observed counts. Instead, it shows uncorrelated and rebinned excess counts, whereas a larger binning can help to suppress fluctuations in the histograms and thus visualise general morphological features.

A slice region of $0.1^\circ \times 2.5^\circ$ is centred on HESS J1023–575 and aligned along different angles to investigate the emission within the 2σ contours of the ring background method. The counts are combined in bins of $0.1^\circ \times 0.1^\circ$ with Poisson errors, being the square root of the total counts (*not* the excess counts) per bin. The results for four differently aligned slices are shown in Fig. 5.18 *left* with the respective slice regions being depicted on the *right*. The histograms reveal a complex structure of emission around the central source HESS J1023–575:

- **Slice A** is aligned at an angle of 15°, thus including parts of HESS J1026–582. The histogram shows the expected peak at -0.6° with an extension up to -1°. Towards positive distances from HESS J1023–575, an extension of the excess up to 0.5° can be seen. The excess directly around HESS J1023–575 does not show a clear peak but rather a plateau.
- **Slice B** (42° inclination) goes through the excess seen to the south-east of HESS J1023–575. As for slice A, the excess extends up to $\sim -1^\circ$ and shows a peak around -0.6°. Another peak not compatible with 0 can be seen at 0.8° where the slice goes through a hotspot north-west of HESS J1023–575.
- **Slice C** is inclined at -12° and goes through the large excess seen to the east and west of HESS J1023–575. To the west, the excess extends $> 0.5^\circ$ with a bump and fluctuates with a strong peak at 0.9° where a hotspot can also be seen in the sky map.
- **Slice D** inclined at 72° goes through the slight lobe of excess extending from HESS J1023–575 to the north. The histogram shows fluctuating excess up to 1.3° that is not compatible with 0, in contrast to the excess towards negative distances from the slice centre, which is well compatible with 0. There, HESS J1023–575 extends up to around -0.5°.

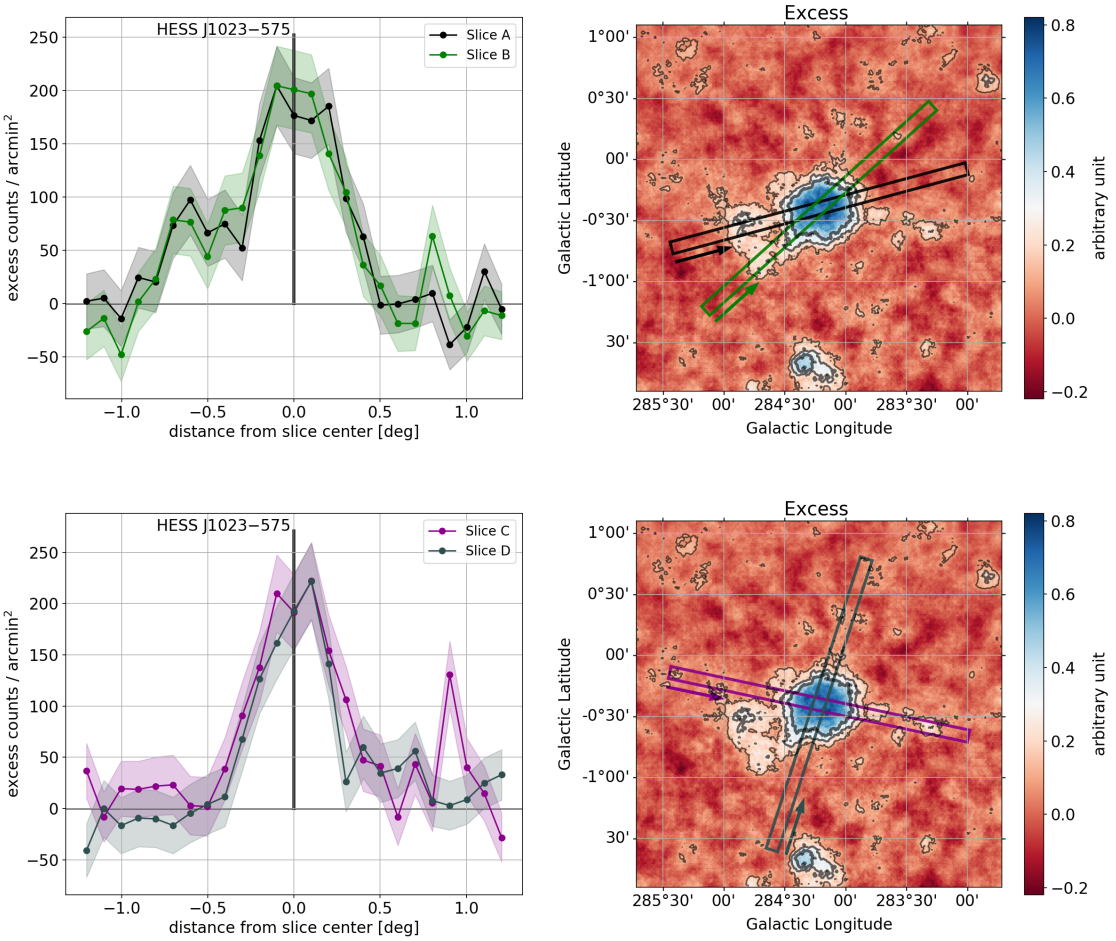

FIGURE 5.18: Slice plots for four selected slice regions labelled A, B (*upper panel*), C and D (*lower panel*), all centred on HESS J1023–575. The left panels show the counts along the long axis of the slices from left to right, the error regions are taken as $\pm\sqrt{N_{counts}}$. For visualisation, the $2, 4$ and 6σ contours from the significance map in Fig. 5.9 are shown in grey. See the main text for the discussion of the individual slices.

5.4.3 Defining regions of interest

For a better discussion of individual parts of the detected emission, regions of interest (RoIs) are defined. Each RoI covers apparent hotspots and visible features in the significance map. The defined RoIs, as shown in Fig. 5.19, are:

- **Region A** or the *central region*: It includes HESS J1023–575 and its direct vicinity. The emission shows a few interesting features such as a lobe extending to the north-east, a slight extension of the central source to the north to north-west as well as an elongated extension to the south-east (which is fully covered by region C).
- **Region B** covers the emission extending to the west of the central region. This region shows two larger apparent hotspots which can also be seen in Slice C in Sec. 5.4.2, with two additional smaller features.

- **Region C** encloses the emission extending to the south-east of the central region. In this region, the central source shows a prominent elongation extending to the south-east, which is coincident with the so called *jet* cloud found in radio data [3].
- **Region D** includes HESS J1026–582 and its close proximity. The 2σ contours show a fuzzy extension to the north-east.
- **Region E** covers a hotspot 2° north-west of Westerlund 2.

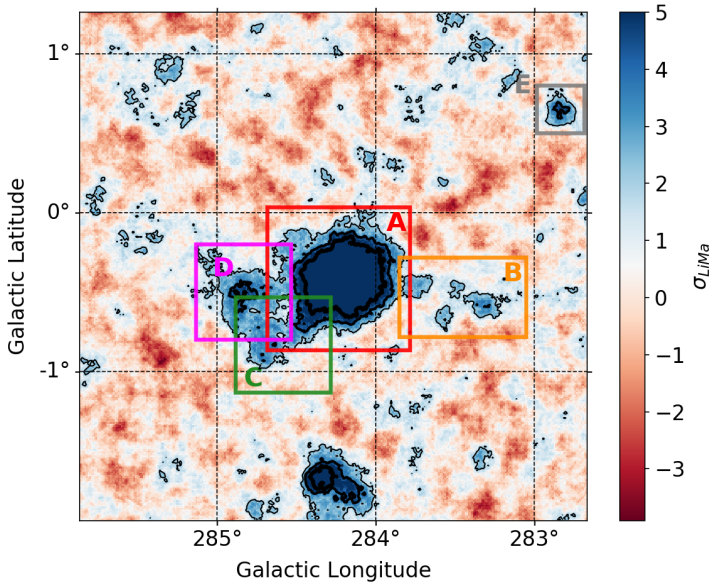

FIGURE 5.19: Positions of sub-regions of interest, defined to better discuss different parts of the emission seen in the Westerlund 2 region. The underlying map is the saturated significance map also shown in Fig. 5.9 overlayed with the $2, 4$ and 6σ significance contours.

As seen in Fig. 5.19, regions B, C and D are all connected to the central region A. Especially regions A, C and D form an apparent entity of emission regions that merge into each other, almost forming a triangle with peaks at the edges (the centres of regions A, C and D) and a deficit in the centre (seen in the overlapping area of regions A, C and D). Despite their close proximity to one another this proposes separate γ-ray sources. The literature suggests that Region D with HESS J1026–582 is *not* connected to the emission in region A and C [2] while the emission in region A and C could be connected [3]. For the following examination of the RoIs, these three regions, also referred to as the Westerlund 2 *core region* are therefore discussed together while region B and region E are treated individually.

With these defined features and the RoIs, an elaborate fitting procedure of source components can be performed to determine the positions and spectral properties of individual sources as presented in the following Sec. 5.5.

5.5 Morphology and spectral analyses

The previous sections present the morphology of the emission around Westerlund 2 in the full available energy range in the selected dataset from $\sim$ 400 GeV to $\sim$ 85 TeV. The studies show a rather complex morphology in the vicinity of the stellar cluster with apparently individual components in close proximity and a potential diffuse component in the FoV. A detailed investigation of the spatial and spectral properties of the emission in the RoIs can help to distinguish individual γ-ray sources and to separate emission of different physical origin, especially for the Westerlund 2 core region. Two different approaches can be taken to extract spectral properties:

- The spectra of subregions can be extracted with the reflected regions method by defining ON and OFF regions and performing a maximum likelihood fit on the spectral distribution of the excess (see Sec. 3.4.6). A disadvantage of this approach is that the spectra are extracted for the ON region as a whole, meaning that the spectra of potentially overlapping components within the ON region are combined. An advantage on the other hand is the quality of the background estimate, as it is done run-wise for each telescope pointing position.
- A 3D fit can be performed where the morphology and spectra of components are fitted in combination. This method uses the energy binned count maps together with the exposure maps and the background estimate from the ring-background method and performs a maximum likelihood fit as outlined in Sec. 3.4.5. A disadvantage of this approach is the dependency on the ring background method which can be susceptible to incorrectly modelled background. A big advantage is however that the emission of potentially overlapping components can be disentangled, providing spectral properties for each morphological component individually.

Both approaches are used in the following. For lucidity, the RoIs are combined into three sets that are discussed individually in the next sections:

1. Region A, C and D are analysed in combination as the Westerlund 2 core region presented in Sec. 5.5.1.
2. The analysis of region B with two larger hotspots is discussed in Sec. 5.5.2.
3. The analysis of the single hotspot in region E is presented in Sec. 5.5.3.

5.5.1 The Westerlund 2 core region

The properties of the Westerlund 2 core region are determined in multiple steps. First, spectral maps are created by applying the reflected regions method. In the second step, a

3D fit procedure is performed to get adequate spatial and spectral models of the individual components. Finally, an ON-OFF spectral analysis is performed with the reflected regions method for the source regions determined in the 3D fit procedure to investigate the spectral properties in more detail.

5.5.1.1 Spectral maps

In Sec. 5.4.1, the energy flux was extracted for several equally spaced spatial bins in the Westerlund 2 region by stacking the observation runs and fitting a power law spectrum, resulting in a spectral flux map of the Westerlund 2 region as shown in Fig. 5.17. From the same analysis, a sky map showing the spectral index at each position can be created. As mentioned before, the spectral maps are created with the *improved* exclusion regions (see Sec. 5.2 for details). A $0.1^\circ \times 0.1^\circ$ binning is used with an integration radius of 0.2° to allow for sufficient statistics per bin. This correlates the bins of the maps up to the second order, i.e. up to the second next neighbour of each bin. Nevertheless, it shows the trend of the spectrum across the Westerlund 2 region. Figure 5.20 shows the maps with the spectral index (*top*) and flux normalisation (*bottom*) per bin overlayed with the $2, 4$ and 6σ significance contours together with the outlines and positions of the previously published TeV sources in the FoV.

The upper panel in Fig. 5.20 shows the spectral index, where a clear spatial correlation can be seen across the region of significant emission with a gradient of the spectral index from a soft index of > 2.5 in the north-west with a hardening towards the south-east. This suggests that different physical processes are at work in the Westerlund 2 core region. The close proximity of pools of emission and their overall extension and shape suggests a high potential of source confusion. To disentangle the potentially overlapping sources of emission in the vicinity of Westerlund 2 in the RoIs A, C and D, a 3D fit procedure can be performed as presented in the following section.

5.5.1.2 3D fit with gammapy

To model the central emission region around Westerlund 2, the detection level data is binned into $0.02^\circ \times 0.02^\circ$ spatial bins with 1.0° radius around the galactic position ($l = 284.5^\circ$, $b = -0.5^\circ$) and binned into six equally spaced logarithmic energy bins from 400 GeV to 85 TeV. The exposure maps, energy dispersions and PSFs are generated and a background model is created with the ring background method for every bin in energy. With this, a 3D fit procedure with model selection is performed as outlined in Sec. 3.4.5. Figure 5.21 shows the correlated count and background maps summed over all energy bands.

The first step for a 3D fit procedure with model selection is the set up of a candidate collection of adequate models to fit to the data. For this analysis, the collection consists

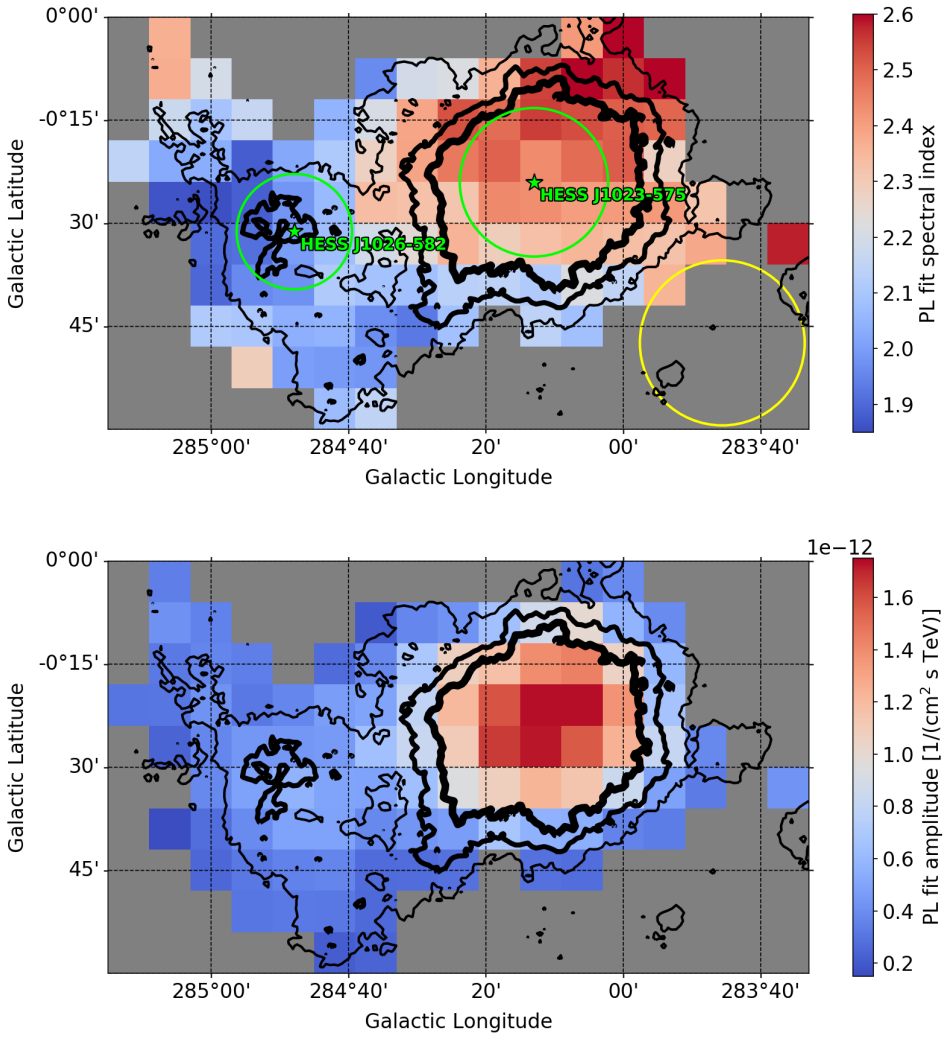

FIGURE 5.20: Spectral maps of the Westerlund 2 core region. The *top* panel shows the index of a power law fit, the *bottom* panel shows the respective amplitude. Grey bins depict regions where the fit does not yield a valid result or errors in index or amplitude of $> 50\%$. Both maps are saturated for visualisation purposes. The $2, 4$ and 6σ significance contours are shown in black for orientation. The yellow circle in the upper panel denotes the size of the integration region used per bin while the green markers and circles show the position and extension of the two sources in the FoV published in [2].

of 11 models which are motivated by findings from the literature, visible features in the sky maps and findings from the analyses presented in Sec. 5.4. Each model consists of source components that model the spatial and spectral properties of potential γ-ray sources on top of the background model for which the amplitude is adjusted in the fit. The collection covers models that are known to underfit the data (i.e. the model is likely unable to describe the data sufficiently) up to models that likely overfit the data (i.e. capture more than the general features of the data). This is done to gradually extend the complexity of the models in the candidate collection to observe how the AIC score is first reduced with rising number of free model parameters (and thus improving the

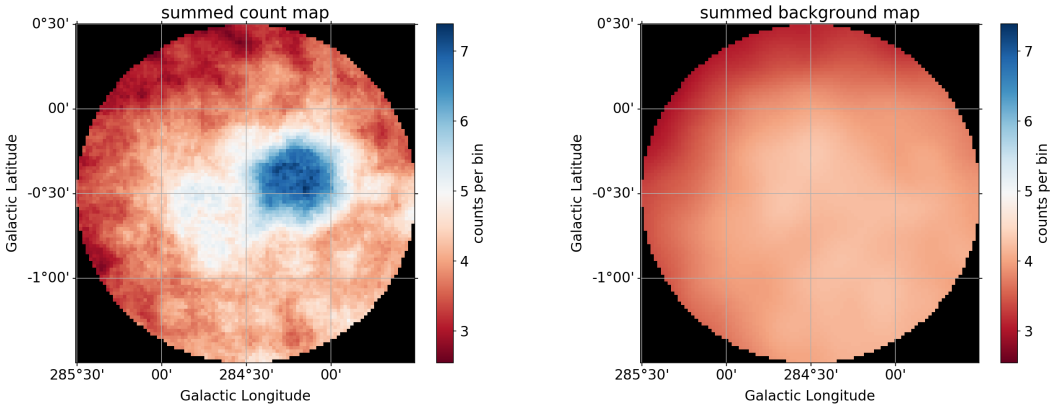

FIGURE 5.21: Summed count (*left*) and background map (*right*) for the 3D fit of the Westerlund 2 core region. The maps are correlated with a disk kernel of 0.09° radius. The black shaded region is excluded from the fit procedure.

model-to-data discrepancies) up to the turning point where the added complexity starts to reduce the AIC score again (see Sec. 3.4.5 for details on the whole procedure).

The first and simplest model in the candidate collection is a single Gaussian centred on HESS J1023–575 on top of the background model (which is shown in Fig. 5.21 *right*). The following models in the collection gradually extend the number of free parameters by adding components and exchanging simpler geometries with more complex ones, like replacing Gaussians with disks or ellipses (where disks and ellipses also have the option for smooth edges, which describe the width of the border of the shape in which its amplitude drops from 95% to 5%). The fitted components for each model are outlined and motivated in the following:

- **model_A**: One Gaussian component; Expected to underfit as at least two sources in the FoV are known to exist;
- **model_B**: Two Gaussian components; The model motivated by the H.E.S.S. publication from 2011 [2];
- **model_C**: One disk and one Gaussian; Component for HESS J1023–575 modelled with a disk as suggested by Fermi-LAT publication [119];
- **model_D**: Three Gaussian components; Added an additional component for faint hotspot already seen in the H.E.S.S. paper from 2011 [2];
- **model_E**: One disk and two Gaussian components; Variation of model_D;
- **model_F**: One disk, one Gaussian and one ellipse; Further variation of model_D with additional degrees of freedom; The ellipse is also motivated by elongated cloud found in CO data, coincident with VHE hotspot [124, 3];
- **model_G**: Two Gaussian components and an ellipse; Variation of model_F;

- **model_H**: One disk and three Gaussian components; Extension of model_E;
- **model_I**: One disk, two Gaussians and an ellipse; Extension of model_F;
- **model_J**: One disk, one Gaussian, an ellipse and a large disk with fixed width and position as a diffuse component, motivated by the indication of a large scale diffuse emission as discussed in Sec. 5.4.1; Extension of model_F;
- **model_K** One disk and five Gaussian components; Extension of model_H;

All these models are fitted to the data in a maximum likelihood fit procedure using the C statistic in `gammapy` with the `iminuit` backend. The most appropriate model is selected by using the AIC as outlined in Sec. 3.4.5. Table 5.3 summarises the total number of free parameters, the respective AIC scores of the fitted models as well as the difference ΔAIC of each model to the model with the lowest AIC score in the collection (model_F, marked in bold). The details of the fits for all models in the candidate collection can be found in Appendix D, where maps of the models and the residuals are shown together with the initial and best-fit values of the parameters and the significances of the components within the models.

Model	**# Parameters**	**AIC**	**ΔAIC**
model_A	6	34881.42	133.42
model_B	11	34769.20	21.20
model_C	12	34766.00	18.00
model_D	16	34753.70	5.70
model_E	17	34751.81	3.81
model_F	**19**	**34748.00**	**0.00**
model_G	18	34755.87	7.87
model_H	22	34748.17	0.17
model_I	24	34750.23	2.23
model_J	21	34752.00	4.00
model_K	32	34753.94	5.94

TABLE 5.3: Models of the candidate collection in alphabetical order. The ΔAIC column shows the difference of the respective model's AIC score to the AIC score of model_F, the model with the lowest AIC score in the collection.

A plot of the C statistic values and the ΔAIC of the models in the candidate collection against the number of free model parameters is shown in Fig. 5.22. It can be seen how the C statistic gradually decreases with rising number of model parameters as expected, whereas the ΔAIC reaches a minimum at 19 parameters with model_F and then starts to rise again. The plot and Tab. 5.3 show that only model_H gives a $\Delta\text{AIC} < 2$ and is thus equally supported by the data as model_F. Nevertheless, as model_F has fewer free parameters and shows a slightly lower AIC score, it is taken as the preferred model and is discussed in detail in the following.

As pointed out in Sec. 3.4.5, so called *fake* data created by simulating observations from the best-fit model can be used to perform a hypothesis test to probe the probability that the observed data did not originate from the best-fit model. The model is thereby fitted

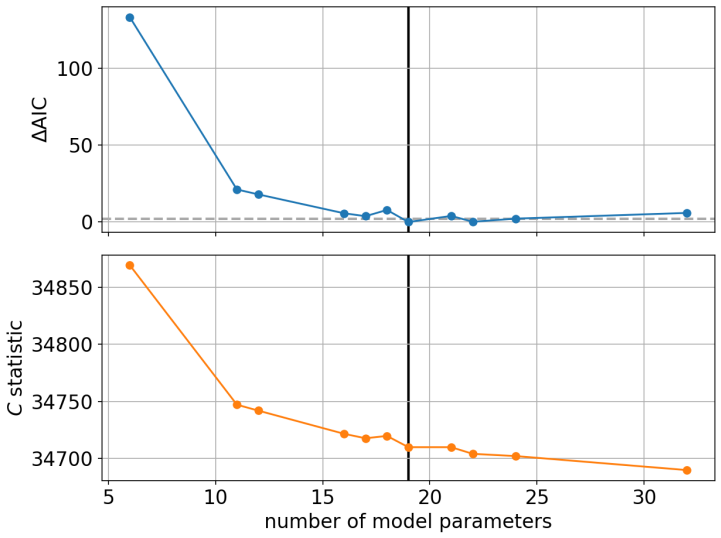

FIGURE 5.22: ΔAIC and C statistic values plotted against the number of free model parameters of the models listed in Tab. 5.3. The black vertical lines depict model_F, the model yielding the lowest AIC score. The dashed grey line in the upper panel marks the ΔAIC= 2 threshold, under which models can be assumed to be equally supported by the data.

to every set of fake data and the resulting distribution of C statistic values is compared to the statistic value of the observed data. For the test of model_F, 2×10^4 sets of fake data are generated. The resulting distribution of statistic values is shown in Fig. 5.23 (*left*) with the according cumulative distribution (*right*). The distribution shows a p-value of ~ 0.43, meaning that the hypothesis that the data originated from model_F can not be significantly rejected. This suggests a high goodness of fit.

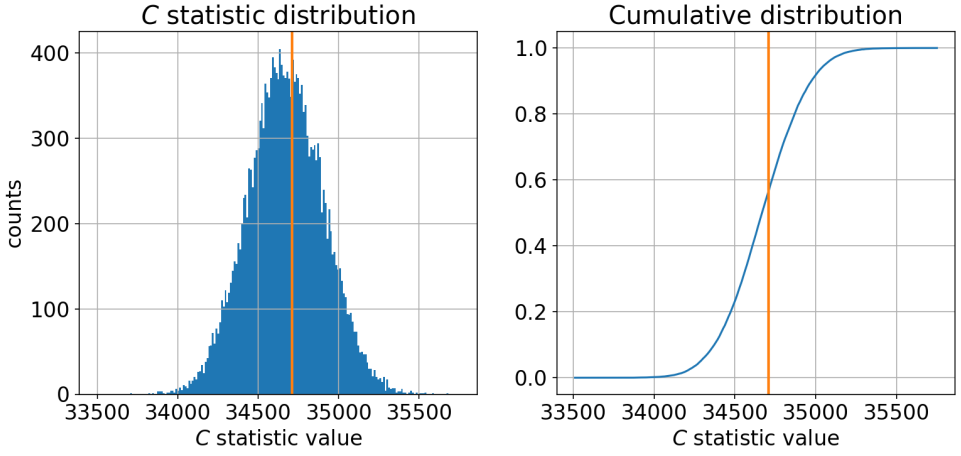

FIGURE 5.23: C statistic distribution for 20000 fake data sets generated from model_F shown in blue on the (*left*). The according cumulative distribution is shown on the (*right*). The orange line depicts the C statistic value of the best-fit model_F and the observed data. The resulting p-value is ~ 0.43.

Figure 5.24 shows the data and model counts and excess as well as the residuals between the data and model_F. The residual counts show an even distribution around 0 with the expected statistical fluctuations across the fitted region, also depicting an adequate goodness of fit. A slight excess can be seen on the right edge of the FoV. This excess belongs to the adjacent RoI region B, which is discussed separately in Sec. 5.5.2.

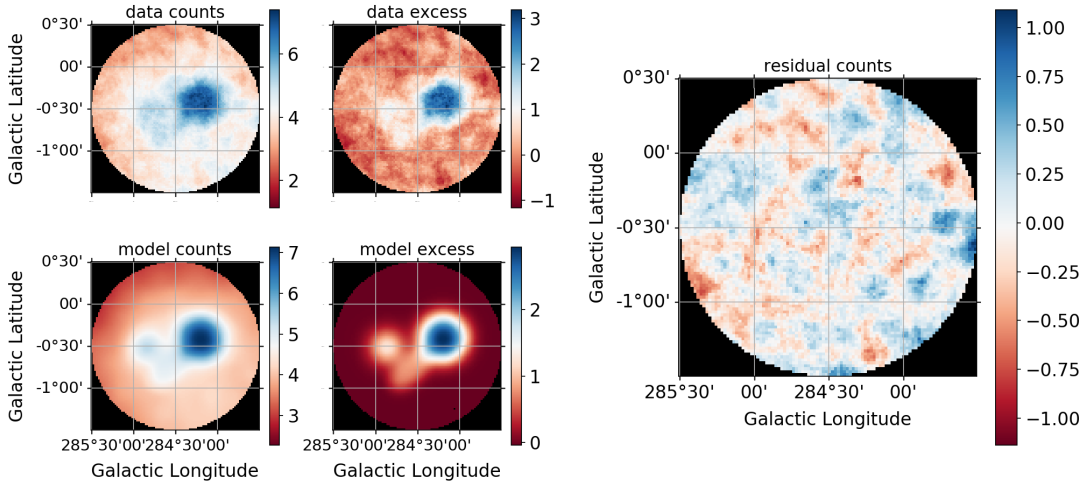

FIGURE 5.24: Data and model counts, excess and residual of model_F, the preferred model with the lowest AIC score from the candidate collection. All sky maps show the summed counts over all energy bins and are correlated with a disk kernel of 0.09° radius.

The 3D fit of the Westerlund 2 core region with model_F gives three separate sources, a disk for HESS J1023–575, a Gaussian for HESS J1026–582 and an elliptical excess coincident with the so called *jet* cloud seen in CO data (see [124, 3]). Due to this spatial coincidence, the source will be referred to as jet cloud or TeV *jet* cloud in the following. Each source component shows a statistical significance within the fit of $\geq 6\sigma$ (see Tab. D.11 for details). The fit yields a correlation matrix that does not show strong correlations between the source components as seen in the matrix shown in Fig. 5.25. The parameters *lon_0* and *lat_0* are the galactic longitude and latitude of the centre of the source components. Furthermore, *r_0* depicts the radius of the disk and *edge* is the annulus describing the smoothed edge of the disk[2]. The *sigma* parameter is the 1σ width of the Gaussian, while the ellipse is described by the *semi_major* axis, the eccentricity *e* and the inclination angle *theta*. The background (BG) has only one free parameter referred to as *norm* that describes the relative amplitude or normalisation of the BG model. All spectra are modelled as power law functions that have a free *amplitude* (i.e. the flux normalisation) and a free *index* parameter.

The strongest correlation between model components of around -0.3 is between the background normalisation and the amplitudes of the Gaussian and the disk modelling HESS J1026–582 and HESS J1023–575. This behaviour is to be expected as excess counts

[2]See App. D.3 and Fig. D.4 for a description.

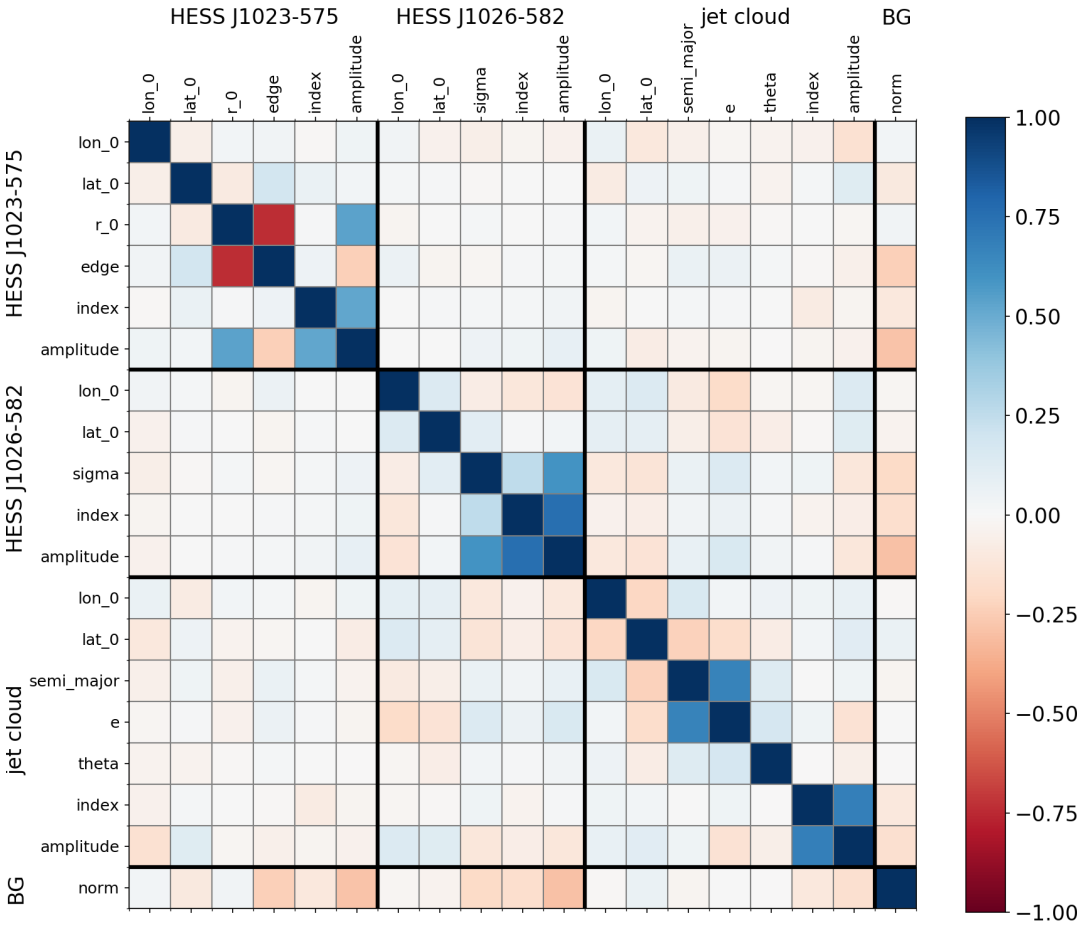

FIGURE 5.25: Correlation matrix for free parameters of model_F with colour coded correlation coefficients.

can be either attributed to the source components or the background. Stronger correlation of around ±0.75 can be seen between parameters within source components. The radius and the edge of the disk modelling HESS J1023-575 show a strong negative correlation. As the radius decreases, the edge increases and vice versa to conserve the total area that is covered by the source. Further expected correlations can be seen between the components' amplitudes and their spatial extensions. As the size increases, the amplitudes increase along with it. The spectral parameters within all three source components of the model show a strong positive correlation. As the amplitude of the sources increase, the index values also increase, meaning that the spectra get steeper.

The best-fit parameters of model_F along with the statistical errors are given in Tab. 5.4. The *semi_major* axis and the eccentricity e are converted to *width* (2 times the *semi_major* parameter) and *height* (the *semi_major* times the eccentricity) of the ellipse for convenience. The errors are calculated with the according error propagation via the covariance matrix.

To better visualise the model, Fig. 5.26 shows the positions and outlines of the disk and the ellipse as well as the 1σ width of the Gaussian in green on top of a significance map

	best-fit value ± stat. error	[unit]
HESS J1023–575		
Disk		
gal. position (lon., lat.)	$(284.191 \pm 0.011, -0.401 \pm 0.010)$	([deg], [deg])
disk radius	0.253 ± 0.017	[deg]
disk edge	0.244 ± 0.067	[deg]
PL index	2.399 ± 0.044	
PL amplitude	3.397 ± 0.246	$[10^{-12}$ cm^{-2}s^{-1}TeV$^{-1}]$
HESS J1026–582		
Gaussian		
gal. position (lon., lat.)	$(284.868 \pm 0.022\ -0.512 \pm 0.021)$	([deg], [deg])
1σ width	0.125 ± 0.016	[deg]
PL index	1.939 ± 0.080	
PL amplitude	0.668 ± 0.151	$[10^{-12}$ cm^{-2}s^{-1}TeV$^{-1}]$
Jet cloud		
Ellipse		
gal. position (lon., lat.)	$(284.575 \pm 0.017, -0.768 \pm 0.017)$	([deg], [deg])
width	0.634 ± 0.044	[deg]
height	0.274 ± 0.048	[deg]
angle*	133.716 ± 5.593	[deg]
PL index	2.137 ± 0.118	
PL amplitude	0.576 ± 0.140	$[10^{-12}$ cm^{-2}s^{-1}TeV$^{-1}]$

TABLE 5.4: Best-fit parameters of Model_F. *The angle of the ellipse is measured anti-clockwise from north of the galactic plane.

of the core region with $2, 4$ and 6σ contours (shown in grey). The dashed green circle shows the outline of the disk's *r_0* + *edge*, where the amplitude of the disk modelling HESS J1023–575 has dropped to 0%.

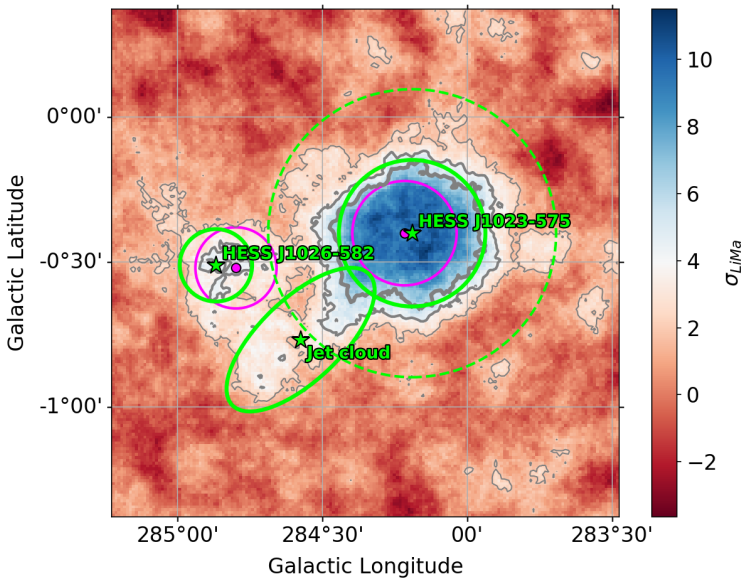

FIGURE 5.26: Position and outlines of the best-fit source components of model_F shown in green on top a significance map of the region. The positions and 1σ widths of the sources published in the H.E.S.S. paper from 2011 are shown in magenta. The $2, 4$ and 6σ contours are shown in grey.

The map in Fig. 5.26 also shows the source positions and extensions published by H.E.S.S. in 2011 [2]. It can be seen that HESS J1023–575 and HESS J1026–582 have slightly shifted away from each other compared to the previously published results. The position of HESS J1023–575 has shifted by $\sim 0.026°$ while HESS J1026–582 has shifted by $\sim 0.070°$. Both best-fit positions still agree with the previously published positions within statistical errors as shown in Fig. 5.27. The systematic error on source positions is estimated to be $20''$ per axis, as suggested in [2] and worked out in [133].

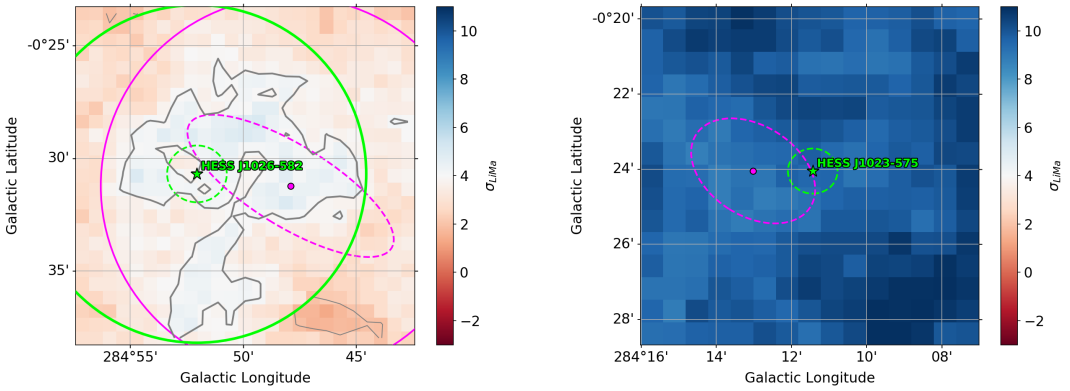

FIGURE 5.27: Enlarged cut outs of the sky map shown in Fig. 5.26 with the statistical error ellipses for the best-fit positions of the performed 3D fit with model_F in dashed green and for the previously published positions in dashed magenta.

Performing a slice analysis on the excess map of the core region confirms the disk morphology of HESS J1023–575 with a smooth edge. Figure 5.28 shows two slices centred on the best-fit position of HESS J1023–575, where a plateau can clearly be seen around the source's best-fit position. As per definition, the amplitude of a disk with a smooth edge drops to 50% at a distance of the disk radius parameter from the center, which in this case is $\sim 0.25°$. An according behaviour can be seen in the slice plot, where the excess per bin is at ~ 35 counts at $\pm 0.25°$ compared to the ~ 70 counts in the centre.

The according best-fit spectra for the three model components are shown in Fig. 5.29. Flux point markers with arrows indicate upper limits. Calculating the difference between the spectral indices of the three components shows that the indices are not compatible within statistical errors as shown in Tab. 5.5. This suggests different physical processes that produce the respective emission, as further discussed in Chap. 6. Taking into account a systematic uncertainty of 20% on the flux and ± 0.1 on spectral index as outlined in Sec. 3.5 or even ± 0.2 on spectral index as suggested in [2] weakens this conclusion. Nevertheless, the spatial separation between the components strengthens the hypothesis of individual sources.

The hint of diffuse emission around Westerlund 2 as discussed in Sec. 5.4.1 is the motivation for model_J, which is an extension of the preferred model_F with two more free

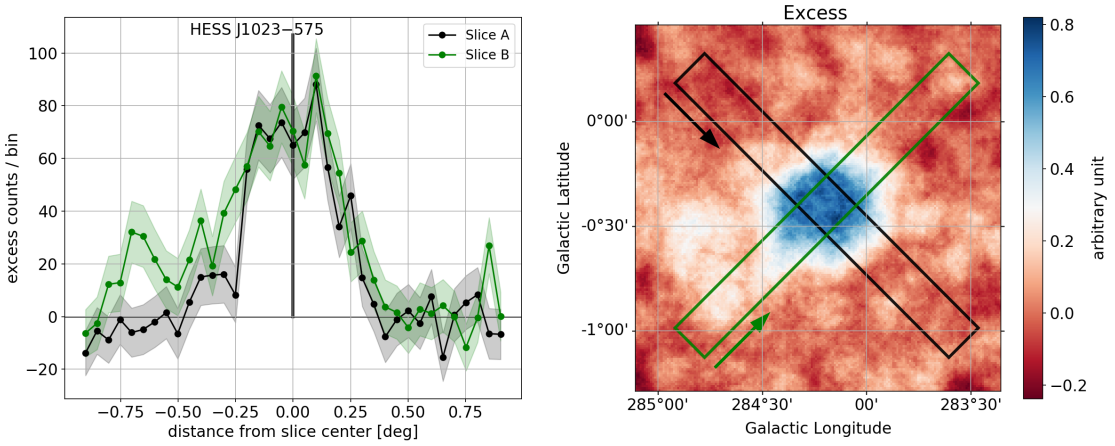

FIGURE 5.28: Slice plot for two slices aligned at −45° and 45° from the best-fit position of HESS J1023–575 in model_F.

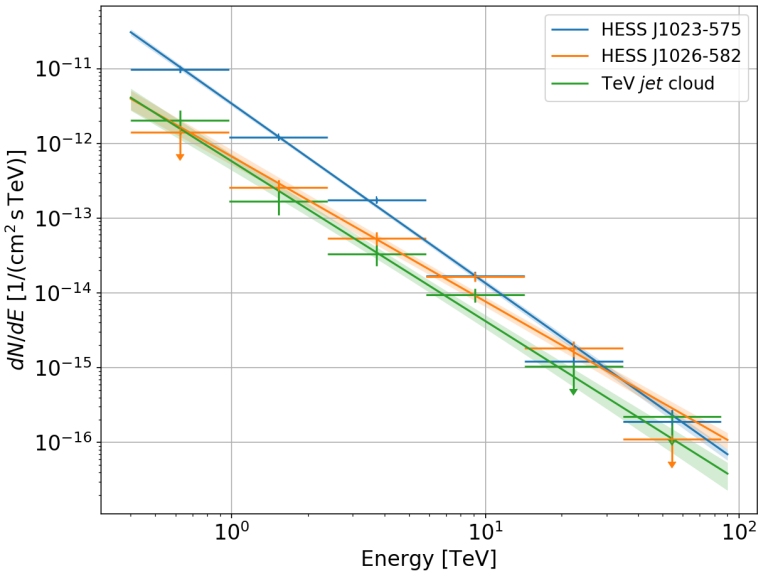

FIGURE 5.29: Best-fit spectra and flux points from the 3D fit of model_F. Statistical error regions are shown as colour coded butterflys and markers with arrows indicate upper limits.

Component pair	$\Delta\Gamma \pm$ stat. error
HESS J1023–575 vs. HESS J1026–582:	0.460 ± 0.092
HESS J1023–575 vs. Jet cloud:	0.262 ± 0.124
HESS J1026–582 vs. Jet cloud:	0.198 ± 0.141

TABLE 5.5: Difference between the best-fit spectral indices of the sources determined from model_F. The errors are calculated via error propagation with the covariance matrix.

parameters to model the spectrum of a potential diffuse component. This diffuse component nevertheless shows no significance in the 3D fit, whereas the remaining model components show the same significance as in model_F. Model_J is therefore not considered.

The properties of a potential diffuse component cannot be derived in this 3D fit procedure for the regarded field of view. To determine the properties of the diffuse emission, data over a much larger field of view has to be used as in the study done on Fermi-LAT data presented in [120], for which further large-scale H.E.S.S. observations of the region are needed.

5.5.1.3 Reflected regions analysis

With the results of the 3D fit presented in the previous Sec. 5.5.1.2, a reflected regions analysis can be conducted to extract spectra and flux points for each component with a finer and individual binning. An arising issue is thereby that the three sources are relatively close to each other and overlap to a certain degree. As the reflected regions method extracts the spectra for an ON region as a whole, the flux contribution or contamination from other sources to each ON region should be taken into account. To get an estimate on this relative contamination, the best-fit model components from the 3D fit can be used. The first step is to define the ON regions for each component. For the Gaussian modelling HESS J1026–582, a circular ON region with a radius of 0.3° is chosen, which corresponds to an $\sim 95\%$ containment of the flux predicted by the Gaussian model. The ON region for HESS J1023–575 is chosen as a circle with 0.375° radius, which, accounting for the smooth edge of the disk model, corresponds to $\sim 98\%$ containment of the predicted flux. As ON region for the TeV *jet* cloud, the outline of an ellipse is taken with the best-fit parameters from the 3D fit, but slightly adapted width and height of 0.633° and 0.317° respectively, which corresponds to an $\sim 98\%$ containment of the predicted flux. The relative contamination for each component's ON region then describes how many percent of the total emission in the region can be attributed to the other two sources.

Figure 5.30 shows the predicted flux maps of the source components in the best-fit model_F from the 3D fit at the center of each energy bin of the data set. The three different ON regions for the sources are marked by the blue, orange and green shapes. It can be seen how the relative amplitude of the different components change with energy. HESS J1023–575 (blue circle) is the brightest source at lower energies, whereas HESS J1026–582 (orange circle) gets the brightest at higher energies. The relative contamination per energy bin for each ON region is shown in Fig. 5.31. It can be seen that, according to the model, the TeV *jet* cloud is most affected with an overall relative contamination of $> 12\%$. This is expected as it is the faintest of the three sources and has a large relative overlap with both, HESS J1023–575 and HESS J1026–582.

The relative contamination is an estimate on the basis of the results from the 3D fit procedure that can help to interpret the results from the reflected regions analysis. An estimated correction can also be applied by subtracting the percentage of excess counts in every region that is predicted to originate from the other sources. As a conservative approach, an overall contamination of 10% is assumed for HESS J1023–575 and HESS J1026–582

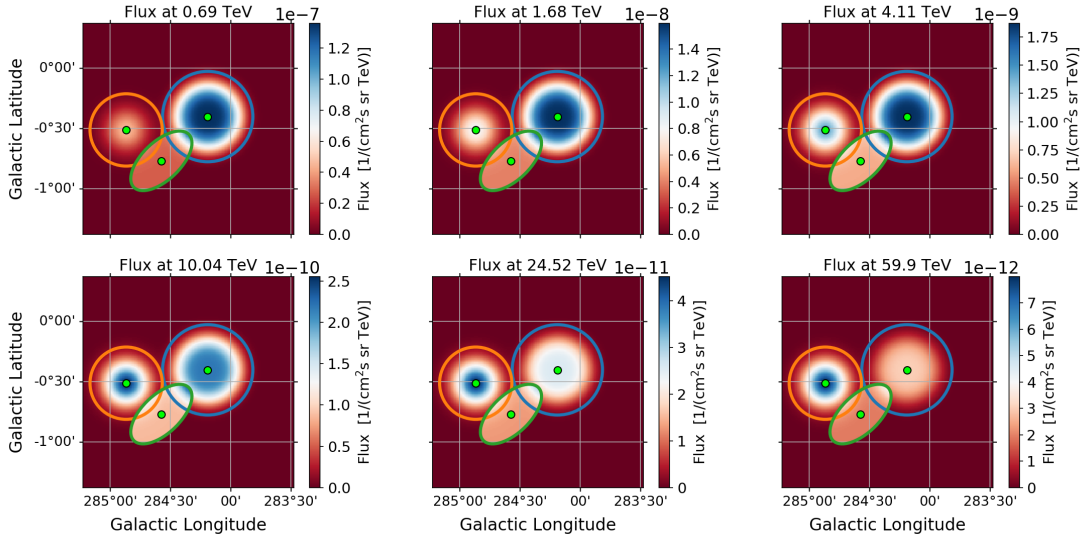

FIGURE 5.30: Flux maps at the center of each energy bin of the 3D fit data set. The ON region for the reflected regions analysis of each component are marked in blue for HESS J1023–575, orange for HESS J1026–582 and green for the *jet* cloud.

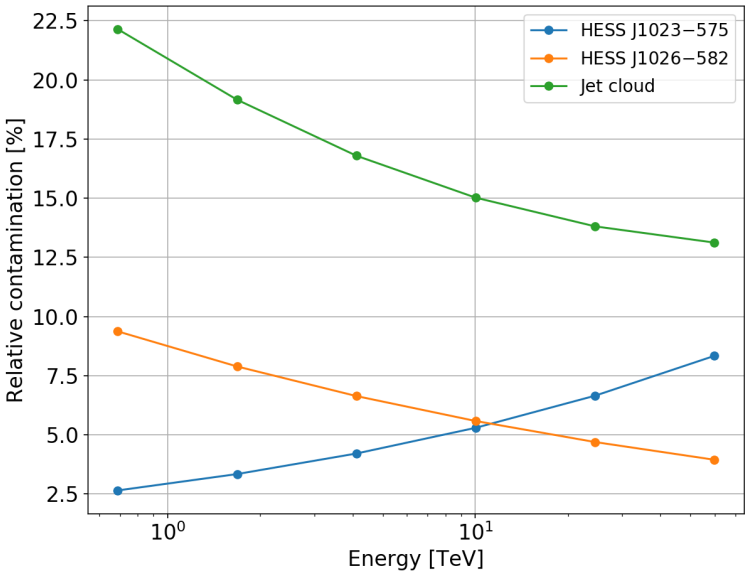

FIGURE 5.31: The relative contamination shows the predicted flux contribution from the respectively other two sources from the 3D fit of model_F to each ON region in percent.

and 25% for the TeV *jet* cloud. The detection significance σ_{LiMa} and the accordingly corrected detection significance $\tilde{\sigma}_{LiMa}$ are shown in Tab. 5.6 together with the statistics for each ON region. It can be seen that even applying the conservative contamination correction results in highly significant detections of emission in all three ON regions.

In the next step, the reflected regions method is used to extract the spectral properties

Component	N_{ON}	N_{OFF}	N_{excess}	σ_{LiMa}	$\tilde{\sigma}_{LiMa}$
HESS J1023–575	4324	12440	2727.9	56.2	51.3
HESS J1026–582	2481	12756	1165.1	28.6	26.0
TeV *jet* cloud	1571	8513	727.5	22.3	17.2

TABLE 5.6: Count statistics for the reflected regions analysis of every source component in the Westerlund 2 core region. The parameter $\tilde{\sigma}_{LiMa}$ is calculated with conservative contamination corrected numbers as outlined in the main text.

for each of the components' ON region. The counts in the ON and OFF regions are binned into 40 equally spaced logarithmic energy bins between $\sim 50\,\mathrm{GeV}$ and $100\,\mathrm{TeV}$ and a maximum likelihood fit using the W statistic is performed to fit spectral models (as outlined in Sec. 3.4.6). First, power law (PL) spectra are fitted to get a direct comparison to the results from the 3D fit. The best-fit models and extracted flux points for the three source components are shown together with the respective residuals (normalised to the model prediction) in Fig. 5.32 with the respective best-fit parameters, errors and AIC scores given in Tab. 5.7. The shown energy range and binning of the flux points is adapted to the individual sources.

HESS J1023–575	
AIC score	35.3
PL index	(2.397 ± 0.062)
PL amplitude	$(3.338 \pm 0.295)\ \times 10^{-12}\ \mathrm{cm}^{-2}\mathrm{s}^{-1}\mathrm{TeV}^{-1}$
HESS J1026–582	
AIC score	51.4
PL index	(2.011 ± 0.090)
PL amplitude	$(0.721 \pm 0.145)\ \times 10^{-12}\ \mathrm{cm}^{-2}\mathrm{s}^{-1}\mathrm{TeV}^{-1}$
TeV *jet* cloud	
AIC score	21.1
PL index	(2.153 ± 0.126)
PL amplitude	$(0.534 \pm 0.125)\ \times 10^{-12}\ \mathrm{cm}^{-2}\mathrm{s}^{-1}\mathrm{TeV}^{-1}$

TABLE 5.7: Best-fit parameters and stat. errors of the spectral fits with a power law using the reflected regions method for the ON regions of the three source components in the Westerlund 2 core region. The AIC score of the fit is shown as well.

It can be seen in Tab. 5.7 that the best-fit indices and amplitudes determined with the reflected regions method agree with the results from the 3D fit given in Tab. 5.4 within statistical errors. The estimated relative contamination for all three sources is low enough to fall within the statistical error regions and does thus not affect the results. A contamination correction of the extracted spectra is therefore not done in the following.

As an alternative spectral model, a power law with an exponential cut-off (ePL) of the form $\phi(E) = \phi_0 \left(\frac{E}{E_0}\right)^{-\Gamma} \exp(-\lambda E)$ is fitted to the data. The parameter λ is thereby the inverse of the so called cut-off energy E_{cutoff}. The results of this fit are shown in Tab. 5.8. Comparing the AIC score between the PL and the ePL fits of the three sources shows that for HESS J1023–575 and for the TeV *jet* cloud, the PL is the preferred model. This can also be seen on the best-fit values for lambda with the relatively large errors, which also suggest that an ePL is not an appropriate model. The ePL fit of HESS J1026–582

on the other hand shows a far lower AIC score than for the PL fit. This suggests that an ePL is the preferred model for this source. The according plot of the best-fit ePL model and flux points with residuals is shown in Fig. 5.33.

HESS J1023–575	
AIC score	36.9
ePL index	(2.336 ± 0.116)
ePL amplitude	$(3.280 \pm 0.309) \times 10^{-12}$ cm^{-2}s^{-1}TeV^{-1}
lambda	$(0.085 \pm 0.141) \times 10^{-1}$ TeV^{-1}
HESS J1026–582	
AIC score	27.1
ePL index	(0.784 ± 0.357)
ePL amplitude	$(0.288 \pm 0.123) \times 10^{-12}$ cm^{-2}s^{-1}TeV^{-1}
lambda	$(1.300 \pm 0.396) \times 10^{-1}$ TeV^{-1}
TeV *jet* cloud	
AIC score	21.4
ePL index	(1.830 ± 0.296)
ePL amplitude	$(0.437 \pm 0.140) \times 10^{-12}$ cm^{-2}s^{-1}TeV^{-1}
lambda	$(0.345 \pm 0.307) \times 10^{-1}$ TeV^{-1}

TABLE 5.8: Best-fit parameters and stat. errors of the spectral fits with an exponential cut-off power law using the reflected regions method for the ON regions of the three source components in the Westerlund 2 core region. The AIC score of the fit is shown as well.

For HESS J1023–575 and for the TeV *jet* cloud, the best-fit PL spectra are therefore used for further analyses and discussion. For HESS J1026–582, the ePL spectrum is used.

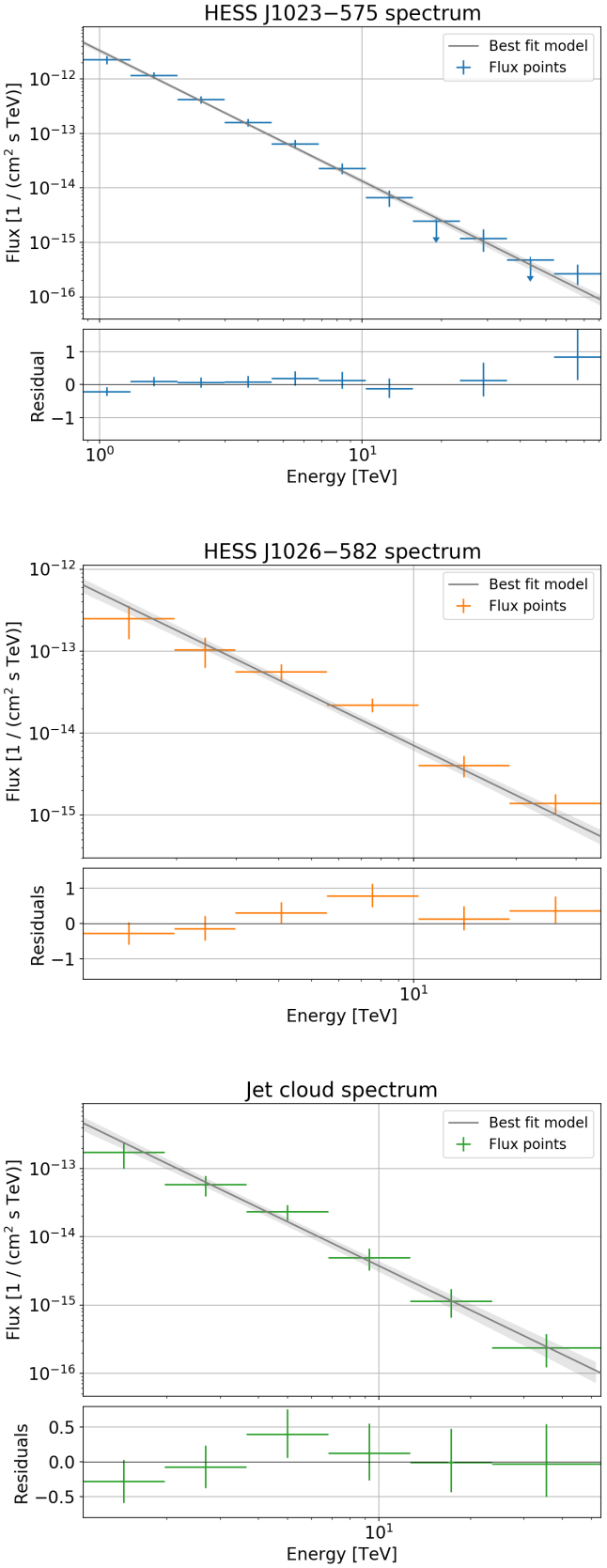

FIGURE 5.32: Power law spectrum fits with the reflected regions method for the three source components in the Westerlund 2 core region. The residuals are normalised to the respective best-fit model.

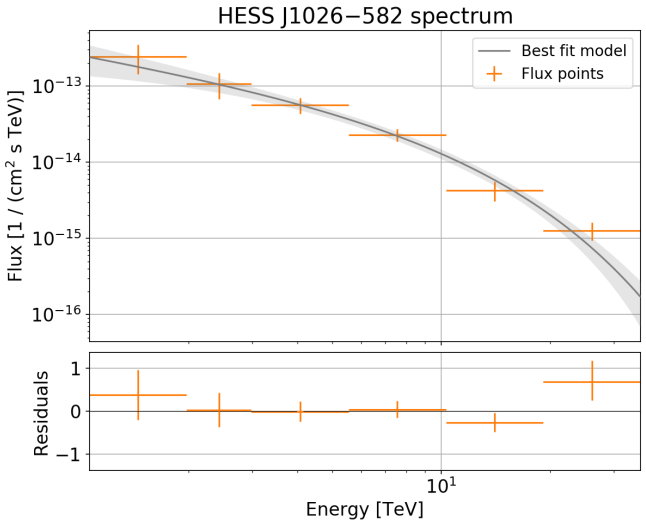

FIGURE 5.33: Exponential cut-off power law spectrum fit with the reflected regions method for HESS J1026–582. The residuals are the difference of the flux points to the respective best-fit model which are then divided by the model.

5.5.1.4 Energy dependent morphology

As pointed out in the H.E.S.S. publication on Westerlund 2 from 2011 [2], the γ-ray emission around Westerlund 2 shows an energy dependent morphology. This is also seen in the dataset analysed in this work as presented in Sec. 5.3 with Fig. 5.12 showing the significance maps for energies above and below 2.5 TeV. Comparing the two maps, one can see that HESS J1026–582 gets brighter at higher energies, whereas the emission of HESS J1023–575 changes in shape with an increasing emission towards the region of the TeV *jet* cloud at higher energies. The best-fit PL spectrum of HESS J1023–575 in the upper panel of Fig. 5.32 shows a notable feature where the flux points $\gtrsim 10$ TeV appear to rise above the best-fit model, suggesting a hardening of the spectrum. To investigate this feature, a spectral fit of the HESS J1023–575 ON region is performed separately for energies above and below 8 TeV. The properties of the resulting spectra are given in Tab. 5.9 with the best-fit spectra, flux points and residuals shown in Fig. 5.34.

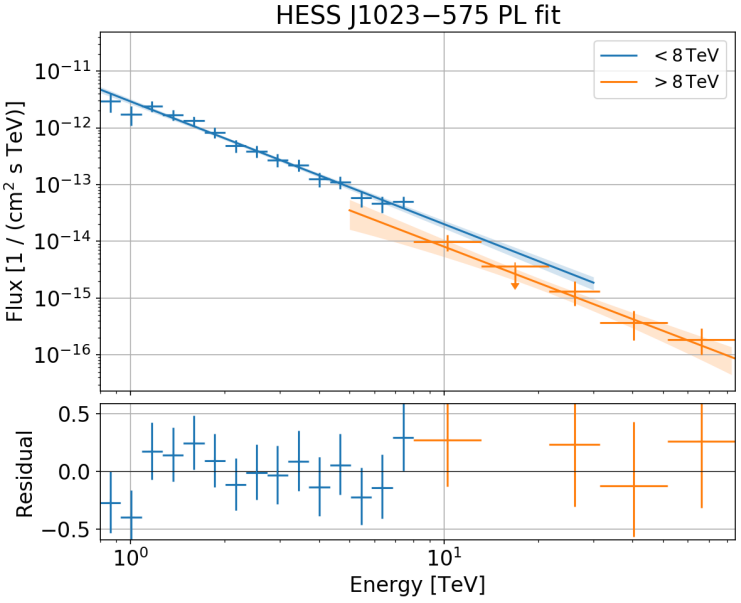

FIGURE 5.34: Spectral models and extracted flux points for separate fits of HESS J1023–575 with the reflected regions method above and below 8 TeV. The lines and shaded regions depict the best-fit models with the statistical errors. Flux points are shown with statistical error bars and upper limits (flux points with TS values < 4) are denoted by downward arrows.

It can be seen that the spectral indices of the two PL fits agree within statistical errors at ~ 2.1 (which also agrees with the spectral index of the TeV *jet* cloud). The flux predicted by the two models at 8 TeV however does not agree. The flux level of the best-fit spectrum < 8 TeV is ~ 2.5 times higher than of the best-fit spectrum > 8 TeV. The spectral fit over the full energy range presented in Sec. 5.5.1.3 results in a PL with an index of 2.397 ± 0.062. The index of the PL spectrum > 8 TeV agrees with this value within statistical errors, whereas the spectrum < 8 TeV shows a significantly harder index.

HESS J1023–575, PL fit $< 8\,\mathrm{TeV}$	
Spectral index	(2.162 ± 0.098)
Flux at 1 TeV	$(2.921 \pm 0.304) \times 10^{-12}$ cm^{-2}s^{-1}TeV^{-1}
Flux at 8 TeV	$(3.259 \pm 0.446) \times 10^{-14}$ cm^{-2}s^{-1}TeV^{-1}
HESS J1023–575, PL fit $> 8\,\mathrm{TeV}$	
Spectral index	(2.123 ± 0.341)
Flux at 8 TeV	$(1.299 \pm 0.519) \times 10^{-14}$ cm^{-2}s^{-1}TeV^{-1}

TABLE 5.9: Spectral properties of PL fits for HESS J1023–575, fitted separately $> 8\,\mathrm{TeV}$ and $< 8\,\mathrm{TeV}$.

To further probe the energy dependent morphology, normalised excess maps of the Westerlund 2 region are shown in Fig. 5.35 for the three energy bands $< 1\,\mathrm{TeV}$, from 1 TeV to 8 TeV and $> 8\,\mathrm{TeV}$. The maps are correlated with a disk kernel of 0.09° radius.

In the low energy band $< 1\,\mathrm{TeV}$, the highest excess is seen to the north of the Westerlund 2 star cluster (marked by the green star in Fig. 5.35). Furthermore, a clear excess can be seen along the major axis of the TeV *jet* cloud. In this low energy band, no excess emission can be seen at the position of HESS J1026–582. In the medium energy range from 1 TeV to 8 TeV, the highest excess emission is seen around the centre of HESS J1023–575. In the region of HESS J1026–582, a pool of excess emission appears, which is slightly shifted towards HESS J1023–575 but is clearly separated from it. A faint excess can also be seen in the TeV *jet* cloud region, even though the excess is much fainter compared to the excess of the other two sources. In the high energy band $> 8\,\mathrm{TeV}$, the highest excess is seen around the position of HESS J1026–582 with an extension to the east towards the pulsar PSR J1028–5746 (marked by the green cross in Fig. 5.35). The emission of HESS J1023–575 in the high energy band shows a shift to the southern half of the source region with a strong deficit of emission in the northern half. Furthermore, a hotspot with excess emission in the high and low energy channel can be seen to the north east of the best-fit position of HESS J1023–575. This hotspot is located close to the position of WR 21a (green triangle in Fig. 5.35).

For better visualisation, the three normalised excess maps are shown in Fig. 5.36 as a three colour image with the low energy channel shown in red, the medium energy channel in green and the high energy channel in blue.

The spatial characteristics of the energy dependent morphology is clearly visible in the three colour image in Fig. 5.36. The main morphological traits that can be observed are:

1. HESS J1023–575 shows more emission from the low energy channel in the north around the star cluster Westerlund 2 and more high energy emission in the south. The main emission is seen in the medium energy range, which is more or less evenly distributed within the best-fit radius of the source region.

2. HESS J1026–582 is not seen $< 1\,\mathrm{TeV}$. With rising energy, the emission appears to extend towards the position of the pulsar PSR J1028–5746 to the east.

3. The TeV *jet* cloud mainly shows emission $< 1\,\mathrm{TeV}$, with a slight excess in the medium energy channel towards its north west and in the high energy channel towards the south east.

4. A hotspot in the high and low energy channel can be seen to the north east of Westerlund 2 close to the position of WR 21a. The low energy part is thereby located closer to WR 21a while the high energy part is located further away to the north east.

Overall, the γ-ray emission in the Westerlund 2 region shows a strong energy dependency over the three investigated energy ranges. This can also be seen in the spectrum of HESS J1023–575, showing the drop in flux $> 8\,\mathrm{TeV}$, which can be interpreted as a sign of different overlapping γ-ray sources. As the emission $> 8\,\mathrm{TeV}$ is however relatively faint and has limited statistics, the best-fit spectrum over the full energy range as determined in Sec. 5.5.1.3 is used for the main interpretation of the results presented in Chap. 6. The energy dependent morphology should however be investigated in more detail in future studies, preferably using a larger VHE data set and combining it with data from other wavelengths.

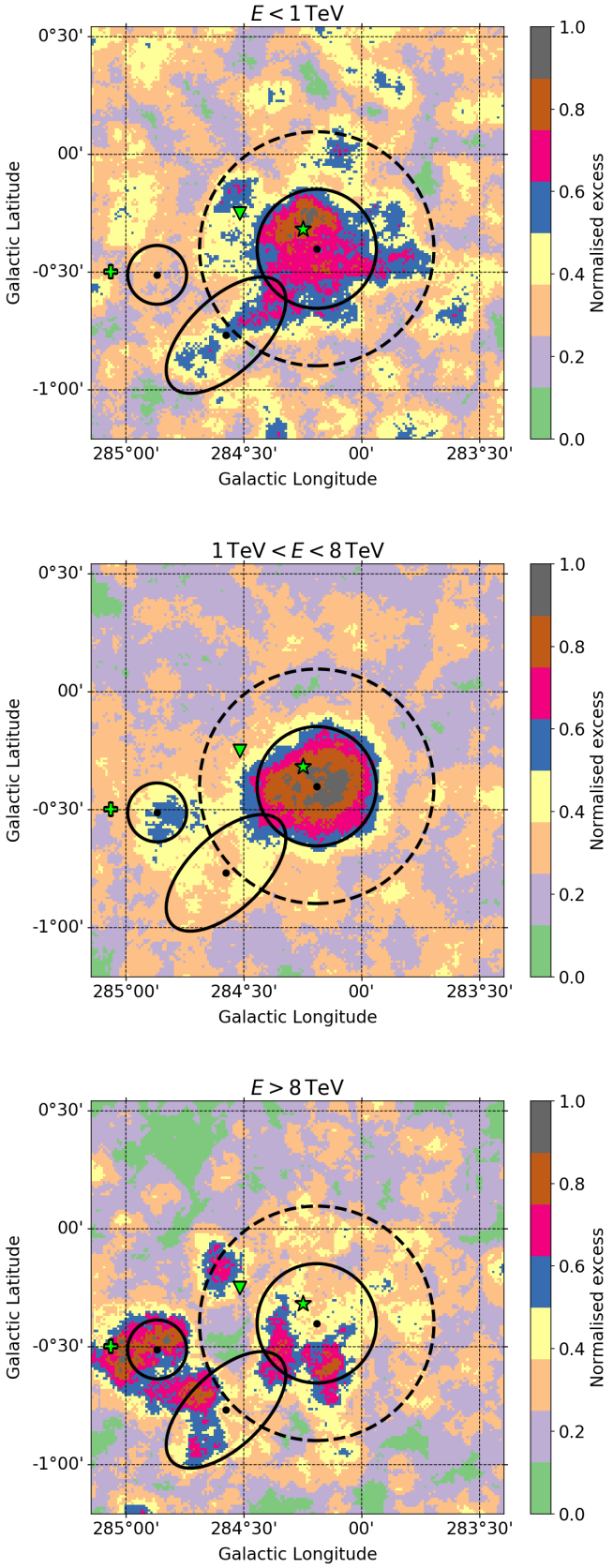

FIGURE 5.35: Normalised TeV excess maps of the Westerlund 2 core region in three given energy ranges. The maps are correlated with a disk kernel of 0.09° radius. The maximum excess counts per 0.01° × 0.01° bin of the uncorrelated maps are 3.9, 5.6 and 2.0 for the low, medium and high energy band respectively. The position of Westerlund 2, the pulsar PSR J1028–5746 and the colliding binary system WR 21a is marked with a green star, cross and triangle. The positions and outlines of the best-fit components from the 3D fit are marked in black.

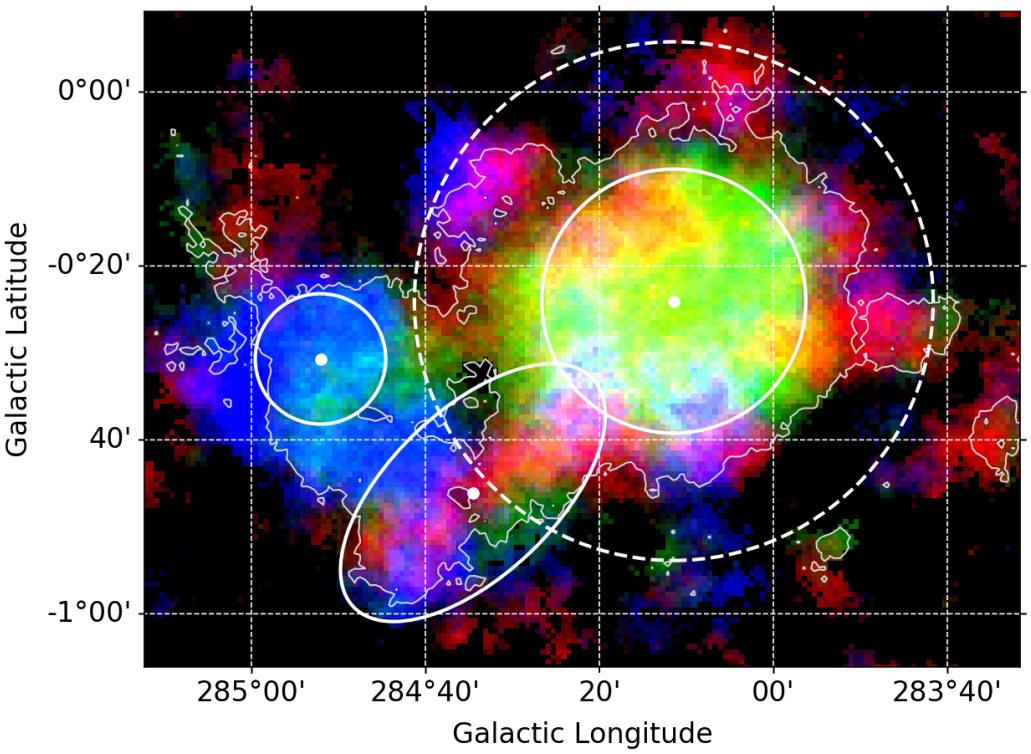

FIGURE 5.36: Three colour excess map of the Westerlund 2 core region. The red, green and blue colour channels correspond to the normalised excess maps in the energy ranges $<$ 1 TeV (low), 1 to 8 TeV (medium) and $>$ 8 TeV (high) respectively. The colour intensities do not represent the γ-ray intensity in the individual energy bands. A minimum pixel threshold is applied and the intensities per channel are scaled for better visualisation. The 2σ significance contours using the ring background method is shown in grey with the outlines and best-fit positions of source components from the 3D fit in white.

5.5.2 Region B

Region B (see Fig. 5.19) hosts two larger hotspots. To determine the morphological and spectral properties of these hotspots, a 3D fit and a spectral analysis using the reflected regions method is performed. The results are presented in the following subsections.

5.5.2.1 3D fit with gammapy

As for the Westerlund 2 core region, the 3D fit for region B is performed on the detection level data set, binned into $0.02° \times 0.02°$ spatial and six equally spaced logarithmic energy bins from 400 GeV to 85 TeV. A background model is created with the ring background method. The maps are centred on the galactic position ($l = 282.85°$, $b = -0.50°$) and masked to only include a circular region with 1° radius.

The model fitted to the data contains two Gaussian sources, labelled as hotspot (HS) B1 and B2, on top of the background model. Details and initial fit values can be found in App. E. The best-fit model and data counts summed over all energy bins are shown together with the summed residuals in Fig. 5.37. The data and model count maps show a strong decrease of counts from left to right. This is due to the decreasing exposure of the data set towards lower galactic latitudes. The count statistics in this region are therefore very limited. The best-fit parameters are given in Tab. 5.10. The best-fit width of both Gaussian components is $< 0.01°$. Both sources can thus be considered as being point-like.

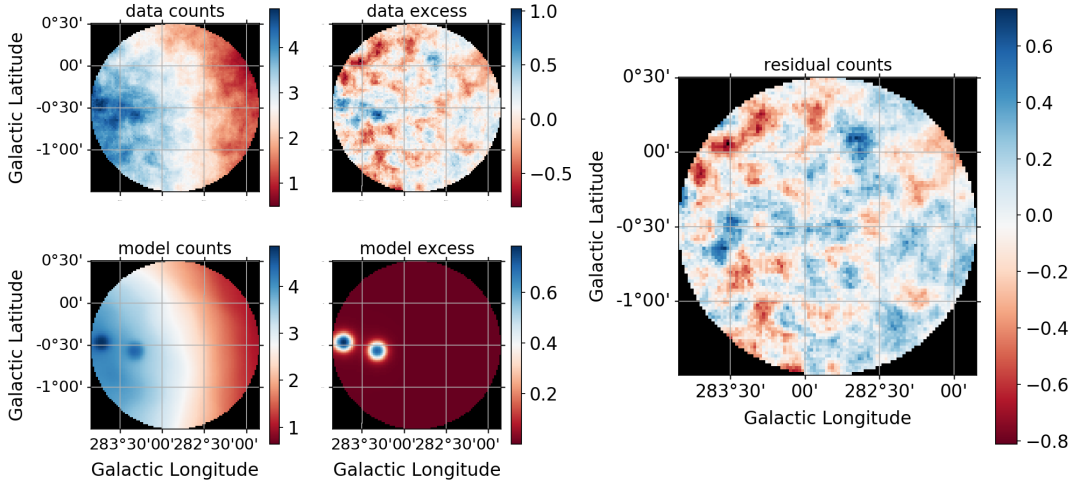

FIGURE 5.37: Data and model counts, excess and residual of the best-fit model for region B from the 3D fit. All sky maps show the summed counts over all energy bins and are correlated with a disk kernel of 0.09° radius.

The best-fit spectra and extracted flux points of the two components are shown in Fig. 5.38. It can be seen that the statistical errors are rather large, compared to the results of the 3D fit of the Westerlund 2 core region. This can be explained by the lower

	best-fit value ± stat. error	[unit]
Hotspot B1		
Point-like		
gal. position (lon., lat.)	$(283.716 \pm 0.002,\ -0.460 \pm 0.0003)$	([deg], [deg])
PL index	2.660 ± 0.292	
PL amplitude	3.176 ± 1.149	$[10^{-12}\ \mathrm{cm^{-2}s^{-1}TeV^{-1}}]$
Hotspot B2		
Point-like		
gal. position (lon., lat.)	$(283.317 \pm 0.003\ -0.575 \pm 0.0003)$	([deg], [deg])
PL index	2.661 ± 0.341	
PL amplitude	3.292 ± 1.271	$[10^{-12}\ \mathrm{cm^{-2}s^{-1}TeV^{-1}}]$

TABLE 5.10: Best-fit model parameters for the 3D fit analysis for region B. Both components are fitted as Gaussians but can be considered point-like.

exposure of the data set in this region. The spectra depict very similar properties, suggesting a common underlying physical process. Furthermore, the spectra agree with the spectrum of HESS J1023–575, which is directly adjacent to the east of region B.

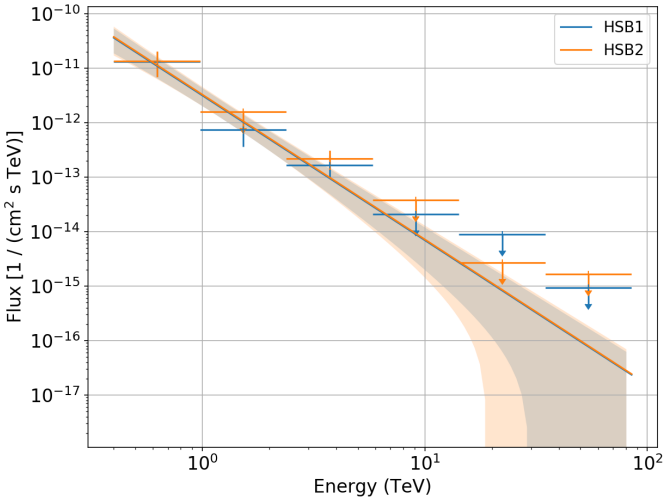

FIGURE 5.38: Best-fit spectra from the 3D fit of the two hotspots in region B with statistical error bands. Markers with arrows depict upper limits.

Both sources, HS B1 and HS B2, show a very low significance within the fitted model of 2.7σ and 2.3σ respectively. This would suggest that the hotspots can rather be interpreted as statistical fluctuations than actual γ-ray sources. To investigate this further, a separate analysis is performed using the reflected regions method.

5.5.2.2 Reflected regions analysis

For the reflected regions analysis of region B, two ON regions are defined. The regions are centred on the respective best-fit positions of the two Gaussians determined in the 3D

fit of the region with a radius of 0.1°. A significance map of the area with the indicated ON regions is shown in Fig. 5.39.

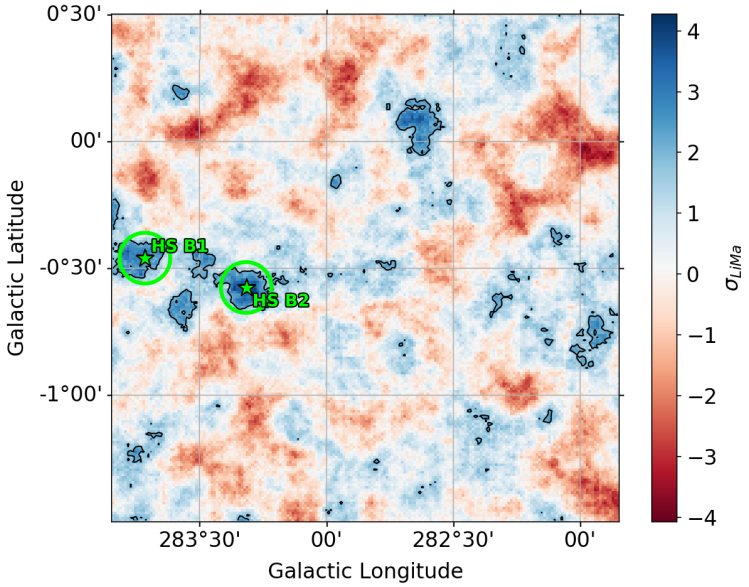

FIGURE 5.39: Positions and extensions of the two ON regions for the hotspots in region B shown in green on top of a significance map.

In contrast to the relatively low significances of the two hotspots in the 3D fit of region B, the reflected regions analysis of hotspot B1 and hotspot B2 show very significant emission with 11σ and 10σ respectively. The count statistics for the two regions are given in Tab. 5.11.

Component	N_{ON}	N_{OFF}	N_{excess}	σ_{LiMa}
HS B1	361	5668	170.9	11.0
HS B2	349	6521	154.5	10.0

TABLE 5.11: Count statistics for the reflected regions analysis of the two ON regions in region B.

The spectra are extracted for the two regions in the same way as in the reflected regions analysis of the Westerlund 2 core region presented in Sec. 5.5.1.3. The resulting spectra are shown in Fig. 5.40 with the parameters of the PL fit given in Tab. 5.12.

Hotspot B1	
PL index	(2.135 ± 0.285)
PL amplitude	$(1.071 \pm 0.602) \times 10^{-13}$ cm^{-2}s^{-1}TeV^{-1}
Hotspot B2	
PL index	(2.529 ± 0.346)
PL amplitude	$(1.453 \pm 0.679) \times 10^{-13}$ cm^{-2}s^{-1}TeV^{-1}

TABLE 5.12: Best-fit parameters and statistical errors of the spectral fits with a power law spectrum using the reflected regions method for the ON regions of the two source components in region B.

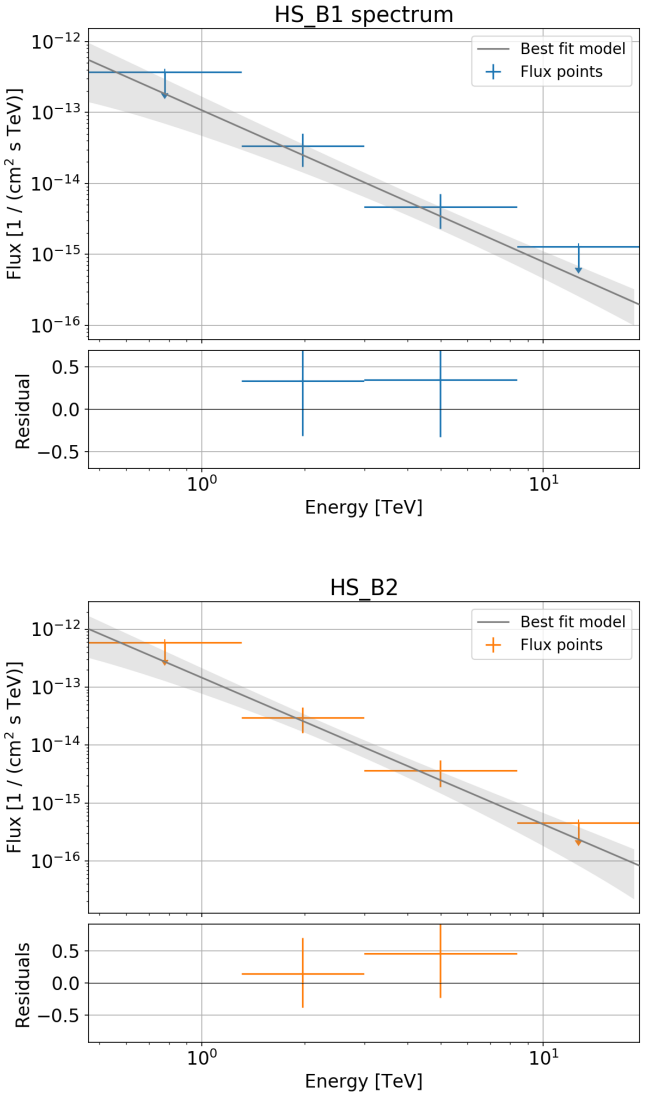

FIGURE 5.40: Power law spectrum fit with the reflected regions method for the hotspots B1 and B2. The residuals are normalised to the respective best-fit model.

The reflected regions analysis of region B shows that emission is significantly detected in the ON regions of the hotspots. Nevertheless, due to the low statistics, spectral properties can only be extracted with large statistical uncertainties in a very limited energy range.

5.5.3 Region E

A single hotspot can be seen in region E north west of the Westerlund 2 core region. As region B, region E lies at the edge of the region covered by the dataset where the exposure decreases towards lower galactic longitude and higher latitude. The region is analysed with a 3D fit and the reflected regions method with the results presented in the following subsections.

5.5.3.1 3D fit with gammapy

The 3D fit of region E is performed in the same way as the 3D fits of the Westerlund 2 core region and region B with the same settings and background model. The regarded sky map region is centred on the galactic position ($l = 282.850°$, $b = 0.633°$) and masked to only include a circular region of 1° radius. The model fitted to the data consists of one Gaussian component on top of the background model. Details about the 3D fit can be found in App. F. Figure 5.41 shows the summed model and data count maps and the residual between data and best-fit model with the best-fit parameters shown in Tab. 5.13.

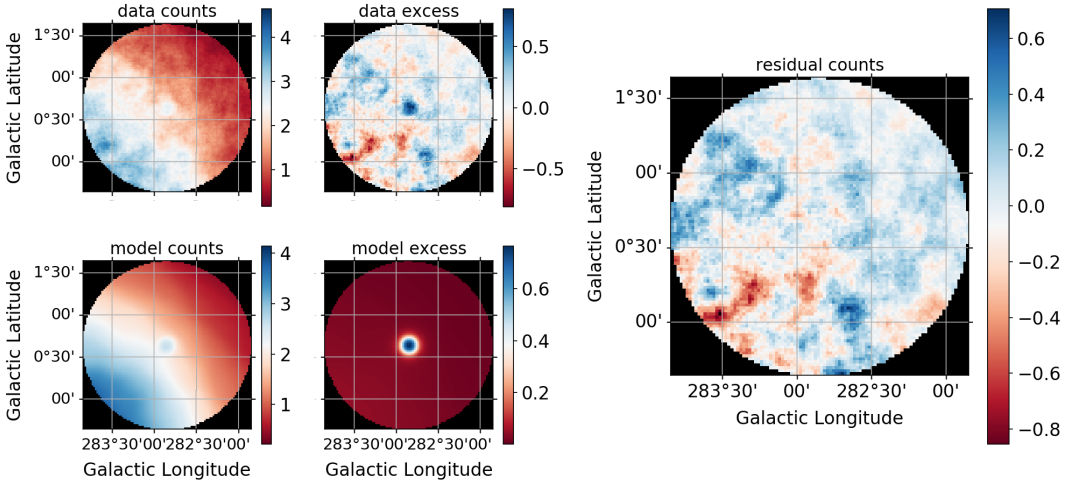

FIGURE 5.41: Data and model counts, excess and residuals of the best-fit model for region E from the 3D fit. All sky maps show the summed counts over all energy bins and are correlated with a disk kernel of 0.09° radius.

	best-fit value ± stat. error	[unit]
Hotspot E		
Gaussian / Point-like		
gal. position (lon., lat.)	$(282.843 \pm 0.012,\ 0.637 \pm 0.011)$	([deg], [deg])
width	0.012 ± 0.015	[deg]
PL index	2.531 ± 0.270	
PL amplitude	4.295 ± 1.399	$[10^{-13}$ cm^{-2}s^{-1}TeV$^{-1}]$

TABLE 5.13: Best-fit model parameters for the 3D fit of the hotspot in region E. The hotspot is fitted with Gaussian but can be considered point-like due to the small width and its large error.

Due to the small width of the Gaussian fitted to hotspot E and its large error, the component can be considered as point-like. The component shows a significance of 4.2σ within the model. The best-fit spectrum and extracted flux points are shown in Fig. 5.42.

Like the spectra of the two hotspots in region B, the spectrum of hotspot E shows large errors. To further investigate hotspot E in more detail, a reflected regions analysis is performed.

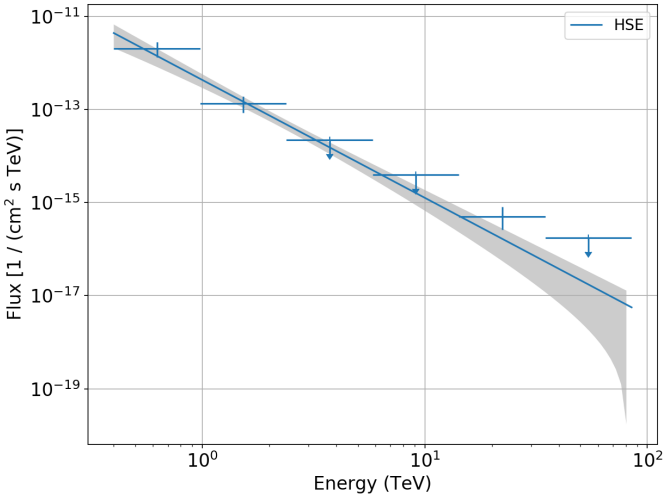

FIGURE 5.42: Best-fit spectrum with extracted flux points of hotspot E from the 3D fit procedure.

5.5.3.2 Reflected regions analysis

For the reflected regions analysis of region E, a circular ON region is defined at the best-fit position of the Gaussian from the 3D fit and a radius of 0.1°. The region is depicted on a significance map of the region in Fig. 5.43. The count statistics from the analysis are given in Tab. 5.14.

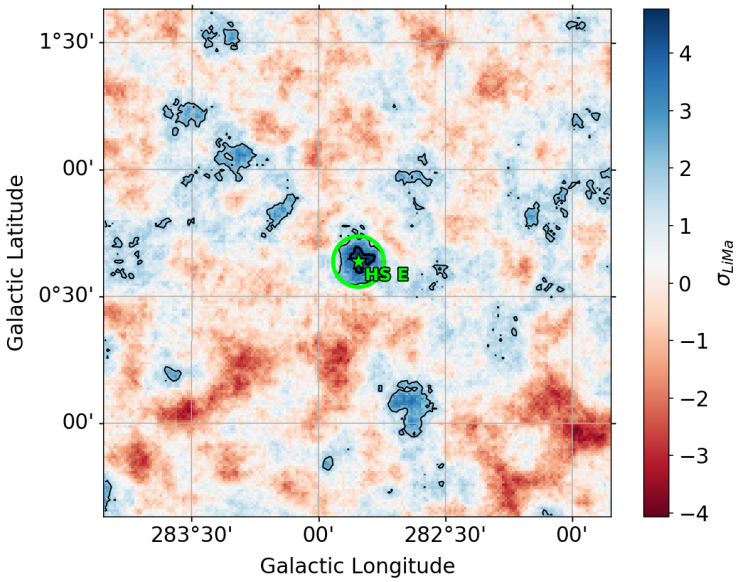

FIGURE 5.43: Positions and extensions of the two ON regions of the hotspot E shown in green on top of a significance map.

Component	N_{ON}	N_{OFF}	N_{excess}	σ_{LiMa}
HS E	208	6569	86.0	7.1

TABLE 5.14: Count statistics for the reflected regions analysis of the ON region around the hotspot in region E.

The statistics of the analysis show that emission is significantly detected in the ON region with 7.1σ. The according spectral fit is shown in Fig. 5.44 with the best-fit parameters and statistical errors given in Tab. 5.15.

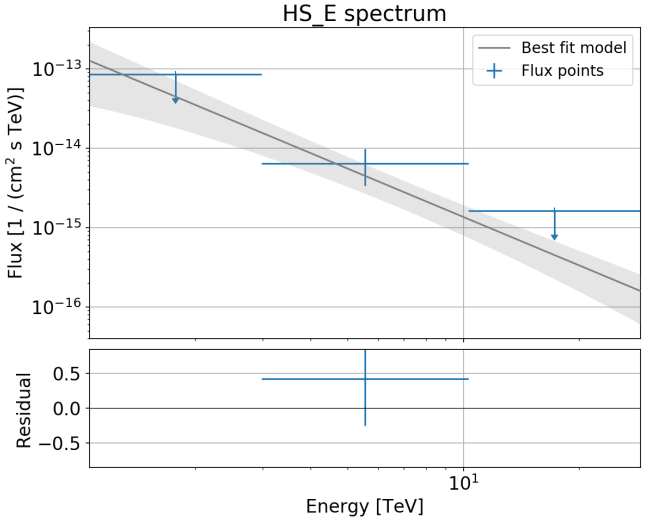

FIGURE 5.44: Power law spectrum fit with the reflected regions method for the hotspot E. The residuals are normalised to the best-fit model.

Hotspot E	
PL index	(2.021 ± 0.331)
PL amplitude	$(1.425 \pm 1.065)\ \times 10^{-13}$ cm^{-2}s^{-1}TeV^{-1}

TABLE 5.15: Best-fit parameters and statistical errors of the spectral fits with a power law using the reflected regions method for the ON region of the source component in region E.

The spectral fit from the reflected regions analysis shows rather large errors. Also, only one of the three extracted flux points is not an upper limit. Furthermore, the amplitudes of the reflected regions analysis and the 3D fit are not compatible.

5.5.3.3 Concluding the morphology and spectral analyses

The results of the detailed analyses of the Westerlund 2 core region shows that three highly significant and most likely separate sources in close proximity to each other could be found around the Westerlund 2 star cluster. The properties of these three components were determined by conducting an extensive 3D fit procedure with an information-theory

based approach to model selection. The results were cross-checked with the reflected regions method, taking into account the relative overlap of the components on the basis of the results from the 3D fit. The results of the reflected regions analysis set the basis for the interpretation and discussion presented in Chap. 6.

As found in the literature, the TeV emission around Westerlund 2 shows a clear energy dependent morphology. With the dataset regarded in this work, the morphology of the emission could be shown in three instead of two energy channels as in the 2011 publication by the H.E.S.S. collaboration on Westerlund 2 [2]. The energy dependent morphology suggests potential source confusion which needs to be investigated in more detail. For the following interpretation of the three sources HESS J1023–575, HESS J1026–582 and the TeV *jet* cloud, the best-fit properties obtained from the source regions are used without sub-dividing the regions further as this would go beyond the scope of this work. It should however be approached in future analyses.

Apart from the three main source components in the Westerlund 2 core region, a total of three weak but statistically significant point-like hotspots were found in the dataset (a trial factor is however not taken into account here). The exposure of the two regions, which are both located at the edge of the data set, is not high enough to yield stable statistics for a robust analysis. Further observations of the regions are needed to perform a more elaborate analysis of the hotspots. These three potential sources are therefore only marginally discussed in Chap. 6.

5.6 Comparison to data from other wavelengths

To get a better view of the findings in a multi-wavelength context, the results from the presented analysis of H.E.S.S. data are compared to data from other wavelengths. In the following, brief analyses and sky maps combining the TeV results with data from other wavelengths are presented. These comparisons motivate emission scenarios that are discussed in detail in Chap. 6.

5.6.1 Comparison to optical data from the DSS2 survey

As the Westerlund 2 star cluster and surrounding clouds and dust are well visible in the optical range, a sky map with optical data from the red channel of the second digitized sky survey (DSS2) overlayed with VHE data is shown in Fig. 5.45 for HESS J1023–575. All WR stars in the region found in the Simbad astronomical database[3] are marked with blue stars. The stellar cluster Westerlund 2 is marked with a yellow arrow. The H II region RCW 49, in which Westerlund 2 is embedded, is clearly visible with its bright features.

[3] `http://simbad.u-strasbg.fr/simbad/`

For orientation, the $2, 4$ and 6σ significance contours of the VHE data are shown in grey with the positions and outlines of the best-fit components from the 3D fit shown in green.

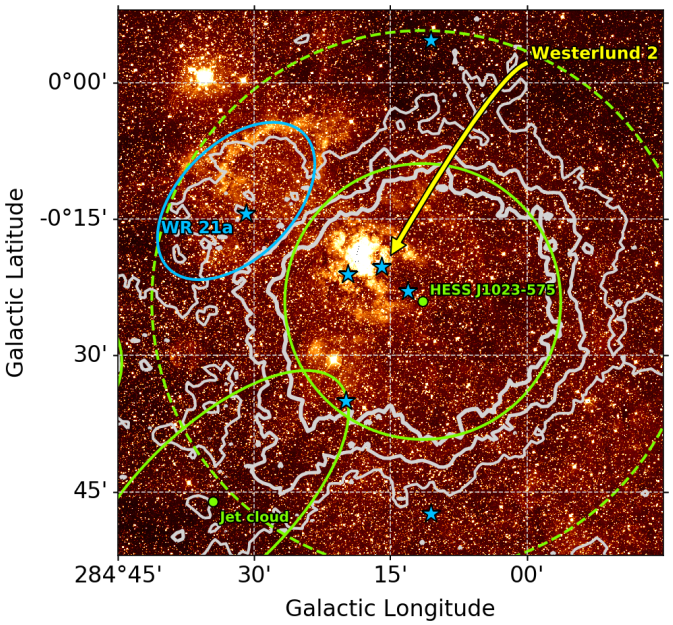

FIGURE 5.45: The Westerlund 2 region in the red optical band. The data is extracted from HiPS maps of the second digitized sky survey (see `http://alasky.u-strasbg.fr/DSS/DSS2Merged`). The grey contours depict the $2, 4$ and 6σ significance contours from the TeV ring background analysis. The green markers and lines depict the positions and outlines from the best-fit components of the 3D fit from Sec. 5.5.1.2. The blue stars mark the WR stars in the region, while the blue ellipse depicts the ON region around WR 21a.

As seen in Fig. 5.45, Westerlund 2 and the bright core of RCW 49 are located to the north-east of the best-fit centre of the HESS J1023–575 disk, but within the disk's radius. All WR stars known in the region are furthermore positioned within the total spatial extension of HESS J1023–575 (within the *edge*, marked by the dashed green circle). Collective stellar winds are therefore a possible explanation for the detected emission, as further discussed in Sec. 6.1.2.3.

Notable is also the position of WR 21a north east of Westerlund 2 within a lobe of significant emission (which is also seen in the excess maps depicting the energy dependent morphology in Sec. 5.5.1.4) that coincides with dust structures seen in the DSS2 data. The region is marked with a light blue ellipse in Fig. 5.45. The probed model_I of the candidate collection for the 3D fit of the Westerlund 2 core region includes a Gaussian component around the position of this WR 21a ON region. Nevertheless, the component is not significant within the model. Even though this region is partly included in the reflected regions analysis and the 3D fit of HESS J1023–575 (and thus contributes to the resulting flux estimates), a dedicated reflected regions analysis is conducted to extract spectral properties of the direct surrounding of WR 21a. Taking the marked elliptical region ($l = 284.533°$, $b = -0.217°$, width: $0.35°$, height: $0.21°$, angle: $135°$) as ON region

for a reflected regions analysis yields an excess emission with 20.4σ significance. The best-fit spectrum for this region is shown in Fig. 5.46 with the best-fit parameters and statistical errors in Tab. 5.16.

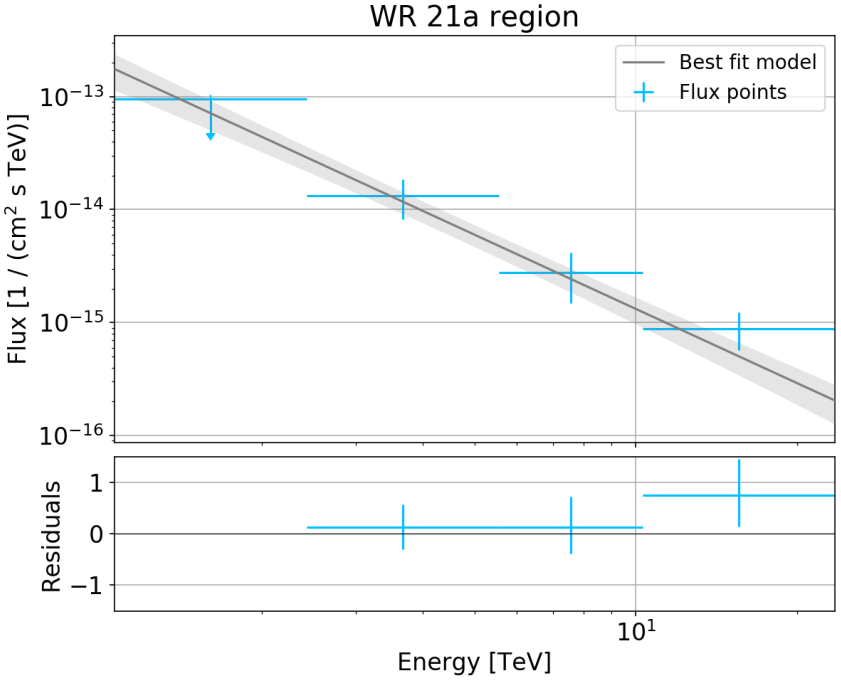

FIGURE 5.46: Best-fit spectrum and residuals with extracted flux points for the reflected regions analysis of the elliptical ON region around WR 21a, shown in Fig. 5.45. The grey area depicts the 1σ statistical error of the PL fit.

WR 21a region	
PL index	(2.18 ± 0.19)
PL amplitude	$(2.00 \pm 0.72) \times 10^{-13}$ cm^{-2}s^{-1}TeV^{-1}

TABLE 5.16: Best-fit parameters and stat. errors of the spectral fits with a power law using the reflected regions method for the ON region around WR 21a.

The best-fit indices of the WR 21a region and of HESS J1023–575 are compatible within statistical errors. Due to their close proximity, it is not possible to distinguish the WR 21a region as an individual source. Nevertheless, a possible scenario in which the emission detected in this region is connected to WR 21a is discussed in Sec. 6.1.5.

5.6.2 Comparison to HE data from Fermi-LAT

The Fermi-LAT satellite takes data in the MeV to GeV energy range which therefore complements the H.E.S.S. data towards lower energies that are not accessible to the H.E.S.S. telescopes. To get an impression on how the Westerlund 2 region looks in the HE range compared to the VHE range, a very basic Fermi-LAT data analysis is performed.

The data taken with the Fermi-LAT are openly available and can be downloaded from an online archive[4] where one selects a time window and an area on the celestial sky for which observational data and instrument response functions should be obtained. For the following brief analysis, Fermi-LAT data within a radius of 3.5° around the position of Westerlund 2 taken in the time between 2008-08-04 and 2019-04-23 was downloaded. Furthermore, the openly available `fermitools`[5] are used in version 1.0.2 to combine the observational data files and extract the exposure, PSF and IRFs in fits format. For all steps, default parameters are used and no specific cuts are applied. The further analysis is performed with `gammapy` in version 0.13. As background model, an isotropic spectral template[6] provided by the Fermi collaboration is used. The resulting sky map ($0.02° \times 0.02°$ spatial binning) with the Fermi-LAT excess counts around the Westerlund 2 core region from 100 MeV to 1 TeV, smoothed with a disk kernel of 0.1° radius, is shown in Fig. 5.47. The skymap is overlayed with the $2, 4$ and 6σ significance contours determined in the H.E.S.S. data analysis presented in Sec. 5.4. Additionally, the positions and outlines of the final source components determined in the 3D fit procedure are shown, together with the positions of pulsars from the ATNF pulsar catalogue[7] marked with yellow stars.

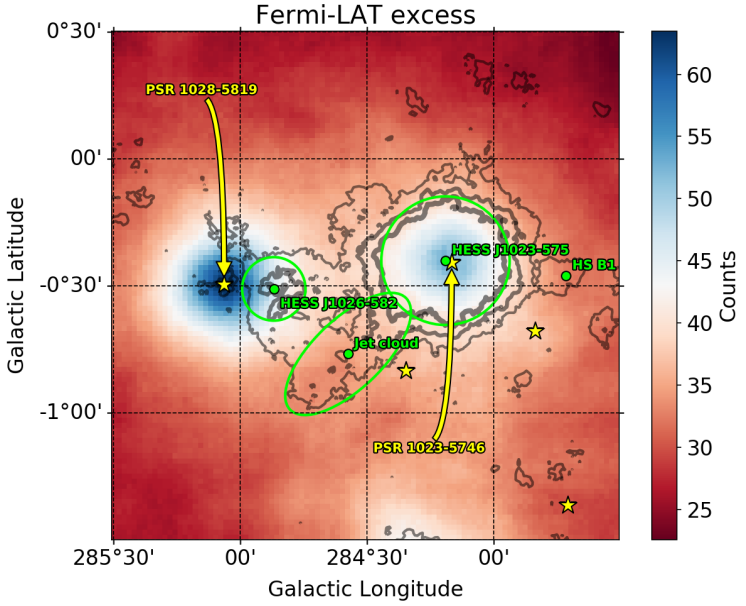

FIGURE 5.47: Smoothed excess map for Fermi-LAT data between 100 MeV and 1 TeV (see main text for analysis details). The positions and outlines of the best-fit components from the 3D fit are shown in green. The positions of pulsars in the region from the ATNF pulsar catalogue are marked with yellow stars.

In Fig. 5.47, it can be seen that multiple pulsars are in close proximity to the detected HE and VHE emission, proposing PWN scenarios. A clear excess in the Fermi-LAT data

[4] `https://fermi.gsfc.nasa.gov/cgi-bin/ssc/LAT/LATDataQuery.cgi`
[5] See `https://github.com/fermi-lat/Fermitools-conda` for details
[6] version iso_P8R3_SOURCE_V2_v1; see `https://fermi.gsfc.nasa.gov/ssc/data/access/lat/BackgroundModels.html`
[7] `https://www.atnf.csiro.au/research/pulsar/psrcat/`

can be seen within the best-fit region of HESS J1023–575. This is in agreement with the results of a study investigating extended sources in Fermi-LAT data [119]. The positional proximity of HESS J1023–575 and the pulsar PSR 1023–5746 suggests a PWN scenario, which is further discussed in Sec. 6.1.2.1. For HESS J1026–582, the Fermi-LAT excess is shifted towards the east of the H.E.S.S. best-fit position. This Fermi-LAT excess could be associated to the pulsar PSR J1028–5819 [112], which encourages a PWN scenario for HESS J1026–582 as discussed in Sec. 6.1.1. For the region of the TeV *jet* cloud, no apparent excess can be seen in the Fermi-LAT data.

A more elaborate analysis of Fermi-LAT data including a pulsar gating analysis to disentangle the pulsed emission by pulsars and other components of emission would be needed to get deeper insights into the interplay of the HE and VHE emission around Westerlund 2. A combined analysis of the H.E.S.S. and Fermi-LAT datasets could thereby yield very interesting results. This would nevertheless go beyond the scope of this work and is suggested for future analyses of the Westerlund 2 region in HE and VHE γ-rays.

5.6.3 Comparison to H I and CO data

Two clouds of molecular gas with a distinctive *arc* and *jet* shape are found in radio data in the Westerlund 2 region as presented in [124] (NANTEN data) and [3] (NANTEN2 and Mopra data). Additionally, a shell-like feature is found in H I data. Both publications present skymaps that show TeV emission contours in combination with H I and CO data. To reproduce these sky maps with the results presented in this work, H I data from the Parkes and ATCA experiments is retrieved via the Southern Galactic Plane Survey (SGPS) [134, 135] in fits format[8]. The $^{12}\mathrm{CO}(J = 1 - 0)$ (from here onwards referred to as CO) data taken with the NANTEN telescope, from which analysis results are presented in [124], are kindly provided by Prof. Yasuo Fukui.

The *arc* and *jet* clouds with their according features in H I and CO data are found in a velocity range of roughly $[20, 32]\,\mathrm{km/s}$, whereas for this study, the velocity range of $\sim [24, 32]\,\mathrm{km/s}$ is chosen. As the CO and H I data sets have different resolutions in velocity, the regarded ranges of the two datasets slightly differ in the following. The error on the velocities is not regarded in the calculations. Additionally, there is another group of molecular clouds detected in the velocity range of $\sim [-10, 20]\,\mathrm{km/s}$. As outlined in [3], these show "tight correlation" with Westerlund 2 and RCW 49 and that an enhanced $^{12}\mathrm{CO}(J = 2 - 1)/(J = 1 - 0)$ line intensity ratio suggests that these clouds are heated by RCW 49 and/or Westerlund 2. Such an enhancement is not seen for the *arc* and *jet* cloud. The authors therefore suggest that the *arc* and *jet* cloud are physically separated from Westerlund 2 and are located farther away. The cloud group in the lower velocity range does not show a spatial correlation to the VHE emission as the *arc* and *jet* cloud, and are therefore not further regarded in this work.

[8] See `https://www.atnf.csiro.au/research/hi/sgps/fits_files.html`

To avoid confusion, the elongated γ-ray source south-east of HESS J1023–575 will be referred to as "TeV *jet* cloud" with the corresponding feature in H I and CO data referred to as "molecular *jet* cloud" or simply "*jet* cloud". Furthermore, it is important to note, that the analyses presented in this section only make use of CO and H I data, not taking into account dark gas components that are not visible in CO and H I (see for example [136] and [137]). The fraction of dark gas in molecular clouds can be $\sim 30\%$ [136]. Therefore, the cloud masses deduced in this section may be too low.

5.6.3.1 H I emission around Westerlund 2

Figure 5.48 shows the integrated H I data from the SGPS in the range between 23.6 and 31.8 km/s overlayed with the VHE significance contours and the component positions and outlines from the 3D fit (model_F) presented in Sec. 5.5.1.2. A spatial coincidence between H I data and the VHE emission can be seen. The H I distribution around HESS J1023–575 appears like a shell of similar extension as the 2σ significance contours of the VHE emission. Towards the centre of HESS J1023–575, a decrease of H I intensity can be seen. This shell-like feature is also noted in [124]. Furthermore, the TeV *jet* cloud also shows a spatial agreement with an elongated structure in the H I data. The good agreement of the VHE significance contours with the H I data in general suggests a possible connection.

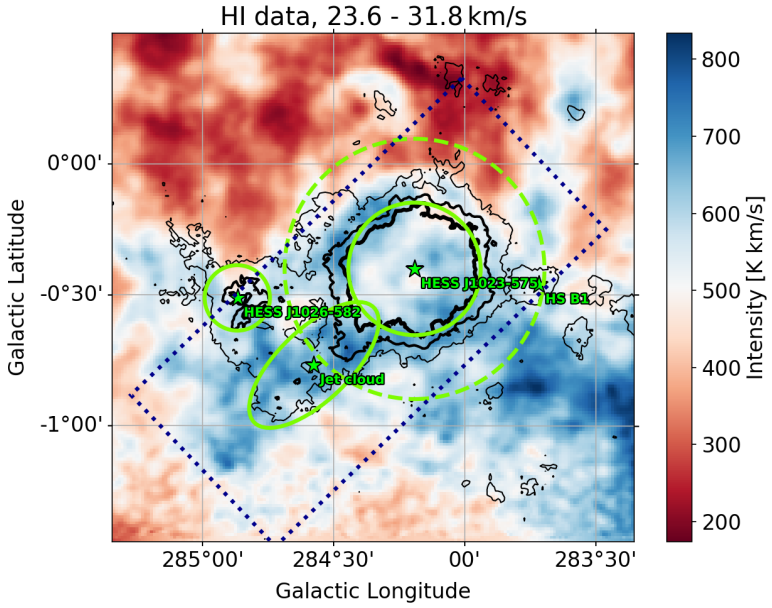

FIGURE 5.48: Integrated H I data in the 23.6 to 31.8 km/s range. The black contours depict the $2, 4$ and 6σ significance levels from the H.E.S.S. data. The best-fit components from the 3D fit are shown in green. The dotted rectangle denotes a cutout region for further investigations.

To further investigate the H I distribution, data is extracted for a cutout region (marked by the dotted rectangle in Fig. 5.48) that is aligned with the major axis of the TeV *jet* cloud

component and centred on the galactic position ($l = 284.367°$, $b = -0.567°$). The binned H I data is projected onto the coordinate system of the cutout with Cartesian coordinate axes x_c and y_c. Furthermore, the resolution is increased and the data is smoothed with a spline interpolation to reduce resampling artefacts. The smoothed brightness temperature or intensity distribution along x_c is shown in the bottom panel of Fig. 5.49. The top panel shows the integrated brightness temperature distribution in the cutout for the velocity range depicted in the bottom panel (non-greyed out). As a visual guide, the positions and outlines of the components from the 3D fit are shown in green, with the position of the TeV *jet* cloud and the position of HESS J1023–575 along x_c marked by the black dotted lines.

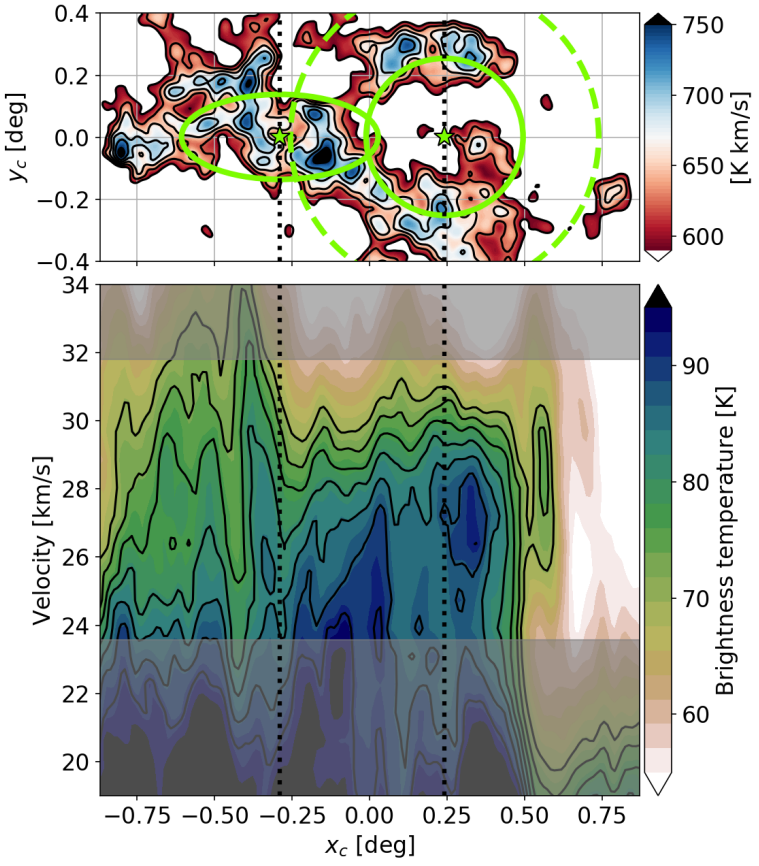

FIGURE 5.49: *Bottom panel:* Velocity distribution in the cutout region shown in Fig. 5.48 along the x_c-axis. The data is upsampled and smoothed to reduce resampling artefacts. *Top panel:* Integrated H I intensity in coordinates of the cutout region. The data is rotated, upsampled and smoothed. The integrated velocity range is non-greyed in the bottom panel.

The shell-like H I distribution can clearly be distinguished around the position of HESS J1023–575 within the dashed green outline of the disk model in the upper panel of Fig. 5.49. A lack of H I emission is nevertheless seen for $x_c > 0.5$ within the dashed outline of

HESS J1023–575. Also the velocity distribution in the bottom panel shows a drop in brightness temperature for $x_c > 0.5$ over the regarded velocity range.

5.6.3.2 CO emission around Westerlund 2

The coloured contours of the NANTEN CO data complementing the H I data is shown in Fig. 5.50. The plot shows a H.E.S.S. significance map in the background overlayed with the CO intensity integrated from 23.9 to 32.0 km/s for bins ≥ 2 K km/s. Here, a spatial correlation between CO and TeV data can also be seen. The *arc* cloud aligns with the disk geometry of HESS J1023–575 to the north-west. Furthermore, the molecular *jet* cloud aligns with the ellipse of the TeV *jet* cloud from the 3D fit. The orientation of the best-fit line along the molecular *arc* and *jet* clouds determined in [3] (in the $24 - 32$ km/s range, shown in yellow in Fig. 5.50) agrees with the orientation of the ellipse of the TeV *jet* cloud from the 3D fit within statistical errors.

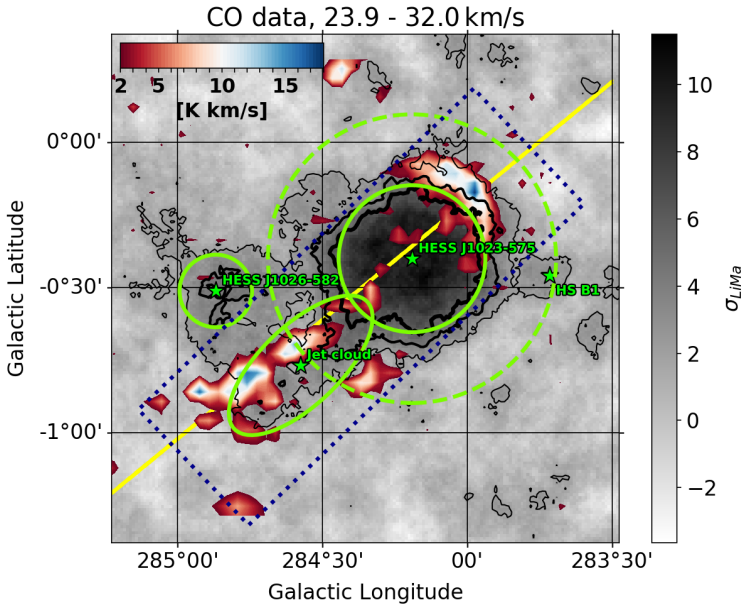

FIGURE 5.50: H.E.S.S. significance map overlayed with NANTEN CO brightness temperature integrated between 23.9 and 32.0 km/s, shown in a red-blue colour map. The yellow line shows the best-fit line along which the *arc* and *jet* cloud are aligned as determined in [3]. The $2, 4$ and 6σ contours are shown in black with the best-fit components from the 3D fit in green. The dotted rectangle denotes a cutout region for further investigations. The NANTEN data is kindly provided by Prof. Yasuo Fukui.

As for the H I data, the CO data is projected to the rotated coordinate system (x_c, y_c) and the data is upsampled and smoothed for the cutout region marked by the dotted rectangle in Fig. 5.50. Figure 5.51 shows the CO velocity distribution of the cutout in the bottom panel with the integrated spatial intensity distribution shown in the top panel for the depicted velocity range (non-greyed in bottom panel). Here, individual components

of the cloud structures can be determined in the velocity distribution. A detailed analysis of these structures is presented in [3].

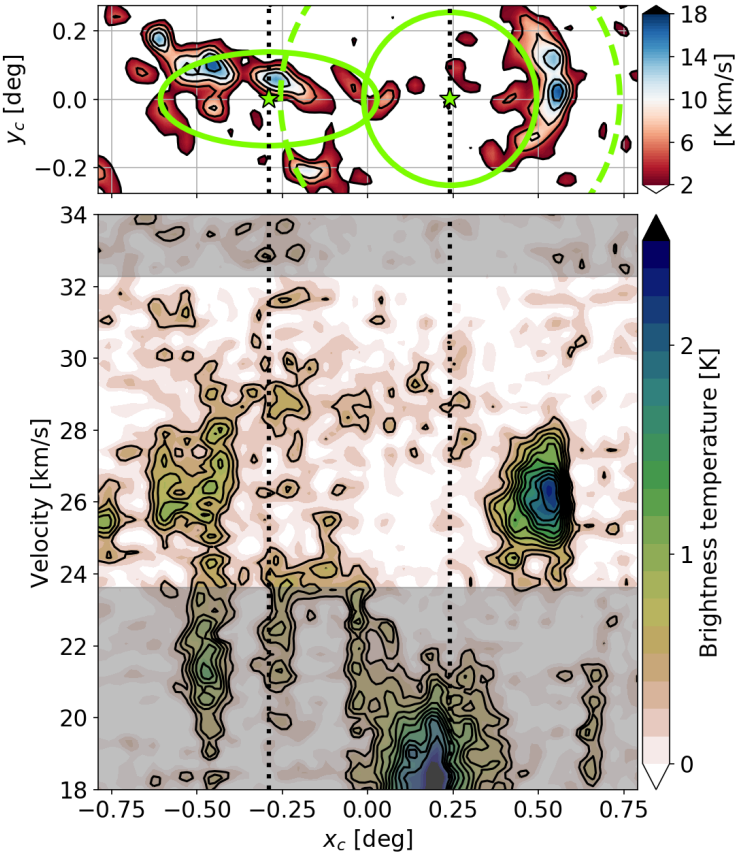

FIGURE 5.51: *Bottom panel:* Velocity distribution in the cutout region shown in Fig. 5.50 along the x_c-axis. The data is upsampled and smoothed. *Top panel:* Integrated CO intensity in coordinates of the cutout region. The NANTEN data is rotated, upsampled and smoothed. The integrated velocity range is non-greyed in the bottom panel.

5.6.3.3 Calculating the distance to the detected clouds

To determine the distance d of a molecular cloud in our galaxy to the Sun, the so called kinematic distance ambiguity (KDA) method can be used as outlined in [138]. The method utilises a rotation curve model that states the expected rotational velocity V at a distance r to the centre of the Milky Way to geometrically determine the distance of the cloud via calculating its galactocentric radius r_c. The two formulas that are needed are

$$r_c(r) = R_0 \sin(l) \frac{V(r)}{V_r + V_0 \sin(l)} \tag{5.1}$$

and

$$d(r) = R_0 \cos(l) \pm \sqrt{r_c(r)^2 - R_0^2 \sin^2(l)} \tag{5.2}$$

where R_0 is the Sun's distance to the galactic centre and V_0 is its rotational velocity in the Milky Way. The galactic longitude of the cloud is l with V_r as the cloud's line of sight velocity measured by the observer. Equation 5.2 holds for clouds in the inner galaxy (i.e. $r_c < R_0$) for which two distances are possible, as a cloud with a measured V_r can be placed at a far or a near distance to the observer. If a cloud is in the outer galaxy with $r_c > R_0$, the KDA method has a unique solution using the '+' version of Eq. 5.2. For the following distance calculations, a model from McMillan [139] and from Bovy [140] as implemented in the `galpy` software package[9] (named *McMillan17* and *MWPotential2014* respectively in the software) is used with default parameters [140].

A common approach to determine a cloud's distance d is to assume a flat rotation curve and approximating $V(r)$ with V_0, which removes the r dependency of r_c. This directly yields a value for r_c, but depending on the rotation curve model this approximation may not be appropriate. A different numerical approach is to set $r \approx r_c$ so that Eq. 5.1 is approximately fulfilled and inserting this r_c into Eq. 5.2. Figure 5.52 shows the rotation curves for the two here regarded models in the *left* panel, while the determination of the cloud distance d from the Bovy model is visualised in the *right* panel for a cloud at galactic longitude l and a line of sight velocity V_r as given below. The idea can be explained in a graphical manner: First, the point where $r_c(r) \approx r_c$ is found by following the grey bisection line in Fig. 5.52 (*right*) to its intersection with the solid curve $r_c(r)$ which is marked with a green dot. From this point, following the dashed black vertical line to its intersection with the dashed curve $d(r)$ (marked by the red dot) yields the distance $d(r \approx r_c)$ of the cloud.

Assuming a mean velocity along the line of sight of the molecular *arc* and *jet* cloud of $V_r = 26.25\,\mathrm{km/s}$ (which is roughly the intensity peak of the *arc* cloud as seen in Fig. 5.51) and a mean galactic longitude of $l = 284.25°$ yields an $r_c > 9\,\mathrm{kpc}$, reducing Eq. 5.2 to the solution with the '+'. The resulting distance is then $d \sim 6.8\,\mathrm{kpc}$ and $d \sim 6.6\,\mathrm{kpc}$ for the McMillan and the Bovy models respectively. This is shorter than the distance of $7.5^{+0.2}_{-0.5}\,\mathrm{kpc}$ determined in [3], where the authors use yet another rotation curve model. This shows how the assumed rotation curve can have a significant impact on the resulting distance estimate. Furthermore, it is important to note that the KDA method "can be rendered quite inaccurate by localized velocity perturbations"[138]. Assuming local velocity fluctuations up to the order of $\sim 10\,\mathrm{km/s}$ (as suggested in [141]) on the rotation curve and using the regarded velocity range of $\sim [24, 32]\,\mathrm{km/s}$ as bounds for V_r yields distance estimates of around $6.8^{+1.2}_{-1.1}\,\mathrm{kpc}$ for the McMillan model and of $6.6^{+1.1}_{-1.1}\,\mathrm{kpc}$ for the Bovy model. Additional uncertainties are introduced by errors on the mean galactic

[9] `https://github.com/jobovy/galpy`, used in version 1.6.0

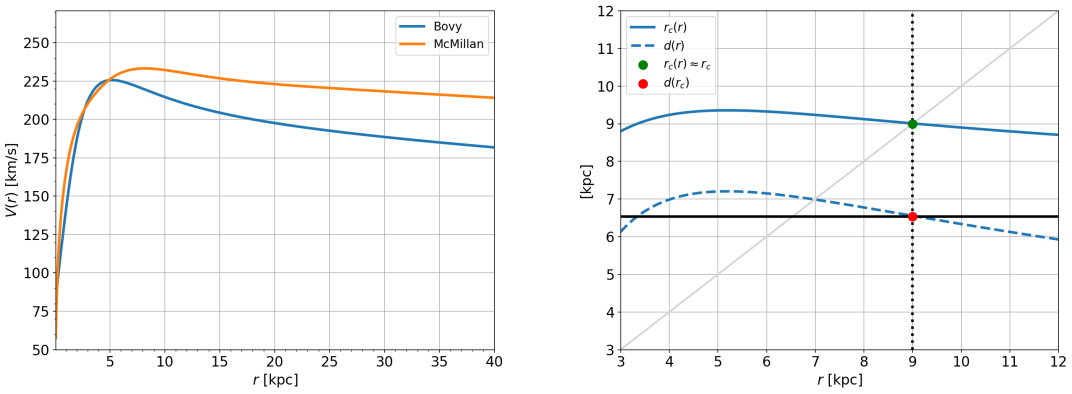

FIGURE 5.52: *Left*: Rotation curves of the two models used to determine the distance of the H I and CO clouds. *Right*: Visualisation of the approach used to determine the distances of the detected galactic clouds via the KDA method with the Bovy model.

longitude of the cloud as well as a possible proper motion of the cloud relative to the motion of its galactic environment. These are however neglected in this calculation.

5.6.3.4 Combining H I and CO data

An overlay of the upsampled and smoothed CO and H I contours from Fig. 5.49 and 5.51 is shown in Fig. 5.53. The overlayed contours show that the *arc* cloud fills the void in the shell-like distribution of H I. Together, the CO and H I data form a complete shell of hydrogen gas that coincides with the TeV emission of HESS J1023–575. This feature is further on called "hydrogen shell". Furthermore, the *jet* cloud in CO coincides with the elongated feature seen in the H I distribution. A large part of this molecular *jet* cloud coincides with the ellipse region of the TeV *jet* cloud.

The origin and interplay of the structures seen in CO and H I data that form the hydrogen shell and the molecular *jet* cloud are discussed in the literature, with main points summarised in the following: The *arc* cloud is suggested to be "part of a swept-up shell" as stated in [124], which could well originate from SN activity. Its small velocity dispersion thereby suggests that it "has already been significantly decelerated". The publication [3] also finds that the *arc* cloud does not appear to be expanding, as this would show a different signature in its velocity distribution (see App. A in [3]). Alternatively, the authors suggest that the *arc* cloud is a "thin filamentary feature" of the H I shell. An H I–H_2 conversion in the shell could be an explanation for observed decrease of H I intensity at the position of the *arc* cloud [124]. The coincident features seen in H I and CO along the TeV *jet* cloud could be explained by "in situ conversion of H I into molecular gas by shock compression"[124]. The high energy jet from an anisotropic SN explosion or from a microquasar is mentioned as a possible object that could create the *arc* cloud and the molecular *jet* cloud. To probe this hypothesis, magneto-hydrodynamic simulations were

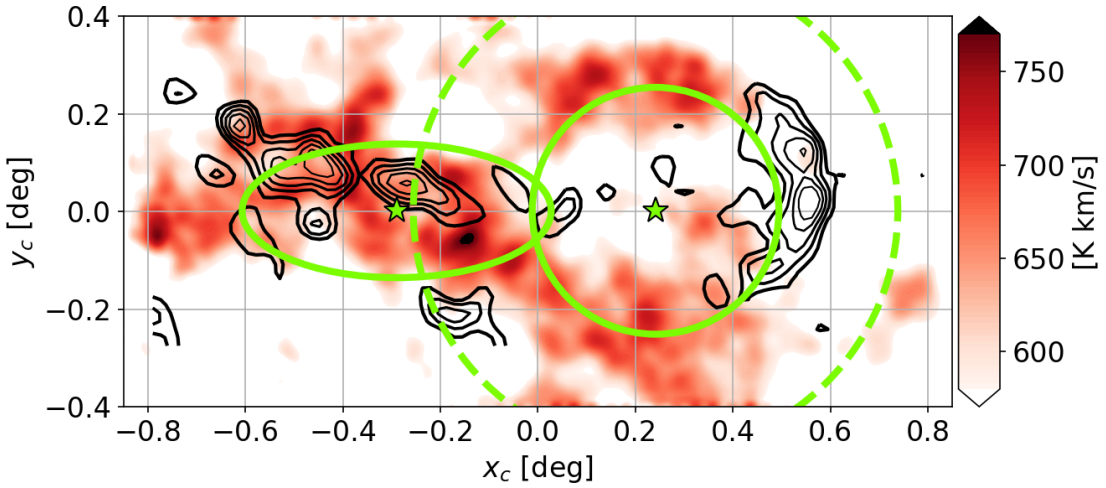

FIGURE 5.53: Intensity distribution of H I data in the cutout coordinate system in the range from 23.6 to 31.8 km/s shown in red. The black contours depict levels of integrated CO intensity in the range from 23.9 to 32.0 km/s. The contour lines show levels from 3 to 13 K km/s in five steps. The data is saturated for a better visualisation of the geometrical features. The positions and outlines of the best-fit γ-ray sources are shown in green.

performed that show how structures like the *arc* and *jet* cloud can be formed by a high energy jet that interacts with gas of different densities [142].

5.6.3.5 Gas in the region of HESS J1023–575

Due to the good spatial agreement of the hydrogen shell with HESS J1023–575, the structure is investigated in more detail. As H I and CO emission are tracers for hydrogen, the measured intensities can directly be converted to column densities of gas. This is done by multiplying with the so called X-factors. For CO in the Milky Way, the factor X_{CO} has been determined with values ranging from 0.9 to $4.2 \times 10^{20}\,\mathrm{cm}^{-2}(\mathrm{K\ km/s})^{-1}$ (see [143] for an extensive study on variations of X_{CO}), whereas a value of $X_{\mathrm{CO}} = 2 \times 10^{20}\,\mathrm{cm}^{-2}(\mathrm{K\ km/s})^{-1}$ is used here, as suggested in [144]. For H I, the X-factor is taken as $X_{\mathrm{H\,I}} = 1.823 \times 10^{18}\,\mathrm{cm}^{-2}(\mathrm{K\ km/s})^{-1}$ as stated in [145]. Column density maps are obtained by multiplying the integrated H I and CO intensity maps of the Westerlund 2 core region with the corresponding X-factor, resulting in maps that give the column density in [cm^{-2}] for each pixel of the map. These column density maps derived from CO and H I data are shown in Fig. 5.54.

Plotting the radial column density distribution of the CO and H I data around the best-fit position of HESS J1023–575 (which appears to coincide with the centre of the hydrogen shell) helps to investigate the observed shell-like geometry in detail. To conserve the area of the radial bins of the distributions, the data have to be equally binned in θ^2, where θ is the offset from the best-fit position of HESS J1023–575. The radial column density

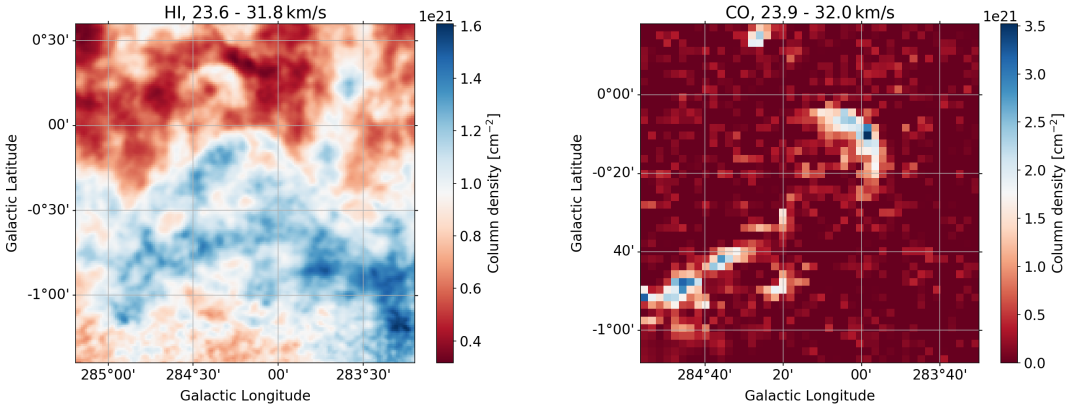

FIGURE 5.54: Column density maps of the Westerlund 2 region derived from H I (*left*) and CO data (*right*).

distributions are shown in Fig. 5.55. The histograms show the relative CO and H I density with respect to the highest bin of the respective dataset. The solid thick lines are three bin averages to reduce fluctuations. Additionally, the γ-ray intensity profile of the best-fit disk component from the 3D fit of HESS J1023–575 is shown in green on the right y-axis with the disk's radius and edge marked by the solid and dashed black lines. The statistical error bands for the disk model are depicted by the faint green and grey regions.

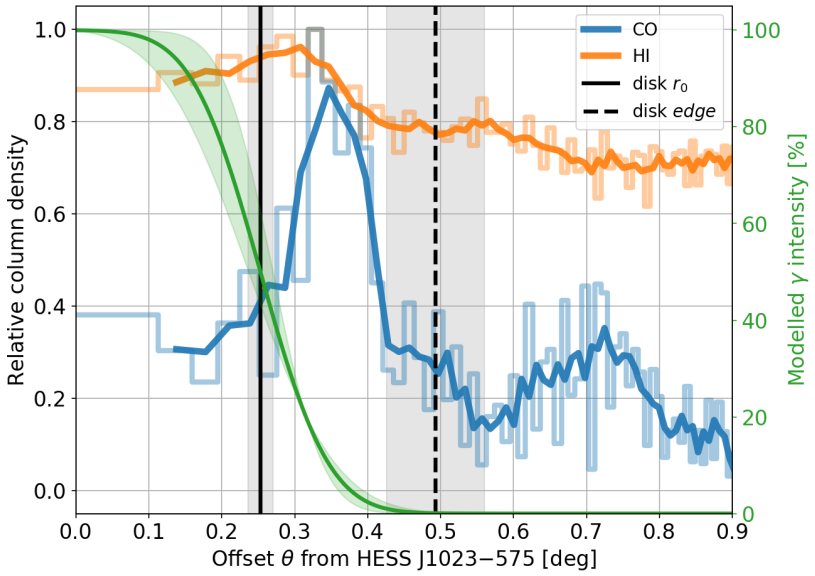

FIGURE 5.55: Radial distribution of relative H I and CO column densities shown in Fig. 5.54. The distributions are scaled to the highest bin. The thick orange and blue lines depict three bin averages to reduce fluctuations. For comparison, the γ-ray intensity profile of the best-fit disk component from the 3D fit of HESS J1023–575 is shown in green on the right y-axis with the disk's radius r_0 and *edge* marked by the black solid and dashed line respectively. The respective statistical error bands are shown in grey. The error band for the intensity profile from the anti-correlated error bands of the radius and edge (see correlation matrix in Fig. 5.25) is shown in faint green.

To better understand the observed radial column density profiles, it helps to look at how the density distribution of gas in a 3-dimensional spherical shell looks when projected to 2 dimensions. An idealised simulation for the observed setup, with the *arc* cloud modelled as a cap of the shell is shown in App. G, where it can be seen that the shell's inner and outer radius can be roughly deduced from the density profile as well as the rough orientation of the cap to the line of sight. The H I density profile in Fig. 5.55 increases from the centre until it reaches a peak at around $\theta = 0.3°$. Above 0.3° the distribution decreases and appears to stabilise from $\theta \sim 0.45°$ on. The CO distribution shows a similar progression as the H I distribution. The distribution rises to reach its peak around $\theta = 0.35°$ and then drops towards $\theta \sim 0.45$ like the H I distribution. This offset overlaps with the error limits of the TeV disk's edge that is marked by the grey band around the dashed vertical line. The approximate inner radius r_i, outer radius r_o and the width w_s of the shell at the minimum, mean and maximum distance determined with the Bovy model in Sec. 5.6.3.3 are given in Tab. 5.17.

Parameter at distance	**Value** [deg]	**Projected** [pc] 5.5 kpc	6.6 kpc	7.7 kpc
Inner radius r_i	0.30	28.8	34.6	40.3
Outer radius r_o	0.45	43.2	51.8	60.5
Width w_s	0.15	14.4	17.3	20.2

TABLE 5.17: Approximate dimensions of the hydrogen shell as determined from the radial density profile shown in Fig. 5.55.

By comparing the radial CO density profile with the simulated distributions shown in Figs. G.2 and G.3 shows that the *arc* cloud appears to be oriented perpendicular to the line of sight.

Looking at the modelled γ-ray intensity predicted by the disk model as shown on the right y-axis of Fig. 5.55 shows that the intensity has dropped to $< 1\%$ at the outer edge of the shell. It can thus be said that the full emission of HESS J1023–575 completely coincides with the apparent shell of neutral and molecular hydrogen.

5.6.3.6 Gas in the region of the TeV *jet* cloud

The elongated *jet* cloud seen in CO and H I to the south-east of HESS J1023–575 coincides partly with the TeV *jet* cloud. Especially the alignment of the cloud features with the ellipse region of the TeV source is striking. In H I the cloud shows a length of $\sim 0.8°$ and a width of $\sim 0.3°$, as seen in Fig. 5.53. For a distance of (6.6 ± 1.1) kpc and assuming that the cloud is oriented perpendicular to the line of sight, this corresponds to physical dimensions of $\sim (98 \pm 15)$ pc in length and $\sim (40 \pm 7)$ pc in width. The TeV *jet* cloud is roughly 25% smaller with $\sim (73 \pm 13)$ pc in length and $\sim (32 \pm 5)$ pc in width.

5.6.3.7 Determining cloud masses

To calculate the mass of detected neutral and molecular hydrogen per sky map pixel, the CO and H I column density maps can be multiplied by the projected area of a pixel for a given distance. This yields maps that state the number of H_2 and H I particles per pixel. The total mass of a cloud or cloud component is then obtained by adding up all pixels that fall into the component's region. An additional factor of $\mu = 2.8$ is thereby used to convert from CO column density to molecular mass, accounting for a helium abundance of 20%, as suggested in [3]. To relate the observed γ-ray emission to the detected gas, the masses are calculated for the regions in which γ-ray emission is observed and not for the whole cloud structures. The molecular and neutral hydrogen mass is therefore determined within the elliptical region of the TeV *jet* cloud and within the determined outer radius of the hydrogen shell of 0.45° around HESS J1023–575.

It is important to note that the *jet* cloud and the hydrogen shell overlap in the column density maps and therefore share a certain amount of mass. The determined masses for the two components are given in Tab. 5.18 together with the amount of shared mass. The masses are furthermore given for the according minimum, mean and maximum distances as determined with the rotation curve by Bovy as outlined in Sec. 5.6.3.3. The mass of a hydrogen atom (assumed to be the same as the mass of a proton) and the solar mass are thereby taken from the `astropy` software package[10].

Region	**H I mass** $[10^4 M_\odot]$			**H_2 mass from CO** $[10^4 M_\odot]$		
at distance	5.5 kpc	6.6 kpc	7.7 kpc	5.5 kpc	6.6 kpc	7.7 kpc
HESS J1023–575 shell	4.98	7.17	9.76	3.60	5.81	7.05
TeV *jet* cloud	1.20	1.72	2.34	1.70	2.45	3.34
Shared	0.40	0.57	0.78	0.34	0.49	0.67

TABLE 5.18: Masses of the neutral and molecular parts of the hydrogen shell surrounding HESS J1023–575 and of the elongated *jet* cloud within the TeV *jet* cloud region for different distances. The last row presents the mass determined in the overlap of the two regions.

The masses of the two cloud components are in general agreement with the masses stated in [3] for the *arc* and *jet* cloud as well as for the H I mass in the region.

The density n_{gas} of hydrogen atoms in the clouds can be determined by relating the total measured mass of a cloud with its volume. For the gas around HESS J1023–575 a 3-dimensional spherical shell as determined in Sec. 5.6.3.5 is assumed. For the gas within the TeV *jet* cloud's elliptical region a 3-dimensional ellipse that is rotation symmetric along the major axis is assumed (see Sec. 5.6.3.6). The resulting densities, assuming that the total mass of H-atoms is evenly distributed in the clouds' volumes, are given in Tab. 5.19.

[10] version 3.1.2, $m_p = 1.672621898 \times 10^{-27}$ kg, $M_\odot = 1.98840987^{30}$ kg

Object	**Density** n_{gas} [H-atoms / cm^3]		
at distance	5.5 kpc	6.6 kpc	7.7 kpc
HESS J1023–575 shell	278	243	198
TeV jet cloud ellipse	53	44	38

TABLE 5.19: Densities of H-atoms, assuming the total gas detected in the respective regions can be ascribed to the clouds with their assumed geometry (see main text).

This approach implies that the density of the clouds' environment (i.e. also inside the spherical shell) has a density of $n_{\mathrm{env}} = 0\,\mathrm{cm}^{-3}$. This may however not be accurate. Figure 5.56 shows the H I column density with the geometries of the hydrogen shell and the *jet* cloud marked by the dashed and dotted shapes respectively. The regions around the assumed cloud shapes show column densities around $[0.3, 1.6] \times 10^{21}\,\mathrm{cm}^{-2}$, showing that the environment of the hydrogen shell and the *jet* cloud are far from having a density of $0\,\mathrm{cm}^{-3}$.

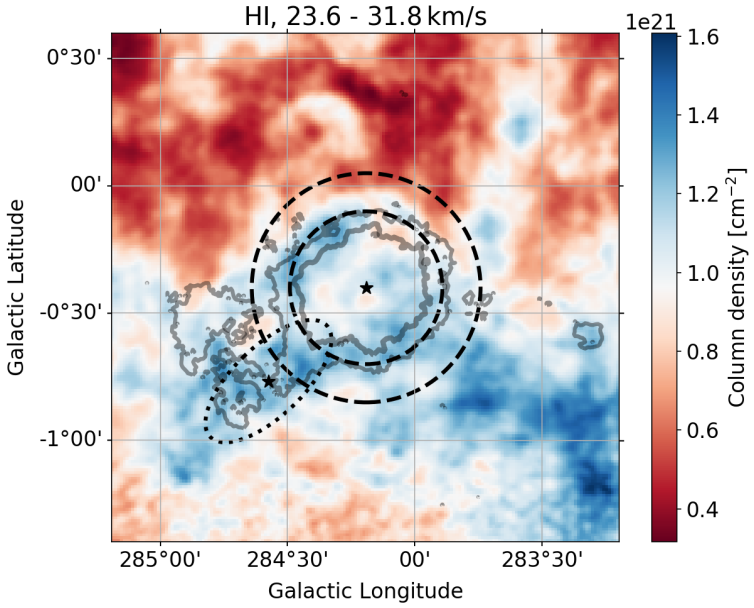

FIGURE 5.56: Column density map of the Westerlund 2 region derived from H I data overlayed with the 3 and 6σ significance contours of the TeV emission in grey. The dashed circles depict the inner and outer radius of the hydrogen shell. The dotted ellipse depicts the region of the TeV *jet* cloud.

For $n_{\mathrm{env}} > 0\,\mathrm{cm}^{-3}$, the densities of the clouds and thus cloud masses would decrease. To correct for a dense environment, it is required to make assumptions about the distribution of gas around the clouds and the physical depth along the line of sight over which the column density is extracted. The stated masses and densities of the hydrogen shell and the *jet* cloud can therefore be regarded as upper limits[11] for the according distance estimates.

[11] This may in turn compensate for mass contributions of dark gas components which are not taken into account here.

5.6.3.8 Concluding the comparison

The results presented in this section show that the γ-ray emission from HESS J1023–575 and from the TeV *jet* cloud show spatial correlations with the distribution of neutral and molecular hydrogen detected towards Westerlund 2. A cloud with an apparent shell-like geometry appears to coincide with the TeV emission of HESS J1023–575. The profile of the γ-ray emission thereby does not follow the profile of gas column density. Rather, the TeV emission appears to be enclosed by a shell of hydrogen gas. The elongated molecular *jet* cloud coincides partly with the γ-ray emission of the TeV *jet* cloud. The alignment of the elliptical TeV source and the elongated cloud structure shows a striking agreement. Additionally, the centre of HESS J1023–575 and the hydrogen shell lies on a line along the major axis of the TeV *jet* cloud ellipse.

Using the KDA method, a distance to the cloud structures of $\sim (6.6 \pm 1.1)\,\mathrm{kpc}$ is determined, which is in agreement with the distance estimate for the Westerlund 2 cluster of $(5 \pm 1)\,\mathrm{kpc}$ [89]. An association of the clouds and the star cluster is therefore possible. A connection between the molecular clouds and the γ-ray emission around Westerlund 2 appears likely, regarding the good spatial agreement. Possible scenarios are discussed in detail in Sec. 6.1.2 for the hydrogen shell in connection with HESS J1023–575, in 6.1.3 for the *jet* cloud and in Sec. 6.1.4 for the two sources together.

Chapter 6

Discussion and interpretation

This section presents the interpretation of the results shown in Chap. 5 and discusses the possibility of selected astro-physical scenarios that could explain the observed emission in the Westerlund 2 region. It is important to note that there are different aspects that complicate this task and affect the interpretation of the results:

1. As the Westerlund 2 region is located close to the tangential point of the Carina arm of the Milky Way, a multitude of stellar objects is in close proximity around the line of sight to the stellar cluster. In general, a high degree of source confusion is thus likely, especially with the evidence of diffuse emission in the region and the energy dependent morphology of the detected VHE emission in general. The detected γ-ray emission at any position can thus potentially be a superposition of different sources. Lower flux levels than the ones determined in the analysis are therefore possible for all sources.

2. Published parameters like distance and age estimates of stellar objects in the Westerlund 2 region partly differ in the literature. As the distance to a γ-ray source is in general deduced from an associated stellar object, this demands the consideration of different sets of parameters to evaluate how likely a certain scenario may be under the assumed conditions. It would go beyond the scope of this work to evaluate every possible set of parameters. Thus, only a limited number of parameter sets for each source is discussed.

3. As the regarded region of the galactic sky is crowded with a multitude of objects and environments that can potentially produce VHE emission, only a limited selection of emission scenarios can be discussed in detail.

In the following, the γ-ray emission and sources around Westerlund 2 that are detected in the presented analyses are discussed in the context of a selected number of scenarios.

6.1 γ-Ray sources in the Westerlund 2 core region

The extensive analysis of the Westerlund 2 core region (see Sec. 5.5.1) yields three different VHE sources in close proximity to the stellar cluster Westerlund 2. Two of these sources, HESS J1023–575 and HESS J1026–582 were already presented and discussed in previous H.E.S.S. publications, while the hint of a third source was found in an analysis published in 2011, but without further investigation. This third source is significantly detected in the analysis presented in Sec. 5.5.1 and is called TeV *jet* cloud, due to its coincidence with the elongated cloud structures found in CO and H I data. To get a better overview of the arrangement of the VHE emission and the cloud structures found in CO and H I data (see Sec. 5.6.3), a rough sketch of the γ-ray emission and the main cloud structures is shown in Fig. 6.1, with markings of important distances used in the following discussions. It is important to note that for the interpretation of the TeV *jet* cloud, only the CO and H I gas detected within the elliptical region of the TeV emission is regarded, even though the clouds spatially extend beyond the TeV emission to the south east. Emission scenarios motivated by the investigations presented in Sec. 5.6 and suggested in the literature are discussed in the following.

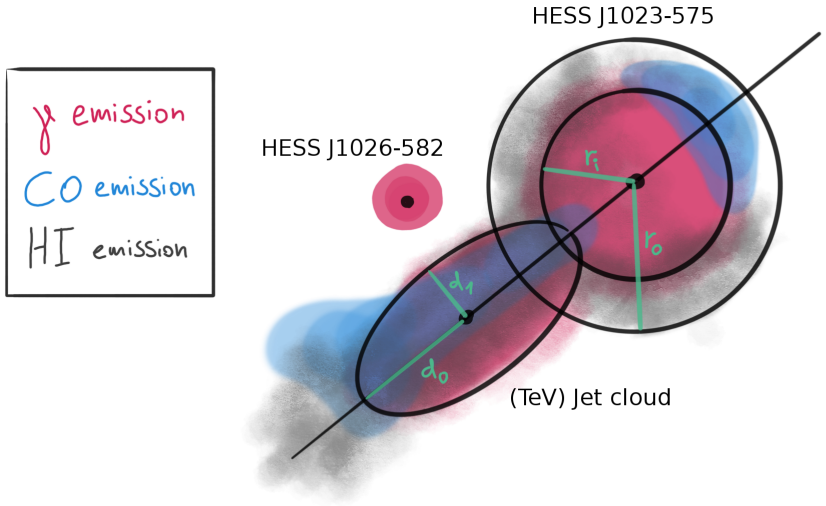

FIGURE 6.1: Simplified sketch of the three detected γ-ray sources together with schematic distributions of H I (grey) and CO (light blue) emission. Distances used in calculations in the following sections are depicted. The H I shell has inner and outer radius r_i and r_o. The elliptical TeV *jet* cloud has semi major and minor axes of length d_0 and d_1. The shown morphologies and distances are not to scale.

6.1.1 HESS J1026–582 - A PWN candidate

The VHE emission detected at the position of HESS J1026–582 is very likely associated with the pulsar PSR J1028–5819, which is in close proximity. The pulsar was first detected

PSR J1028–5819 properties

Set	**Gal. Pos.** (l, b) [deg]	**Distance** d_{PSR} [kpc]	**Char. Age** τ_c [kyr]	**Spindown** $\dot{E}$ [10^{35} erg/s]	**Ref.**
A	$(285.065, -0.496)$	1.42	90	8.3	[147]
B	$(285.071, -0.455)$	2.3	89	8.3	[2]
C	$(285.065, -0.496)$	2.76	90	8.3	[148]
D	$(285.074, -0.460)$	2.3	92.1	8.43	[112]

TABLE 6.1: Different sets of PSR J1028–5819 properties taken from literature. The parameters in the first row are taken from the ATNF pulsar catalogue in version 1.63.

HESS J1026–582 as PWN associated with PSR J1028–5819

Set	**Radius** R_{PWN} [pc]	**Offset** o_{PSR}[pc]	**Velocity** v_{PSR} [km/s]	**Luminosity** $L_{1\text{-}10\,\mathrm{TeV}}$ [10^{33} erg/s]	**Efficiency** $\varepsilon_{\mathrm{TeV}}$ [%]
A	3.1 ± 0.4	4.9 ± 1.1	53 ± 12	0.70 ± 0.10	0.08 ± 0.01
B	5.0 ± 0.6	8.5 ± 1.8	93 ± 20	1.85 ± 0.26	0.22 ± 0.03
C	6.0 ± 0.8	9.5 ± 2.1	104 ± 23	2.66 ± 0.37	0.32 ± 0.04
D	5.0 ± 0.6	8.5 ± 1.8	91 ± 19	1.85 ± 0.26	0.22 ± 0.03

TABLE 6.2: PSR J1028–5819 parameters in connection with HESS J1026–582 as a PWN for the according sets given in Tab. 6.1.

in the radio band by the Australia Telescope Compact Array (ATCA) and the Parkes radio telescope and was associated with the EGRET source 3EG 1027–5817 [146]. A pulsed γ-ray signal was later found in Fermi-LAT data in agreement with the radio source [112]. This pulsed γ-ray source, also named 0FGL J1028.6–5817 or 2FGL J1028.5–5819, is displaced from the position of HESS J1026–582 determined in this work by $\sim 0.2^\circ$ (see also Sec. 5.6.2), encouraging the PWN scenario [2].

Different properties like the distance d_{PSR} and position of PSR J1028–5819, its spin down energy $\dot{E}$ and characteristic age τ_c are stated in the literature and in the ATNF pulsar catalogue[1]. These properties are used to calculate parameters that describe a PWN scenario like the radius of the PWN R_{PWN}, the pulsar velocity v_{PSR} (assuming that the pulsar originates from the best-fit position of the PWN) or the offset distance of the pulsar to the PWN o_{PSR}. Further descriptive parameters are the luminosity of the PWN in the 1 to 10 TeV range $L_{1\text{-}10\,\mathrm{TeV}}$, the so called efficiency $\varepsilon_{\mathrm{TeV}} = L_{1\text{-}10\,\mathrm{TeV}}/\dot{E}$ and the surface brightness of the PWN $S = L_{1\text{-}10\,\mathrm{TeV}}/(4\pi R^2_{\mathrm{PWN}})$. The different parameter sets describing PSR J1028–5819 that are regarded in this work are given in Tab. 6.1. The resulting parameters of the PWN scenario for these sets of parameters calculated with the best-fit parameters of HESS J1026–582 deduced in Sec. 5.5.1 are given in Tab. 6.1. The luminosity is thereby calculated using the ePL fit from the reflected regions analysis (using the predicted 95% containment radius from the 3D fit, see Tab. 5.8) whereas the extension of the PWN is deduced from the best-fit width of the Gaussian from the 3D fit of HESS J1026–582. The stated errors correspond to the statistical errors propagated from the fit uncertainties.

[1] ATNF catalogue: `https://www.atnf.csiro.au/research/pulsar/psrcat/`, version 1.63

To probe how good HESS J1026–582 fits a PWN scenario for the given sets of pulsar parameters, the results from Tab. 6.2 can be compared to the properties of other known PWNe. The H.E.S.S. collaboration has published an extensive study of PWNe in the TeV range in 2018 [149]. In this study, a multi-parameter model is presented that describes the typical evolution of a TeV PWN. Furthermore, a so called *star-rating* is presented to rank PWN-candidates and decide if a PWN scenario is consistent with the observations at VHE energies. This star-rating comprises four rating criteria that compare different parameters of the potential PWN to the PWN-evolution model. For each fulfilled requirement, the TeV source + pulsar pair is "awarded" a star, hence the name *star-rating*. The rating criteria are:

1. *Containment ratio*: The pulsar should be less than 1.5 times the extension radius of the PWN away from the centre of the PWN.
2. *TeV extension vs. pulsar age*: The logarithm of the ratio between measured and predicted PWN extension for the given pulsar age should be within 2 standard deviations of the model ($\sigma_{\lg \mathrm{R}} = 0.39$).
3. *TeV luminosity vs. pulsar spin-down*: The logarithm of the ratio between measured and predicted luminosity for the given pulsar spin-down energy should be within 2 standard deviations of the model ($\sigma_{\lg \mathrm{L}} = 0.83$).
4. *Surface-brightness vs. pulsar spin-down*: The logarithm of the ratio between the measured and predicted PWN surface-brightness for the given pulsar spin-down energy should be within 2 standard deviations of the model ($\sigma_{\lg \mathrm{S}} = 0.30$).

To perform this PWN star-rating, the parameters of the baseline model given in Tab. A.2 of [149] are extracted and a linear interpolation is applied to evaluate the model at arbitrary points. It should be noted that the luminosities in the H.E.S.S. PWN study are calculated from the integrated photon flux $> 1\,\mathrm{TeV}$, the best-fit index of a PL fit to the source and the estimated distance (see Eq. 1 in the paper). In the pulsar population study by the H.E.S.S. collaboration, the luminosity of HESS J1026–582 is given as $L_{1\text{-}10\,\mathrm{TeV}} = (1.7 \pm 0.5) \times 10^{33}\,\mathrm{erg/s}$ (see Tab. 4 in the paper) which, using the there assumed distance of 2.33 kpc, results in a total flux in the 1 to 10 TeV range of $(2.62 \pm 0.77) \times 10^{-12}\,\mathrm{erg/(cm^2\ s)}$. This is compatible with the $(2.92 \pm 0.41) \times 10^{-12}\,\mathrm{erg/(cm^2\ s)}$ calculated from the best-fit ePL spectrum presented in Sec. 5.5.1.3.

Fig. 6.2 shows the results with statistical errors for each criterion of the probed parameter sets for PSR J1028–5819. Grey shaded areas in the plots depict parameter ranges in which a criterion is fulfilled.

The results for the PWN star-rating shown in Fig. 6.2 show that for all parameter sets, the best-fit containment ratio (criterion 1) is lying outside the accepted parameter range. This confirms the results from [149] where HESS J1026–582 also does not fulfil criterion

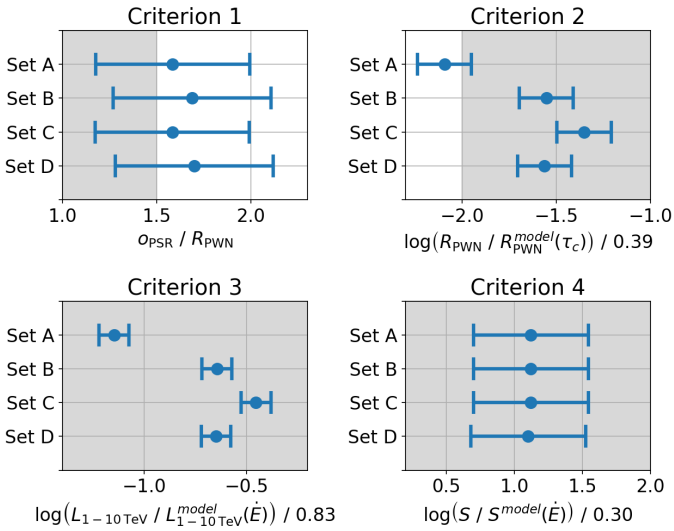

FIGURE 6.2: PWN star-rating parameters of HESS J1026–582 for the different sets of properties for PSR J1028–5819. The errors are propagated from the statistical uncertainties of the associated parameters from the spatial and spectral fits. Grey shaded areas depict parameter ranges in which a result fulfils a criterion.

1. Furthermore, the best-fit PWN extension ratio (criterion 2) of set A is not fulfilled. Nevertheless, all criteria are fulfilled within statistical errors for each set. Therefore, a PWN scenario for HESS J1026–582 can not be rejected.

As this is in agreement with the results of many other publications without favourable alternatives being suggested in the literature, the PWN scenario appears to be the most plausible explanation for the γ-ray source HESS J1026–582.

6.1.2 HESS J1023–575

For HESS J1023–575, a number of different scenarios have been proposed in the literature. As shown in Chap. 4, these range from a PWN over collective stellar winds to a hyper- or supernova and a microquasar. The PWN, SN and stellar wind scenarios are first discussed in the following for the source HESS J1023–575 alone. A discussion of the full compound of HESS J1023–575 and the TeV *jet* cloud in combination with the findings from CO and H I data analyses is given in Sec. 6.1.4.

6.1.2.1 HESS J1023–575 as a PWN

HESS-J1023–575 as a PWN presents a potential scenario regarding the number of pulsars found in the vicinity of the detected γ-ray signal. PSR J1023–5746, a highly energetic pulsar, is thereby the most prominent candidate as associated pulsar as it is located very close to the best-fit position of HESS J1023–575 with an angular separation of $\sim 0.025°$ (see also Fig. 5.47).

PSR J1023–5746 properties

Set	Gal. Pos. (l, b) [deg]	Distance d_{PSR} [kpc]	Char. Age τ_c [kyr]	Spindown $\dot{E}$ [10^{37} erg/s]	Ref.
A	$(284.166, -0.407)$	2.08	4.6	1.1	[147]
B	$(284.166, -0.407)$	8	4.6	1.1	[149]
C	$(284.166, -0.407)$	1.8^{*}	4.6	1.0955	[116]
D	$(284.17, -0.41)$	$4.5^{\dagger}$	$46^{\ddagger}$	1.1	[148]

TABLE 6.3: Different sets of PSR J1023–5746 properties taken from literature. The parameters in the first row are taken from the ATNF pulsar catalogue in version 1.63. *The distance of set C corresponds to the so called pseudo distance, see Eq. 2 in [116]. †The distance of set D is a "crude estimate [...] to be regarded with caution" [148]. ‡The age of set D looks suspicious compared to the other sets, it might be a typographical error in the Chandra pulsar survey. It should also be regarded with caution.

HESS J1023–575 as PWN associated with PSR J1023–5746

Set	Radius R_{PWN} [pc]	Offset o_{PSR}[pc]	Velocity v_{PSR} [km/s]	Luminosity $L_{1\text{-}10\,\mathrm{TeV}}$ [10^{33} erg/s]	Efficiency $\varepsilon_{\mathrm{TeV}}$ [%]
A	6.3 ± 0.3	0.9 ± 0.8	196 ± 170	4.18 ± 0.26	0.038 ± 0.002
B	24.3 ± 1.3	3.5 ± 3.1	752 ± 654	61.83 ± 3.88	0.562 ± 0.035
C	5.5 ± 0.3	0.8 ± 0.7	172 ± 147	3.13 ± 0.20	0.029 ± 0.002
D	13.7 ± 0.7	1.8 ± 1.7	38 ± 37	19.57 ± 1.23	0.178 ± 0.011

TABLE 6.4: PSR J1023–5746 parameters in connection with HESS J1023–575 as a PWN for the according sets given in Tab. 6.3.

As for the discussion of the PWN scenario for HESS J1026–582 in Sec. 6.1.1, multiple sets of parameters are found in the literature for the associated pulsar PSR J1023–5746. The here regarded sets of properties are given in Tab. 6.3. The resulting parameters characterising the potential PWN are given in Tab. 6.4 with errors being propagated from the statistical errors of the spectral and spatial fits. The radius of the PWN is thereby deduced from the Gaussian component for HESS J1023–575 from the 3D fit of the Westerlund 2 core region with model_B (using a Gaussian instead of a disk) whereas the luminosity is calculated by integrating the best-fit PL spectrum from the reflected regions analysis of HESS J1023–575 presented in Sec. 5.5.1.3.

Performing the PWN star-rating proposed in the H.E.S.S. PWN population study [149] (see Sec. 6.1.1 for details) results in all four rating criteria being fulfilled for all four sets of parameters, which is in agreement with the results on HESS J1023–575 from the PWN study itself. Figure 6.3 shows the parameters with accordingly propagated statistical errors and the allowed parameter ranges shown in grey. It should be noted that (as for HESS J1026–582) the luminosity is calculated differently than in the H.E.S.S. PWN population study. To cross-check the result, the flux calculated from the best-fit PL spectrum and the flux deduced in the H.E.S.S. publication can be compared. The best-fit PL spectrum predicts a flux in the 1 to 10 TeV range of $(8.08 \pm 0.51) \times 10^{-12}\,\mathrm{erg/(cm^2\ s)}$. This is in agreement with the $(8.75 \pm 0.65) \times 10^{-12}\,\mathrm{erg/(cm^2\ s)}$ calculated from the luminosity and distance given in the H.E.S.S. PWN population study [149].

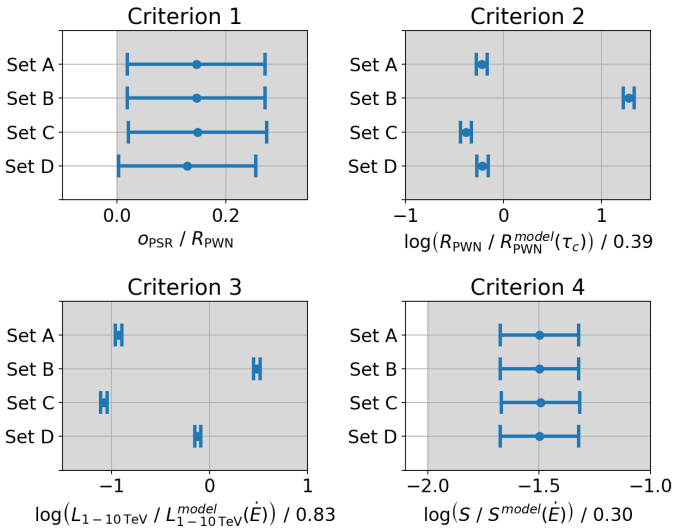

FIGURE 6.3: PWN star-rating parameters of HESS J1023–575 for the different sets of properties for PSR J1023–5746. The errors are propagated from the statistical uncertainties of the associated parameters from the spatial and spectral fits. Grey shaded areas depict parameter ranges in which a result fulfils a criterion.

The interpretation of the γ-ray emission from HESS J1023–575 as a PWN was previously stated as "unsettled" [3]. A PWN scenario can also not be ruled out on the basis of the criteria of the presented PWN star-rating. The PWN hypothesis is furthermore encouraged by several analyses of observations in other wavebands. A detailed Fermi-LAT analysis of the HE γ-ray emission at the position of HESS J1023–575 has been published in 2010 and found the off-pulse emission from the source around PSR J1023–5746 as a "highly plausible candidate" for a PWN [150]. Additionally, recent analyses of Chandra observations of the RCW 49/Westerlund 2 region published in 2019 have found diffuse X-ray emission around PSR J1023–5746 [131]. This supports the PWN hypothesis which is also favoured in the Chandra pulsar survey [148]. In summary, it can be said that multiple findings encourage the PWN scenario for HESS J1023–575, making this a viable explanation.

A point to note here is the potential source confusion suggested by the energy dependent morphology of HESS J1023–575 as outlined in Sec. 5.5.1.4. Assuming that only a part of the detected γ-ray emission originates from a PWN, the flux has to be reduced accordingly. By assuming that the potential PWN dominates in the low to medium energy range up to $\sim 8\,\mathrm{TeV}$, one can subtract the flux predicted by the best-fit spectrum $> 8\,\mathrm{TeV}$ from the flux of the best-fit spectrum $< 8\,\mathrm{TeV}$ to obtain the contribution of the potential PWN. Doing so yields a total flux in the $1-10\,\mathrm{TeV}$ range for the PWN of $(5.55 \pm 2.50) \times 10^{-12}\,\mathrm{erg/(cm^2 s)}$. The flux shows a rather large error due to the large errors of the best-fit model $> 8\,\mathrm{TeV}$, but it results in all four star rating criteria to be fulfilled within statistical errors. Therefore, even taking source confusion into account does not allow to reject the PWN hypothesis.

6.1.2.2 HESS J1023–575 associated with a SNR and molecular clouds

Apart from finding diffuse X-ray emission around PSR J1023–5746, the study presented in [131] also reports hard diffuse X-ray emission around PSR J1023–5746 and its potential PWN, which "may trace a cavity SNR" as the authors outline. The distance of the pulsar is thereby assumed to be the same as for RCW 49, which is stated as 4.21 kpc. Another indication of SN activity might be given by the structure seen in H I and CO data, where the *arc* cloud and H I shell in combination form a shell-like structure (hereafter referred to as "hydrogen shell") that surrounds HESS J1023–575 as investigated in detail in Sec. 5.6.3. A SN explosion is also stated as "an obvious explanation" for the *arc* cloud in [3]. Analyses of X-ray data of the Westerlund 2 region taken by the Suzaku satellite support the SN scenario even further. The analysis shows spectra with an overabundance of α elements, which may suggest SN related activities [130]. The authors propose that the potential SN progenitor could have been associated with Westerlund 2. Regarding the relatively low age and high masses of stars in the Westerlund 2 cluster, even a hypernova that occurred $\sim 10^5$ to 10^6 yr ago is suggested by the authors. This would however disqualify an association with PSR J1023–5746, as the characteristic age of the pulsar with 4.6 kyr is two to three orders of magnitude smaller. In [3], the authors probe the SN scenario by calculating the radius and swept-up mass of a SNR with an analytical model for SNR evolution (see App. B in [3]) for different sets of initial conditions, and compare the results with the projected radius and estimated mass of the shell. The authors find combinations of ISM density and initial explosion energy that could explain the observations for the assumed distance of 7.5 kpc and a shell mass of $\sim 5 \times 10^5\,\mathrm{M}_\odot$. Nevertheless, the authors further outline that the discrepancy of measured H I to CO column density disfavours the SN scenario [3] as it "is questionable if the shell can expand to a similar radius for such density contrast".

In the following, the SN scenario is investigated. The SNR shell is thereby assumed to be the hydrogen shell as described in Sec. 5.6.3. Adopting the hypothesis from the Suzaku publication [130] (association to Westerlund 2, SN explosion 10^5 to 10^6 yr ago) puts constraints on the distance and age of the SNR. The distance of the hydrogen shell is determined in Sec. 5.6.3 as $\sim (6.6 \pm 1.1)$ kpc. For an association with Westerlund 2, the lower bound of 5.5 kpc is therefore assumed for the distance. Taking the outer radius of the hydrogen shell as the outer edge of the blast shock-wave yields a radius of $r_o \sim 43$ pc. As the shell does not appear to be expanding (as shown by the velocity distribution of the *arc* cloud) [3], it is assumed that the SNR has reached the dissipation phase where the shock wave merges with the ISM. Additionally, the according total mass of the hydrogen shell of $\sim 8.6 \times 10^4\,\mathrm{M}_\odot$ is assumed to be gas that was swept up by the shock wave from its environment. Summing up, conditions are needed that yield a SNR that merges with the ISM after $\sim 10^5$ to 10^6 yr at a radius of ~ 43 pc. Additionally, the environment of the SN progenitor has to have a density of $\sim 10\,\mathrm{cm}^{-3}$ to explain a swept-up mass of $\sim 8.6 \times 10^4\,\mathrm{M}_\odot$.

To find such a set up, the open source tool `SNRPy` can be used to model the evolution of SNRs under different conditions for multiple evolutionary models [151, 152]. It is available on github[2] and is used here in version 2.0. The software provides a very wide range of customisable parameters for the different SNR models. For example, for the SN explosion itself, the ejected mass, element abundances in the ejecta and the initial explosion energy can be set. For the ISM, parameters like temperature, density, element abundances and turbulence can be adjusted. Using the *standard* SNR evolution model provided in `SNRPy`, and using default parameters except for an initial explosion energy of $\sim 5 \times 10^{51}$ erg, an ISM density of $10\,\mathrm{cm}^{-3}$ and an ejected mass of $5\,M_\odot$ yields a SNR that merges with the ISM after $\sim 8.8 \times 10^5$ yr with a radius of 42.6 pc, thus fulfilling the requirements of the observed hydrogen shell. Figure 6.4 shows the evolution of the blast shock wave and the reverse shock in this set up, with the transition between the ejecta dominated (ED) phase, the Sedov-Taylor (ST) phase and the pressure driven snowplough (PDS) phase marked by vertical lines (see [151] for a detailed explanation of the phases). To end up with a similar SNR using the so called *cloudy ISM* model, in which the environment of the SN does not have a uniform density distribution, the explosion energy has to be increased to $\sim 1 \times 10^{52}$ erg. The explosion energies needed to explain the observations in both models are higher than the commonly assumed 1×10^{51} erg for an average SN, but agree with the possibility of a very massive star exploding in the form of a hypernova which can have explosion energies exceeding 1×10^{52} erg [153].

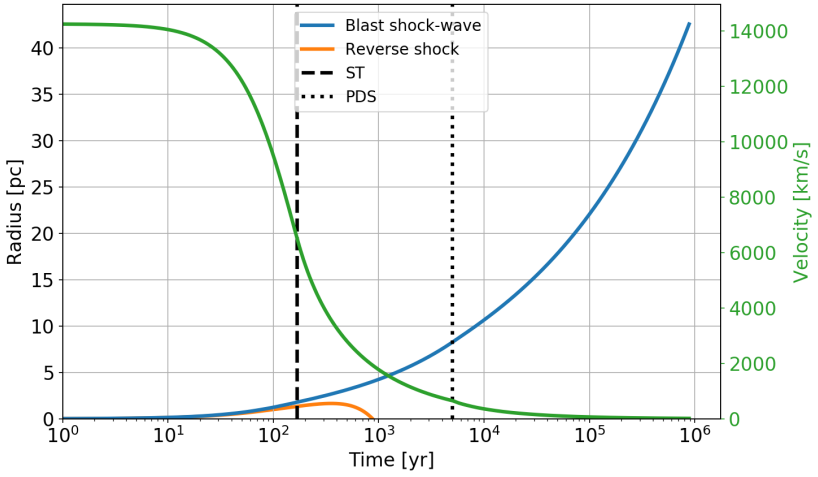

FIGURE 6.4: Radius (blue, left y-axis) and velocity (green, right y-axis) evolution of the forward shock wave for a supernova with an explosion energy of 5×10^{51} erg in an environment with a density of $10\,\mathrm{cm}^{-3}$ and an ejected mass of $5\,M_\odot$. The radius of the reverse shock is shown in orange. The dotted and dashed lines mark the transitions between evolutionary phases.

The hydrogen shell thus agrees with the hypothesis of SN activity. The open question is if the detected γ-ray emission of HESS J1023–575 can originate from this SNR shell. The main difference to other SNRs detected at TeV energies is the age of the remnant. The

[2] `https://github.com/denisleahy/SNRmodels`, accessed 01.05.2020

currently eight firmly identified shell-type SNRs detected in the H.E.S.S. Galactic plane scan [121] for example have ages in the kyr range [154]. The age of the regarded hydrogen shell is around two to three orders of magnitude higher. The shell is no longer expanding with no active shock acceleration to be expected. Therefore, the processes that produce the γ-ray emission in younger SNRs should no longer be active. As outlined in a review on SNRs at high energies by Reynolds [19], after $\sim 1.5 - 1.9$ times the transition time to the radiative or pressure driven snowplough phase t_{PDS} (marked by the dotted horizontal line in Fig. 6.4), a cold and dense shell of gas is formed. After $(2-3)t_{\mathrm{PDS}}$, the shock velocity has dropped to ~ 100 to 300 km/s, with which the velocity of the blast shock wave is too low to accelerate particles high enough to produce keV to TeV photons. For the modelled evolution of the SNR shown in Fig. 6.4, this means that TeV γ-ray production would be expected to stop at an age of $\lesssim 1.5 \times 10^4$ yr. The SNR shell can therefore be regarded as a molecular cloud.

Molecular clouds can however act as targets for CRs and can thereby emit γ radiation in hadronic emission scenarios via π^0 decay (as outlined in Sec. 2.1.2.2). For clouds with masses above a certain threshold, the interaction with the Galactic background of CRs is enough to produce TeV emission. Such clouds are referred to as passive molecular clouds. The expected γ-ray flux of a molecular cloud with mass M at distance d can be expressed as

$$F_\gamma(> E_\gamma) \approx 2 \times 10^{-13} \delta \left(\frac{M_5}{d^2_{\mathrm{kpc}}} \right) \left(\frac{E_\gamma}{\mathrm{TeV}} \right)^{-1.7} \mathrm{cm}^{-2}\mathrm{s}^{-1} \tag{6.1}$$

as outlined in [155], with $M_5 = (M/10^5 M_\odot)$ and $d_{\mathrm{kpc}} = (d/\mathrm{kpc})$. The factor δ thereby quantifies the enhancement or overdensity of CRs compared to the Galactic background radiation observed around the Sun. To detect a typical molecular cloud at TeV energies with IACTs like the H.E.S.S. telescopes, either the mass of the cloud has to be far greater than $10^5\, M_\odot$ or the CR density has to be enhanced by $\delta > 10$ [155].

The total mass of the hydrogen shell as determined in this work is $M \sim 8.6 \times 10^4\, \mathrm{M}_\odot$ at a distance of $d = 5.5$ kpc. Calculating the total γ-ray flux in the region of the hydrogen shell from the extracted spectral flux points[3] (as shown in the upper panel of Fig. 5.32) yields $F_\gamma(> 1\,\mathrm{TeV}) \sim (2.41 \pm 0.46) \times 10^{-12}\,\mathrm{cm}^{-2}\mathrm{s}^{-1}$. Putting all this together into Eq. 6.1 gives a CR overdensity of $\delta \sim 468 \pm 89$. Such high values for the cosmic ray enhancement factor are not uncommon, as for example seen in an analysis of HESS J1714–385 presented in [156], where cosmic ray enhancement factors > 1000 are reported.

Contrasting to the expression given in Eq. 6.1, according to [157], the expected γ-ray flux for energies $E_\gamma > 1$ TeV is

[3] See `https://docs.gammapy.org/dev/api/gammapy.estimators.FluxPointsEstimator.html` for details on flux point estimation (accessed 27.05.2020).

$$F_\gamma(> E_\gamma) \approx 2.85 \times 10^{-13} \delta \left(\frac{M_5}{d^2_{\mathrm{kpc}}} \right) \left(\frac{E_\gamma}{\mathrm{TeV}} \right)^{-1.6} \mathrm{cm}^{-2}\mathrm{s}^{-1} \ . \tag{6.2}$$

Using this expression instead of Eq. 6.1 yields $\delta \sim 326 \pm 62$. The difference in δ values resulting from Eq. 6.1 and Eq. 6.2 shows that different approaches to estimate the cosmic ray enhancement factor can yield quite different results. Thus, the values stated for δ should be regarded with caution as they incorporate a number of assumptions about the diffusion coefficient and source of CRs. Yet another expression to estimate δ from $F_\gamma(> E_\gamma)$ incorporating the assumed spectral index of the incident CRs is for example given in [158] (see Eq. 2.5 in the publication). Another assumption in the presented approach that influences the cosmic ray enhancement factor is that the full amount of gas is expected to be acting as target material, which is not necessarily true. Furthermore, the mass of the cloud could be higher when taking dark gas components into account, which would result in lower δ factors. However, it can be assumed that a cosmic ray enhancement factor of $\delta > 100$ in general suggests that some CR acceleration process is driving the emission of the hydrogen shell at TeV energies. The cosmic ray enhancement factor can furthermore be regarded as independent of the assumed cloud distance, as also the mass of the cloud increases with larger distances. Therefore, taking the upper bound of the estimated cloud distances of 7.7 kpc does not rule out a hadronic emission scenario for HESS J1023–575 in connection with the hydrogen shell. This would however be in conflict with an association to the stellar cluster Westerlund 2.

If HESS J1023–575 is associated with the hydrogen shell with an assumed outer radius of $r_o \sim 43\,\mathrm{pc}$, mass $M = 8.6 \times 10^4\, M_\odot$ and distance $d = 5.5\,\mathrm{kpc}$, the best-fit model from the 3D fit predicts a luminosity in the $1 - 10\,\mathrm{TeV}$ range of $L_\gamma(1 - 10\mathrm{TeV}) \approx (3.05 \pm 0.24) \times 10^{34}\,\mathrm{erg/s}$. Following [159] and [3], the energy in protons needed to produce this γ-ray luminosity can be estimated as

$$W_\mathrm{p}(10 - 100\,\mathrm{TeV}) = L_\gamma(1 - 10\mathrm{TeV}) \cdot t_\mathrm{pp} \tag{6.3}$$

where t_pp is the cooling time of the CR protons by interaction with a gas of number density n_gas. The cooling time is given by

$$t_\mathrm{pp} = \frac{1}{n_\mathrm{gas} c \kappa \sigma_\mathrm{pp}} \approx 6 \times 10^5 \left(\frac{n_\mathrm{gas}}{100\,\mathrm{cm}^{-3}} \right)^{-1} \mathrm{yr} \ . \tag{6.4}$$

The parameter κ thereby gives the inelasticity and σ_pp the cross-section of the proton-proton interaction. For the hydrogen shell with $n_\mathrm{gas} = 278\,\mathrm{cm}^{-3}$ as given in Tab. 5.19, this results in $t_\mathrm{pp} \sim 2.16 \times 10^5\,\mathrm{yr}$ and thus $W_\mathrm{p}(10 - 100\,\mathrm{TeV}) \sim (2.08 \pm 0.16) \times 10^{47}\,\mathrm{erg}$. The SN explosion that may have formed the hydrogen shell with an initial explosion energy of $> 10^{51}\,\mathrm{erg}$ would thus provide sufficient energy to explain the TeV emission. To

probe if the CRs produced in the SN can still be present in the region of the hydrogen shell, one can calculate the time t_{prop} which protons would need to propagate through the cloud from the centre of the shell. According to [159] this propagation time for relativistic protons with energies $> 1\,\mathrm{GeV}$ can be approximated by the sum of the diffusion time t_{diff} and crossing time t_{cross} of a proton in the cloud. While t_{cross} only depends on the distance r a proton travels through the cloud and the speed of light c, the diffusion time depends on r and the diffusion coefficient D inside the cloud. This diffusion coefficient D depends on the energy of the proton E_{p}, the magnetic field in the cloud B and a factor χ which describes the deviation of the diffusion coefficient to the galactic average. It is given as

$$D(E_{\mathrm{p}}, B) = \chi \times 10^{28} \left(\frac{E_{\mathrm{p}}}{10\,\mathrm{GeV}}\right)^{0.5} \left(\frac{B}{3\,\mu\mathrm{G}}\right)^{-0.5} \mathrm{cm^2 s^{-1}} \ . \tag{6.5}$$

The propagation time is then approximated as

$$t_{\mathrm{prop}} \approx t_{\mathrm{diff}} + t_{\mathrm{cross}} = \frac{r^2}{6D(E,B)} + \frac{r}{c} \ . \tag{6.6}$$

Taking into account that the gas of density n_{gas} is only present within the shell of inner and outer radius r_i and r_o and thus width $w_s = r_{\mathrm{o}} - r_{\mathrm{i}}$ (and assuming a gas of negligible density inside the shell), the propagation time for a proton in the hydrogen shell is

$$t_{\mathrm{prop}} \approx \frac{w_s^2}{6D(E,B)} + \frac{r_o}{c} \ . \tag{6.7}$$

Following [160], the magnetic field strength B_0 in a molecular cloud can be expressed as

$$B_0 = 1.4 \times \beta^{-0.5} \left(\frac{T}{10\,\mathrm{K}}\right)^{0.5} \left(\frac{n_{\mathrm{gas}}}{100\,\mathrm{cm^{-3}}}\right)^{0.5} \mu\mathrm{G} \tag{6.8}$$

where β characterises the initial magnetic field strength (*weak*, *moderate* and *strong* magnetic field modelled with $\beta = 0.01$, 0.1 and 1 respectively) and T is the temperature of the cloud. According to [3], the *arc* cloud shows temperatures of $T \sim 10\,\mathrm{K}$. Together with the density of $n_{\mathrm{gas}} = 278\,\mathrm{cm^{-3}}$ this yields $B_0 \sim 2.3, 7.4$ and $23.3\,\mu\mathrm{G}$ for a weak, moderate and strong initial magnetic field. Putting this B_0 and $\chi = 0.01$ (for example due to magnetic turbulence caused by a SN explosion [3]) into Eq. 6.7 results in propagation times for a 10 TeV proton of $t_{\mathrm{prop}} \sim (1-3) \times 10^4\,\mathrm{yr}$, which is around one to two orders of magnitude smaller than the assumed age of the SNR of $10^5 - 10^6\,\mathrm{yr}$. This means that the CRs that were accelerated in the SN (with particle acceleration up to an age of $\sim 1.5 \times 10^4\,\mathrm{yr}$) should have escaped the shell after at least $\sim 4.5 \times 10^4\,\mathrm{yr}$. The only remaining explanation for a hadronic emission scenario of the hydrogen shell is a more or less continuous injection of CRs, at least over the past $\sim 10^4\,\mathrm{yr}$. Assuming that the total

energy $W_{\mathrm{p}}(10 - 100\,\mathrm{TeV}) \sim (2.08 \pm 0.16) \times 10^{47}\,\mathrm{erg}$ is continuously injected over the past t_{prop} yields an average power injected into CRs of up to $(7.05 \pm 0.55) \times 10^{35}\,\mathrm{erg/s}$ in CR production for a weak magnetic field and $(2.25 \pm 0.18) \times 10^{35}\,\mathrm{erg/s}$ for a strong magnetic field. One object that could be the stellar remnant of a SN explosion and provide enough energy is a microquasar, as suggested in [3]. The microquasar scenario is further discussed in Sec. 6.1.3 and 6.1.4.

In general, a hadronic scenario for HESS J1023–575 seems to be likely, if the detected γ-ray emission is associated with the molecular clouds in the region. The high photon energies of $> 80\,\mathrm{TeV}$ and the spectral shape with an index of ~ 2.4 also support a hadronic emission scenario as outlined in [155]. Additionally, analyses of data from IceCube and ANTARES show HESS J1023–575 as a source candidate for neutrinos [132], which encourages a hadronic emission scenario even further.

6.1.2.3 HESS J1023–575 and stellar winds

Due to the large number of stars, including very massive and hot stars in the region of HESS J1023–575 as shown in Fig. 5.45, emission scenarios connected to stellar winds provide a possible explanation for the observed γ-ray signal. Most stars continuously eject material from their outer layers via so called stellar winds. Depending on the properties of a star like mass and age, the processes driving its stellar winds and the rate $\dot{M}$ at which mass is ejected can vary strongly. Material can be driven away from the star by thermal or radiative pressure and stellar magnetic fields can interact with these winds and accelerate charged particles. After $\mathcal{O}(10^5)\,\mathrm{yr}$, stellar winds can form bubbles or cavities in the ISM with radii of up to tens of parsec [161]. For massive stars in binary systems, the winds of the two companions are thought to interact in collisions and accelerate particles up to multi-TeV energies via diffusive shock acceleration. A brief review on γ-ray production in massive colliding wind binaries can be found in [162] with more detailed studies in the references therein. In certain environments such as star clusters where stars are in close proximity to each other, individual star winds can combine to form so called collective stellar winds. The acceleration processes in collective stellar winds are expected to produce large-scale shocks where particles are accelerated up to very high energies (see for example [161, 163]).

Interpreting HESS J1023–575 in terms of stellar wind scenarios has been proposed in the past [110, 128, 164]. Especially due to the initial lack of other associations in this region of the sky, stellar winds and the CR acceleration in stellar clusters offered an exciting type of γ-ray source when the first γ-ray emission was detected around Westerlund 2. In more recent publications, the general prospects of star clusters as sources of galactic CRs has been addressed [165], including the case of Westerlund 2 [166]. A detailed presentation of such a study on Westerlund 2 is given in [120]. Here, Yang et al. study the potential CR distribution in a large region around Westerlund 2. The basis of the study are H I, H II

and CO observations and the large-scale extended GeV γ-ray source FGES J1036.4–5834 which can be described by a disk with a $\sim 2.4^\circ$ radius. The authors propose a hadronic emission scenario where CRs from Westerlund 2 interact with the ambient gas. A leptonic origin is theoretically possible but discouraged, as in this case, the extension of the γ-ray source would be expected to be limited to the extension of the stellar cluster itself. The radial CR distribution shows a $1/r$ dependency (where r is the distance from the cluster) which, according to the authors, can be explained by a continuous injection of CRs.

The H.E.S.S. data presented in this thesis covers a relatively small region of the sky which only contains a fraction of the extended Fermi-LAT source (as seen in Fig. 6.6 where FGES J1036.4–5834 is shown as a hatched circle). Also, the source FGES J1023.3–574, which is associated with HESS J1023–575, is not regarded in the context of γ-ray emission from Westerlund 2 in the publication [120]. The authors present a pulsar gating analysis to separate pulsed and unpulsed γ-ray emission in the region. This shows a periodic signal from FGES J1023.3–574 and yields "that the extrapolation of the low energy emission is significantly below the flux of HESS J1023–575". The authors propose that the HE emission may originate from a pulsar, whereas the VHE emission comes from the associated PWN. As discussed in Sec. 6.1.2.1, a PWN scenario can not be excluded for the emission of HESS J1023–575, whereas the striking coincidence of the γ-ray signal with the shell-like cloud of atomic and molecular hydrogen (as presented in Sec. 5.6.3 and 6.1.2.2) proposes hadronic CR interactions. The presence of multiple coincident source components is therefore a viable option. It would be possible that the pulsar PSR J1023–5746 and its PWN lie at a different distance along the line of sight towards Westerlund 2 and are not physically associated with the hydrogen shell. The gas of the hydrogen shell could however still act as target for CRs and emit TeV γ radiation. The CRs could thereby also be provided by stellar winds originating from the stars of Westerlund 2. The calculations presented in Sec. 6.1.2.2 yield a continuous power injection of $\sim 10^{35}$ erg/s to explain the total γ-ray luminosity of HESS J1023–575 in the context of illuminated clouds of gas. The kinetic wind energy of the binary system WR 20a embedded in Westerlund 2 is estimated to be $\sim 10^{37}$ erg/s [110], thus providing enough power on its own to potentially explain the observed γ emission, especially, if one takes into account that HESS J1023–575 might be a superposition of multiple γ-ray sources with only a fraction of the detected flux originating from stellar winds. Due to the extension of HESS J1023–575, it is however unlikely that a single star or binary system can be the origin of the detected γ-ray signal [110]. Collective stellar winds on the other hand could be able to explain the extension of the source [110] and provide more than enough kinetic wind energy to power the observed VHE emission.

6.1.3 The *jet* cloud

The spatial coincidence of γ-ray emission with the *jet* cloud in CO and H I data suggests a connection between the TeV and the radio signal. Following the idea of a hadronic origin

of the TeV emission in which CRs are interacting with the dense gas of an atomic or molecular cloud, one can calculate the cosmic ray enhancement factor for the *jet* cloud as done for HESS J1023–575 in Sec. 6.1.2.2. The TeV *jet* cloud shows a flux of $F_\gamma(> 1\,\mathrm{TeV}) \sim (3.8 \pm 1.4) \times 10^{-13}\,\mathrm{cm}^{-2}\mathrm{s}^{-1}$. Using Eq. 6.2 and assuming a distance of 5.5 kpc and the according mass for the *jet* cloud of $\sim 2.90 \times 10^4\,M_\odot$ (see Tab. 5.18) yields a cosmic ray enhancement factor of $\delta \sim 153 \pm 56$. This shows that the *jet* cloud is likely not a passive cloud and that particle acceleration takes place in its vicinity. Following the analysis of HESS J1023–575 presented in Sec. 6.1.2.2, one can calculate the cooling and propagation time of protons in the *jet* cloud[4]. Using Eq. 6.4 with the density of $\sim 53\,\mathrm{cm}^{-3}$ from Tab. 5.19 yields a cooling time for protons in the *jet* cloud of $t_{\mathrm{pp}} \sim 1.1 \times 10^6\,\mathrm{yr}$. With a luminosity of $L_\gamma(1-10\,\mathrm{TeV}) \sim (6.0 \pm 0.9) \times 10^{33}\,\mathrm{erg/s}$ for the *jet* cloud and using Eq. 6.3, this results in a total energy in protons of $W_\mathrm{p}(10 - 100\,\mathrm{TeV}) \sim (2.2 \pm 0.3) \times 10^{47}\,\mathrm{erg}$. Assuming a temperature of $\sim 20\,\mathrm{K}$ as suggested in [3] and using Eq. 6.8 yields a magnetic field within the region of the TeV *jet* cloud between 1.4 and 14.4 μG for a weak to strong initial magnetic field. Adapting Eq. 6.4 for a 10 TeV proton travelling along the major axis of the *jet* cloud (as sketched in Fig. 6.1, $2d_0$ which is $\sim 60\,\mathrm{pc}$ at a distance of 5.5 kpc) results in t_{prop} between $\sim$ 1.3 and $4.0 \times 10^5\,\mathrm{yr}$. This suggests that a 10 TeV proton injected into the TeV *jet* cloud can escape it before it looses its energy due to hadronic interactions. If the deduced energy in protons W_p is provided over the propagation time along the major axis of the elliptical TeV *jet* cloud, the source must have a power of $\sim (5.4 \pm 0.8) \times 10^{34}\,\mathrm{erg/s}$. A source that could provide such power would for example be the jets of a microquasar like SS 433, which can provide up to $\sim 10^{39}\,\mathrm{erg/s}$ [167]. The microquasar scenario is further discussed in the following Sec. 6.1.4.

6.1.4 The *arc* and *jet* cloud in combination with HESS J1023–575 - a microquasar?

A clear connection between HESS J1023–575, the *arc* cloud together with the detected H I shell and the *jet* cloud with its newly detected potential TeV counterpart is not yet established. The symmetry and spatial agreement of the TeV and the radio signals however suggest a common origin. Figure 6.1 shows a simplified sketch of the geometry of the detected signals. The main geometric traits are:

- The γ-ray emission of HESS J1023–575 is coincident with shell-like cloud structures. The TeV signal thereby appears to be surrounded by a hydrogen shell, which consists of the H I shell and the complementing CO *arc* cloud.

[4]It should be noted that the *jet* cloud is hereby reduced to gas in the region where γ-ray emission is detected. The signal seen in H I and CO data extends beyond the boundaries of the elliptical TeV source as sketched in Fig. 6.1. Masses and densities from the extensive CO and H I analyses presented in [3] are therefore different.

- The elliptical TeV *jet* cloud coincides with large parts of the elongated *jet* cloud seen in H I and CO data. Furthermore, the major axis of the TeV *jet* cloud aligns with the best-fit axis of the detected CO signal.
- The best-fit position of HESS J1023–575 lies very close to the major axis of the *jet* cloud. The *arc* cloud is also aligned symmetrically to the major axis of the TeV *jet* cloud.

In general it can be said that the morphology of the observed structures in radio and γ-ray data appears to be symmetrical to the major axis of the TeV *jet* cloud. As discussed in Sec. 5.6.3.5, the *arc* cloud seems to be oriented more or less perpendicular to the line of sight towards the observed region. As outlined in [3], a shorter "counter *jet* cloud" is found within the *arc* cloud, which is also aligned along the major axis of the TeV *jet* cloud. This suggests the major axis of the *jet* cloud itself to be oriented roughly perpendicular to the observer's line of sight.

A detailed investigation of the *arc* and *jet* cloud in combination with the TeV γ-ray signal presented in the 2011 H.E.S.S. publication on Westerlund 2 [2] was presented by Furukawa et al. in 2014 [3]. A complementing MHD simulation study was published in 2017 [142]. The authors of [3] argue that a "SNR or a PWN is not likely as the origin for HESS J1023–575, if the jet and arc clouds and HESS J1023–575 are due to a single object". Alternatively, they present CRs from a microquasar jet or from an anisotropic SN explosion with a microquasar jet from the stellar remnant which interacts with the ISM as "the only remaining possible candidate". A microquasar is not known to exist in the vicinity of HESS J1023–575, whereas the observed "strong and complicated" radio emission towards RCW 49 may aggravate its detection [3]. The studies presented in [142] aim to explain the formation of the *arc* and *jet* cloud detected in CO data. Three dimensional MHD simulations are applied to model the interaction of a high energy jet with an ISM of different and varying densities. The results show that molecular clouds of comparable size and shape like the observed *arc* and *jet* cloud can be formed by a high energy jet that interacts with the ISM over several 10^6 yr.

On the basis of the findings from this work at hand, the microquasar scenario provides the most comprehensive explanation for multiple of the discussed aspects. A very massive star, potentially originating from RCW 49 or Westerlund 2, may have exploded $> 10^5$ yr ago in a fairly dense ISM, which resulted in the observed hydrogen shell at the last stage of the SNR's evolution. The CRs accelerated in this SN and in the following expansion of the SNR have already cooled or escaped the region. The stellar remnant at the centre of the hydrogen shell could be an undetected microquasar, which continuously injects CRs into its environment. These CRs interact with the hydrogen shell and produce TeV γ-rays. The jets of this microquasar interact with the ISM along the jet axis. To the north west of HESS J1023–575, the jet interacts with a rather dense ISM, forming the molecular *arc* cloud. To the south east of HESS J1023–575, the jet interacts with an ISM of lower

density, driving out molecular gas along the jet axis as outlined in [142]. VHE emission at energies $\gtrsim 25\,\mathrm{TeV}$ has been found from the jets of a microquasar with the HAWC experiment, as reported in 2018 for the microquasar SS 433 [33]. This discovery has motivated many further studies like searches for GeV counterparts to the TeV emission [168] and multi wavelength modelling studies [167]. SS 433 is a very complicated object, as it is located in the expanding SNR shell W 50 with multiple dense molecular clouds in its environment. The SN explosion that formed W 50 took place $\mathcal{O}(10^4)\,\mathrm{yr}$ ago, which would make the SS 433/W 50 system a somewhat younger version of HESS J1023–575 and the TeV *jet* cloud. Nevertheless, the wide range of possible conditions in which such a system can evolve limits the comparability of these two systems.

Overall, a microquasar scenario offers many explanations for the observed emission in the Westerlund 2 region. However, further multi wavelength data and a detailed modelling of the system are essential to draw further conclusions.

6.1.5 γ-Ray emission from WR 21a?

As pointed out in Sec. 5.6.1, a lobe can be seen in the TeV emission of HESS J1023–575 towards the north east of Westerlund 2 that coincides with WR 21a (see Fig. 5.45). This lobe could be part of the extended emission of HESS J1023–575, but it could also be an individual source (even though with a high chance of contamination from HESS J1023–575). WR 21a is a binary system of an O and a WR star with masses of $\sim 58\,M_\odot$ and $\sim 104\,M_\odot$ respectively, which might have been ejected from the Westerlund 2 star cluster [169]. Its distance is however not well constrained as for many objects in this region. It is detected in X-rays [170] and has in the past been proposed to be associated with the γ-ray emission detected in the Westerlund 2 region [171]. γ-Ray emission from colliding wind binaries has been proposed in the past [172] and has been detected for example from the colliding wind binary η Car with the recent detection of VHE emission up to $\sim 400\,\mathrm{GeV}$ with the H.E.S.S. experiment [173].

As outlined in [174], around $0.1\% - 10\%$ of the kinetic wind power of a colliding wind binary goes into the interaction of the stellar winds. From there, $\sim 1\% - 10\%$ of the power budget are converted to accelerated particles of which $\sim 90\% - 99\%$ go to hadron acceleration and $\sim 1\% - 10\%$ to lepton acceleration. For WR 21a, a kinetic wind power of $2.0 \times 10^{37}\,\mathrm{erg/s}$ can be found in the literature [174] for an assumed distance of 3 kpc (see Tab. A.5 in [174]). At 5.5 kpc this corresponds to $6.7 \times 10^{37}\,\mathrm{erg/s}$. This suggests a power of around $6.1 \times 10^{32}\,\mathrm{erg/s}$ to $6.7 \times 10^{35}\,\mathrm{erg/s}$ in accelerated hadrons and $6.7 \times 10^{30}\,\mathrm{erg/s}$ to $6.7 \times 10^{34}\,\mathrm{erg/s}$ in accelerated leptons. Taking the best-fit PL model from the results of the reflected regions analysis presented in Sec. 5.6.1 and assuming a distance for WR 21a of 5.5 kpc (to be compatible with Westerlund 2) results in a luminosity in the $1 - 10\,\mathrm{TeV}$ range of $\sim (2.2 \pm 0.5) \times 10^{33}\,\mathrm{erg/s}$, which should be regarded as an upper limit accounting for a contamination from HESS J1023–575. The observed luminosity would thus be

compatible with a hadronic emission scenario in which $\sim 1\%$ of the energy in accelerated protons from WR 21a is converted to γ-rays.

The lobe of detected γ-ray emission around WR 21a is a striking hint towards TeV emission from a colliding wind binary and should be investigated more thoroughly in future studies. A detailed 3D analysis with variability studies and a combination with multi wavelength data may yield more insights.

6.2 Diffuse emission in the Westerlund 2 region

As mentioned above, a large-scale diffuse HE emission could be found in the Westerlund 2 region in Fermi-LAT data [119, 120]. This large-scale extended source FGES J1036.4–5834 is best described by a uniform disk with a radius of $\sim 2.4^\circ$ centred on the galactic position ($l = 286.053^\circ, b = -0.125^\circ$) [120]. The best-fit spectrum from 0.3 to 250 GeV is a PL with an index of ~ 2.0 with a total flux above 1 GeV of $\sim 4.2 \times 10^{-8}\,\mathrm{cm^{-2}s^{-1}}$. The spectral properties of the potentially diffuse emission seen in this work at hand can not be extracted due to limited statistics and no appropriate background region. A more detailed analysis is therefore needed with a dataset that covers a larger field of view. Nevertheless, the morphology of the extended emission can be investigated.

In Sec. 5.4.1, the hint of a diffuse emission in the presented VHE dataset is obtained with a spatially binned reflected regions analysis, where multiple bins around the known TeV sources show significances $> 5\sigma$ as seen in Fig. 5.14. To reduce fluctuations and to get a more general view of the spatial distribution of the emission, this map is convolved with a disk kernel of 0.2° radius. This convolved map, saturated to 8σ significance, is shown in Fig. 6.5 where it is overlayed with the $2, 4$ and 6σ significance contours from the ring background analysis. Furthermore, the extended Fermi-LAT source is depicted with a hatched disk. It can be seen that the extended Fermi-LAT source covers the complete Westerlund 2 core region and the major part of bins with significances $> 3\sigma$. A large part of the potentially diffuse TeV emission observed in this work is thus coincident with the diffuse emission detected in Fermi-LAT data.

A sky map showing the γ-ray emission in the Carina region above 100 MeV as seen in AGILE data [175] (see Fig. 2 in the publication) reveals the large scale structures and complexity of the HE emission in the region. For the following investigation, a total of ~ 11 yr of AGILE data of the Westerlund 2 region in the range from 100 MeV to 50 GeV is obtained via the AGILE Data Center[5]. The photon counts are provided as sky maps with a binning of $0.25^\circ \times 0.25^\circ$ in fits format. Figure 6.6 shows a 30° wide skymap of the count data in galactic coordinates of the Carina region correlated with a Gaussian kernel of 0.25° width. The Fermi-LAT source FGES J1036.4–5834 is shown as a hatched disk

[5] AGILE Data Center website: `https://agile.ssdc.asi.it/`; Interactive mission archive: `https://www.ssdc.asi.it/mmia/index.php?mission=agilelv3mmia`; Search query: *Westerlund 2*; (accessed 05.06.2020)

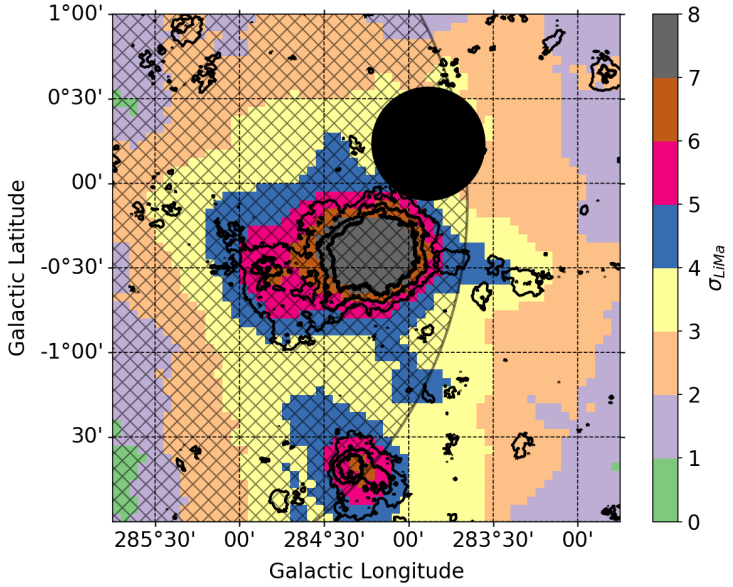

FIGURE 6.5: Saturated significance map obtained from a spatial reflected regions analysis. The LiMa significance is calculated for each $0.05° \times 0.05°$ bin and the map is then convolved with a disk kernel of $0.2°$ radius to reduce fluctuations. The black disk covers bins where the reflected regions method can not be applied due to limited statistics caused by the exclusion regions. The $2, 4$ and 6σ contours from the ring background analysis are shown in black. The area covered by the extended Fermi-LAT source FGES J1036.4–5834 is depicted by the hatched disk.

with the outlines of the three TeV sources found in the Westerlund 2 core region shown in green.

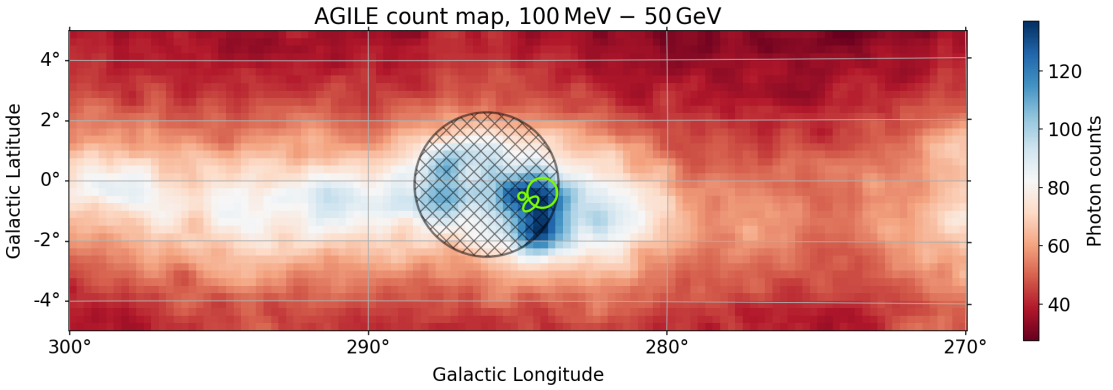

FIGURE 6.6: Photon counts from $\sim 11\,\mathrm{yr}$ of AGILE data taken between 2007 and 2019 of the Carina region. The count data is correlated with a Gaussian of $0.25°$ width. The diffuse emission in the form of the disk-like extended source FGES J1036.4–5834 detected by Fermi-LAT is shown as a hatched circle. The outlines of the best-fit components from the 3D fit of the Westerlund 2 core region presented in Sec. 5.5.1.2 are shown in green.

Figure 6.7 shows an enlarged cutout from this sky map. Additionally, the region covered by the significance map from the reflected regions study shown in Fig. 6.5 is depicted by the dashed black square with the 3σ contours from this map shown as solid black lines.

Furthermore, all source positions from the 3FHL [176] and the 3FGL [177] catalogue are marked in yellow and magenta respectively. The extension of FGES J1036.4–5834 (or 3FHL J1036.3–5833e) is shown as a yellow circle.

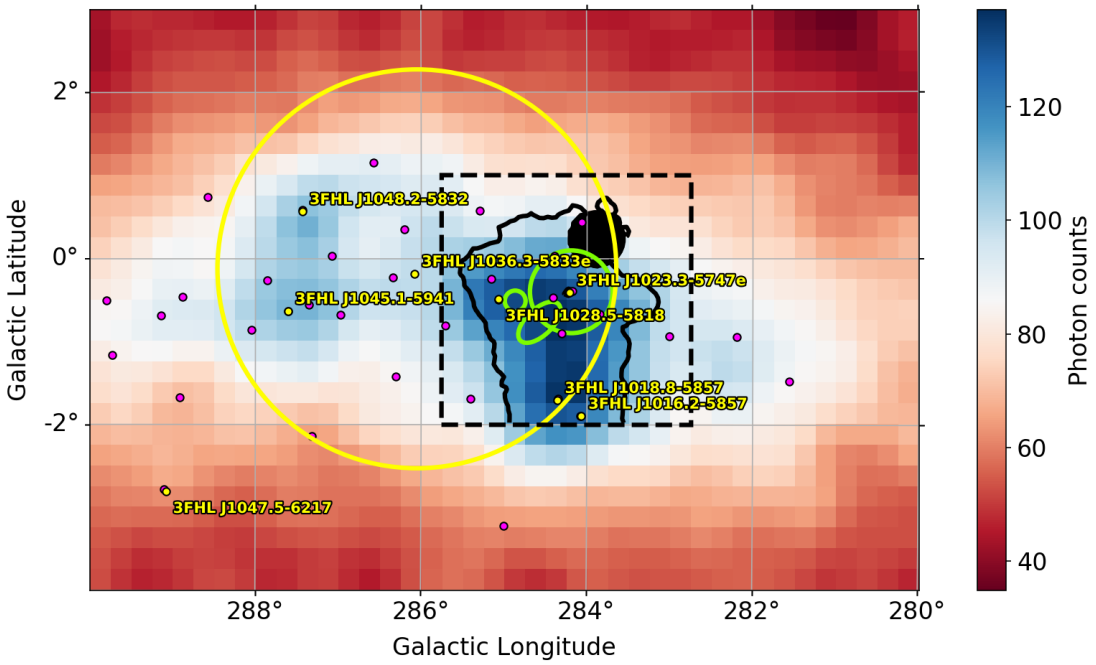

FIGURE 6.7: Cutout of AGILE count map shown in Fig. 6.6. The region covered by the significance map shown in Fig. 6.5 is marked by the black dashed square with the 3σ contour of the map shown as a solid black line. The extended Fermi-LAT source is shown as a yellow circle with source positions of objects from the 3FHL and 3FGL catalogues depicted by yellow and magenta dots respectively. A correlation between the 3σ significance contour and the AGILE photon count distribution can be seen.

In Fig. 6.7, it can be seen that the 3σ contour of the correlated significance map from Fig. 6.5 agrees with the distribution of counts measured by AGILE. The distribution of sources from the 3FGL and 3FHL catalogues shows the multitude of γ-ray sources and the complexity of the emission in the FoV. In general the hints of a diffuse VHE emission in the Westerlund 2 region agree with findings in the HE regime. Nevertheless, a more elaborate analysis of VHE data for a larger FoV is needed in order to draw conclusions. One aspect that could significantly complicate this task is the influence of strong night sky background as encountered in the H.E.S.S. analysis of the η Car region [173], which is $< 4°$ east of Westerlund 2 (the source 3FHL 1045.1–5941 in Fig. 6.7).

6.3 Hotspots around Westerlund 2

The detailed analysis of the emission around the Westerlund 2 core region showed three point-like hotspots with significant γ-ray emission, as outlined in Sec. 5.5.2 and Sec. 5.5.3. The emission is however too weak for a detailed study and the results of the spectral fits from the 3D fit and the reflected regions analysis are not compatible within statistical

errors. More data with a better exposure of the hotspots are needed for an elaborate analysis and interpretation. The regions of the celestial sky around these hotspots are nevertheless searched for potential counterparts as presented in the following.

6.3.1 Region B - Hotspots west of HESS J1023–575

There are two larger hotspots found in region B west of HESS J1023–575 as outlined in Sec. 5.5.2. Figure 6.8 shows the region in the red optical band from the second digitized sky survey (DSS2 red), overlayed in white with the $2, 4$ and 6σ contours from the significance map shown in Fig. 5.9. The positions of objects found in the Simbad astronomical database[6] are marked (see figure caption for details). It can be seen that there is no pulsar, WR star or radio source within the 2σ contours around HS B1. Due to its close proximity to HESS J1023–575 to the east, HS B1 could be an extension of this source. HS B2 on the other hand does have a WR star and a radio source at $< 0.1^\circ$ angular distance within the 2σ significance contours. The WR star with the identifier 2MASS J10162622–5728057 is listed in [178] under the name 668_4. It is a WN5b type WR star at an estimated distance of $\sim (4.3 \pm 1.1)\,\mathrm{kpc}$ and is not known to be a binary system such as WR 21a. The mean H I temperature distribution (SGPS data, see Sec. 5.6.3) in a circular region with 0.1° radius around the best-fit position of HS B2 is shown in Fig. 6.9. Multiple peaks can be seen, which suggests molecular clouds along the line of sight to the hotspot. The NANTEN CO data used in Sec. 5.6.3 does not cover this region. Complementing CO data would be needed to conduct more detailed studies. Additionally, the unidentified γ-ray source 4FGL J1016.2–5729c is located only $\sim 0.12^\circ$ south west of HS B2.

Two pulsars are found around HS B1 and HS B2, PSR J1019–5749 and PSR J1015–5719. The properties of these two pulsars from the ATNF pulsar catalogue [147] (version 1.63) are given in Tab. 6.5. The pulsar PSR J1015–5719 has an angular distance of $\sim 0.23^\circ$ to HS B2. At a distance to the Sun of 2.73 kpc, this yields $\sim 11\,\mathrm{pc}$ between the pulsar and the γ-ray hotspot. Combined with the characteristic age, this yields a pulsar velocity of $v_{\mathrm{PSR}} \sim 280\,\mathrm{km/s}$. Taking the results from the spectral fit with the reflected regions analysis presented in Sec. 5.5.2 yields a luminosity in the $1 - 10\,\mathrm{TeV}$ range of $L_{1-10\,\mathrm{TeV}} \sim (2.8 \pm 0.9) \times 10^{32}\,\mathrm{erg/s}$ at 2.73 kpc. This would be $\sim 0.03\%$ of the spin down power of PSR J1015–5719. A PWN scenario thus appears possible for the hotspot HS B2 but needs further investigation.

6.3.2 Hotspot HS E

The region around hotspot HS E is shown in Fig. 6.10 in the red optical band (DSS2 red), overlayed with the 2 and 4σ significance contours from Fig. 5.9. Pulsars and X-ray sources listed in the Simbad astronomical database are marked in grey and yellow respectively.

[6] `http://simbad.u-strasbg.fr/simbad/`

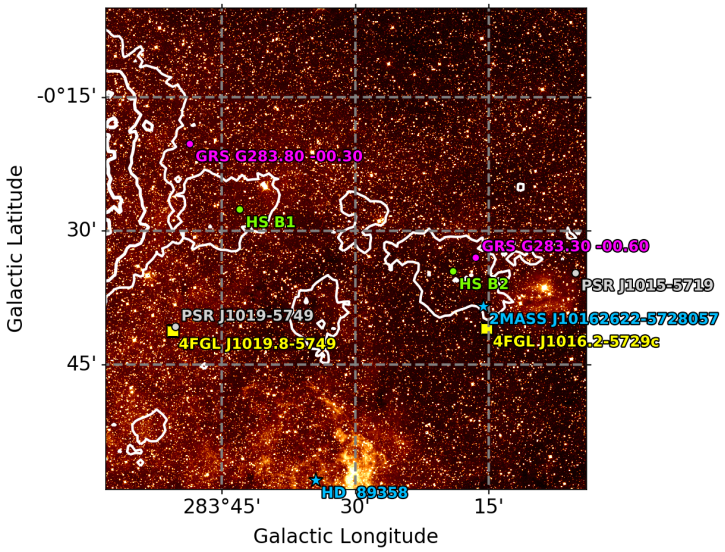

FIGURE 6.8: Optical (DSS2 red) image of the galactic sky of the region west of HESS J1023–575 with hotspots B1 and B2 marked in green. The white contours depict the $2, 4$ and 6σ significance contours of the TeV emission. Pulsars, radio sources and WR stars from the Simbad astronomical database are marked in grey, magenta and blue respectively. Sources from the 4FGL-DR2 catalogue by the Fermi-LAT collaboration are marked with yellow squares.

Pulsar	**Gal. Pos.** (l, b) [deg]	**Distance** d_{PSR} [kpc]	**Char. Age** τ_c [yr]	**Spindown** $\dot{E}$ [erg/s]
PSR J1015–5719	$(283.088, -0.578)$	2.73	3.86×10^4	8.3×10^{35}
PSR J1019–5749	$(284.837, -0.679)$	10.91	1.28×10^5	1.8×10^{35}

TABLE 6.5: Properties of pulsars in the region around the hotspots HS B1 and HS B2 from the ATNF pulsar catalogue [147] in version 1.63.

The properties from the ATNF pulsar catalogue [147] (in version 1.63) of the two pulsars PSR J1021–5601 and PSR J1017–5621 are listed in Tab. 6.6. Both pulsars have rather low $\dot{E}$, making it rather unlikely that potentially associated PWNe could be detected in the regarded H.E.S.S. data. The X-ray source 1RSX J101838.4–560621 [179] has an angular distance to the best-fit position of hotspot HS E of $\sim 0.1°$. It is associated with the high proper motion star HD 89569, also referred to as HIP 50493 (the bright star just below the position of the X-ray source in Fig. 6.10) located at a distance of $\sim 36\,\mathrm{pc}$ to the Sun. According to the Simbad database, HD 89569 is of spectral type F6V C, making it a so called yellow-white dwarf. Studies on γ-ray emission from white dwarfs have been conducted in the past, as for example presented in [180] and [181].

Examining the H I data from the SGPS (introduced in Sec. 5.6.3) in a circular region around HS E with $0.1°$ radius shows multiple peaks in the mean H I brightness temperature. This suggests cloud structures along the line of sight towards HS E. The CO data taken with the NANTEN telescope of the Westerlund 2 region presented in Sec. 5.6.3

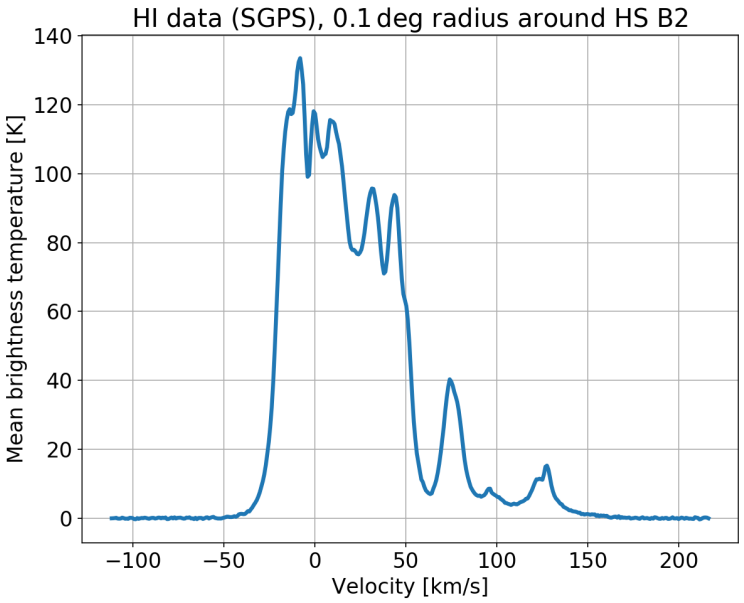

FIGURE 6.9: Mean H I brightness temperature (SGPS data) in a 0.1° radius region around hotspot HS B2.

does not cover this part of the galactic sky. Therefore, complementing CO data should be analysed for a detailed analysis of the hotspot in the context of molecular clouds.

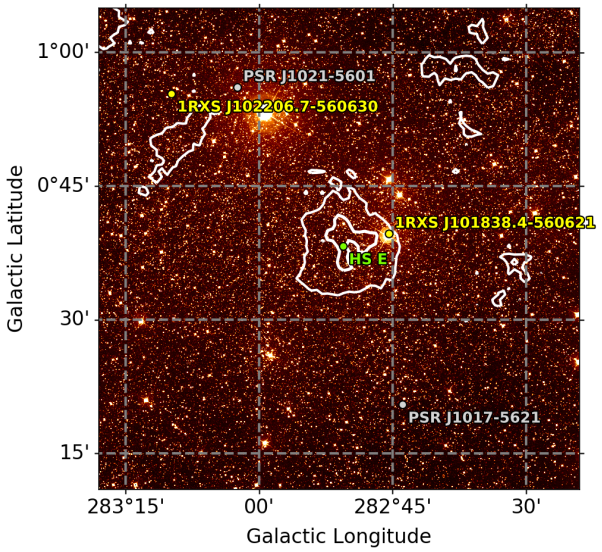

FIGURE 6.10: Optical (DSS2 red) image of the galactic sky around hotspot E marked in green. The white contours depict the 2 and 4σ significance contours of the TeV emission. Pulsars and X-ray sources from the Simbad astronomical database are marked in grey and yellow respectively.

Pulsar	**Gal. Pos.** (l, b) [deg]	**Distance** d_{PSR} [kpc]	**Char. Age** τ_c [yr]	**Spindown** $\dot{E}$ [erg/s]
PSR J1021–5601	$(283.041, +0.935)$	2.43	1.99×10^8	7.0×10^{30}
PSR J1017–5621	$(282.732, +0.341)$	3.51	2.54×10^6	9.7×10^{32}

TABLE 6.6: Properties of pulsars in the region around hotspot HS E from the ATNF pulsar catalogue [147] in version 1.63.

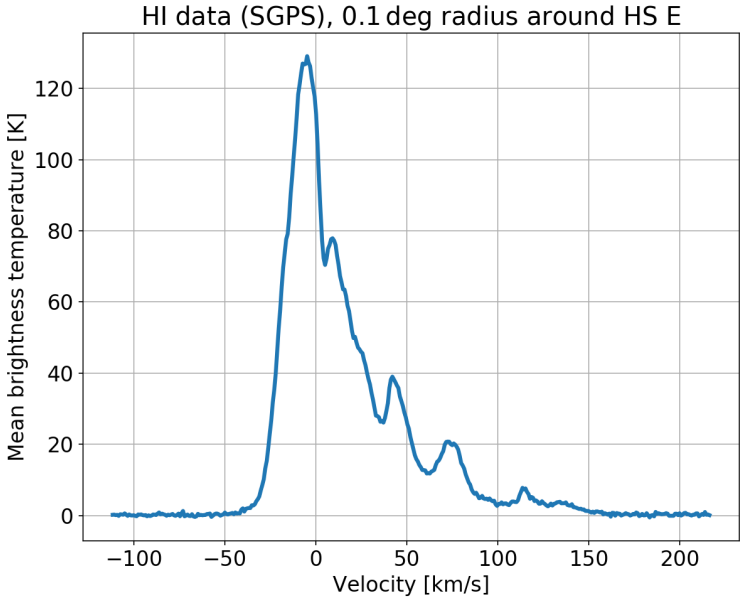

FIGURE 6.11: Mean H I brightness temperature (SGPS data) in a 0.1° radius region around hotspot HS E.

6.4 Concluding remarks

As outlined before, the fairly complex environment around Westerlund 2 makes an interpretation of the observed γ-ray signals and associations to other stellar objects a challenging task. For HESS J1026–582, a PWN scenario in association with the pulsar PSR J1028–5819 appears to be the favoured scenario. For HESS J1023–575 and the TeV *jet* cloud, different scenarios provide viable explanations. Regarding the overall morphology of the VHE γ-ray emission of HESS J1023–575 and the TeV *jet* cloud with the coinciding atomic and molecular clouds, a hadronic emission scenario appears likely with a microquasar offering the best explanation for the observed features. A PWN scenario for HESS J1023–575 can however not be rejected on the basis of the presented analyses and is also suggested by observations in the GeV γ-ray and X-ray regime. A superposition of multiple γ-ray sources along the line of sight towards HESS J1023–575 has to be considered after all and should be investigated further in future studies. Only a SNR can so far be excluded as association to the VHE emission of HESS J1023–575 by assuming a connection to Westerlund 2 and taking into account the properties of the ambient gas.

All in all, HESS J1023–575 as well as the TeV *jet* cloud can therefore still be regarded as unidentified γ-ray sources.

For the γ-ray hotspots found to the west and north west of HESS J1023–575 as well as the lobe of VHE emission coinciding with the colliding wind binary WR 21a, the VHE data does not allow to draw substantial conclusions as of yet. Nevertheless, the presence of potential counterparts suggests that more detailed investigations should be conducted.

The apparent presence of a diffuse and large scale γ-ray emission agrees with findings from the HE regime whereas the emission at VHE energies can not be characterised in detail due to the limited field of view that is regarded in this work.

Overall, a VHE dataset with a wider field of view and a more even exposure should be analysed to get deeper insights. Alternatively, different data selection criteria could be applied to make use of more data that has been taken by the H.E.S.S. experiment of the Westerlund 2 region. Additionally, a multitude of multi-wavelength data is available. Besides the openly accessible Fermi-LAT data, data products from the studies on X-ray data of the Carina region published in [131] are available online [182]. For future studies, a detailed multi-wavelength analysis incorporating this X-ray data with HE data from the Fermi-LAT and the VHE data taken with the H.E.S.S. telescopes is strongly suggested to build a better understanding of the underlying physical processes acting in the Westerlund 2 region. Additionally, a thorough modelling of different non-thermal radiative processes with software packages like `naima`[7][183] can help to disentangle the origin of the detected γ-ray emission. A detailed temporal analysis of the data would shed light on potential variability of the γ-ray sources in the Westerlund 2 region and is also suggested for future studies.

[7] Official `naima` documentation: `https://naima.readthedocs.org` (accessed 31.05.2020)

Chapter 7

Summary and conclusion

For this work, a partly unpublished set of high quality data taken with the H.E.S.S. telescopes between 2006 and 2015 of the region around the galactic star cluster Westerlund 2 has been analysed, mainly using the open-source software package `gammapy`. The dataset comprises a total of $\sim 80\,\mathrm{h}$ of observation time. Exclusion regions are generated by using an iterative approach combining the ring background method and the reflected regions method, successively shielding hotspots of emission from the regions used for background estimation. The sky maps generated with these exclusion regions show significant γ-ray excess with a complex morphology around Westerlund 2 and spectra which are in agreement with previously published results.

Applying the reflected background method and comparing the results to that of the extragalactic source PKS 2155–304 shows a hint of diffuse emission in the regarded region of the sky around Westerlund 2. This is consistent with published findings from the HE regime. A detailed description of this potentially diffuse emission is however not possible due to the limited FoV and exposure of the regarded set of observations.

Using an extensive 3-dimensional fit procedure, it has been possible to determine the spatial and spectral properties of three individual VHE source components in the Westerlund 2 region. The final model is thereby selected from a collection of different models constructed from various combinations of source components by applying the Akaike information criterion. The three sources include the previously detected sources HESS J1026–582 and HESS J1023–575. Additionally, an elongated component referred to as "TeV *jet* cloud" with an elliptical shape is significantly detected. The sources are in close proximity to each other and appear to overlap. Correcting for the overlap yields conservative detection significances of 51σ, 26σ and 17σ for the signal regions of HESS J1023–575, HESS J1026–582 and the TeV *jet* cloud respectively. The systematic uncertainties of the spectra given in the following are computed as outlined in Sec. 3.5.

The best-fit model for HESS J1023–575 shows a disk-like morphology centred on the galactic position ($l = 284.191^\circ \pm 0.011^\circ_{\mathrm{stat}},\ b = -0.401^\circ \pm 0.010^\circ_{\mathrm{stat}}$). The disk has a best-fit radius of $r_0 = 0.253^\circ \pm 0.017^\circ_{\mathrm{stat}}$ with a smooth edge extending the whole source up to $0.497^\circ \pm 0.084^\circ_{\mathrm{stat}}$. The spectrum of HESS J1023–575 as determined with the reflected regions method is a power law spectrum with an index of $\Gamma = (2.40 \pm 0.06_{\mathrm{stat}} \pm 0.10_{\mathrm{sys}})$ and a normalisation at 1 TeV of $\phi_0 = (3.34 \pm 0.30_{\mathrm{stat}} \pm 0.66_{\mathrm{sys}}) \times 10^{-12}\,\mathrm{cm^{-2}s^{-1}TeV^{-1}}$.

For HESS J1026–582, the best-fit model is a two-dimensional Gaussian at the galactic position ($l = 284.868^\circ \pm 0.022^\circ_{\mathrm{stat}},\ b = -0.512^\circ \pm 0.021^\circ_{\mathrm{stat}}$) with a width of $\sigma = 0.125^\circ \pm 0.016^\circ_{\mathrm{stat}}$. Here, the best-fit spectrum is an exponential cut-off power law with an index of $\Gamma = (0.78 \pm 0.36_{\mathrm{stat}} \pm 0.20_{\mathrm{sys}})$, a normalisation at 1 TeV of $\phi_0 = (0.29 \pm 0.12_{\mathrm{stat}} \pm 0.07_{\mathrm{sys}}) \times 10^{-12}\,\mathrm{cm^{-2}s^{-1}TeV^{-1}}$ and $\lambda = (0.13 \pm 0.04_{\mathrm{stat}})\,\mathrm{TeV^{-1}}$, which translates to a cut-off energy of $E_{\mathrm{cut}} = (7.7^{+3.4_{\mathrm{stat}}}_{-1.8_{\mathrm{stat}}} \pm 1.5_{\mathrm{sys}})$ TeV.

The best-fit model for the TeV *jet* cloud is an ellipse centred on ($l = 284.575^\circ \pm 0.017^\circ_{\mathrm{stat}},\ b = -0.768^\circ \pm 0.017^\circ_{\mathrm{stat}}$) aligned at an angle of $\sim 134^\circ \pm 6^\circ_{\mathrm{stat}}$ (anti-clockwise from north in galactic coordinates) with a width along the major axis of $0.634^\circ \pm 0.044^\circ_{\mathrm{stat}}$ and along the minor axis of $0.274^\circ \pm 0.048^\circ_{\mathrm{stat}}$. The best-fit spectrum of the TeV *jet* cloud is a power law with an index of $\Gamma = (2.15 \pm 0.13_{\mathrm{stat}} \pm 0.43_{\mathrm{sys}})$ and a normalisation at 1 TeV of $\phi_0 = (0.53 \pm 0.13_{\mathrm{stat}} \pm 0.05_{\mathrm{sys}}) \times 10^{-12}\,\mathrm{cm^{-2}s^{-1}TeV^{-1}}$.

The energy dependent morphology of the detected γ-ray signals shows very different signatures over the regions of significant excess. Especially within the signal region of HESS J1023–575, a peak of excess is seen at energies < 1 TeV at the position of Westerlund 2, which shifts south with increasing energy. This could point to a superposition of multiple γ-ray sources. To disentangle potentially overlapping sources, deeper investigations are however needed.

Interpreting the presented VHE data in terms of the three best-fit source components mentioned above yields different possible emission scenarios. For HESS J1026–582, the association as a PWN with the pulsar PSR J1028–5819 appears likely and could not be rejected on the basis of this work through a comparison to a general evolution model of VHE PWNe. The association for HESS J1023–575 and the TeV *jet* cloud however is not as conclusive. With the densely populated sky towards Westerlund 2, a wide range of emission scenarios with different associated objects can explain the observations. For HESS J1023–575, an association as a PWN with the pulsar PSR J1023–5746 can not be ruled out on the basis of this work.

The agreement between the VHE emission of HESS J1023–575 and the TeV *jet* cloud with cloud structures seen in CO and H I radio data proposes a common origin, likely in a mainly hadronic emission scenario. Furthermore, the spatial coincidence of the major axis of the TeV *jet* cloud and the best-fit position of HESS J1023–575 as well as the partial overlap of these two γ-ray sources proposes a connection whereas their spectra suggest different underlying physical processes.

Analyses of CO data have previously revealed two compounds of molecular clouds that show spatial correlation with the detected VHE γ-ray emission. One component is the so-called *arc* cloud which aligns with the disk-like morphology of HESS J1023–575. The second component is the so-called *jet* cloud which aligns with the TeV *jet* cloud. A detailed investigation of H I data furthermore shows an atomic hydrogen cloud with an apparent shell-like morphology at the position of HESS J1023–575, also aligning with the *arc* cloud. The emission of HESS J1023–575 thereby appears to be enclosed by a shell of hydrogen gas seen in CO and H I data. A SN explosion may have formed this structure, whereas CRs accelerated in the initial SN explosion or the following SNR evolution have most probably cooled or left the region of the γ-ray emission. H I column density maps furthermore show an elongated feature which is in spatial agreement with the CO *jet* cloud and the TeV *jet* cloud. In the case of a hadronic emission scenario in which CRs interact with the dense clouds of gas, accelerated particles have to be injected more or less continuously. An association with a high-energy jet as provided by a microquasar offers a favourable explanation for the structures of the clouds and the TeV emission for both, HESS J1023–575 and the TeV *jet* cloud. If this emission is in fact associated with an unidentified microquasar, this could be the first discovery of VHE γ-ray emission from microquasar jets with IACTs.

Applying the KDA method on the radio data yields a kinematic distance between 5.5 and 7.7 kpc for the *arc* and *jet* cloud structures which is compatible with the 5 ± 1 kpc distance estimate found in the literature for Westerlund 2. The gas clouds may thus be physically connected to Westerlund 2. This association could also be true for the detected γ-ray emission, which retains the option that the collective stellar winds of Westerlund 2 might be powering at least parts of the detected γ-ray emission.

Apart from the three main γ-ray sources discussed above, a number of hotspots is significantly detected in the data which are located close to stellar objects that could potentially produce VHE γ-rays. A larger dataset and more detailed analyses are however needed to get deeper insights and draw further conclusions about the origin of these hotspots.

Overall, we know that the Westerlund 2 region hosts a number of intriguing stellar objects that could explain the detected γ-ray emission and the various other signals that are found in its vicinity all over the electromagnetic spectrum. The studies shown in this thesis present an as yet undetected γ-ray source, expanding our knowledge of this highly complex part of the Galactic sky. The fact that detected γ-ray signals match with the morphology of coinciding cloud structures suggests hadronic emission scenarios, whereas the potential origin of accelerated cosmic rays in the region that interact with the gas of the clouds can currently not be ascertained. Regarding the stellar population of Westerlund 2 and the vicinity of RCW 49, stellar winds may still contribute a significant fraction of cosmic rays. By gathering further data with different experiments and combining these in detailed analyses, our understanding of the Westerlund 2 region will improve further. For such studies, future releases of the `gammapy` software will help by providing a modern

and flexible environment for extensive combined analyses. Together with the next generation of γ-ray experiments and further theoretical work, a more conclusive picture of the processes acting in the Westerlund 2 region will certainly emerge.

Appendix A

The goodness of fit problem and the C statistic

In the literature, it is often stated that a problem with the statistic $\tilde{C}^p$ as introduced in Sec. 3.4.5.2 (see Eq. 3.14) is that it cannot be used to determine a goodness of fit. A given reason is that it does not have a quantity corresponding to the reduced χ^2 value [65]. In other words, the minimum value of $\tilde{C}^p$ cannot easily be interpreted on its own. To overcome this issue, a goodness of fit test can be performed. In general, such a goodness of fit test tests the compatibility between a fitted model and the observed data. This can be done with a test statistic and a set of simulations based on the best-fit model. The choice of the test statistic is in principal arbitrary, whereas different statistics will be differently sensitive to deviations between data and model. In the test, the null hypothesis "the observed data originates from the best-fit model" is probed against the alternative hypothesis "the observed data does *not* originate from the best-fit model". Finally, a confidence level can be deduced with which the null hypothesis can be rejected. In order to make a statistically sound statement on the basis of such a test, the test should be gauged, meaning that for a given confidence level the test has to yield the respective false-positive rate. To show that the cash statistic $\tilde{C}^p$ is not interpretable on its own and also not an adequate test statistic for such a goodness of fit test in general, a small toy experiment can be conducted as outlined in the following.

The observed data in the toy experiment consists of 100 measurements of a constant count rate with Poisson fluctuations around the expectation value $\lambda = 5$. This parameter is not known to the experimenter, for whom the task is to find a suitable model that describes the measured data and to determine a goodness of fit. It is known that the expectation value is constant for all measurements, therefore, the best-fit model is taken to be the mean of all measured values. Figure. A.1 shows the observed count rates as blue data points with the true and the best-fit expectation value in green and orange respectively.

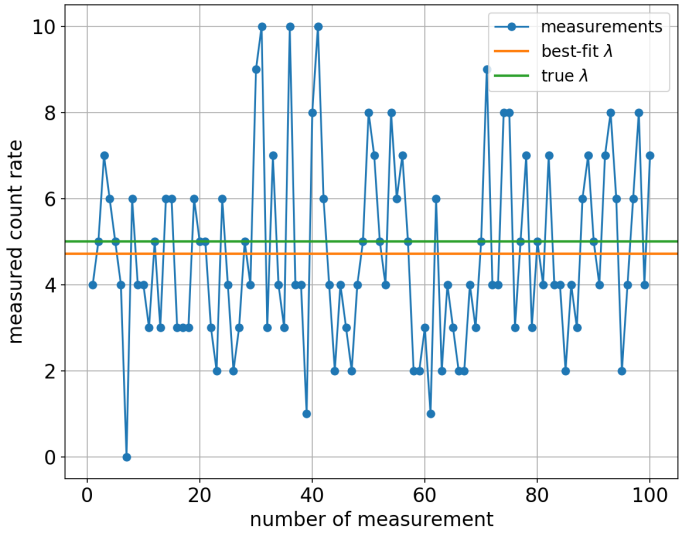

FIGURE A.1: Toy experiment data: Measurement of a constant count rate with Poisson fluctuations. The best-fit expectation value is the mean of the observed count rates.

To perform a goodness of fit test on the best-fit model, so called *fake* measurements are generated by simulating data based on the best-fit model. A best-fit model for each of the fake datasets is then determined by performing the maximum likelihood fit and the according test statistic value is calculated. This is done for 10^4 sets of fake data and the test statistic values are recorded in a histogram. The resulting distribution of test statistic values can be seen as a probability density from which the cumulative distribution can be used to determine a p-value, which gives a confidence level at which the null hypothesis can be rejected. If the test fails to reject the null hypothesis, the model can be regarded as fitting the data well. These distributions are shown in Fig. A.2 for $\tilde{C}^p$ and, as a comparison, for $\tilde{C}$ in the upper and lower panels respectively. It can be seen that both test statistics yield a p-value around 0.5, thus confirming a good fit with both test statistics.

The test statistics $\tilde{C}$ and $\tilde{C}^p$ can now be gauged by conducting the toy experiment multiple times and looking at the distribution of p-values. Such a distribution is shown for 1000 of such toy experiments in Fig. A.3. It can be seen that $\tilde{C}^p$ yields a p-value around 0.5 in all cases while $\tilde{C}$ shows a uniform distribution.

This shows that the practical implementation of the cash statistic $\tilde{C}^p$ is in fact not an adequate test statistic for a goodness of fit test, as the null hypothesis is failed to be rejected in all of the conducted toy experiments, irrespective of a given CL. The exact cash statistic $\tilde{C}$ on the other hand shows the correct false-positive rates at a given CL as expected for a suitable test statistic.

The pendant to a reduced χ^2 would be the reduced $\tilde{C}^p$ and the reduced $\tilde{C}$, which would be calculated by dividing the statistic value by the degrees of freedom D_f of the fit. The degrees of freedom is the sample size minus the number of free fit parameters, which in this

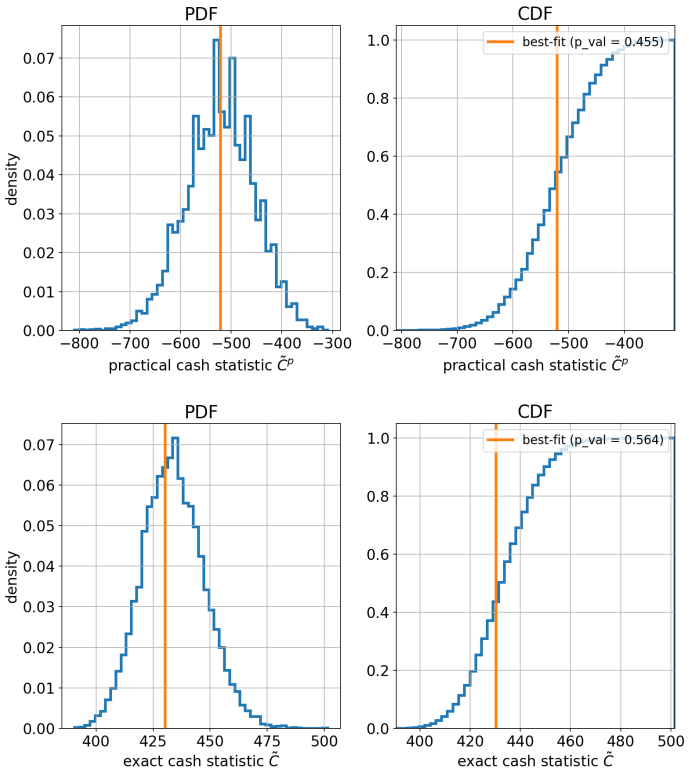

FIGURE A.2: Probability density distributions (*left*) and the respective cumulative distributions (*right*) for $\tilde{C}^p$ (*upper panel*) and $\tilde{C}$ (*lower panel*) for the toy data shown in Fig. A.1. The orange line depicts the respective test statistic value for the measured data.

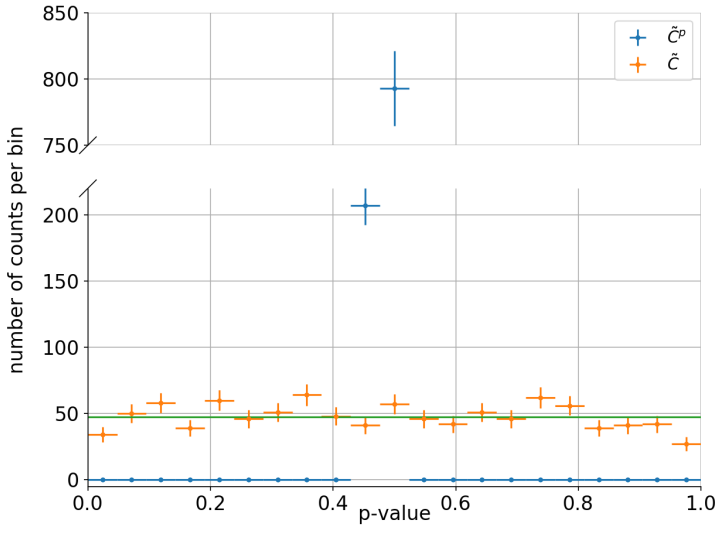

FIGURE A.3: P-value distributions for $\tilde{C}$ and $\tilde{C}^p$ for 1000 toy experiments. The horizontal errorbars show the bin width while the vertical errorbars depict 1 standard deviation. The green horizontal line shows the expected number of counts per bin for a uniform distribution of p-values.

case of 100 measurements and a single fit parameter is $D_f = 100 - 1 = 99$. For a good fit, the reduced χ^2 is supposed to be around 1. Looking at the plots in Fig. A.2 already shows that $\tilde{C}$ and $\tilde{C}^p$ have very different ranges of statistic values that are both not ~ 1 when divided by $D_f = 99$. Both reduced statistic values are furthermore strongly influenced by the total measured count rates. This can be seen by running the toy experiment with different expectation values for the generating Poisson distribution. Figure A.4 shows the mean of the reduced statistic values from 1000 toy experiments (with 100 measurements per experiment) run with different expectation values. The plots show a clear correlation between the total observed counts and the reduced statistic. While $\tilde{C}^p$ appears to fall almost linearly with rising counts (note the log-scale of the x-axis), $\tilde{C}$ appears to grow logarithmically (which is expected as the only difference between the two statistics is the term $\ln(D_i!)$).

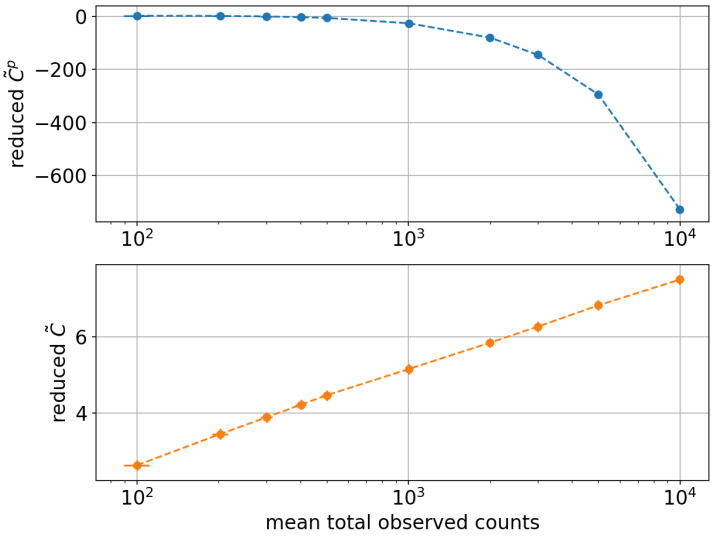

FIGURE A.4: Mean reduced statistic values from 1000 toy experiments for different total counts. A clear correlation can be seen. The errorbars show the 1σ standard deviation over the 1000 conducted experiments per data point.

Concluding the toy experiment, it can be said that on their own, neither $\tilde{C}^p$ nor $\tilde{C}$ can be used to determine a goodness of fit. And while $\tilde{C}$ can still be used in a goodness of fit test involving simulations, $\tilde{C}^p$ also fails in this regard.

To counteract this issue of $\tilde{C}^p$ not being suitable for a goodness of fit in general, another version of the cash statistic, often referred to as C statistic or simply *cstat* was introduced. It is implemented in common software packages like `gammapy`, `sherpa` and `xspec`[1]. In this implementation (which is also used in the fit procedures for this thesis) the factorial term in Eq. 3.12 is replaced with the Stirling's approximation $\ln(D_i!) \approx D_i \ln(D_i) - D_i$, resulting in

[1]For details on cstat, see e.g. `https://cxc.cfa.harvard.edu/sherpa/statistics` and `https://heasarc.gsfc.nasa.gov/xanadu/xspec/manual/XSappendixStatistics.html` (accessed 28.01.2020).

$$C = 2\sum_i [M_i - D_i + D_i(\ln D_i - \ln M_i)]. \tag{A.1}$$

Using an approximation at this point is in general not necessary and might be a relic from times when the evaluation of factorial terms posed a computational challenge. Furthermore, its application is somewhat contradictory as the cash statistic was introduced for the case of *low* bin counts, whereas Stirling's approximation is adequate for *high* bin counts. Nevertheless, the C statistic in Eq. A.1 can also be motivated differently[2], as it is exactly the same as a ratio between the log-likelihoods of L for the assumed model M and of $\hat{L}$ for a "perfect" model that predicts the exact counts of the observed data:

$$\begin{aligned} -2\ln\left(\frac{L}{\hat{L}}\right) &= -2\sum_i \left[D_i \ln M_i - M_i - \ln(D_i!) - D_i \ln D_i + D_i + \ln(D_i!)\right] \\ &= -2\sum_i \left[D_i \ln M_i - M_i - D_i \ln D_i + D_i\right] \\ &= 2\sum_i [M_i - D_i + D_i(\ln D_i - \ln M_i)] \end{aligned}$$

Yet another motivation for the form of the C statistic in Eq. A.1 is given in [184]. Here, the authors propose to simply add the term $D_i \ln D_i - D_i - \ln(D_i!)$ to the negative log likelihood in Eq. 3.12 because data-only dependent terms do not affect the shape of the likelihood distribution. This also results in the C statistic. Approximating the term $\ln D_i - \ln M_i$ with the first two terms of its Taylor expansion for $D_i \approx M_i$ yields an expression that resembles a χ^2 likelihood, which, as pointed out by the authors, allows to deduce an approximate goodness of fit from the reduced C statistic analogous to the reduced χ^2 statistic. In a paper by Baker & Cousins, the C statistic is introduced under the name *Poisson likelihood* χ^2 and is derived via the likelihood ratio test theorem [185]. Here, the authors also point out that the C statistic can be used for point estimation as well as confidence level estimation and goodness of fit testing.

This can be verified by running the above mentioned toy experiment with the C statistic instead of $\tilde{C}^p$ and $\tilde{C}$. Figure A.5 shows the distribution of the C statistic for the same set of simulations generated for the distributions shown in Fig. A.2. The distribution shows that the C statistic also yields a p-value around 0.5, confirming a good fit. The p-value distribution for C as test statistic in multiple toy experiments shows a uniform distribution as seen in Fig. A.6, which verifies C to be suitable in goodness of fit tests. Furthermore, the reduced C statistic is compatible with 1, at least for > 1 counts per bin as seen in Fig. A.7.

[2]Pointed out by Dr. G. Spengler in a private communication.

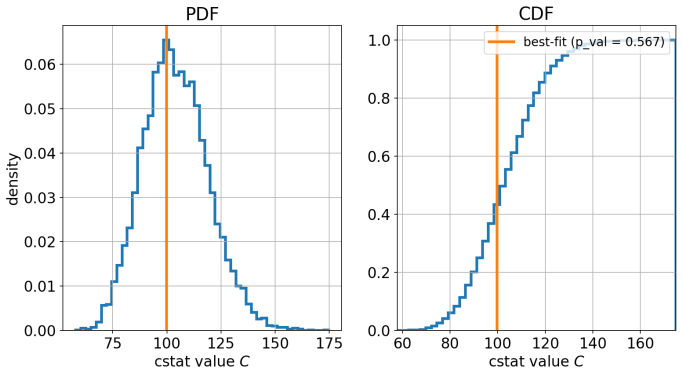

FIGURE A.5: Probability density distribution (*left*) and the respective cumulative distribution (*right*) for the C statistic of the toy data shown in Fig. A.1. The orange line depicts the test statistic value for the measured data.

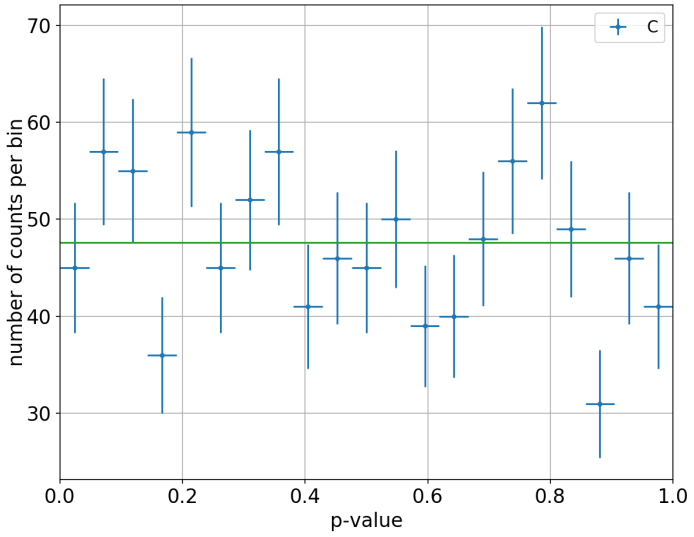

FIGURE A.6: P-value distribution for 1000 toy experiments. The horizontal errorbars show the bin width while the vertical errorbars depict 1 standard deviation. The green horizontal line shows the expected number of counts per bin for a uniform distribution of p-values.

This shows that the C statistic can be used for the maximum likelihood fit as well as for goodness of fit tests, on its own in the form of an approximate reduced χ^2 and more exact in a goodness of fit test using simulations from the best-fit model.

A goodness of fit test using the C statistic can also be conducted without running extensive simulations as pointed out in [65]. The publication states that for datasets with at least 10 to 30 counts, the C statistic distribution of a model approximately follows a Gaussian (as seen in Fig. A.5) which can be approximated from the contributions of the observed and expected counts. The author also presents an algorithm to determine the properties of the C statistic distribution. Nevertheless, this approach as well as the reduced C statistic only approximate a goodness of fit. A statistically more sound and reliable estimate is

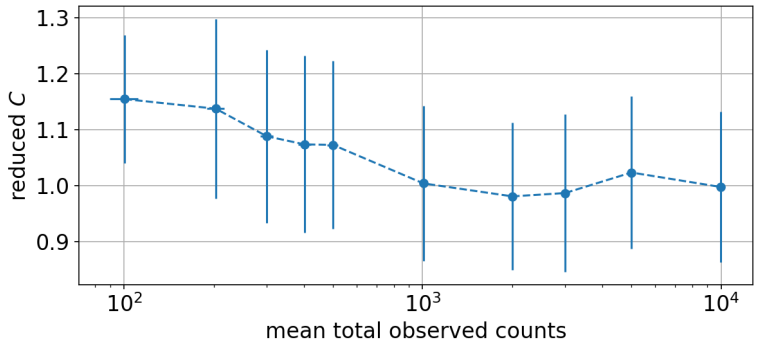

FIGURE A.7: Mean reduced C statistic from 1000 toy experiments per data point with 100 measurements of a count rate sampled from Poisson distributions with different expectation values. A mean total of 100 counts corresponds to an expectation value of $\lambda = 1$, a total mean around 200 to $\lambda = 2$ and so on. The errorbars show the 1σ standard deviation over the 1000 conducted experiments per data point.

achieved by simulating measurements from the best-fit model to determine the actual distribution of the test statistic.

It is possible to apply further goodness of fit tests to inspect the data-model-discrepancy, where each test may be sensitive to different features. One important feature to test for the case regarded in this work (an IACT data set to which morphological models are fitted) is that the residuals, i.e. the difference between model and data, should only show random fluctuations without any spatial traits of the model components. In other words, geometric features of the model should not be visible in the residual sky maps. Furthermore, the correlated[3] bin counts of the map should be distributed around 0. There is a number of so called statistical paired difference tests that could be adapted to inspect the bin-wise differences between the model and data maps. Examples would be the sign test, the paired t-test or the Wilcoxon signed-rank test. The problem is that geometric discrepancies are likely spatially confined. The tests would thus have to be applied to subsets of the residual maps to have a good sensitivity and find the regions where the discrepancies are large. The issue thereby is that the size of components and the resolution of the map would influence the optimal size of these subsets. Therefore, it is in general more convenient to inspect the residuals by eye to locate regions in the maps where the model does not fit the data well. The concept can be illustrated with an example by simulating and fitting an IACT observation (as shown in a `gammapy` tutorial[4]). The simulated source is a Gaussian with a width of 0.3°. The fitted model component is a 2-dimensional Gaussian and, as example for a bad fit, a 2-dimensional disk. Figure A.8 shows the simulated correlated count map (*top*) and the according residuals of the Gauss and the disk fit (*bottom left* and *right* respectively). It can easily be seen that the residual of the disk fit shows an annular imprint around the source position, suggesting that a disk

[3]In case of a sparse spatial sampling of a dataset, the bins are commonly correlated with a Gaussian or disk kernel for better visualisation and to reduce fluctuations in sky maps.

[4]See `https://docs.gammapy.org/0.13/notebooks/simulate_3d.html` (Accessed 10.03.2020)

is not an appropriate spatial model. The residual of the Gaussian on the other hand does not show geometrical features, as expected for an appropriate spatial model.

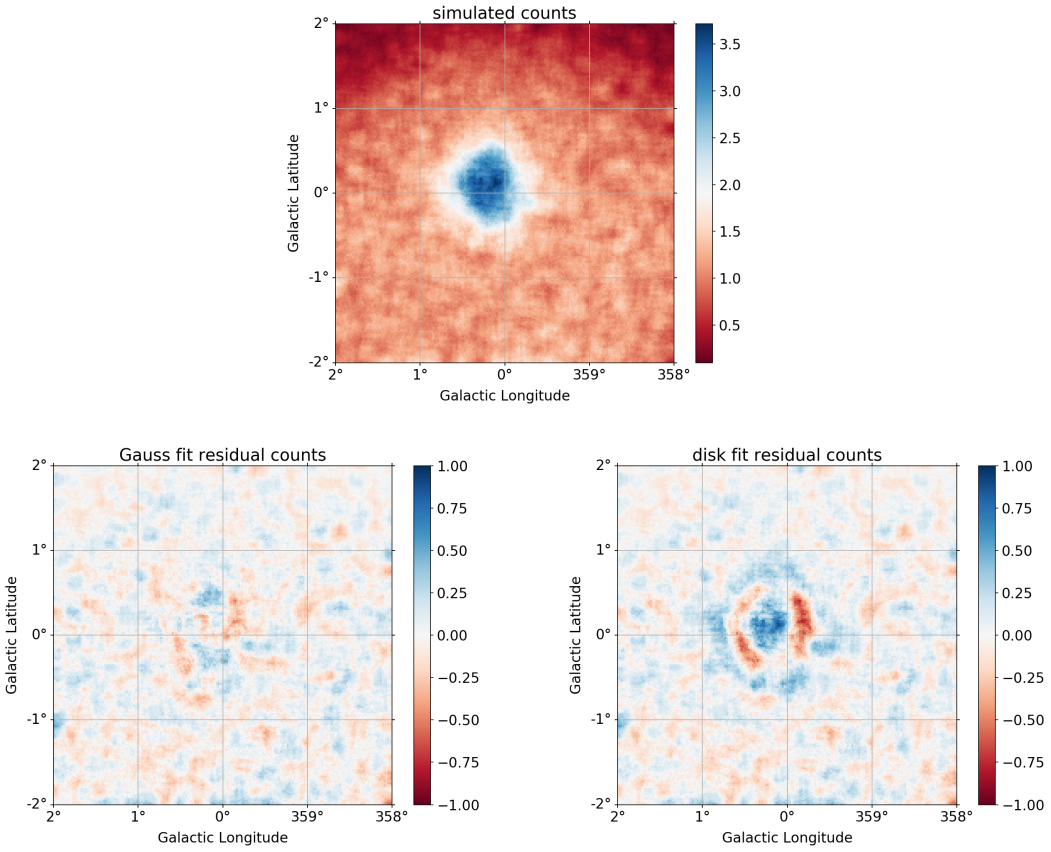

FIGURE A.8: *Top panel*: Correlated count map of a simulated γ-ray source with a Gaussian extension. *Bottom left*: Residual of a model with a Gaussian source subtracted from the count map. *Bottom right*: Residual of a disk-like source subtracted from the count map.

To summarise, if no apparent artefacts can be seen in the residuals of a best-fit model and the simulations from this model yield a C statistic distribution that shows a good agreement between observed data and model, this best-fit model can be regarded as fitting the data well.

Appendix B

γ-Ray sources in the Westerlund 2 region

The following two tables list a number of γ-ray sources that have been detected in the Westerlund 2 region over time. Details are presented in Sec. 4.2.

Name	**Energy**	**Gal. lon.**[deg]	**Gal. lat.** [deg]	**Ref.**	**Year**
2CG 284–00	$> 100\,\mathrm{MeV}$	284.3	-0.5	[102]	1981
GRO J1021–58	$> 100\,\mathrm{MeV}$	284.36	-1.09	[103]	1994
2EG J1021–5835	$> 100\,\mathrm{MeV}$	284.45	-1.20	[104]	1995
GRO J1025–5814	$> 1\,\mathrm{GeV}$	284.75	-0.60	[105]	1997
GEV J1025–5809	$> 1\,\mathrm{GeV}$	284.62	-0.58	[106]	1997
3EG J1027–5817	$> 100\,\mathrm{MeV}$	284.94	-0.52	[107]	1999
EGR J1021–5831	$> 100\,\mathrm{MeV}$	284.40	-1.16	[109]	2008

TABLE B.1: Sources of γ-ray emission around the position of Westerlund 2 found in COS-B and EGRET data. The first column states the name of the source. The second column gives the energy threshold above which the source is detected with the best-fit positions in galactic coordinates given in column three and four. Column five gives the reference to the original publication with the year of publication in the last column.

Source Name	**Energy**	**Gal. lon.** [deg]	**Gal. lat.**[deg]	**Ref.**	**Year**
HESS J1023–575	> 380 GeV	284.19	−0.39	[110]	2007
0FGL J1024.0–5754	> 100 MeV	284.346	−0.453	[113]	2009
0FGL J1028.6–5817	> 100 MeV	285.074	−0.459	[113]	2009
1AGL J1022–5822	> 100 MeV	283.39	−0.98	[114]	2009
1FGL J1023.0–5746	100 MeV – 100 GeV	284.166	−0.409	[115]	2010
1FGL J1028.4–5819	100 MeV – 100 GeV	285.065	−0.495	[115]	2010
HESS J1023–575	$\gtrsim 800$ GeV	284.217	−0.401	[2]	2011
HESS J1026–582	$\gtrsim 800$ GeV	284.798	−0.520	[2]	2011
2FGL J1022.7-5741	100 MeV – 100 GeV	284.090	−0.374	[186]	2012
2FGL J1023.5-5749c	100 MeV – 100 GeV	284.252	−0.429	[186]	2012
2FGL J1027.4-5730c	100 MeV – 100 GeV	284.530	+0.123	[186]	2012
2FGL J1028.5-5819	100 MeV – 100 GeV	285.077	−0.505	[186]	2012
1FHL J1022.6-5745	> 10 GeV	284.124	−0.430	[187]	2013
1FHL J1028.4-5819	> 10 GeV	285.069	−0.495	[187]	2013
1AGLR J1022-5751	30 MeV – 50 GeV	284.040	−0.580	[188]	2013
1AGLR J1022-5825	30 MeV – 50 GeV	284.360	−1.060	[188]	2013
AGL J1029-5836	30 MeV – 50 GeV	285.320	−0.680	[188]	2013
3FGL J1020.0-5749	20 MeV – 300 GeV	283.851	−0.669	[177]	2015
3FGL J1021.9-5815c	20 MeV – 300 GeV	284.309	−0.905	[177]	2015
3FGL J1023.1-5745	20 MeV – 300 GeV	284.174	−0.392	[177]	2015
3FGL J1024.3-5757	20 MeV – 300 GeV	284.409	−0.470	[177]	2015
3FGL J1025.7-5659c	20 MeV – 300 GeV	284.067	+0.438	[177]	2015
3FGL J1026.2-5730	20 MeV – 300 GeV	284.394	+0.033	[177]	2015
3FGL J1028.4-5819	20 MeV – 300 GeV	285.069	−0.495	[177]	2015
2FHL J1022.0-5750	50 GeV – 2 TeV	284.093	−0.537	[189]	2016
3FHL J1023.3-5747e	10 GeV – 2 TeV	284.209	−0.410	[176]	2017
3FHL J1028.5-5818	10 GeV – 2 TeV	285.068	−0.487	[176]	2017
3FHL J1036.3–5833e	10 GeV – 2 TeV	286.081	−0.181	[176]	2017
FGES J1023.3–5747	> 10 GeV	284.209	−0.410	[119]	2017
FGES J1036.6–5834	> 10 GeV	286.081	−0.181	[119]	2017
2AGL J1020–5752	100 MeV – 10 GeV	283.92	−0.67	[122]	2019
2AGL J1029–5834	100 MeV – 10 GeV	285.21	−0.70	[122]	2019
Westerlund 2 (2AGL)	100 MeV – 10 GeV	284.21	−0.41	[122]	2019
HESS J1026–582 (2AGL)	100 MeV – 10 GeV	284.79	−0.53	[122]	2019
4FGL J1023.0-5745	50 MeV – 1 TeV	284.168	−0.398	[123]	2020
4FGL J1023.3-5747e	50 MeV – 1 TeV	284.209	−0.410	[123]	2020
4FGL J1026.2-5731	50 MeV – 1 TeV	284.405	0.022	[123]	2020
4FGL J1028.5-5819	50 MeV – 1 TeV	285.071	−0.492	[123]	2020
4FGL J1036.3-5833e	50 MeV – 1 TeV	286.081	−0.182	[123]	2020
4FGL J1037.8-5810c	50 MeV – 1 TeV	286.061	0.244	[123]	2020

TABLE B.2: Selected sources of γ-ray emission around the position of Westerlund 2 found in Fermi-LAT, AGILE and H.E.S.S. data until 2020.

Appendix C

Run list

The following multi page table lists the H.E.S.S. internal run numbers identifying the individual runs analysed in this thesis. Additionally, the observation date and mean zenith angle as well as the quality of the each run (*detection* or *spectral*) is given. All four H.E.S.S. phase I telescopes participated in each run of the regarded dataset.

Run Nr.	**Obs. date**	**Zenith angle** [deg]	**Quality**
30492	2006-03-03	38.76	detection
30493	2006-03-03	40.83	detection
30498	2006-03-03	48.54	spectral
30531	2006-03-03	37.77	spectral
30532	2006-03-04	40.41	spectral
30533	2006-03-04	43.52	spectral
30534	2006-03-04	47.04	spectral
30555	2006-03-04	38.03	spectral
30557	2006-03-05	43.78	spectral
31660	2006-05-02	40.73	spectral
31663	2006-05-02	52.65	spectral
31693	2006-05-03	48.63	spectral
31694	2006-05-03	51.85	spectral
32345	2006-05-24	43.16	spectral
32346	2006-05-24	46.54	spectral
32347	2006-05-24	50.21	spectral
32366	2006-05-25	35.6	spectral
32398	2006-05-26	35.7	spectral
32425	2006-05-27	35.99	spectral
32426	2006-05-27	38.44	spectral
32449	2006-05-28	36.08	spectral
32450	2006-05-28	38.35	spectral

Run Nr.	**Obs. date**	**Zenith angle** [deg]	**Quality**
32481	2006-05-29	38.95	spectral
32482	2006-05-29	42.0	spectral
32483	2006-05-29	45.6	spectral
32484	2006-05-29	49.19	spectral
32831	2006-06-13	40.4	spectral
32852	2006-06-15	41.84	spectral
32890	2006-06-16	41.97	spectral
32916	2006-06-18	42.81	spectral
36830	2007-01-20	33.2	spectral
36831	2007-01-20	35.17	spectral
36862	2007-01-21	33.57	spectral
36863	2007-01-21	35.33	spectral
36927	2007-01-24	35.23	spectral
37658	2007-03-18	37.85	spectral
37660	2007-03-18	35.79	detection
37663	2007-03-18	36.48	spectral
37689	2007-03-19	36.75	detection
37700	2007-03-19	36.63	detection
37720	2007-03-20	35.99	detection
37744	2007-03-22	35.76	spectral
37770	2007-03-23	38.4	spectral
45121	2008-04-27	34.91	spectral
45122	2008-04-27	36.3	spectral
45132	2008-04-28	34.99	spectral
45152	2008-04-29	35.36	spectral
45243	2008-05-03	35.53	spectral
45244	2008-05-03	35.8	spectral
45245	2008-05-03	37.12	spectral
45282	2008-05-04	34.35	spectral
45283	2008-05-04	34.71	spectral
45365	2008-05-07	35.59	spectral
50066	2009-01-29	35.74	spectral
50116	2009-01-31	36.54	spectral
50117	2009-01-31	38.02	spectral
50344	2009-03-20	37.48	spectral
50345	2009-03-20	39.45	spectral
50357	2009-03-21	36.03	spectral
50450	2009-03-25	37.08	detection
51320	2009-05-14	38.83	spectral

Run Nr.	**Obs. date**	**Zenith angle** [deg]	**Quality**
51333	2009-05-15	37.88	detection
51362	2009-05-17	36.03	spectral
51363	2009-05-17	37.97	spectral
51383	2009-05-18	37.6	spectral
51384	2009-05-18	40.04	spectral
51404	2009-05-19	40.41	detection
51428	2009-05-20	39.81	detection
51474	2009-05-22	38.87	detection
51579	2009-05-26	40.3	spectral
51792	2009-06-10	43.48	spectral
51821	2009-06-11	41.67	spectral
51858	2009-06-12	42.07	detection
51867	2009-06-13	40.93	spectral
51868	2009-06-13	44.05	spectral
51883	2009-06-14	41.33	spectral
51884	2009-06-14	44.51	spectral
51914	2009-06-16	42.13	spectral
51915	2009-06-16	45.39	spectral
51933	2009-06-17	42.51	spectral
51934	2009-06-17	45.85	spectral
51957	2009-06-18	43.05	detection
51981	2009-06-20	43.82	spectral
51982	2009-06-20	47.29	spectral
52018	2009-06-21	48.04	spectral
52046	2009-06-23	45.19	spectral
64713	2011-06-17	42.11	spectral
64738	2011-06-18	44.8	spectral
64739	2011-06-18	48.25	spectral
64806	2011-06-20	45.86	spectral
64807	2011-06-20	49.4	spectral
64859	2011-06-21	45.19	spectral
64860	2011-06-21	48.68	spectral
69386	2012-01-23	40.4	spectral
69387	2012-01-23	38.15	spectral
69392	2012-01-24	36.66	spectral
69474	2012-01-25	38.15	spectral
69475	2012-01-25	36.86	spectral
69476	2012-01-26	36.07	spectral
69477	2012-01-26	35.74	spectral

Run Nr.	**Obs. date**	**Zenith angle** [deg]	**Quality**
69478	2012-01-26	36.22	spectral
69501	2012-01-26	39.94	spectral
69502	2012-01-26	38.26	detection
69504	2012-01-27	36.14	spectral
69505	2012-01-27	35.74	spectral
69506	2012-01-27	36.15	spectral
69507	2012-01-27	37.33	spectral
69508	2012-01-27	39.2	spectral
69557	2012-01-28	36.41	detection
69833	2012-02-18	36.49	spectral
69834	2012-02-18	35.8	spectral
69917	2012-02-28	35.77	spectral
69918	2012-02-28	35.96	spectral
81177	2013-02-12	36.01	detection
81180	2013-02-12	35.86	spectral
81182	2013-02-13	36.69	spectral
81231	2013-02-13	37.05	detection
81232	2013-02-14	37.08	spectral
82928	2013-04-05	39.76	spectral
82929	2013-04-05	37.74	spectral
82935	2013-04-05	35.97	spectral
82968	2013-04-06	37.11	spectral
82974	2013-04-06	35.76	spectral
82977	2013-04-06	36.26	spectral
83006	2013-04-07	38.48	spectral
83053	2013-04-08	36.96	detection
83118	2013-04-09	40.54	spectral
83119	2013-04-09	38.94	spectral
83747	2013-05-01	35.77	spectral
83748	2013-05-01	36.4	spectral
83750	2013-05-01	38.67	spectral
83751	2013-05-01	40.99	spectral
83770	2013-05-02	36.09	spectral
83842	2013-05-03	35.78	spectral
83847	2013-05-03	36.42	spectral
83853	2013-05-03	37.81	spectral
83854	2013-05-03	39.85	spectral
83855	2013-05-03	42.46	spectral
83882	2013-05-04	37.41	spectral

Run Nr.	**Obs. date**	**Zenith angle** [deg]	**Quality**
83888	2013-05-04	41.49	spectral
83936	2013-05-05	36.02	spectral
83977	2013-05-06	38.05	spectral
84067	2013-05-08	36.6	spectral
84073	2013-05-08	38.1	spectral
84080	2013-05-08	40.52	spectral
84184	2013-05-10	36.09	spectral
84185	2013-05-10	37.21	spectral
84265	2013-05-11	35.75	spectral
84342	2013-05-12	36.72	spectral
84400	2013-05-13	41.53	spectral
93517	2014-04-04	36.18	spectral
102993	2015-01-16	43.41	spectral
102994	2015-01-16	40.46	spectral
103061	2015-01-18	40.43	spectral
103104	2015-01-20	36.03	spectral
103107	2015-01-20	35.12	spectral
103109	2015-01-20	38.09	spectral
103289	2015-01-29	40.16	spectral
104069	2015-02-15	54.95	spectral
104564	2015-02-26	45.99	spectral
105078	2015-03-19	53.06	spectral
105167	2015-03-21	36.59	spectral
105168	2015-03-21	35.5	spectral
105254	2015-03-24	51.48	spectral
105255	2015-03-24	55.27	spectral
105292	2015-03-25	54.94	spectral
105424	2015-03-28	52.37	detection
106964	2015-05-12	52.03	spectral
108069	2015-06-05	43.41	spectral
108140	2015-06-06	43.87	spectral
108261	2015-06-08	44.57	spectral
108265	2015-06-08	51.66	spectral
108296	2015-06-09	39.96	spectral
108298	2015-06-09	43.3	spectral
108302	2015-06-09	50.3	spectral
108418	2015-06-11	42.8	spectral
108420	2015-06-11	46.07	spectral
108481	2015-06-12	43.48	spectral

Run Nr.	**Obs. date**	**Zenith angle** [deg]	**Quality**
108483	2015-06-12	46.8	spectral
108485	2015-06-12	50.39	spectral
108547	2015-06-13	47.02	spectral
108613	2015-06-14	47.58	spectral

Appendix D

3D fit Parameters: Westerlund 2 core region

The following sections show the details of the different models from the candidate collection probed in the 3D fit analysis of the Westerlund 2 core region from Sec. 5.5.1.2. The sections present a short introduction of the model, the significances and the initial and best-fit parameters of the individual components. In all fits the normalisation of the background is also left free to be optimised. The parameter tables show the names of the components in the fit, the initial and best fit values, the 1σ statistical errors as well as the units and if the parameter is frozen or not (meaning that the parameters is fixed or free to be optimised in the fit). For spatial components, the type of spatial model (i.e. Gaussian, disk or ellipse) is stated under each component name.

The initial values for the spatial components were determined in a brief fitting procedure on the complete count map without binning in energy using the `sherpa` software package and by assessing the sky maps by eye. The initial values for the spectral part of the fits were deduced from the spectral maps shown in Fig. 5.20.

Only power law spectra of the form

$$\phi(E) = \phi_0 \cdot \left(\frac{E}{E_0}\right)^{-\Gamma} \tag{D.1}$$

are fitted to model the flux of the components. In the fit packages nomenclature, Φ_0 is the *amplitude*, E_0 is the *reference* and Γ is the *index*.

D.1 Model_A

Model_A is the simplest model in the candidate collection. It consists of the background model with one Gaussian component with a power law spectrum.

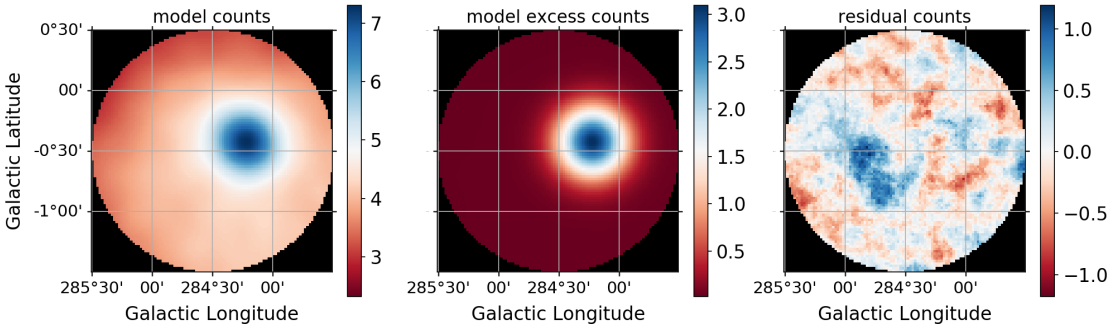

FIGURE D.1: Count map, excess map and residual to the observed data counts for model_A. The maps show the total counts summed over all energy bins. Black pixels are not regarded in the fit procedure.

Component	ΔC	P-value	significance [σ]
HESS J1023–575			
Gaussian	708	8.65×10^{-151}	26.2

TABLE D.1: Model_A component statistics.

name	initial_value	best fit value	error	unit	frozen
HESS J1023–575					
Gaussian					
lon_0	−75.500	−75.781	0.013	deg	False
lat_0	−0.500	−0.416	0.011	deg	False
sigma	2.000	0.187	0.011	deg	False
index	2.300	2.360	0.042		False
amplitude	1.000	4.127	0.334	10^{-12} cm^{-2}s^{-1}TeV^{-1}	False
reference	1.000	1.000	0.000	TeV	True
Background					
norm	1.100	1.009	0.007		False
tilt	0.000	0.000	0.000		True
reference	1.000	1.000	0.000	TeV	True

TABLE D.2: Model_A 3D fit parameters.

D.2 Model_B

Model_B is the equivalent of the model suggested in [2]. It consists of the background model with two Gaussian components with power law spectra.

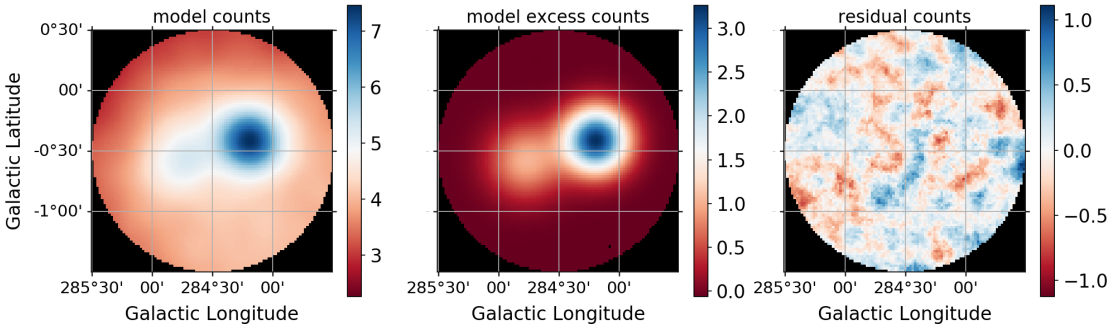

FIGURE D.2: Count map, excess map and residual to the observed data counts for model_B. The maps show the total counts summed over all energy bins. Black pixels are not regarded in the fit procedure.

Component	ΔC	P-value	significance [σ]
HESS J1023–575			
Gaussian	717	1.12×10^{-152}	26.3
HESS J1026–582			
Gaussian	151	7.76×10^{-31}	11.5

TABLE D.3: Model_B component statistics.

name	initial_value	best fit value	error	unit	frozen
HESS J1023–575					
Gaussian					
lon_0	−75.803	−75.812	0.014	deg	False
lat_0	−0.406	−0.405	0.011	deg	False
sigma	0.180	0.174	0.009	deg	False
index	2.400	2.403	0.044		False
amplitude	2.500	4.076	0.323	10^{-12} cm^{-2}s^{-1}TeV^{-1}	False
reference	1.000	1.000	0.000	TeV	True
HESS J1026–582					
Gaussian					
lon_0	−75.181	−75.213	0.039	deg	False
lat_0	−0.534	−0.574	0.028	deg	False
sigma	0.140	0.204	0.028	deg	False
index	2.000	2.039	0.073		False
amplitude	1.000	1.347	0.333	10^{-12} cm^{-2}s^{-1}TeV^{-1}	False
reference	1.000	1.000	0.000	TeV	True
Background					
norm	1.100	0.986	0.008		False
tilt	0.000	0.000	0.000		True
reference	1.000	1.000	0.000	TeV	True

TABLE D.4: Model_B 3D fit parameters.

D.3 Model_C

Model_C is deduced from the results presented in [119] where HESS J1023–575 is fitted with a disk. The model therefore consists of a disk and a Gaussian, whereas the disk has an additional fit parameters that allows the disk to have a smooth edge. This parameters gives the width of the annulus in which the disk's amplitude drops from 95% to 5%[1]. The parameter *r_0* therefore describes the outline of the component where its amplitude is at 50%. The spectra of the components are modelled with power laws.

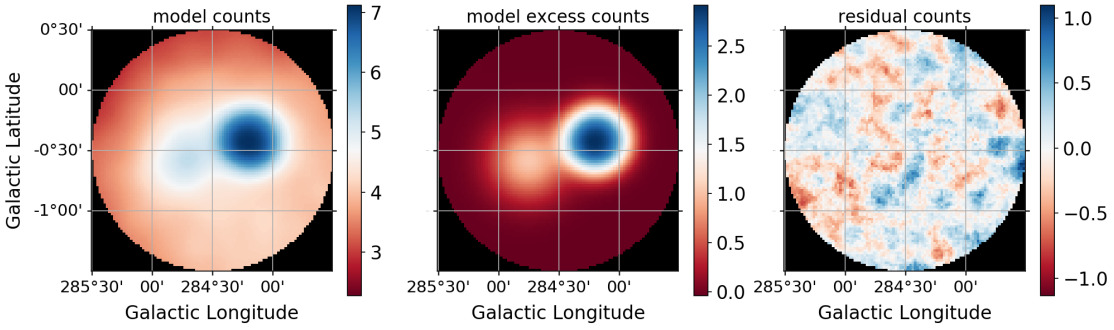

FIGURE D.3: Count map, excess map and residual to the observed data counts for model_C. The maps show the total counts summed over all energy bins. Black pixels are not regarded in the fit procedure.

Component	ΔC	P-value	significance [σ]
HESS J1023–575			
Disk	687	4.89×10^{-145}	25.6
HESS J1026–582			
Gaussian	159	1.36×10^{-32}	11.9

TABLE D.5: Model_C component statistics.

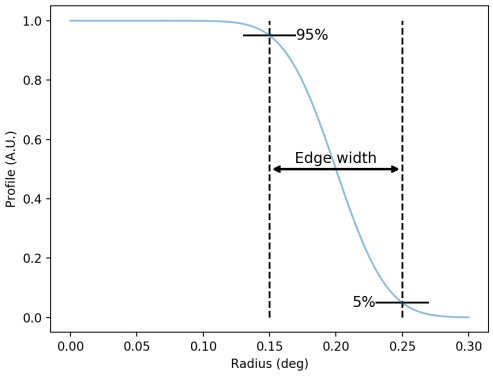

FIGURE D.4: Definition of the *edge* parameter of a disk model. The plot shows the amplitude distribution for a disk with a radius of 0.2° and an edge of 0.1°.

[1]See also `https://docs.gammapy.org/0.13/api/gammapy.image.models.SkyDisk.html` (accessed 10.02.2020)

name	initial_value	best fit value	error	unit	frozen
HESS J1023–575					
Disk					
lon_0	−75.803	−75.814	0.012	deg	False
lat_0	−0.406	−0.406	0.010	deg	False
r_0	0.286	0.255	0.016	deg	False
edge	0.050	0.228	0.066	deg	False
index	2.400	2.403	0.045		False
amplitude	2.500	3.379	0.247	10^{-12} cm^{-2}s^{-1}TeV^{-1}	False
reference	1.000	1.000	0.000	TeV	True
HESS J1026–582					
Gaussian					
lon_0	−75.181	−75.236	0.037	deg	False
lat_0	−0.534	−0.575	0.027	deg	False
sigma	0.140	0.211	0.025	deg	False
index	2.000	2.051	0.070		False
amplitude	1.000	1.451	0.324	10^{-12} cm^{-2}s^{-1}TeV^{-1}	False
reference	1.000	1.000	0.000	TeV	True
Background					
norm	1.100	0.990	0.008		False
tilt	0.000	0.000	0.000		True
reference	1.000	1.000	0.000	TeV	True

TABLE D.6: Model_C 3D fit parameters.

D.4 Model_D

Model_D extends model_B with a third Gaussian component on the excess seen in the lower half of the map in Fig. D.2 (*right*).

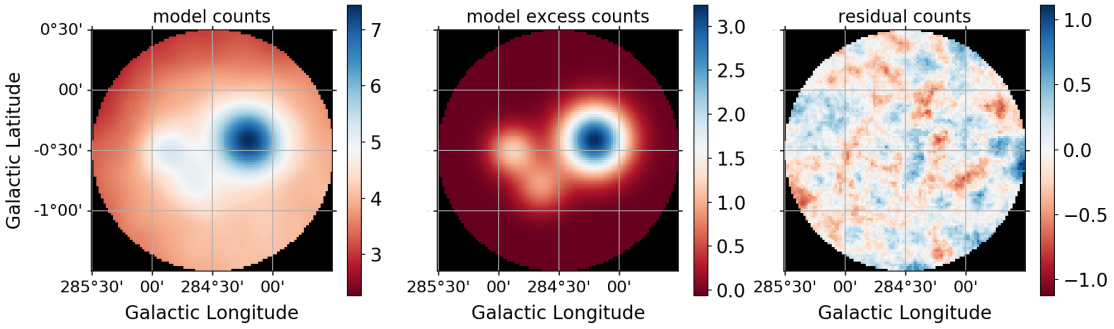

FIGURE D.5: Count map, excess map and residual to the observed data counts for model_D. The maps show the total counts summed over all energy bins. Black pixels are not regarded in the fit procedure.

Component	ΔC	P-value	significance [σ]
HESS J1023–575			
Gaussian	764	7.76×10^{-163}	27.2
HESS J1026–582			
Gaussian	99	9.10×10^{-20}	9.1
Hotspot			
Gaussian	45	1.65×10^{-8}	5.6

TABLE D.7: Model_D component statistics.

name	initial_value	best fit value	error	unit	frozen
HESS J1023–575					
Gaussian					
lon_0	−75.803	−75.800	0.012	deg	False
lat_0	−0.406	−0.406	0.011	deg	False
sigma	0.180	0.180	0.009	deg	False
index	2.400	2.392	0.043		False
amplitude	2.500	4.261	0.326	10^{-12} cm^{-2}s^{-1}TeV^{-1}	False
reference	1.000	1.000	0.000	TeV	True
HESS J1026–582					
Gaussian					
lon_0	−75.181	−75.113	0.025	deg	False
lat_0	−0.534	−0.498	0.025	deg	False
sigma	0.140	0.117	0.017	deg	False
index	2.000	1.915	0.090		False
amplitude	1.000	0.566	0.16	10^{-12} cm^{-2}s^{-1}TeV^{-1}	False
reference	1.000	1.000	0.000	TeV	True
Hotspot					
Gaussian					
lon_0	−75.535	−75.351	0.036	deg	False
lat_0	−0.711	−0.791	0.050	deg	False
sigma	0.061	0.132	0.037	deg	False
index	2.000	2.164	0.063		False
amplitude	1.000	0.587	0.211	10^{-12} cm^{-2}s^{-1}TeV^{-1}	False
reference	1.000	1.000	0.000	TeV	True
Background					
norm	1.100	0.985	0.008		False
tilt	0.000	0.000	0.000		True
reference	1.000	1.000	0.000	TeV	True

TABLE D.8: Model_D 3D fit parameters.

D.5 Model_E

Model_E extends model_C with a second Gaussian component on the excess seen in the lower half of the map in Fig. D.3 (*right*).

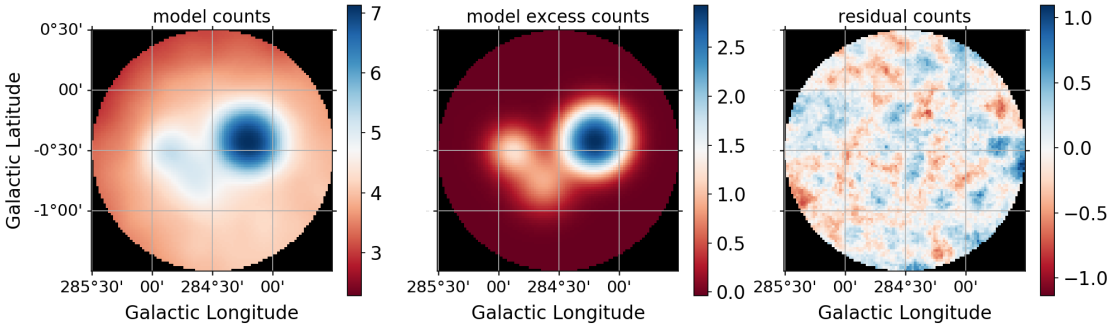

FIGURE D.6: Count map, excess map and residual to the observed data counts for model_E. The maps show the total counts summed over all energy bins. Black pixels are not regarded in the fit procedure.

Component	ΔC	P-value	significance [σ]
HESS J1023–575			
Disk	728	5.10×10^{-154}	26.4
HESS J1026–582			
Gaussian	91	5.14×10^{-18}	8.7
Hotspot			
Gaussian	53	3.21×10^{-10}	6.3

TABLE D.9: Model_E component statistics.

name	initial_value	best fit value	error	unit	frozen
HESS J1023–575					
Disk					
lon_0	−75.803	−75.803	0.013	deg	False
lat_0	−0.406	−0.405	0.011	deg	False
r_0	0.286	0.256	0.018	deg	False
edge	0.050	0.252	0.073	deg	False
index	2.400	2.392	0.043		False
amplitude	2.500	3.47	0.263	10^{-12} cm^{-2}s^{-1}TeV^{-1}	False
reference	1.000	1.000	0.000	TeV	True
HESS J1026–582					
Gaussian					
lon_0	−75.181	−75.112	0.028	deg	False
lat_0	−0.534	−0.495	0.024	deg	False
sigma	0.140	0.116	0.018	deg	False
index	2.000	1.903	0.094		False
amplitude	1.000	0.527	0.174	10^{-12} cm^{-2}s^{-1}TeV^{-1}	False
reference	1.000	1.000	0.000	TeV	True
Hotspot					
Gaussian					
lon_0	−75.535	−75.374	0.041	deg	False
lat_0	−0.711	−0.760	0.060	deg	False
sigma	0.061	0.150	0.038	deg	False
index	2.000	2.160	0.113		False
amplitude	1.000	0.705	0.283	10^{-12} cm^{-2}s^{-1}TeV^{-1}	False
reference	1.000	1.000	0.000	TeV	True
Background					
norm	1.100	0.991	0.007		False
tilt	0.000	0.000	0.000		True
reference	1.000	1.000	0.000	TeV	True

TABLE D.10: Model_E 3D fit parameters.

D.6 Model_F

Model_F is an adaptation of Model_E. Instead of modelling the excess in the lower half of the skymap from Fig. D.3 with a Gaussian, it is modelled with an ellipse. All components are described with power lay spectra.

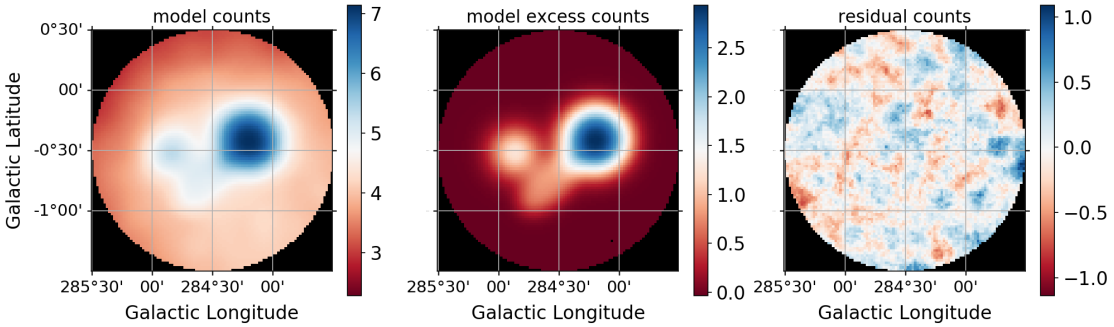

FIGURE D.7: Count map, excess map and residual to the observed data counts for model_F. The maps show the total counts summed over all energy bins. Black pixels are not regarded in the fit procedure.

Component	ΔC	P-value	significance [σ]
HESS J1023–575			
Disk	705	5.95×10^{-149}	26.0
HESS J1026–582			
Gaussian	115	4.55×10^{-23}	9.9
Jet cloud			
Ellipse	54	1.89×10^{-9}	6.0

TABLE D.11: Model_F component statistics.

name	initial_value	best fit value	error	unit	frozen
HESS J1023–575					
Disk					
lon_0	−75.803	−75.809	0.011	deg	False
lat_0	−0.406	−0.401	0.010	deg	False
r_0	0.286	0.253	0.017	deg	False
edge	0.050	0.244	0.067	deg	False
index	2.400	2.399	0.044		False
amplitude	2.500	3.397	0.246	10^{-12} cm^{-2}s^{-1}TeV^{-1}	False
reference	1.000	1.000	0.000	TeV	True
HESS J1026–582					
Gaussian					
lon_0	−75.181	−75.132	0.022	deg	False
lat_0	−0.534	−0.512	0.021	deg	False
sigma	0.140	0.125	0.016	deg	False
index	2.000	1.939	0.080		False
amplitude	1.000	0.668	0.151	10^{-12} cm^{-2}s^{-1}TeV^{-1}	False
reference	1.000	1.000	0.000	TeV	True
Jet cloud					
Ellipse					
lon_0	−75.535	−75.425	0.017	deg	False
lat_0	−0.711	−0.768	0.017	deg	False
semi_major	0.300	0.317	0.022	deg	False
e	0.900	0.865	0.055		False
theta	135.000	133.716	5.593	deg	False
edge	0.010	0.010	0.000	deg	True
index	2.100	2.137	0.118		False
amplitude	1.000	5.76	1.4	10^{-13} cm^{-2}s^{-1}TeV^{-1}	False
reference	1.000	1.000	0.000	TeV	True
Background					
norm	1.100	0.992	0.007		False
tilt	0.000	0.000	0.000		True
reference	1.000	1.000	0.000	TeV	True

TABLE D.12: Model_F 3D fit parameters.

D.7 Model_G

Model_G is an adaptation of model_F where HESS J1023–575 is modelled with a Gaussian instead of a disk.

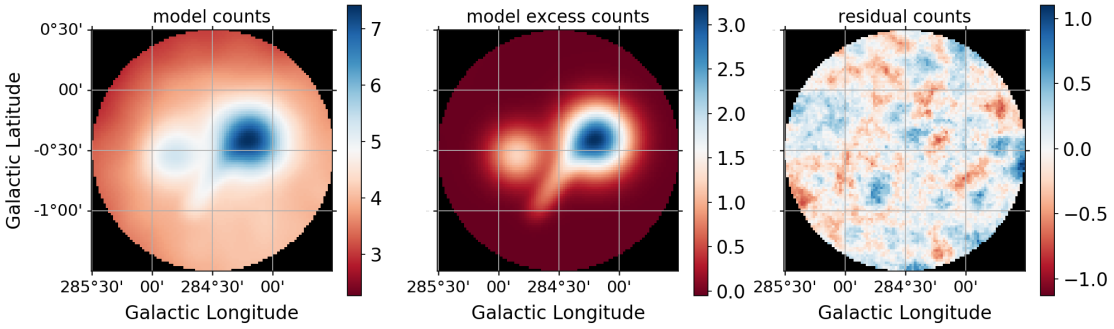

FIGURE D.8: Count map, excess map and residual to the observed data counts for model_G. The maps show the total counts summed over all energy bins. Black pixels are not regarded in the fit procedure.

Component	ΔC	P-value	significance [σ]
HESS J1023–575			
Gaussian	674	1.76×10^{-143}	25.5
HESS J1026–582			
Gaussian	129	4.01×10^{-26}	10.6
Jet cloud			
Ellipse	41	9.72×10^{-7}	4.9

TABLE D.13: Model_G component statistics.

name	initial_value	best fit value	error	unit	frozen
HESS J1023–575					
Gaussian					
lon_0	−75.803	−75.817	0.012	deg	False
lat_0	−0.406	−0.397	0.011	deg	False
sigma	0.180	0.174	0.009	deg	False
index	2.400	2.408	0.045		False
amplitude	2.500	3.985	0.31	10^{-12} cm^{-2}s^{-1}TeV^{-1}	False
reference	1.000	1.000	0.000	TeV	True
HESS J1026–582					
Gaussian					
lon_0	−75.181	−75.148	0.022	deg	False
lat_0	−0.534	−0.532	0.022	deg	False
sigma	0.140	0.141	0.018	deg	False
index	2.000	1.967	0.076		False
amplitude	1.000	0.816	0.178	10^{-12} cm^{-2}s^{-1}TeV^{-1}	False
reference	1.000	1.000	0.000	TeV	True
Jet cloud					
Ellipse					
lon_0	−75.535	−75.496	0.016	deg	False
lat_0	−0.711	−0.726	0.026	deg	False
semi_major	0.300	0.399	0.029	deg	False
e	0.900	1.000	0.000		False
theta	135.000	146.297	2.975	deg	False
edge	0.010	0.010	0.000	deg	True
index	2.100	2.132	0.144		False
amplitude	1.000	1.55	1.57	10^{-13} cm^{-2}s^{-1}TeV^{-1}	False
reference	1.000	1.000	0.000	TeV	True
Background					
norm	1.100	0.988	0.007		False
tilt	0.000	0.000	0.000		True
reference	1.000	1.000	0.000	TeV	True

TABLE D.14: Model_G 3D fit parameters.

D.8 Model_H

Model_H is an adaptation of model_F where the ellipse is replaced with two Gaussian components.

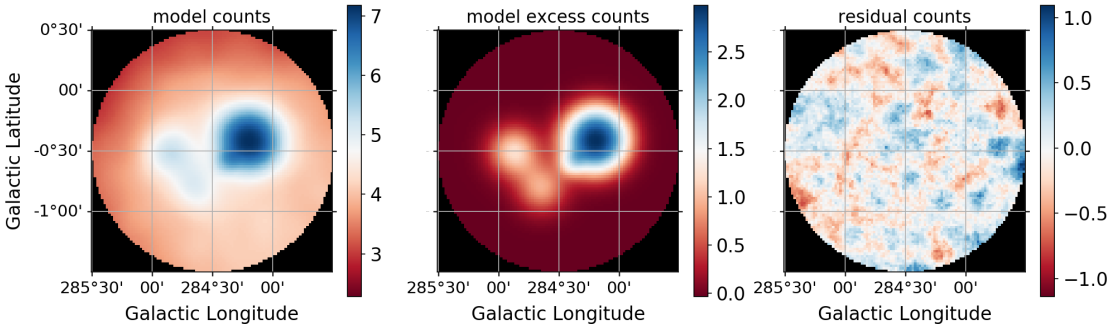

FIGURE D.9: Count map, excess map and residual to the observed data counts for model_H. The maps show the total counts summed over all energy bins. Black pixels are not regarded in the fit procedure.

Component	ΔC	P-value	significance [σ]
HESS J1023–575			
Disk	698	1.37×10^{-147}	25.9
HESS J1026–582			
Gaussian	104	8.81×10^{-21}	9.3
Hotspot 1			
Gaussian	18	2.45×10^{-3}	3.0
Hotspot 2			
Gaussian	41	7.99×10^{-8}	5.4

TABLE D.15: Model_H component statistics.

name	initial_value	best fit value	error	unit	frozen
HESS J1023–575					
Disk					
lon_0	−75.803	−75.810	0.011	deg	False
lat_0	−0.406	−0.399	0.010	deg	False
r_0	0.286	0.246	0.020	deg	False
edge	0.050	0.277	0.076	deg	False
index	2.400	2.414	0.044		False
amplitude	2.500	3.38	0.263	10^{-12} cm^{-2}s^{-1}TeV^{-1}	False
reference	1.000	1.000	0.000	TeV	True
HESS J1026–582					
Gaussian					
lon_0	−75.181	−75.125	0.022	deg	False
lat_0	−0.534	−0.501	0.021	deg	False
sigma	0.140	0.121	0.015	deg	False
index	2.000	1.923	0.076		False
amplitude	1.000	0.604	0.132	10^{-12} cm^{-2}s^{-1}TeV^{-1}	False
reference	1.000	1.000	0.000	TeV	True
Hotspot 1					
Gaussian					
lon_0	−75.535	−75.603	0.016	deg	False
lat_0	−0.711	−0.602	0.015	deg	False
sigma	0.061	0.025	0.015	deg	False
index	2.000	1.760	0.226		False
amplitude	1.000	0.074	0.05	10^{-12} cm^{-2}s^{-1}TeV^{-1}	False
reference	1.000	1.000	0.000	TeV	True
Hotspot 2					
Gaussian					
lon_0	−75.309	−75.355	0.031	deg	False
lat_0	−0.876	−0.801	0.033	deg	False
sigma	0.061	0.122	0.012	deg	False
index	2.000	2.192	0.103		False
amplitude	1.000	0.55	0.142	10^{-12} cm^{-2}s^{-1}TeV^{-1}	False
reference	1.000	1.000	0.000	TeV	True
Background					
norm	1.100	0.992	0.007		False
tilt	0.000	0.000	0.000		True
reference	1.000	1.000	0.000	TeV	True

TABLE D.16: Model_H 3D fit parameters.

D.9 Model_I

Model_I is an extension of model_F where an additional component is added to model the excess to the north-west of HESS J1023–575.

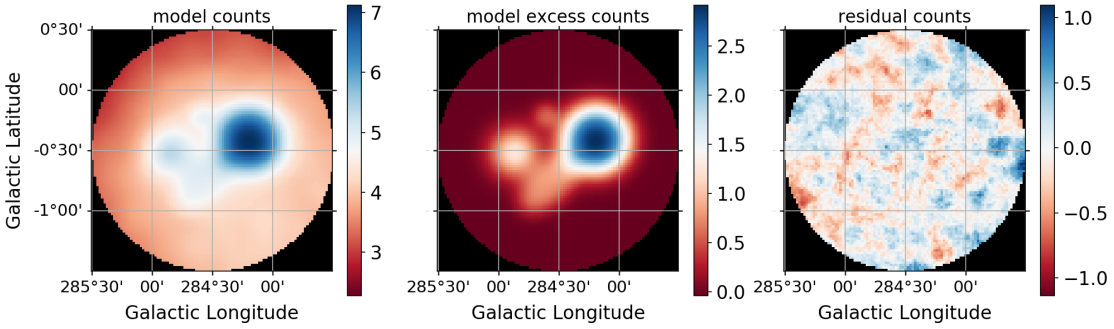

FIGURE D.10: Count map, excess map and residual to the observed data counts for model_I. The maps show the total counts summed over all energy bins. Black pixels are not regarded in the fit procedure.

Component	ΔC	P-value	significance [σ]
HESS J1023–575			
Disk	704	8.03×10^{-149}	26.0
HESS J1026–582			
Gaussian	113	9.60×10^{-23}	9.8
Jet cloud			
Ellipse	57	5.07×10^{-10}	6.2
Hotspot 3			
Gaussian	8	1.52×10^{-1}	1.4

TABLE D.17: Model_I component statistics.

name	initial_value	best fit value	error	unit	frozen
HESS J1023–575					
Disk					
lon_0	−75.803	−75.811	0.011	deg	False
lat_0	−0.406	−0.402	0.011	deg	False
r_0	0.286	0.254	0.010	deg	False
edge	0.050	0.228	0.050	deg	False
index	2.400	2.400	0.043		False
amplitude	2.500	3.402	0.189	10^{-12} cm^{-2}s^{-1}TeV^{-1}	False
reference	1.000	1.000	0.000	TeV	True
HESS J1026–582					
Gaussian					
lon_0	−75.181	−75.130	0.021	deg	False
lat_0	−0.534	−0.514	0.021	deg	False
sigma	0.140	0.121	0.013	deg	False
index	2.000	1.936	0.056		False
amplitude	1.000	0.643	0.119	10^{-12} cm^{-2}s^{-1}TeV^{-1}	False
reference	1.000	1.000	0.000	TeV	True
Jet cloud					
Ellipse					
lon_0	−75.535	−75.424	0.017	deg	False
lat_0	−0.711	−0.767	0.016	deg	False
semi_major	0.300	0.316	0.021	deg	False
e	0.900	0.862	0.052		False
theta	135.000	133.673	5.151	deg	False
edge	0.010	0.010	0.000	deg	True
index	2.100	2.141	0.112		False
amplitude	1.000	5.96	1.33	10^{-13} cm^{-2}s^{-1}TeV^{-1}	False
reference	1.000	1.000	0.000	TeV	True
Hotspot 3					
Gaussian					
lon_0	−75.450	−75.393	0.025	deg	False
lat_0	−0.183	−0.208	0.028	deg	False
sigma	0.050	0.027	0.017	deg	False
index	2.300	2.062	0.321		False
amplitude	1.000	0.88	0.5	10^{-13} cm^{-2}s^{-1}TeV^{-1}	False
reference	1.000	1.000	0.000	TeV	True
Background					
norm	1.100	0.991	0.007		False
tilt	0.000	0.000	0.000		True
reference	1.000	1.000	0.000	TeV	True

TABLE D.18: Model_I 3D fit parameters.

D.10 Model_J

Model_J is another extension of model_F where a diffuse component is added in the form of a disk.

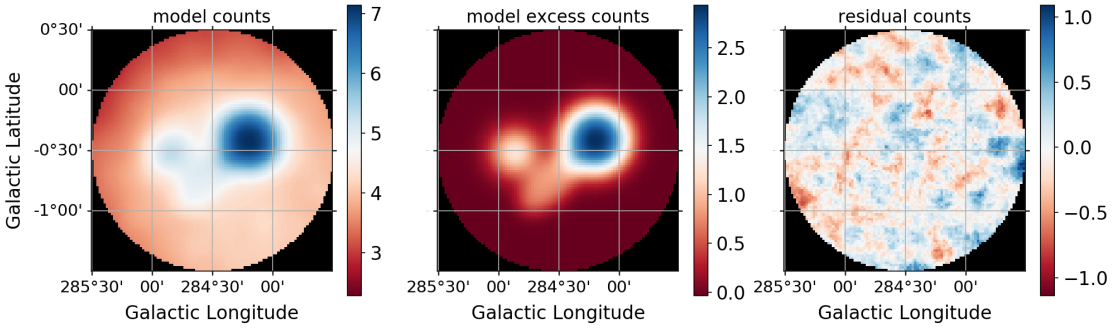

FIGURE D.11: Count map, excess map and residual to the observed data counts for model_J. The maps show the total counts summed over all energy bins. Black pixels are not regarded in the fit procedure.

Component	ΔC	P-value	significance [σ]
HESS J1023–575			
Disk	705	6.09×10^{-149}	26.0
HESS J1026–582			
Gaussian	114	4.61×10^{-23}	9.9
Jet cloud			
Ellipse	54	1.90×10^{-9}	6.0
Diffuse			
Disk	0	1.00	0

TABLE D.19: Model_J component statistics.

name	initial_value	best fit value	error	unit	frozen
HESS J1023–575					
Disk					
lon_0	−75.803	−75.809	0.011	deg	False
lat_0	−0.406	−0.401	0.011	deg	False
r_0	0.286	0.253	0.012	deg	False
edge	0.050	0.244	0.058	deg	False
index	2.400	2.399	0.043		False
amplitude	2.500	3.397	0.196	10^{-12} cm^{-2}s^{-1}TeV^{-1}	False
reference	1.000	1.000	0.000	TeV	True
HESS J1026–582					
Gaussian					
lon_0	−75.181	−75.132	0.023	deg	False
lat_0	−0.534	−0.512	0.021	deg	False
sigma	0.140	0.125	0.013	deg	False
index	2.000	1.938	0.059		False
amplitude	1.000	0.666	0.119	10^{-12} cm^{-2}s^{-1}TeV^{-1}	False
reference	1.000	1.000	0.000	TeV	True
Jet cloud					
Ellipse					
lon_0	−75.535	−75.425	0.015	deg	False
lat_0	−0.711	−0.768	0.018	deg	False
semi_major	0.300	0.317	0.022	deg	False
e	0.900	0.865	0.057		False
theta	135.000	133.719	5.186	deg	False
edge	0.010	0.010	0.000	deg	True
index	2.100	2.138	0.115		False
amplitude	1.000	5.77	0.92	10^{-13} cm^{-2}s^{-1}TeV^{-1}	False
reference	1.000	1.000	0.000	TeV	True
Diffuse					
Disk					
lon_0	−75.733	−75.733	0.000	deg	True
lat_0	−0.338	−0.338	0.000	deg	True
r_0	0.990	0.990	0.000	deg	True
edge	0.000	0.000	0.000	deg	True
index	2.300	5.746	0.000		False
amplitude	0.000	0.0	0.0	10^{+00} cm^{-2}s^{-1}TeV^{-1}	False
reference	1.000	1.000	0.000	TeV	True
Background					
norm	1.100	0.992	0.007		False
tilt	0.000	0.000	0.000		True
reference	1.000	1.000	0.000	TeV	True

Table D.20: Model_J 3D fit parameters.

D.11 Model_K

Model_K is the most complex model in terms of free parameters. In addition to a disk for HESS J1023–575 and a Gaussian for HESS J1026–582, four Gaussian components are fitted.

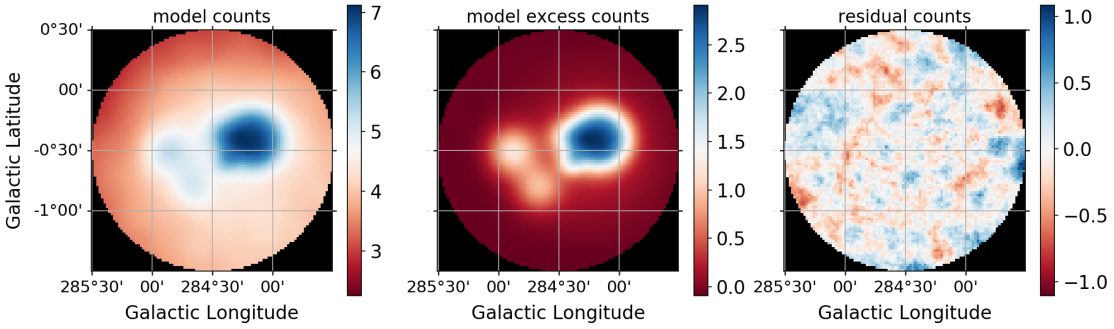

FIGURE D.12: Count map, excess map and residual to the observed data counts for model_K. The maps show the total counts summed over all energy bins. Black pixels are not regarded in the fit procedure.

Component	ΔC	P-value	significance [σ]
HESS J1023–575			
Disk	427	3.76×10^{-89}	20.0
HESS J1026–582			
Gaussian	92	2.88×10^{-18}	8.7
Hotspot 1			
Gaussian	27	5.68×10^{-5}	4.0
Hotspot 2			
Gaussian	30	1.57×10^{-5}	4.3
Hotspot 3			
Gaussian	17	5.12×10^{-3}	2.8
Hotspot 4			
Gaussian	39	2.08×10^{-7}	5.2

TABLE D.21: Model_K component statistics.

name	initial_value	best fit value	error	unit	frozen
HESS J1023–575					
Disk					
lon_0	−75.803	−75.842	0.016	deg	False
lat_0	−0.406	−0.398	0.013	deg	False
r_0	0.286	0.234	0.016	deg	False
edge	0.050	0.167	0.067	deg	False
index	2.400	2.414	0.060		False
amplitude	2.500	2.545	0.402	10^{-12} cm^{-2}s^{-1}TeV^{-1}	False
reference	1.000	1.000	0.000	TeV	True
HESS J1026–582					
Gaussian					
lon_0	−75.181	−75.112	0.024	deg	False
lat_0	−0.534	−0.504	0.022	deg	False
sigma	0.140	0.116	0.015	deg	False
index	2.000	1.908	0.071		False
amplitude	1.000	0.536	0.123	10^{-12} cm^{-2}s^{-1}TeV^{-1}	False
reference	1.000	1.000	0.000	TeV	True
Hotspot 1					
Gaussian					
lon_0	−75.535	−75.604	0.015	deg	False
lat_0	−0.711	−0.601	0.015	deg	False
sigma	0.061	0.028	0.015	deg	False
index	2.000	1.849	0.205		False
amplitude	1.000	0.112	0.063	10^{-12} cm^{-2}s^{-1}TeV^{-1}	False
reference	1.000	1.000	0.000	TeV	True
Hotspot 2					
Gaussian					
lon_0	−75.309	−75.332	0.030	deg	False
lat_0	−0.876	−0.806	0.039	deg	False
sigma	0.061	0.110	0.025	deg	False
index	2.000	2.186	0.158		False
amplitude	1.000	0.434	0.176	10^{-12} cm^{-2}s^{-1}TeV^{-1}	False
reference	1.000	1.000	0.000	TeV	True
Hotspot 3					
Gaussian					
lon_0	−75.450	284.431	0.045	deg	False
lat_0	−0.183	−0.388	0.036	deg	False
sigma	0.050	0.077	0.034	deg	False
index	2.300	2.626	0.259		False
amplitude	1.000	4.09	2.35	10^{-13} cm^{-2}s^{-1}TeV^{-1}	False
reference	1.000	1.000	0.000	TeV	True
Hotspot 4					
Gaussian					
lon_0	−76.283	284.250	0.000	deg	False
lat_0	−0.467	−0.471	0.127	deg	False
sigma	0.050	0.419	0.147	deg	False
index	2.300	2.339	0.158		False
amplitude	1.000	2077.0	1024.0	10^{-15} cm^{-2}s^{-1}TeV^{-1}	False
reference	1.000	1.000	0.000	TeV	True
Background					
norm	1.100	0.978	0.010		False
tilt	0.000	0.000	0.000		True
reference	1.000	1.000	0.000	TeV	True

TABLE D.22: Model_K 3D fit parameters.

Appendix E

3D fit Parameters: Region B

The details of the model probed in the 3D fit analysis of the RoI region B in Sec. 5.5.2 is presented in the following. The parameter tables show the names of the components in the fit, the initial and best fit values, the statistical errors as well as the units and if the parameter is frozen or not (meaning that the parameters is fixed or free to be optimised in the fit). For spatial components, the type of spatial model (i.e. Gaussian, disk or ellipse) is stated under each component name.

The initial values for the spatial components were determined manually by assessing the sky maps by eye.

E.1 Model_A

Model_A is the only model fitted to the region of the two hotspots HS B1 and HS B2. It consists of two symmetrical 2-dimensional Gaussians.

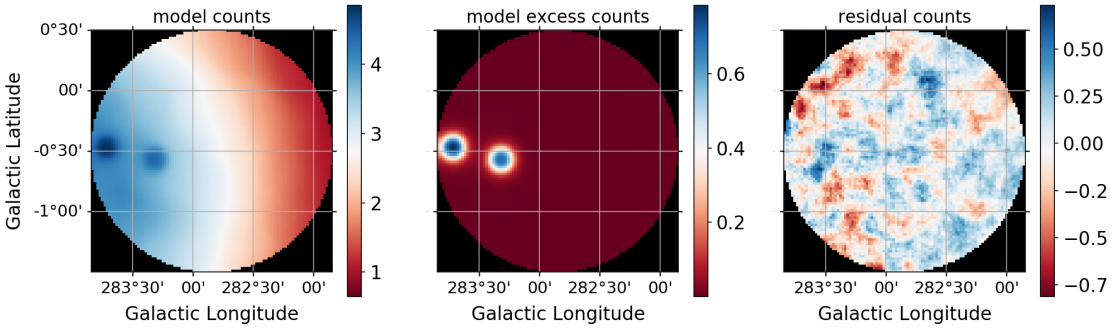

FIGURE E.1: Count map, excess map and residual to the observed data counts for model_A. The maps show the total counts summed over all energy bins. Black pixels are not regarded in the fit procedure.

Component	ΔC	P-value	significance [σ]
Hotspot B1 Gaussian	16	7.85×10^{-3}	2.7
Hotspot B1 Gaussian	13	2.08×10^{-2}	2.3

TABLE E.1: Model_A component statistics.

name	initial_value	best fit value	error	unit	frozen
Hotspot B1 Gaussian					
lon_0	−76.267	−76.284	0.002	deg	False
lat_0	−0.467	−0.460	0.000	deg	False
sigma	0.010	0.003	0.000	deg	False
index	2.300	2.660	0.292		False
amplitude	2.500	3.176	1.149	10^{-12} cm^{-2}s^{-1}TeV^{-1}	False
reference	1.000	1.000	0.000	TeV	True
Hotspot B2 Gaussian					
lon_0	−76.667	−76.683	0.003	deg	False
lat_0	−0.583	−0.575	0.000	deg	False
sigma	0.010	0.002	0.000	deg	False
index	2.300	2.661	0.341		False
amplitude	2.500	3.292	1.271	10^{-12} cm^{-2}s^{-1}TeV^{-1}	False
reference	1.000	1.000	0.000	TeV	True
Background					
norm	1.100	1.001	0.007		False
tilt	0.000	0.000	0.000		True
reference	1.000	1.000	0.000	TeV	True

TABLE E.2: Model_A 3D fit parameters.

Appendix F

3D fit Parameters: Region E

The details of the model probed in the 3D fit analysis of the RoI region E in Sec. 5.5.3 is presented in the following. The parameter tables show the names of the components in the fit, the initial and best fit values, the statistical errors as well as the units and if the parameter is frozen or not (meaning that the parameters is fixed or free to be optimised in the fit). For spatial components, the type of spatial model (i.e. Gaussian, disk or ellipse) is stated under each component name.

The initial values for the spatial components were determined manually by assessing the sky maps by eye.

F.1 Model_A

Model_A consists of a single 2-dimensional Gaussian and is the only model fitted to the hotspot HS E.

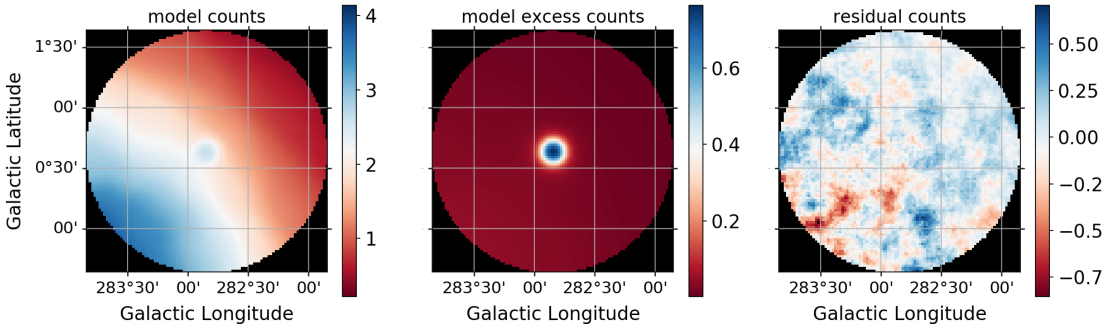

FIGURE F.1: Count map, excess map and residual to the observed data counts for model_A. The maps show the total counts summed over all energy bins. Black pixels are not regarded in the fit procedure.

Component	ΔC	P-value	significance [σ]
Hotspot E			
Gaussian	29	2.82×10^{-5}	4.2

TABLE F.1: Model_A component statistics.

name	initial_value	best fit value	error	unit	frozen
Hotspot E					
Gaussian					
lon_0	−77.150	−77.157	0.012	deg	False
lat_0	0.633	0.637	0.011	deg	False
sigma	0.100	0.012	0.015	deg	False
index	2.300	2.531	0.270		False
amplitude	2.500	0.429	0.14	10^{-12} cm^{-2}s^{-1}TeV^{-1}	False
reference	1.000	1.000	0.000	TeV	True
Background					
norm	1.100	1.013	0.009		False
tilt	0.000	0.000	0.000		True
reference	1.000	1.000	0.000	TeV	True

TABLE F.2: Model_A 3D fit parameters.

Appendix G

Simulating a shell of gas

For the following examples, a spherical shell of atomic or molecular gas with a width of $w_s = 15\,\mathrm{pc}$, with $r_i = 30\,\mathrm{pc}$ and $r_o = 45\,\mathrm{pc}$ is placed at the origin of a coordinate system $[x, y, z]$ that spans $[200, 200, 500]\,\mathrm{pc}$ and is located at $6\,\mathrm{kpc}$ from an observer, with the line of sight (LOS) along the z-axis. The environment around and inside the shell is filled with a gas of density n_{env} and n_{inner} respectively, while the spherical shell itself is filled with a gas of density n_{shell}. Figure G.1 shows a sketch of the set up.

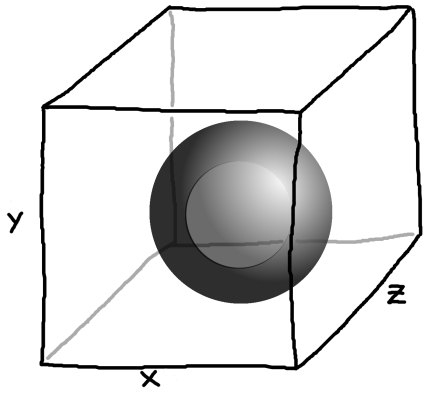

FIGURE G.1: Sketch of a simulated shell.

To get a direct comparison to the observed molecular clouds around Westerlund 2 in H I and CO data as discussed in Sec. 5.6.3, the *arc* cloud is modelled as a cap of the shell for $x >= 0.55 \cdot r_o$. This cap is removed from the rest of the spherical shell and is regarded as a second component that is observed separately. The environment of the cap is thereby *not* filled with gas. Projection effects are neglected in the following.

For this example, the densities are $n_{\mathrm{env}} = 10\,\mathrm{cm}^{-3}$, $n_{\mathrm{inner}} = 5\,\mathrm{cm}^{-3}$ and $n_{\mathrm{shell}} = 50\,\mathrm{cm}^{-3}$. Figure G.2 (*left*) shows the resulting contour map of the column density resulting from a projection along the observer's LOS. The column density of the sphere and its environment is shown in orange, overlayed with the column density contours of the cap in blue. The inner and outer radius of the shell are marked with grey circles. The *right* panel shows

the according radial distribution of the relative column density. The position and width of the simulated shell is marked in grey.

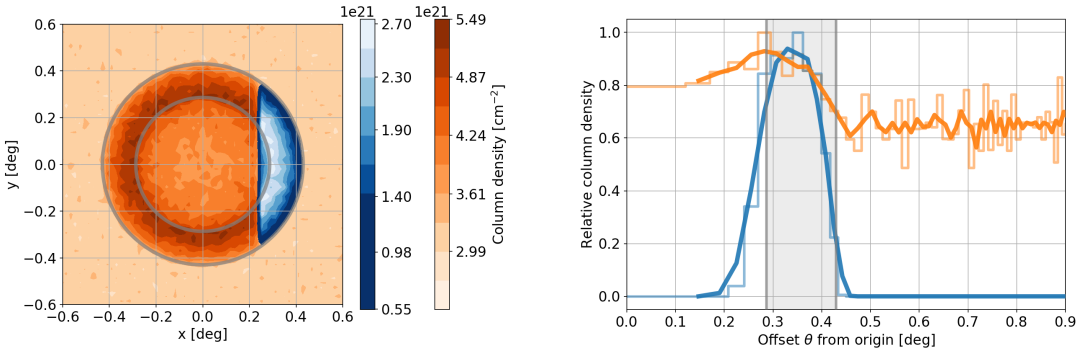

FIGURE G.2: *Left*: Column density map of a simulated spherical shell filled with a gas of a given density in an environment with a lower density (orange contours). A cap of the shell (blue contours) is removed from the shell and regarded separately. See main text for simulation details. *Right*: Colour coded radial distributions of the relative column density of the two components around the center of the projected shell. The thick orange and blue lines show 3-bin averages of the respective histograms of the same colour.

The radial column density distribution of the projected shell and cap show similarities to the observed distributions of the molecular shell and the *arc* cloud in Fig. 5.55. The radial density distribution of the shell peaks at a lower θ than the distribution of the cap. Furthermore, it can be seen that the shell's density peaks around r_{inner} whereas both curves show a decrease towards r_{outer} and then stabilise to the environment's relative density for larger offsets. This shows how the extension and width of the shell can be deduced from the radial profile of the column density.

Additionally, the orientation of the spherical cap towards the LOS can be roughly deduced from the column density map and radial density profiles. The plots in Fig. G.3 show the column density map (*left*) and relative radial densities (*right*) as in Fig. G.2 with the cap rotated around the y-axis towards the observer by different angles φ_y. It can be seen that at lower offsets the radial density distribution of the cap decreases when the cap is rotated towards $\varphi_y \sim 0$.

The column density map or profile can furthermore be used to approximate the shell density n_{shell}. To complement the following explanation, the concept is illustrated in Fig. G.4.

The mean column density of the projected shell's environment is expected to be

$$b_0 = n_{\mathrm{env}} \cdot dz, \tag{G.1}$$

with dz being the depth through the volume along the LOS. If this depth is known, n_{env} can be calculated by approximating b_0 with the mean column density of bins with $\theta > r_o$ from the radial density distribution, or by extracting b_0 from another appropriate region

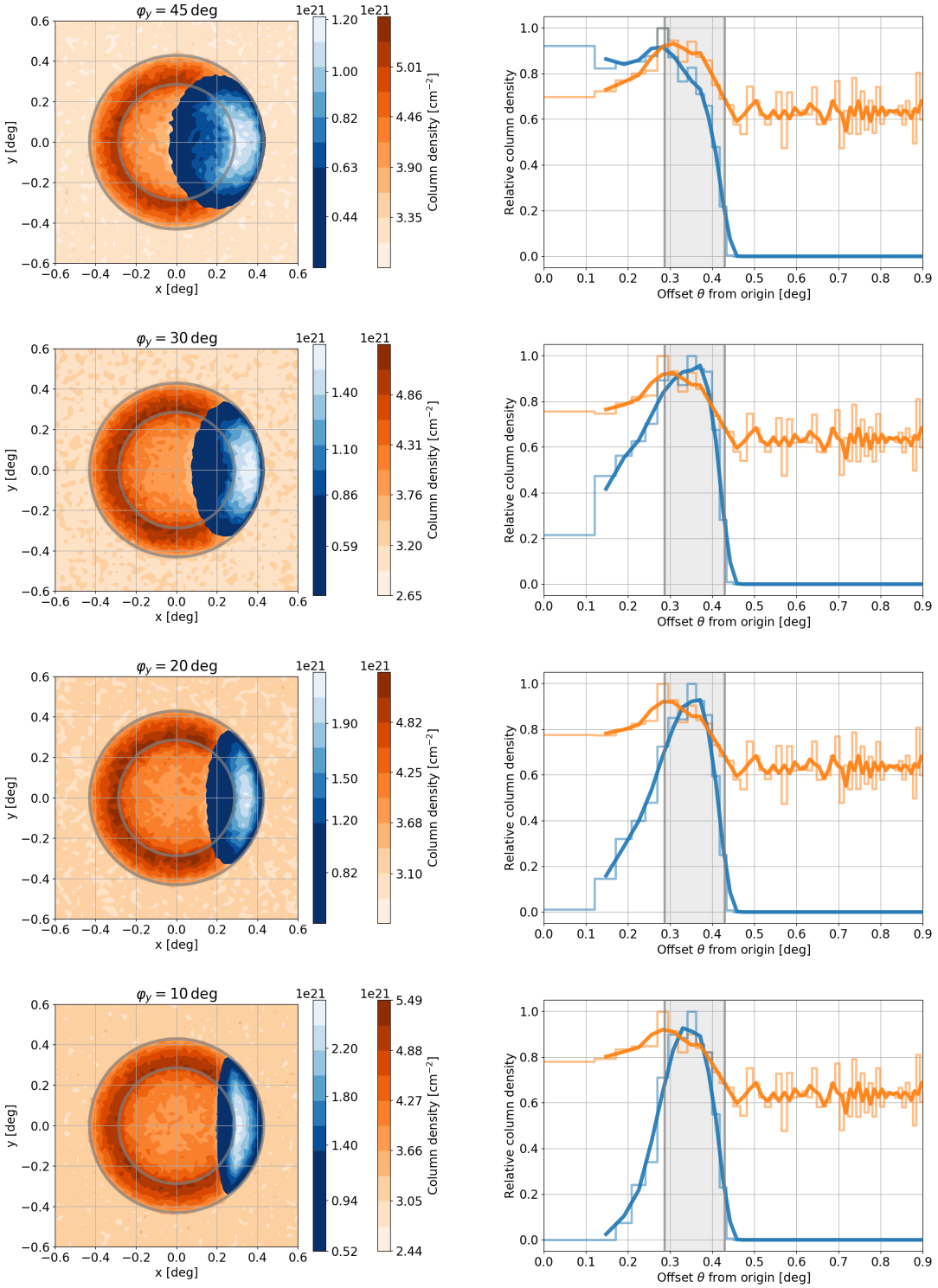

FIGURE G.3: Column density maps (*left*) and relative radial column density distributions (*right*) as shown in Fig. G.2 but for the cap rotated by φ_y around the y-axis.

of the column density map. At the centre of the projected shell, the mean column density is expected to be

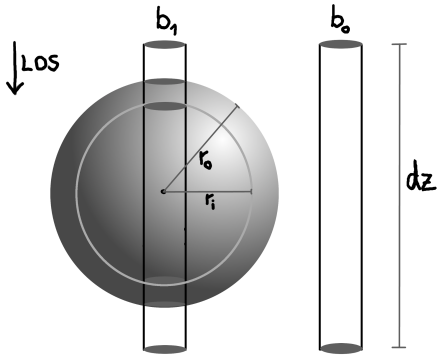

FIGURE G.4: Illustration of column density composition through the projected centre of the spherical shell and through its environment along the LOS.

$$b_1 \approx n_{\text{env}} \cdot (dz - 2w_s - 2r_i) + n_{\text{shell}} \cdot 2w_s + n_{\text{inner}} \cdot 2r_i \ , \tag{G.2}$$

with $w_s = r_o - r_i$. This holds if the projected area of the column perpendicular to the LOS is small enough so that the transitions between the different densities are approximately flat to the LOS. This b_1 can be estimated either by extracting an appropriate density value from the column density map or by approximating it with the first bin of the density profile. Combining the two equations above and rearranging them yields

$$n_{\text{shell}} \approx \frac{b_1 - b_0}{2w_s} - n_{\text{env}} \cdot \left(1 + \frac{r_i}{w_s}\right) - n_{\text{inner}} \cdot \frac{r_i}{w_s} \ . \tag{G.3}$$

If n_{env} and n_{inner} are known or by assuming values (e.g. by an educated guess) the density of the shell can thus be deduced.

It should be noted that the resolution of the column density map and of the radial density profile limit the precision of these results and conclusions that can be inferred from the density distributions. Furthermore, this simulation assumes an *ideal* shell, which may not be appropriate in practice.

Bibliography

[1] Wenger, M., Ochsenbein, F., Egret, D., *et al.* The SIMBAD astronomical database - The CDS reference database for astronomical objects. *Astronomy and Astrophysics Supplement Series*, 143(1):9–22, 2000. doi:10.1051/aas:2000332.

[2] H. E. S. S. Collaboration, A. Abramowski, F. Acero, *et al.* Revisiting the Westerlund 2 field with the HESS telescope array. *Astronomy & Astrophysics*, 525:A46, January 2011. doi:10.1051/0004-6361/201015290.

[3] N. Furukawa, A. Ohama, T. Fukuda, *et al.* THE JET AND ARC MOLECULAR CLOUDS TOWARD WESTERLUND 2, RCW 49, AND HESS J1023–575; 12CO AND13CO (J= 2-1 andJ= 1-0) OBSERVATIONS WITH NANTEN2 AND MOPRA TELESCOPE. *The Astrophysical Journal*, 781(2):70, January 2014. doi:10.1088/0004-637x/781/2/70.

[4] M. Walter and A.W. Wolfendale. Early history of cosmic particle physics. *Eur. Phys. J. H*, 37:323–358, 2012. doi:10.1140/epjh/e2012-30020-1.

[5] M. Amenomori, Y. W. Bao, X. J. Bi, *et al.* First Detection of Photons with Energy beyond 100 TeV from an Astrophysical Source. *Phys. Rev. Lett.*, 123:051101, July 2019. doi:10.1103/PhysRevLett.123.051101.

[6] Thomas K. Gaisser, Ralph Engel, and Elisa Resconi. *Cosmic Rays and Particle Physics.* Cambridge University Press, 2 edition, 2016. doi:10.1017/CBO9781139192194.

[7] Malcolm S. Longair. *High Energy Astrophysics.* Cambridge University Press, 3 edition, 2011. doi:10.1017/CBO9780511778346.

[8] Alessandro De Angelis and Mário Pimenta. *Introduction to Particle and Astroparticle Physics.* Springer International Publishing, 2018. doi:10.1007/978-3-319-78181-5.

[9] W. Hofmann and J. A. Hinton. *Cosmic Particle Accelerators*, pages 827–863. Springer International Publishing, Cham, 2020. doi:10.1007/978-3-030-34245-6_13.

[10] A. De Angelis and M. Mallamaci. Gamma-ray astrophysics. *The European Physical Journal Plus*, 133(8), August 2018. doi:10.1140/epjp/i2018-12181-0.

[11] J.A. Hinton and W. Hofmann. Teraelectronvolt Astronomy. *Annual Review of Astronomy and Astrophysics*, 47(1):523–565, 2009. doi:10.1146/annurev-astro-082708-101816.

[12] D. J. Bird, S. C. Corbato, H. Y. Dai, *et al.* Detection of a cosmic ray with measured energy well beyond the expected spectral cutoff due to cosmic microwave radiation. *The Astrophysical Journal*, 441:144, March 1995. doi:10.1086/175344.

[13] ENRICO Fermi. On the Origin of the Cosmic Radiation. *Phys. Rev.*, 75:1169–1174, April 1949. doi:10.1103/PhysRev.75.1169.

[14] Mario A. Riquelme and Anatoly Spitkovsky. ELECTRON INJECTION BY WHISTLER WAVES IN NON-RELATIVISTIC SHOCKS. *The Astrophysical Journal*, 733(1):63, May 2011. doi:10.1088/0004-637x/733/1/63.

[15] Damiano Caprioli, Ana-Roxana Pop, and Anatoly Spitkovsky. SIMULATIONS AND THEORY OF ION INJECTION AT NON-RELATIVISTIC COLLISIONLESS SHOCKS. *The Astrophysical Journal*, 798(2):L28, December 2014. doi:10.1088/2041-8205/798/2/l28.

[16] A.R. Bell. Cosmic ray acceleration. *Astroparticle Physics*, 43:56 – 70, 2013. doi:https://doi.org/10.1016/j.astropartphys.2012.05.022.

[17] Vladimir Ptuskin, Vladimir Zirakashvili, and Eun-Suk Seo. SPECTRUM OF GALACTIC COSMIC RAYS ACCELERATED IN SUPERNOVA REMNANTS. *The Astrophysical Journal*, 718(1):31–36, June 2010. doi:10.1088/0004-637x/718/1/31.

[18] Kumiko Kotera and Angela V. Olinto. The Astrophysics of Ultrahigh-Energy Cosmic Rays. *Annual Review of Astronomy and Astrophysics*, 49(1):119–153, 2011. doi:10.1146/annurev-astro-081710-102620.

[19] Stephen P. Reynolds. Supernova Remnants at High Energy. *Annual Review of Astronomy and Astrophysics*, 46(1):89–126, 2008. doi:10.1146/annurev.astro.46.060407.145237.

[20] Yuan-Pei Yang and Bing Zhang. Synchrotron Radiation from Electrons with a Pitch-angle Distribution. *The Astrophysical Journal*, 864(1):L16, August 2018. doi:10.3847/2041-8213/aada4f.

[21] Stefan Funk. Ground- and Space-Based Gamma-Ray Astronomy. *Annual Review of Nuclear and Particle Science*, 65(1):245–277, 2015. doi:10.1146/annurev-nucl-102014-022036.

[22] Dmitry Khangulyan, Felix Aharonian, Carlo Romoli, and Andrew Taylor. Extension of the synchrotron radiation of electrons to very high energies in clumpy environments. *arXiv e-prints*, page arXiv:2003.00927, March 2020.

[23] Joshua P. Ellis. TikZ-Feynman: Feynman diagrams with TikZ. *Computer Physics Communications*, 210:103 – 123, 2017. doi:https://doi.org/10.1016/j.cpc.2016.08.019.

[24] Hale Bradt. *Astrophysics Processes: The Physics of Astronomical Phenomena*. Cambridge University Press, 2008. doi:10.1017/CBO9780511802249.

[25] H.E.S.S. Collaboration, Abdalla, H., Abramowski, A., *et al.* H.E.S.S. observations of RX J1713.7-3946 with improved angular and spectral resolution: Evidence for gamma-ray emission extending beyond the X-ray emitting shell. *Astronomy & Astrophysics*, 612:A6, 2018. doi:10.1051/0004-6361/201629790.

[26] H.E.S.S. Collaboration, Abdalla, H., Abramowski, A., *et al.* A search for new supernova remnant shells in the Galactic plane with H.E.S.S. *Astronomy & Astrophysics*, 612:A8, 2018. doi:10.1051/0004-6361/201730737.

[27] S. Ohm, J. A. Hinton, and R. White. γ-ray emission from the Westerlund 1 region. *Monthly Notices of the Royal Astronomical Society*, 434(3):2289–2294, July 2013. doi:10.1093/mnras/stt1170.

[28] M. Ackermann, M. Ajello, A. Allafort, *et al.* A Cocoon of Freshly Accelerated Cosmic Rays Detected by Fermi in the Cygnus Superbubble. *Science*, 334(6059):1103–1107, 2011. doi:10.1126/science.1210311.

[29] Sun, Xiao-Na, Yang, Rui-Zhi, Liang, Yun-Feng, *et al.* Diffuse γ-ray emission toward the massive star-forming region, W40. *Astronomy & Astrophysics*, 639:A80, 2020. doi:10.1051/0004-6361/202037580.

[30] M. M. Kaufman Bernadó and G. E. Romero. Gamma-Ray Emission from Microquasars. *Proceedings of the International Astronomical Union*, 1(S230):86–90, 2005. doi:10.1017/S1743921306007964.

[31] VALENTÍ BOSCH-RAMON and DMITRY KHANGULYAN. UNDERSTANDING THE VERY-HIGH-ENERGY EMISSION FROM MICROQUASARS. *International Journal of Modern Physics D*, 18(03):347–387, 2009. doi:10.1142/S0218271809014601.

[32] Fermi LAT Collaboration, AA Abdo, M Ackermann, *et al.* Modulated high-energy gamma-ray emission from the microquasar Cygnus X-3. *Science (New York, N.Y.)*, 326(5959):1512—1516, December 2009. doi:10.1126/science.1182174.

[33] A. Abeysekara, A. Albert, Romulo Alfaro, *et al.* Very-high-energy particle acceleration powered by the jets of the microquasar SS 433. *Nature*, 562, October 2018. doi:10.1038/s41586-018-0565-5. [Erratum: Nature 564, E38 (2018)].

[34] A. Balzer, M. Füßling, P. Hofverberg, and R. D. Parsons. The Performance of the H.E.S.S.Target of Opportunity Alert System. *Journal of Physics: Conference Series*, 664(8):082002, December 2015. doi:10.1088/1742-6596/664/8/082002.

[35] T. Ashton, M. Backes, A. Balzer, *et al.* A NECTAr-based upgrade for the Cherenkov cameras of the H.E.S.S. 12-meter telescopes. *Astroparticle Physics*, 118:102425, 2020. doi:https://doi.org/10.1016/j.astropartphys.2019.102425.

[36] P. A. Čerenkov. Visible Radiation Produced by Electrons Moving in a Medium with Velocities Exceeding that of Light. *Phys. Rev.*, 52:378–379, August 1937. doi:10.1103/PhysRev.52.378.

[37] I. M. Frank and I. E. Tamm. Coherent visible radiation of fast electrons passing through matter. *Compt. Rend. Acad. Sci. URSS*, 14(3):109–114, 1937. doi:10.1007/978-3-642-74626-0_2.

[38] Walter Heitler. *The quantum theory of radiation; 3rd ed.* International series of monographs on physics. Clarendon Press, Oxford, 1954.

[39] K BERNLOHR. The optical system of the H.E.S.S. imaging atmospheric Cherenkov telescopes. Part I: layout and components of the system. *Astroparticle Physics*, 20(2):111–128, November 2003. doi:10.1016/s0927-6505(03)00171-3.

[40] M. Gaug, S. Fegan, A. M. W. Mitchell, *et al.* Using Muon Rings for the Calibration of the Cherenkov Telescope Array: A Systematic Review of the Method and Its Potential Accuracy. *The Astrophysical Journal Supplement Series*, 243(1):11, July 2019. doi:10.3847/1538-4365/ab2123.

[41] F. Aharonian, A.G. Akhperjanian, K.-M. Aye, *et al.* Calibration of cameras of the H.E.S.S. detector. *Astroparticle Physics*, 22(2):109 – 125, 2004. doi:https://doi.org/10.1016/j.astropartphys.2004.06.006.

[42] S. Funk, G. Hermann, J. Hinton, *et al.* The trigger system of the H.E.S.S. telescope array. *Astroparticle Physics*, 22(3-4):285–296, November 2004. doi:10.1016/j.astropartphys.2004.08.001.

[43] Johannes Knapp Fabian Schmidt. CORSIKA Shower Images. `https://www-zeuthen.desy.de/~jknapp/fs/showerimages.html`, accessed July 2020.

[44] Konrad Bernlöher. Air shower Cherenkov light simulations. `https://www.mpi-hd.mpg.de/hfm/CosmicRay/ChLight/ChLat.html`, accessed July 2020.

[45] M. Holler, J.-P. Lenain, M. de Naurois, R. Rauth, and D.A. Sanchez. A Run-Wise Simulation and Analysis Framework for Imaging Atmospheric Cherenkov Telescope Arrays. *Astroparticle Physics*, page 102491, 2020. doi:https://doi.org/10.1016/j.astropartphys.2020.102491.

[46] D. Heck, J. Knapp, J.N. Capdevielle, G. Schatz, and T. Thouw. CORSIKA: A Monte Carlo code to simulate extensive air showers. February 1998.

[47] Konrad Bernlöher. Simulation of imaging atmospheric Cherenkov telescopes with CORSIKA and sim_telarray. *Astroparticle Physics*, 30(3):149 – 158, 2008. doi:https://doi.org/10.1016/j.astropartphys.2008.07.009.

[48] A. M. Hillas. Cerenkov light images of EAS produced by primary gamma rays and by nuclei. In F. C. Jones, editor, *Proceedings of the 19th International Cosmic Ray Conference*, volume 3, pages 445–448, La Jolla, August 1985.

[49] Mathieu de Naurois. Analysis methods for Atmospheric Cerenkov Telescopes. In *7th Workshop on Towards a Network of Atmospheric Cherenkov Detectors 2005*, pages 149–161, July 2006.

[50] S. Ohm, C. van Eldik, and K. Egberts. γ/hadron separation in very-high-energy γ-ray astronomy using a multivariate analysis method. *Astroparticle Physics*, 31(5):383 – 391, 2009. doi:https://doi.org/10.1016/j.astropartphys.2009.04.001.

[51] W. Hofmann, I. Jung, A. Konopelko, *et al.* Comparison of techniques to reconstruct VHE gamma-ray showers from multiple stereoscopic Cherenkov images. *Astroparticle Physics*, 12(3):135 – 143, 1999. doi:https://doi.org/10.1016/S0927-6505(99)00084-5.

[52] R. Cornils, S. Gillessen, I. Jung, *et al.* The optical system of the H.E.S.S. imaging atmospheric Cherenkov telescopes. Part II: mirror alignment and point spread function. *Astroparticle Physics*, 20(2):129–143, November 2003. doi:10.1016/s0927-6505(03)00172-5.

[53] S. Gillessen. Arcsecond level pointing of the HESS telescopes. In *28th International Cosmic Ray Conference*, pages 2899–2902, July 2003.

[54] M. Lemoine-Goumard, B. Degrange, and M. Tluczykont. Selection and 3D-reconstruction of gamma-ray-induced air showers with a stereoscopic system of atmospheric Cherenkov telescopes. *Astroparticle Physics*, 25(3):195 – 211, 2006. doi:https://doi.org/10.1016/j.astropartphys.2006.01.005.

[55] Mathieu de Naurois and Loïc Rolland. A high performance likelihood reconstruction of γ-rays for imaging atmospheric Cherenkov telescopes. *Astroparticle Physics*, 32(5):231 – 252, 2009. doi:https://doi.org/10.1016/j.astropartphys.2009.09.001.

[56] R.D. Parsons and J.A. Hinton. A Monte Carlo template based analysis for air-Cherenkov arrays. *Astroparticle Physics*, 56:26 – 34, 2014. doi:https://doi.org/10.1016/j.astropartphys.2014.03.002.

[57] Tim Lukas Holch, Idan Shilon, Matthias Büchele, *et al.* Probing Convolutional Neural Networks for Event Reconstruction in γ-Ray Astronomy with Cherenkov Telescopes. *Proceedings of Science*, ICRC2017:795, 2018. doi:10.22323/1.301.0795.

[58] I. Shilon, M. Kraus, M. Büchele, *et al.* Application of deep learning methods to analysis of imaging atmospheric Cherenkov telescopes data. *Astroparticle Physics*, 105:44 – 53, 2019. doi:https://doi.org/10.1016/j.astropartphys.2018.10.003.

[59] Constantin Steppa and Tim L. Holch. HexagDLy - Processing hexagonally sampled data with CNNs in PyTorch. *SoftwareX*, 9:193 – 198, 2019. doi:https://doi.org/10.1016/j.softx.2019.02.010.

[60] Parsons, R. D. and Ohm, S. Background rejection in atmospheric Cherenkov telescopes using recurrent convolutional neural networks. *Eur. Phys. J. C*, 80(5):363, 2020. doi:10.1140/epjc/s10052-020-7953-3.

[61] Aharonian, F., Akhperjanian, A. G., Bazer-Bachi, A. R., *et al.* Observations of the Crab nebula with HESS. *Astronomy & Astrophysics*, 457(3):899–915, 2006. doi:10.1051/0004-6361:20065351.

[62] David Berge, S. Funk, and J. Hinton. Background Modelling in Very-High-Energy gamma-ray Astronomy. *Astron. Astrophys.*, 466:1219–1229, 2007. doi:10.1051/0004-6361:20066674.

[63] T.-P. Li and Y.-Q. Ma. Analysis methods for results in gamma-ray astronomy. *The Astrophysical Journal*, 272:317–324, September 1983. doi:10.1086/161295.

[64] W. Cash. Parameter estimation in astronomy through application of the likelihood ratio. *The Astrophysical Journal*, 228:939–947, March 1979. doi:10.1086/156922.

[65] Kaastra, J. S. On the use of C-stat in testing models for X-ray spectra. *Astronomy & Astrophysics*, 605:A51, 2017. doi:10.1051/0004-6361/201629319.

[66] Philip J. Humphrey, Wenhao Liu, and David A. Buote. χ^2 AND POISSONIAN DATA: BIASES EVEN IN THE HIGH-COUNT REGIME AND HOW TO AVOID THEM. *The Astrophysical Journal*, 693(1):822–829, March 2009. doi:10.1088/0004-637x/693/1/822.

[67] W. Cash. Generation of Confidence Intervals for Model Parameters in X-ray Astronomy. *Astronomy and Astrophysics*, 52:307, October 1976.

[68] Andrew Gelman, Jessica Hwang, and Aki Vehtari. Understanding Predictive Information Criteria for Bayesian Models. *Statistics and Computing*, 24(6):997–1016, November 2014. doi:10.1007/s11222-013-9416-2.

[69] Hirotogu Akaike. *Information Theory and an Extension of the Maximum Likelihood Principle*, pages 199–213. Springer New York, New York, NY, 1998. doi:10.1007/978-1-4612-1694-0_15.

[70] Joseph E. Cavanaugh and Andrew A. Neath. The Akaike information criterion: Background, derivation, properties, application, interpretation, and refinements. *WIREs Computational Statistics*, 11(3):e1460, 2019. doi:10.1002/wics.1460.

[71] S. Kullback and R. A. Leibler. On Information and Sufficiency. *Ann. Math. Statist.*, 22(1):79–86, March 1951. doi:10.1214/aoms/1177729694.

[72] Kenneth P. Burnham, David R. Anderson, and Kathryn P. Huyvaert. AIC model selection and multimodel inference in behavioral ecology: some background, observations, and comparisons. *Behavioral Ecology and Sociobiology*, 65(1):23–35, August 2010. doi:10.1007/s00265-010-1029-6.

[73] Matthew Symonds and Adnan Moussalli. A brief guide to model selection, multimodel inference and model averaging in behavioural ecology using Akaike's information criterion. *Behav. Ecol. Sociobiol.*, 65:13–21, January 2011. doi:10.1007/s00265-010-1037-6.

[74] Roger Mundry. Issues in information theory-based statistical inference - a commentary from a frequentist's perspective. *Behavioral Ecology and Sociobiology*, 65(1):57–68, 2011. doi:10.1007/s00265-010-1040-y.

[75] M Araya. G279.0+1.1: a new extended source of high-energy gamma-rays. *Monthly Notices of the Royal Astronomical Society*, 492(4):5980–5986, January 2020. doi:10.1093/mnras/staa244.

[76] Yu-Liang Xin, Neng-Hui Liao, Xiao-Lei Guo, *et al.* HESS J1640-465: A Gamma-Ray Emitting Pulsar Wind Nebula? *The Astrophysical Journal*, 867(1):55, October 2018. doi:10.3847/1538-4357/aae313.

[77] Ambrogi, L., Zanin, R., Casanova, S., *et al.* Spectral and morphological study of the gamma radiation of the middle-aged supernova remnant HB 21. *Astronomy & Astrophysics*, 623:A86, 2019. doi:10.1051/0004-6361/201833985.

[78] Tibaldo, L., Zanin, R., Faggioli, G., *et al.* Disentangling multiple high-energy emission components in the Vela X pulsar wind nebula with the Fermi Large Area Telescope. *Astronomy & Astrophysics*, 617:A78, 2018. doi:10.1051/0004-6361/201833356.

[79] A. Donath, C. Deil, M. Paz Arribas, *et al.* Gammapy: An open-source Python package for gamma-ray astronomy. In *34th International Cosmic Ray Conference (ICRC2015)*, volume 34, page 789, July 2015.

[80] Nigro, C., Deil, C., Zanin, R., *et al.* Towards open and reproducible multi-instrument analysis in gamma-ray astronomy. *Astronomy & Astrophysics*, 625:A10, 2019. doi:10.1051/0004-6361/201834938.

[81] Mathieu de Naurois and Daniel Mazin. Ground-based detectors in very-high-energy gamma-ray astronomy. *Comptes Rendus Physique*, 16(6):610 – 627, 2015. doi:https://doi.org/10.1016/j.crhy.2015.08.011. Gamma-ray astronomy / Astronomie des rayons gamma.

[82] H.E.S.S. Collaboration, Abdalla, H., Abramowski, A., *et al.* Deeper H.E.S.S. observations of Vela Junior (RX J0852.0-4622): Morphology studies and resolved spectroscopy. *Astronomy & Astrophysics*, 612:A7, 2018. doi:10.1051/0004-6361/201630002.

[83] B. Westerlund. A Heavily Reddened Cluster in Ara. *Astronomical Journal*, 66:57–57, March 1961. doi:10.1086/108585.

[84] Simon F. Portegies Zwart, Stephen L.W. McMillan, and Mark Gieles. Young Massive Star Clusters. *Annual Review of Astronomy and Astrophysics*, 48(1):431–493, 2010. doi:10.1146/annurev-astro-081309-130834.

[85] Mark R. Krumholz, Christopher F. McKee, and Joss Bland-Hawthorn. Star Clusters Across Cosmic Time. *Annual Review of Astronomy and Astrophysics*, 57(1):227–303, 2019. doi:10.1146/annurev-astro-091918-104430.

[86] E. Sabbi, M. Gennaro, J. Anderson, *et al.* Time-domain Study of the Young Massive Cluster Westerlund 2 with the Hubble Space Telescope. I. *The Astrophysical Journal*, 891(2):182, March 2020. doi:10.3847/1538-4357/ab7372.

[87] Y. Fukui, K. Torii, A. Ohama, *et al.* THE TWO MOLECULAR CLOUDS IN RCW 38: EVIDENCE FOR THE FORMATION OF THE YOUNGEST SUPER STAR CLUSTER IN THE MILKY WAY TRIGGERED BY CLOUD–CLOUD COLLISION. *The Astrophysical Journal*, 820(1):26, March 2016. doi:10.3847/0004-637x/820/1/26.

[88] Daniel Rouan. *HII Region*, pages 705–705. Springer Berlin Heidelberg, Berlin, Heidelberg, 2011. doi:10.1007/978-3-642-11274-4_723.

[89] J E Drew, A Herrero, M Mohr-Smith, *et al.* Massive stars in the hinterland of the young cluster, Westerlund 2. *Monthly Notices of the Royal Astronomical Society*, 480(2):2109–2124, July 2018. doi:10.1093/mnras/sty1905.

[90] Peter Zeidler, Elena Sabbi, Antonella Nota, *et al.* A High-resolution Multiband Survey of Westerlund 2 with the Hubble Space Telescope. I. Is the Massive Star Cluster Double? *The Astronomical Journal*, 150(3):78, August 2015. doi:10.1088/0004-6256/150/3/78.

[91] Peter Zeidler, Eva K. Grebel, Antonella Nota, *et al.* A HIGH-RESOLUTION MULTIBAND SURVEY OF WESTERLUND 2 WITH THEHUBBLE SPACE TELESCOPE. II. MASS ACCRETION IN THE PRE-MAIN-SEQUENCE POPULATION. *The Astronomical Journal*, 152(4):84, September 2016. doi:10.3847/0004-6256/152/4/84.

[92] Peter Zeidler, Antonella Nota, Eva K. Grebel, *et al.* A High-resolution Multiband Survey of Westerlund 2 with theHubble Space Telescope. III. The Present-day Stellar Mass Function. *The Astronomical Journal*, 153(3):122, February 2017. doi:10.3847/1538-3881/153/3/122.

[93] Peter Zeidler, Antonella Nota, Eva K. Grebel, *et al.* Erratum: "A High-resolution Multiband Survey of Westerlund 2 with the Hubble Space Telescope. III. The Present-day Stellar Mass Function" (2017, AJ, 153, 122). *The Astronomical Journal*, 159(3):127, February 2020. doi:10.3847/1538-3881/ab701f.

[94] H. Hur, B.-G. Park, H. Sung, *et al.* Reddening, distance, and stellar content of the young open cluster Westerlund 2. *Monthly Notices of the Royal Astronomical Society*, 446:3797–3819, February 2015. doi:10.1093/mnras/stu2329.

[95] Carraro, G., Turner, D., Majaess, D., and Baume, G. The distance to the young open cluster Westerlund 2. *Astronomy & Astrophysics*, 555:A50, July 2013. doi:10.1051/0004-6361/201321421.

[96] Carlos A. Vargas Álvarez, Henry A. Kobulnicky, David R. Bradley, *et al.* THE DISTANCE TO THE MASSIVE GALACTIC CLUSTER WESTERLUND 2 FROM A SPECTROSCOPIC ANDHSTPHOTOMETRIC STUDY,,. *The Astronomical Journal*, 145(5):125, March 2013. doi:10.1088/0004-6256/145/5/125.

[97] Rauw, G., Sana, H., and Nazé, Y. A spectroscopic investigation of early-type stars in the young open cluster Westerlund. *Astronomy & Astrophysics*, 535:A40, 2011. doi:10.1051/0004-6361/201117000.

[98] Paula Benaglia, Baerbel Koribalski, Cintia S. Peri, *et al.* High resolution radio emission from RCW 49/Westerlund 2. *Astronomy & Astrophysics*, 559:A31, 2013. doi:10.1051/0004-6361/201321976.

[99] Rauw, G., De Becker, M., Nazé, Y., *et al.* WR: A massive cornerstone binary system comprising two extreme early-type stars*. *Astronomy & Astrophysics*, 420(2):L9–L13, 2004. doi:10.1051/0004-6361:20040150.

[100] N. Furukawa, J. R. Dawson, A. Ohama, *et al.* MOLECULAR CLOUDS TOWARD RCW49 AND WESTERLUND 2: EVIDENCE FOR CLUSTER FORMATION TRIGGERED BY CLOUD-CLOUD COLLISION. *The Astrophysical Journal*, 696(2):L115–L119, April 2009. doi:10.1088/0004-637x/696/2/l115.

[101] A. Ohama, J. R. Dawson, N. Furukawa, *et al.* TEMPERATURE AND DENSITY DISTRIBUTION IN THE MOLECULAR GAS TOWARD WESTERLUND 2: FURTHER EVIDENCE FOR PHYSICAL ASSOCIATION. *The Astrophysical Journal*, 709(2):975–982, January 2010. doi:10.1088/0004-637x/709/2/975.

[102] B. N. Swanenburg, K. Bennett, G. F. Bignami, *et al.* Second COS B catalog of high-energy gamma-ray sources. *The Astrophysical Journal Letters*, 243:L69–L73, January 1981. doi:10.1086/183445.

[103] C. E. Fichtel, D. L. Bertsch, J. Chiang, *et al.* The first energetic gamma-ray experiment telescope (EGRET) source catalog. *The Astrophysical Journal Supplement Series*, 94:551–581, October 1994. doi:10.1086/192082.

[104] D. J. Thompson, D. L. Bertsch, B. L. Dingus, *et al.* The Second EGRET Catalog of High-Energy Gamma-Ray Sources. *The Astrophysical Journal Supplement Series*, 101:259, December 1995. doi:10.1086/192240.

[105] O. Reimer, B. L. Dingus, P. L. Nolan, and EGRET Collaboration. EGRET Gamma Ray point sources above 1 GeV. *Proceedings of the 25th International Cosmic Ray Conference*, 3:97, 1997.

[106] R. C. Lamb and D. J. Macomb. Point Sources of GeV Gamma Rays. *The Astrophysical Journal*, 488(2):872–880, October 1997. doi:10.1086/304736.

[107] R. C. Hartman, D. L. Bertsch, S. D. Bloom, *et al.* The Third EGRET Catalog of High-Energy Gamma-Ray Sources. *The Astrophysical Journal Supplement Series*, 123(1):79–202, July 1999. doi:10.1086/313231.

[108] G. E. Romero, P. Benaglia, and D. F. Torres. Unidentified 3EG gamma-ray sources at low galactic latitudes. *Astronomy & Astrophysics*, 348:868–876, August 1999.

[109] Casandjian, J.-M. and Grenier, I. A. A revised catalogue of EGRET γ-ray sources. *Astronomy & Astrophysics*, 489(2):849–883, 2008. doi:10.1051/0004-6361:200809685.

[110] F. Aharonian, A. G. Akhperjanian, A. R. Bazer-Bachi, *et al.* Detection of extended very-high-energy γ-ray emission towards the young stellar cluster Westerlund 2. *Astronomy and Astrophysics*, 467(3):1075–1080, June 2007. doi:10.1051/0004-6361:20066950.

[111] M. J. Keith, S. Johnston, M. Kramer, *et al.* A high-frequency search for radio pulsars in three EGRET error boxes. *Monthly Notices of the Royal Astronomical Society*, 389(4):1881–1884, October 2008. doi:10.1111/j.1365-2966.2008.13711.x.

[112] A. A. Abdo, M. Ackermann, W. B. Atwood, *et al.* Discovery of pulsed γ-rays from the young radio pulsar PSR J1028–5819 with the Fermi Large Area Telescope. *The Astrophysical Journal*, 695(1):L72–L77, March 2009. doi:10.1088/0004-637x/695/1/l72.

[113] A. A. Abdo, M. Ackermann, M. Ajello, *et al.* FERMI/LARGE AREA TELESCOPE BRIGHT GAMMA-RAY SOURCE LIST. *The Astrophysical Journal Supplement Series*, 183(1):46–66, June 2009. doi:10.1088/0067-0049/183/1/46.

[114] Pittori, C., Verrecchia, F., Chen, A. W., *et al.* First AGILE catalog of high-confidence gamma-ray sources. *Astronomy & Astrophysics*, 506(3):1563–1574, 2009. doi:10.1051/0004-6361/200911783.

[115] A. A. Abdo, M. Ackermann, M. Ajello, *et al.* FERMI/LARGE AREA TELESCOPE FIRST SOURCE CATALOG. *The Astrophysical Journal Supplement Series*, 188(2):405–436, May 2010. doi:10.1088/0067-0049/188/2/405.

[116] P. M. Saz Parkinson, M. Dormody, M. Ziegler, *et al.* Eight γ-ray pulsars discovered in blind frequency searches of Fermi LAT data. *The Astrophysical Journal*, 725(1):571–584, November 2010. doi:10.1088/0004-637x/725/1/571.

[117] H.E.S.S. Collaboration, Abramowski, A., Acero, F., *et al.* Discovery of VHE emission towards the Carina arm region with the H.E.S.S. telescope array: HESS 1018–589. *Astronomy & Astrophysics*, 541:A5, 2012. doi:10.1051/0004-6361/201218843.

[118] H. E. S. S. Collaboration, A. Abramowski, F. Aharonian, *et al.* Discovery of variable VHE γ-ray emission from the binary system 1FGL J1018.6-5856. *Astronomy & Astrophysics*, 577:A131, May 2015. doi:10.1051/0004-6361/201525699.

[119] M. Ackermann, M. Ajello, L. Baldini, *et al.* Search for Extended Sources in the Galactic Plane Using Six Years of Fermi-Large Area Telescope Pass 8 Data above 10 GeV. *The Astrophysical Journal*, 843(2):139, July 2017. doi:10.3847/1538-4357/aa775a.

[120] Rui-zhi Yang, Emma de Oña Wilhelmi, and Felix Aharonian. Diffuse γ-ray emission in the vicinity of young star cluster Westerlund 2. *Astronomy & Astrophysics*, 611:A77, 2018. doi:10.1051/0004-6361/201732045.

[121] H. E. S. S. Collaboration, H. Abdalla, A. Abramowski, *et al.* The H.E.S.S. Galactic plane survey. *Astronomy & Astrophysics*, 612:A1, April 2018. doi:10.1051/0004-6361/201732098.

[122] Bulgarelli, A., Fioretti, V., Parmiggiani, N., *et al.* Second AGILE catalogue of gamma-ray sources. *Astronomy & Astrophysics*, 627:A13, 2019. doi:10.1051/0004-6361/201834143.

[123] S. Abdollahi, F. Acero, M. Ackermann, *et al.* Fermi Large Area Telescope Fourth Source Catalog. *The Astrophysical Journal Supplement Series*, 247(1):33, March 2020. doi:10.3847/1538-4365/ab6bcb.

[124] Yasuo Fukui *et al.* A peculiar jet and arc of molecular gas toward the rich and young stellar cluster Westerlund 2 and a TeV gamma ray source. *Publ. Astron. Soc. Jap.*, 61:L23, 2009. doi:10.1093/pasj/61.4.L23.

[125] J. HAWKES, G. ROWELL, B. DAWSON, *et al.* INVESTIGATION OF DENSE GAS TOWARDS RELATIVISTIC OUTFLOW SOURCES. *International Journal of Modern Physics: Conference Series*, 28:1460198, January 2014. doi:10.1142/s2010194514601987.

[126] M. Tsujimoto, E. D. Feigelson, L. K. Townsley, *et al.* An X-Ray Imaging Study of the Stellar Population in RCW 49. *The Astrophysical Journal*, 665(1):719–735, August 2007. doi:10.1086/519681.

[127] Nazé, Y., Rauw, G., and Manfroid, J. Chandra monitoring of the very massive binary WR20a and the young massive cluster Westerlund. *Astronomy & Astrophysics*, 483(1):171–182, 2008. doi:10.1051/0004-6361:20078851.

[128] W. Bednarek. γ-ray production in young open clusters: Berk 87, Cyg OB2 and Westerlund 2. *Monthly Notices of the Royal Astronomical Society*, 382(1):367–376, 2007. doi:10.1111/j.1365-2966.2007.12373.x.

[129] Luis A. Anchordoqui, John F. Beacom, Yousaf M. Butt, *et al.* TeV gamma-rays from photo-disintegration/de-excitation of nuclei in Westerlund 2. In *30th International Cosmic Ray Conference*, volume 2, pages 625–628, June 2007.

[130] Yutaka Fujita, Kiyoshi Hayashida, Hiroaki Takahashi, and Fumio Takahara. Suzaku Observation of Diffuse X-Ray Emission from the Open Cluster Westerlund 2: a Hypernova Remnant? *Publications of the Astronomical Society of Japan*, 61(6):1229–1235, December 2009. doi:10.1093/pasj/61.6.1229.

[131] Leisa K. Townsley, Patrick S. Broos, Gordon P. Garmire, and Matthew S. Povich. The Massive Star-forming Regions Omnibus X-ray Catalog, Third Installment. *The Astrophysical Journal Supplement Series*, 244(2):28, October 2019. doi:10.3847/1538-4365/ab345b.

[132] A. Albert, M. André, M. Anghinolfi, *et al.* ANTARES and IceCube Combined Search for Neutrino Point-like and Extended Sources in the Southern Sky. *The Astrophysical Journal*, 892(2):92, April 2020. doi:10.3847/1538-4357/ab7afb.

[133] Stefan Gillessen. *Sub-Bogenminuten-genaue Positionen von TeV-Quellen mit H.E.S.S.* PhD thesis, Ruprecht-Karls-Universität Heidelberg, July 2004. DOI: `https://doi.org/10.11588/heidok.00004754`.

[134] N. M. McClure-Griffiths, John M. Dickey, B. M. Gaensler, *et al.* The Southern Galactic Plane Survey: HI Observations and Analysis. *The Astrophysical Journal Supplement Series*, 158(2):178–187, June 2005. doi:10.1086/430114.

[135] M. Haverkorn, B. M. Gaensler, N. M. McClure-Griffiths, J. M. Dickey, and A. J. Green. The Southern Galactic Plane Survey: Polarized Radio Continuum Observations and Analysis. *The Astrophysical Journal Supplement Series*, 167(2):230–238, December 2006. doi:10.1086/508467.

[136] Mark G. Wolfire, David Hollenbach, and Christopher F. McKee. THE DARK MOLECULAR GAS. *The Astrophysical Journal*, 716(2):1191–1207, May 2010. doi:10.1088/0004-637x/716/2/1191.

[137] Isabelle A. Grenier, Jean-Marc Casandjian, and Régis Terrier. Unveiling Extensive Clouds of Dark Gas in the Solar Neighborhood. *Science*, 307(5713):1292–1295, 2005. doi:10.1126/science.1106924.

[138] Julia Roman-Duval, James M. Jackson, Mark Heyer, *et al.* Kinematic Distances to Molecular Clouds identified in the Galactic Ring Survey. *The Astrophysical Journal*, 699:1153–1170, 2009. doi:10.1088/0004-637X/699/2/1153.

[139] Paul J. McMillan. The mass distribution and gravitational potential of the Milky Way. *Monthly Notices of the Royal Astronomical Society*, 465(1):76–94, October 2016. doi:10.1093/mnras/stw2759.

[140] Jo Bovy. galpy: A python LIBRARY FOR GALACTIC DYNAMICS. *The Astrophysical Journal Supplement Series*, 216(2):29, February 2015. doi:10.1088/0067-0049/216/2/29.

[141] Joss Bland-Hawthorn and Ortwin Gerhard. The Galaxy in Context: Structural, Kinematic, and Integrated Properties. *Annual Review of Astronomy and Astrophysics*, 54(1):529–596, 2016. doi:10.1146/annurev-astro-081915-023441.

[142] Yuta Asahina, Tomohisa Kawashima, Naoko Furukawa, *et al.* Magnetohydrodynamic Simulations of the Formation of Molecular Clouds toward the Stellar Cluster Westerlund 2: Interaction of a Jet with a Clumpy Interstellar Medium. *The Astrophysical Journal*, 836(2):213, February 2017. doi:10.3847/1538-4357/aa5c86.

[143] Munan Gong, Eve C. Ostriker, and Chang-Goo Kim. The X_{CO} Conversion Factor from Galactic Multiphase ISM Simulations. *The Astrophysical Journal*, 858(1):16, April 2018. doi:10.3847/1538-4357/aab9af.

[144] Alberto D. Bolatto, Mark Wolfire, and Adam K. Leroy. The CO-to-H2 Conversion Factor. *Annual Review of Astronomy and Astrophysics*, 51(1):207–268, 2013. doi:10.1146/annurev-astro-082812-140944.

[145] T. M. Dame, Dap Hartmann, and P. Thaddeus. The Milky Way in Molecular Clouds: A New Complete CO Survey. *The Astrophysical Journal*, 547(2):792–813, February 2001. doi:10.1086/318388.

[146] M. J. Keith, S. Johnston, M. Kramer, *et al.* A high-frequency search for radio pulsars in three EGRET error boxes. *Monthly Notices of the Royal Astronomical Society*, 389(4):1881–1884, September 2008. doi:10.1111/j.1365-2966.2008.13711.x.

[147] R. N. Manchester, G. B. Hobbs, A. Teoh, and M. Hobbs. The Australia Telescope National Facility Pulsar Catalogue. *The Astronomical Journal*, 129(4):1993–2006, April 2005. doi:10.1086/428488.

[148] Oleg Kargaltsev, Martin Durant, George G. Pavlov, and Gordon Garmire. CHANDRA PULSAR SURVEY (ChaPS). *The Astrophysical Journal Supplement Series*, 201(2):37, August 2012. doi:10.1088/0067-0049/201/2/37.

[149] H.E.S.S. Collaboration, Abdalla, H., Abramowski, A., *et al.* The population of TeV pulsar wind nebulae in the H.E.S.S. Galactic Plane Survey. *Astronomy & Astrophysics*, 612:A2, 2018. doi:10.1051/0004-6361/201629377.

[150] M. Ackermann, M. Ajello, L. Baldini, *et al.* FERMI-LAT SEARCH FOR PULSAR WIND NEBULAE AROUND GAMMA-RAY PULSARS. *The Astrophysical Journal*, 726(1):35, December 2010. doi:10.1088/0004-637x/726/1/35.

[151] D. A. Leahy and J. E. Williams. A Python Calculator for Supernova Remnant Evolution. *The Astronomical Journal*, 153(5):239, May 2017. doi:10.3847/1538-3881/aa6af6.

[152] Denis Leahy, Yuyang Wang, Bryson Lawton, Sujith Ranasinghe, and Miroslav Filipović. Emission Measures and Emission-measure-weighted Temperatures of Shocked Interstellar Medium and Ejecta in Supernova Remnants. *The Astronomical Journal*, 158(4):149, September 2019. doi:10.3847/1538-3881/ab3d2c.

[153] Ken'Ichi Nomoto. First stars, hypernovae, and superluminous supernovae. *International Journal of Modern Physics D*, 25(10):1630025, July 2016. doi:10.1142/S0218271816300251.

[154] H.E.S.S. Collaboration, Abdalla, H., Abramowski, A., *et al.* Population study of Galactic supernova remnants at very high energies with H.E.S.S. *Astronomy & Astrophysics*, 612:A3, 2018. doi:10.1051/0004-6361/201732125.

[155] Stefano Gabici. Cosmic Rays and Molecular Clouds. In Diego F. Torres and Olaf Reimer, editors, *Cosmic Rays in Star-Forming Environments*, pages 221–247, Berlin, Heidelberg, 2013. Springer Berlin Heidelberg.

[156] Nigel I. Maxted, Gavin P. Rowell, Bruce R. Dawson, *et al.* Interstellar gas towards CTB 37A and the TeV gamma-ray source HESS J1714–385. *Monthly Notices of the Royal Astronomical Society*, 434(3):2188–2201, July 2013. doi:10.1093/mnras/stt1159.

[157] F. A. Aharonian. Very High and Ultra High Energy Gamma-Rays from Giant Molecular Clouds. *Astrophysics and Space Science*, 180(2):305–320, June 1991. doi:10.1007/BF00648185.

[158] Stefano Gabici and Thierry Montmerle. On the connection of gamma rays from supernova remnants interacting with molecular clouds and cosmic ray ionization measured. *PoS*, ICRC2015:029, 2016. doi:10.22323/1.236.0029.

[159] S. Gabici, F. A. Aharonian, and S. Casanova. Broad–band non–thermal emission from molecular clouds illuminated by cosmic rays from nearby supernova remnants. *Monthly Notices of the Royal Astronomical Society*, 396(3):1629–1639, June 2009. doi:10.1111/j.1365-2966.2009.14832.x.

[160] Eve C. Ostriker, James M. Stone, and Charles F. Gammie. Density, Velocity, and Magnetic Field Structure in Turbulent Molecular Cloud Models. *The Astrophysical Journal*, 546(2):980–1005, January 2001. doi:10.1086/318290.

[161] Dani Torres and Eva Domingo-Santamaria. Collective effects of stellar winds and unidentified gamma-ray sources. *Astrophysics and Space Science*, 309:345–350, December 2006. doi:10.1007/s10509-007-9475-y.

[162] Gustavo E. Romero. Gamma rays from colliding winds in massive binaries. *Rendiconti Lincei. Scienze Fisiche e Naturali*, page 3, January 2019. doi:10.1007/s12210-019-00763-2.

[163] Domingo-Santamaría, E. and Torres, D. F. Hadronic processes within collective stellar winds. *Astronomy & Astrophysics*, 448(2):613–622, 2006. doi:10.1051/0004-6361:20054027.

[164] O. Reimer, F. Aharonian, J. Hinton, *et al.* VHE gamma-rays from Westerlund 2 and implications for the inferred energetics. In Wolf-Rainer Hamann, Achim Feldmeier, and Lidia M. Oskinova, editors, *Clumping in Hot-Star Winds*, page 195, April 2008.

[165] Felix Aharonian, Ruizhi Yang, and Emma de Oña Wilhelmi. Massive Stars as Major Factories of Galactic Cosmic Rays. *Nature Astronomy*, 3(6):561–567, 2019. doi:10.1038/s41550-019-0724-0.

[166] Rui-Zhi Yang, Felix Aharonian, and Emma de Oña Wilhelmi. Massive star clusters as the an alternative source population of galactic cosmic rays. *Rendiconti Lincei. Scienze Fisiche e Naturali*, 30:159–164, July 2019. doi:10.1007/s12210-019-00819-3.

[167] Takahiro Sudoh, Yoshiyuki Inoue, and Dmitry Khangulyan. Multiwavelength Emission from Galactic Jets: The Case of the Microquasar SS433. *The Astrophysical Journal*, 889(2):146, February 2020. doi:10.3847/1538-4357/ab6442.

[168] Ke Fang, Eric Charles, and Roger D. Blandford. GeV–TeV Counterparts of SS 433/W50 from Fermi-LAT and HAWC Observations. *The Astrophysical Journal*, 889(1):L5, January 2020. doi:10.3847/2041-8213/ab62b8.

[169] F. Tramper, H. Sana, N. E. Fitzsimons, *et al.* The mass of the very massive binary WR21a. *Monthly Notices of the Royal Astronomical Society*, 455(2):1275–1281, November 2015. doi:10.1093/mnras/stv2373.

[170] Gosset, Eric and Nazé, Yaël. The X-ray light curve of the massive colliding wind Wolf-Rayet + O binary WR. *Astronomy & Astrophysics*, 590:A113, 2016. doi:10.1051/0004-6361/201527051.

[171] Benaglia, P., Romero, G. E., Koribalski, B., and Pollock, A. M. T. Multiwavelength studies of WR 21a its surroundings. *A&A*, 440(2):743–750, 2005. doi:10.1051/0004-6361:20042617.

[172] Benaglia, P. and Romero, G. E. Gamma-ray emission from Wolf-Rayet binaries. *Astronomy & Astrophysics*, 399(3):1121–1134, 2003. doi:10.1051/0004-6361:20021854.

[173] H.E.S.S. Collaboration, Abdalla, H., Adam, R., *et al.* Detection of very-high-energy emission from the colliding wind binary with H.E.S.S. *Astronomy & Astrophysics*, 635:A167, 2020. doi:10.1051/0004-6361/201936761.

[174] De Becker, M. and Raucq, F. Catalogue of particle-accelerating colliding-wind binaries. *Astronomy & Astrophysics*, 558:A28, 2013. doi:10.1051/0004-6361/201322074.

[175] S. Sabatini, M. Tavani, E. Pian, *et al.* Galactic sources science with AGILE: The case of the Carina Region. *Nuclear Instruments and Methods in Physics Research Section A: Accelerators, Spectrometers, Detectors and Associated Equipment*, 630(1):193 – 197, 2011. doi:https://doi.org/10.1016/j.nima.2010.06.062. Proceedings of the 2nd Roma International Conference on Astroparticle Physics (RICAP 2009).

[176] M. Ajello, W. B. Atwood, L. Baldini, *et al.* 3FHL: The Third Catalog of Hard Fermi -LAT Sources. *The Astrophysical Journal Supplement Series*, 232(2):18, September 2017. doi:10.3847/1538-4365/aa8221.

[177] F. Acero, M. Ackermann, M. Ajello, *et al.* FERMI/LARGE AREA TELESCOPE THIRD SOURCE CATALOG. *The Astrophysical Journal Supplement Series*, 218(2):23, June 2015. doi:10.1088/0067-0049/218/2/23.

[178] Michael M. Shara, Anthony F. J. Moffat, Jill Gerke, *et al.* A NEAR-INFRARED SURVEY OF THE INNER GALACTIC PLANE FOR WOLF-RAYET STARS. I. METHODS AND FIRST RESULTS: 41 NEW WR STARS. *The Astronomical Journal*, 138(2):402–420, June 2009. doi:10.1088/0004-6256/138/2/402.

[179] Christian Bernt Haakonsen and Robert E. Rutledge. XID II: STATISTICAL CROSS-ASSOCIATION OF ROSAT BRIGHT SOURCE CATALOG X-RAY SOURCES WITH 2MASS POINT SOURCE CATALOG NEAR-INFRARED SOURCES. *The Astrophysical Journal Supplement Series*, 184(1):138–151, August 2009. doi:10.1088/0067-0049/184/1/138.

[180] Ikhsanov, N. R. and Biermann, P. L. High-energy emission of fast rotating white dwarfs. *Astronomy & Astrophysics*, 445(1):305–312, 2006. doi:10.1051/0004-6361:20053179.

[181] Pieter Meintjes, Q Kaplan, Krishna Singh, H. van, and F Ramamonjisoa. White Dwarf Pulsars as Possible Gamma-Ray Sources. *Proceedings of Science*, HEASA2018:037, July 2019. doi:10.22323/1.338.0037.

[182] Leisa K. Townsley and Patrick S. Broos. MOXC3 data products, June 2019. doi:10.5281/zenodo.3367450.

[183] V. Zabalza. naima: a Python package for inference of relativistic particle energy distributions from observed nonthermal spectra. *Proc. of International Cosmic Ray Conference 2015*, page 922, 2015.

[184] Volker Blobel and Erich Lohrmann. *Statistische und numerische Methoden der Datenanalyse*. Teubner Studienbücher Physik. Teubner, Stuttgart, 1998.

[185] Steve Baker and Robert D. Cousins. Clarification of the use of CHI-square and likelihood functions in fits to histograms. *Nuclear Instruments and Methods in Physics Research*, 221(2):437 – 442, 1984. doi:https://doi.org/10.1016/0167-5087(84)90016-4.

[186] P. L. Nolan, A. A. Abdo, M. Ackermann, *et al.* FERMI/LARGE AREA TELESCOPE SECOND SOURCE CATALOG. *The Astrophysical Journal Supplement Series*, 199(2):31, March 2012. doi:10.1088/0067-0049/199/2/31.

[187] M. Ackermann, M. Ajello, A. Allafort, *et al.* THE FIRSTFERMI-LAT CATALOG OF SOURCES ABOVE 10 GeV. *The Astrophysical Journal Supplement Series*, 209(2):34, November 2013. doi:10.1088/0067-0049/209/2/34.

[188] Verrecchia, F., Pittori, C., Chen, A. W., *et al.* An updated list of AGILE bright sources and their variability in pointing mode. *Astronomy & Astrophysics*, 558:A137, 2013. doi:10.1051/0004-6361/201321452.

[189] M. Ackermann, M. Ajello, W. B. Atwood, *et al.* 2FHL: THE SECOND CATALOG OF HARD FERMI -LAT SOURCES. *The Astrophysical Journal Supplement Series*, 222(1):5, January 2016. doi:10.3847/0067-0049/222/1/5.